UNIVERSITY OF OKLAHOMA
GRADUATE COLLEGE

# EXPERIMENTAL TESTING, IMAGE-BASED ANALYSIS, AND FINITE ELEMENT SIMULATION OF THE TRICUSPID VALVE: TOWARDS PERSONALIZED MANAGEMENT OF HYPOPLASTIC LEFT HEART SYNDROME

A DISSERTATION
SUBMITTED TO THE GRADUATE FACULTY
in partial fulfillment of the requirements for the
Degree of
DOCTOR OF PHILOSOPHY

By
COLTON JAY ROSS
Norman, Oklahoma
2023

Downloaded from SHAREOK. Persistent Handle URL: https://hdl.handle.net/11244/337498

EXPERIMENTAL TESTING, IMAGE-BASED ANALYSIS, AND
FINITE ELEMENT SIMULATION OF THE TRICUSPID VALVE:
TOWARDS PERSONALIZED MANAGEMENT OF
HYPOPLASTIC LEFT HEART SYNDROME

A DISSERTATION APPROVED FOR THE
SCHOOL OF AEROSPACE AND MECHANICAL ENGINEERING

BY THE COMMITTEE CONSISTING OF

Dr. Chung-Hao Lee, Chair
Dr. Kuang-Hua Chang
Dr. Yingtao Liu
Dr. Qinggong Tang
Dr. Chenkai Dai

© Copyright by COLTON JAY ROSS 2023
All Rights Reserved.

**To my family**

*Your love and support made this all possible. I could not have done this without you.*

## CONTENTS

**List of Tables** **xi**

**List of Figures** **xxi**

**Acknowledgments** **xxii**

**Abstract** **xxiii**

**1 Introduction** **1**

1.1 Motivation . . . . . 1

1.2 Objective and Scope . . . . . 2

**2 Background and Literature Review** **5**

2.1 The Tricuspid Valve, Tricuspid Regurgitation, and Hypoplastic Left Heart Syndrome . . . . . 5

2.2 Tricuspid Valve Biomechanics . . . . . 6

2.2.1 Leaflet Morphology and Microstructure . . . . . 6

2.2.2 Tissue Biomechanics . . . . . 7

2.2.3 Microstructural Quantification for the TV Leaflets . . . . . 17

2.2.4 Simulation of Tricuspid Valve Function . . . . . 20

2.2.5 Inverse Analysis of Tricuspid Valves . . . . . 22

2.3 Hypoplastic Left Heart Syndrome . . . . . 23

2.3.1 Tricuspid Regurgitation as a Predictor of Mortality . . . . . 25

2.3.2 Identified Indicators of TR in HLHS . . . . . 27

2.4 Lacking Knowledge and Future Perspectives . . . . . 33

2.4.1 Proposed Research in Tricuspid Valve Leaflet Biomechanics . . . . . 34

2.4.2 Propose Studies for Improving the Understanding of HLHS . . . . . 35

2.4.3 An Improved Understanding of TR — Engineering Insights . . . . . 35

2.5 Structure of the Dissertation . . . . . 36

**3 Effects of Enzyme-based Removal of Collagen and Elastin Constituents on the Biaxial Mechanical Responses of Porcine Atrioventricular Heart Valve Anterior Leaflets** **37**
3.1 Motivation . . . 38
3.2 Methods . . . 38
3.2.1 Tissue Acquisition and Preparation . . . 38
3.2.2 Biaxial Testing Procedure . . . 38
3.2.3 Enzymatic Treatment for Elastin and Collagen Degradation . . . 40
3.2.4 Histological Assessment of Tissue Constituents . . . 41
3.2.5 Verification of Histological Analysis Methods . . . 42
3.2.6 Tissue Stretch and Stress Calculations . . . 42
3.2.7 Statistical Analyses . . . 45
3.3 Results . . . 45
3.3.1 Histological Results . . . 45
3.3.2 Histology Analysis Verification . . . 48
3.3.3 Thickness Measurements . . . 48
3.3.4 Biaxial Tensile Testing . . . 48
3.3.5 Biaxial Stress Relaxation . . . 53
3.4 Discussion . . . 58
3.4.1 Overall Findings . . . 58
3.4.2 Study Limitations and Future Extensions . . . 68
3.5 Chapter Summary . . . 71
**4 Evaluation of Affine Fiber Kinematics in Porcine Tricuspid Valve Leaflets Using Polarized Spatial Frequency Domain Imaging and Planar Biaxial Testing** **72**
4.1 Motivation . . . 73
4.2 Methods . . . 73
4.2.1 Tissue Acquisition and Preparation . . . 73
4.2.2 Biaxial Mechanical Testing . . . 74
4.2.3 Quantification of the Load-Dependent Changes in Collagen Fiber Architecture . . . 75
4.2.4 Application of the Affine Fiber Kinematics Theory . . . 76
4.2.5 Statistical Analysis . . . 77
4.3 Results . . . 77

4.3.1 Biaxial Mechanical Properties of the Tricuspid Valve Leaflets . . . . 77
4.3.2 Experimentally Measured Collagen Fiber Architectures . . . . . 79
4.3.3 Evaluation of the AFK Predictivity . . . . . 79
4.4 Discussion . . . . . 86
4.4.1 Differences in Experimental and Predicted Collagen Fiber Reorientations . . . . . 86
4.4.2 Considerations for Constitutive Modeling Using Affine Fiber Kinematics . . . . . 90
4.4.3 Limitations and Future Extensions . . . . . 91
4.5 Chapter Summary . . . . . 91

**5 Non-Invasive Geometric and Engineering Analysis of the HLHS-Afflicted Pediatric Tricuspid Valve Annulus 93**

5.1 Motivation . . . . . 94
5.2 Methods . . . . . 94
5.2.1 Study Population . . . . . 94
5.2.2 Echocardiogram Imaging and Image Segmentation . . . . . 94
5.2.3 Geometry- and Engineering Mechanics-Based Analyses for the TV Annulus . . . . . 98
5.2.4 Statistical Analysis . . . . . 100
5.3 Results . . . . . 101
5.3.1 TV Annulus Geometric Features in Newborns with HLHS . . . . . 101
5.3.2 TV Annulus Mechanics for newborns with HLHS . . . . . 102
5.3.3 Differences between Healthy and HLHS-Afflicted Newborns . . . . . 102
5.4 Discussion . . . . . 111
5.4.1 Comparisons between Healthy and newborns with HLHS . . . . . 111
5.4.2 Development of Tricuspid Regurgitation in newborns with HLHS . . 112
5.4.3 Comparisons to Previous TV Annulus Biomechanics Studies . . . . . 112
5.4.4 Clinical Relevance and Translatability of the TV Annulus Pipeline . . 113
5.4.5 Limitations and Future Extensions . . . . . 113
5.5 Chapter Summary . . . . . 114

**6 Inverse Finite Element Analysis of Nonlinear Materials Using Bayesian Optimization for Applications in Atrioventricular Heart Valve Simulation 115**

6.1 Motivation . . . . . 116
6.2 Inverse Finite Element Analysis Approach . . . . . 116

6.2.1 Objective Function . . . 116
6.2.2 Overview of Bayesian Optimization . . . 117
6.2.3 Implementation of Bayesian Optimization . . . 119
6.2.4 Analysis of Optimization Results . . . 119
6.2.5 Material Modeling . . . 119
6.2.6 Simulation Conditions . . . 120
6.3 Inflation Testing . . . 120
6.3.1 Inflation Simulation Sub-Studies . . . 122
6.4 Leaflet Contact . . . 124
6.4.1 A Novel Approach for iFEA of Leaflet Contact . . . 127
6.5 Idealized Valve Geometry . . . 129
6.5.1 Real Application: Analysis with a Representative Patient with HLHS . . . 129
6.6 Discussion . . . 134
6.6.1 Bayesian Optimization . . . 134
6.6.2 Novel Approach to Inverse Analysis of the Atrioventricular Heart Valves . . . 135
6.6.3 Limitations . . . 136
6.7 Chapter Summary . . . 136

**7 Conclusions and Future Work 137**
7.1 Summary of the Dissertation . . . 137
7.2 Future Investigations . . . 139
7.2.1 Incorporation of Pre-Strains . . . 139
7.2.2 Non-Invasive Analysis of Tissue Biomechanics . . . 144
7.2.3 Statistical Analysis Designs in TR-Related HLHS Research . . . 145

**A Fitted Model Parameters for the Viscoelastic Characterization of Collagen- and Elastin-Removed Tricuspid Valve Leaflets 156**

**B Verification of Bayesian Optimization with the Branin Function 165**

**References 168**

## LIST OF TABLES

Table 2-1 The mean strain values relative to baseline at end-diastole (ED) and end-systole (ES) for each level of De Vega (DV) cinching [46]. Note that each step of DV cinching is $\sim$2 mm of the total annular diameter. Abbreviations: circ, circumferential; rad, radial. . . . . 17

Table 3-1 Quantified area fraction of elastin in three control and elastase-treated MVAL and TVAL tissues from the intermediate study (see **Section 3.2.4**) over a 120 min treatment time. The results are shown as mean$\pm$SEM. Note:$\sim$100% elastin reduction for the treated samples indicate almost traceless elastin components in the histology images. *Only one of the three analyzed specimens contained quantifiable elastin contents. . . . . 46

Table 3-2 Quantified area fraction of collagen in three control and collagenase-treated MVAL and TVAL tissues from the intermediate study (see **Section 3.2.3**) over a 120 min treatment time. The results are shown as mean$\pm$SEM. . 48

Table 3-3 Quantified median fiber angle and half of the interquartile range (IQR) for control (–C) and elastin-removed (–T) MVAL and TVAL specimens ($n = 5$), as obtained from polarized spatial frequency domain imaging. Half of the IQR is reported for easier interpretation of the results. Note that the 0° reference angle corresponds to the tissue's circumferential (circ) direction. . . 69

Table 3-4 Quantified median fiber angle and half of the interquartile range (IQR) for control (–C) and elastin- and collagen-removed (–T) MVAL and TVAL specimens ($n = 5$), as obtained from polarized spatial frequency domain imaging. Half of the IQR is reported for easier interpretation of the results. Note that the 0° reference angle corresponds to the tissue's circumferential (circ) direction. . . . . 70

Table 4-1 The post-preconditioning (PPC) stretches and peak stretches of the TVAL, TVPL, and TVSL specimens under the five applied biaxial tensions ($T_{\text{circ}}$:$T_{\text{rad}}$). Results are presented as the mean$\pm$SEM. Abbreviations: circ, circumferential; rad, radial. . . . . 83

Table 4-2 Comparisons of the collagen fiber angle between the pSFDI measurements and AFK predictions at the post-preconditioning (PPC) and peak equibiaxial deformations ($T_{\text{circ}}$:$T_{\text{rad}} = 1$:1) for all TVAL specimens. $\theta_{\text{median}}$ and IQR are provided for the $100 \times 100$ grids considered for each specimen, and the $\theta_{\text{error}}$ between the measured and predicted fiber orientations at the peak deformation are expressed as the mean$\pm$SD. . . . . 83

Table 4-3 Comparisons of the collagen fiber angle between the pSFDI measurements and AFK predictions at the post-preconditioning (PPC) and peak equibiaxial deformations ($T_{\text{circ}}$:$T_{\text{rad}} = 1$:1) for all TVPL specimens. $\theta_{\text{median}}$ and IQR are provided for the $100 \times 100$ grids considered for each specimen, and the $\theta_{\text{error}}$ between the measured and predicted fiber orientations at the peak deformation are expressed as the mean$\pm$SD. . . . . 84

Table 4-4 Comparisons of the collagen fiber angle between the pSFDI measurements and AFK predictions at the post-preconditioning (PPC) and peak equibiaxial deformations ($T_{\text{circ}}$:$T_{\text{rad}} = 1$:1) for all TVSL specimens. $\theta_{\text{median}}$ and IQR are provided for the $100 \times 100$ grids considered for each specimen, and the $\theta_{\text{error}}$ between the measured and predicted fiber orientations at the peak deformation are expressed as the mean$\pm$SD. . . . . 85

Table 5-1 Patient characteristics for the HLHS-afflicted and healthy newborns considered in this study. Note that the diameter of the ascending aorta, RVFAC, and TAPSE scores were not measured in the healthy patients. Abbreviations: TAPSE – tricuspid annular plane systolic excursion; RVFAC – right ventricular fractional area change; MS – mitral stenosis; AoS – aortic stenosis; AoA – aortic atresia. . . . . 95

Table 7-1 Range of geometric parameters used to construct the pseudo-population for the multivariate logistic modeling demonstration. Note that the mentioned average values are based on our preliminary observations of a cohort of $n = 8$ neonates born with HLHS. . . . . 147

Table 7-2 Coefficients determined for the multivariate logistic models considering 3, 5 or 7 terms, together with the respective area under the curve to assess the model accuracy. It should be noted that the number of parameters was chosen to obtain unique ROC curves to demonstrate the statistical technique. . . . . 150

Table A-1 Stress-relaxation parameters for the modified 3-parameter standard solid model for each control (–C) and treated (–T) specimen pair from the elastin-removal study – circumferential direction, MVAL. . . . . 157
Table A-2 Stress-relaxation parameters for the modified 3-parameter standard solid model for each control (–C) and treated (–T) specimen pair from the elastin-removal study – circumferential direction, TVAL. . . . . 158
Table A-3 Stress-relaxation parameters for the modified 3-parameter standard solid model for each control (–C) and treated (–T) specimen pair from the elastin-removal study – radial direction, MVAL. . . . . 159
Table A-4 Stress-relaxation parameters for the modified 3-parameter standard solid model for each control (–C) and treated (–T) specimen pair from the elastin-removal study – radial direction, TVAL. . . . . 160
Table A-5 Stress-relaxation parameters for the modified 3-parameter standard solid model for each control (–C) and treated (–T) specimen pair from the collagen-removal study – circumferential direction, MVAL. . . . . 161
Table A-6 Stress-relaxation parameters for the modified 3-parameter standard solid model for each control (–C) and treated (–T) specimen pair from the collagen-removal study – circumferential direction, TVAL. . . . . 162
Table A-7 Stress-relaxation parameters for the modified 3-parameter standard solid model for each control (–C) and treated (–T) specimen pair from the collagen-removal study – radial direction, MVAL. . . . . 163
Table A-8 Stress-relaxation parameters for the modified 3-parameter standard solid model for each control (–C) and treated (–T) specimen pair from the collagen-removal study – radial direction, TVAL. . . . . 164

## LIST OF FIGURES

Figure 2-1 (a) Overview of the tricuspid valve anatomy and (b) the characteristics of hypoplastic left heart syndrome (HLHS). . . . . 7

Figure 2-2 (a) Schematic of the leaflet microstructure, depicting the extracellular matrix (ECM) and four morphologically distinct layers (from the atrium to the ventricle), i.e., the atrialis (A), the spongiosa (S), fibrosa (F), and ventricularis (V). (b) Visualization of collagen fiber transformational changes during biaxial tensile loading. . . . . 8

Figure 2-3 Characterized biaxial mechanical behaviors of the three TV leaflets: stress-stretch data in the tissue's (a) circumferential, and (b) radial directions. Results are presented as mean $\pm$ standard error of the mean (SEM). Piola-Kirchhoff is abbreviated as P-K. . . . . 10

Figure 2-4 Quantified regional variations in the biaxial mechanical properties of the TVAL: (a) The anisotropy index for the six leaflet regions, and (b) the circumferential (i.e., solid bars) and radial (i.e., patterned bars) tissue deformations for the six regions. Values are in mean $\pm$ SEM. . . . . 12

Figure 2-5 (a) Comparison of the TV leaflet microstructure (*top*) before and (*bottom*) after the enzyme degradation (scale is 200 $\mu$m, Alcian blue stain). Membrane tension vs. stretch responses in the (b) circumferential, and (c) radial directions before and after the enzyme degradation treatment. Results are presented in mean $\pm$ SEM. . . . . 14

Figure 2-6 Biaxial mechanical results for the separated tissue layers of the TVAL in the (a) circumferential, and (b) radial directions. Values are in mean $\pm$ SEM. Abbreviations: P-K, Piola-Kirchhoff; A/S, atrialis/spongiosa; F/V, fibrosa/ventricularis. . . . . 15

Figure 2-7 Quantification of the load-dependent collagen fiber architecture for a representative TVAL specimen using our integrated opto-mechanical instrument: (a) applied membrane tension vs. tissue stretch in the tissue circumferential (blue) and radial (red) directions and (b) results of collagen fiber orientation (dashed lines) and degree of optical anisotropy (DOA, in colormaps). . . . . 19
Figure 2-8 Finite element simulation results for the (a) healthy, and the diseased TVs: (b) chordae rupture, (c) combined flattened annulus and papillary muscle displacement, and (d) combined flattened annulus and annulus dilation. Abbreviations: AL, anterior leaflet; PL, posterior leaflet; SL, septal leaflet. . . . . 21
Figure 2-9 Number of citations per year with the search term "hypoplastic left heart syndrome" (*gray bars*), superimposed with the subset of citations with the search term "hypoplastic left heart syndrome regurgitation" (*blue bars*) (Data courtesy of Lens). . . . . 24
Figure 2-10 Overview of the timeline and surgical corrections for the three-stage cardiac palliative surgeries in HLHS. . . . . 25
Figure 2-11 Outlining the predominant mechanisms of tricuspid regurgitation in HLHS. . . . . 28

Figure 3-1 (a) Porcine MVAL and TVAL specimens sectioned to a $10 \times 10$ mm region for (b) biaxial mechanical testing at various ratios of the peak membrane tensions ($T_{\text{circ}}$:$T_{\text{rad}} = 1{:}1,\ 0.5{:}1$, and $1{:}0.5$) and for stress relaxation tests ($T_{\text{max}}$ denotes the peak biaxial membrane tension). (c) Parameters quantified from biaxial tension tests, including the tissue stretch $\lambda$, the index of extensibility $\lambda^*$, the low-tension modulus $E^{\text{LT}}$, and the high-tension modulus $E^{\text{HT}}$. (d) Parameters quantified from biaxial stress relaxation data, which include the rate of change of membrane tension at the initial and the saturated relaxation regimes, i.e., $\mathrm{d}T^1/\mathrm{d}t$ and $\mathrm{d}T^2/\mathrm{d}t$, respectively. Note: In (c) and (d) a smaller number of data points are visualized than the actual number of data points analyzed in order to improve visual clarity. . . . . 39

Figure 3-2 Verhoeff-Van Gieson-stained histological images demonstrating the progression of the elastin constituent removal for: (a) MVAL (representative specimen) and (b) TVAL (representative specimen) at various enzyme treatment time point. Scale bars $= 200\,\mu$m. The quantified constituent degradation at each analyzed point in time can be found in **Table 3-1**. . . . . 47
Figure 3-3 Masson's trichrome-stained histological images demonstrating the progression of the collagen constituent removal for: (a) MVAL (representative specimen) and (b) TVAL (representative specimen) at various enzyme treatment time points. Scale bars $= 200\,\mu$m. The quantified constituent degradation at each analyzed point in time can be found in **Table 3-2**. . . . . 47
Figure 3-4 (a) Overview of the second harmonic generation imaging-based procedure to (b) verify the color deconvolution methods used to quantify the constituent area fractions in histological micrographs. Scale bars $= 200\,\mu$m. . . . 49
Figure 3-5 (a) Preconditioning stretch ${}^{1}_{0}\lambda$ of the control (–C) and elastase-treated (–T) MVAL and TVAL specimens. Stretch ${}^{2}_{1}\lambda$ of the MVAL and TVAL specimens at the three biaxial tensions protocols: (b) $T_{\text{circ}}$:$T_{\text{rad}} = 1$:1., (c) $T_{\text{circ}}$:$T_{\text{rad}} = 1$:0.5, and (d) $T_{\text{circ}}$:$T_{\text{rad}} = 0.5$:1 ($n = 18$). * denotes statistically significant ($p < 0.05$). . . . . 51
Figure 3-6 Comparison of (a) the low-tension modulus $E^{\text{LT}}$, (b) high-tension modulus $E^{\text{HT}}$, and (c) the index of extensibility $\lambda^{*}$ between the control (–C) and elastase-treated (–T) MVAL and TVAL tissue specimens ($n = 18$) with three different biaxial tensions ($T_{\text{circ}}$:$T_{\text{rad}} = 1$:1, 0.5:1, and 1:0.5). * denotes statistically significant ($p < 0.05$). . . . . 52
Figure 3-7 (a) Preconditioning stretches ${}^{1}_{0}\lambda$ of the control (–C) and collagenase-treated (–T) MVAL and TVAL specimens. Stretches ${}^{2}_{1}\lambda$ of the MVAL and TVAL specimens at the three biaxial tensions protocols: (b) $T_{\text{circ}}$:$T_{\text{rad}} = 1$:1, (c) $T_{\text{circ}}$:$T_{\text{rad}} = 1$:0.5, and (d) $T_{\text{circ}}$:$T_{\text{rad}} = 0.5$:1 ($n = 16$). * denotes statistically significant ($p < 0.05$). . . . . 54
Figure 3-8 Comparisons of: (a) the low-tension modulus $E^{\text{LT}}$, (b) the high-tension modulus $E^{\text{HT}}$, and (c) the index of extensibility $\lambda^{*}$ between the control (–C) and the collagenase-treated (–T) MVAL and TVAL tissue specimens ($n = 16$) with three different biaxial tensions ($T_{\text{circ}}$:$T_{\text{rad}} = 1$:1, 0.5:1, and 1:0.5). * denotes statistically significant ($p < 0.05$). . . . . 55

Figure 3-9 Stress relaxation results of the control (–C) and elastase-treated (–T) MVAL and TVAL tissue specimens ($n = 18$). Membrane tension reduction in (a) the circumferential direction, and (b) the radial direction, and (c) the initial and (d) the saturated slopes of the stress relaxation reduction behavior. * denotes statistically significant ($p < 0.05$). . . . . 57

Figure 3-10 Stress relaxation results of the control (–C) and collagenase-treated (–T) MVAL and TVAL tissue specimens ($n = 16$). Membrane tension reduction in: (a) the circumferential direction, (b) the radial direction, and (c) the initial and (d) the saturated slopes of the stress relaxation reduction behavior. * denotes statistically significant ($p < 0.05$). . . . . 59

Figure 3-11 Comparisons of the percent change between tissues subjected to collagen-, elastin-, and GAG-removal with: (a) the preconditioning stretch ${}^{1}_{0}\lambda$, and the stretch ${}^{2}_{1}\lambda$ at the three biaxial tension protocols: (b) $T_{\text{circ}}$:$T_{\text{rad}}$ = 1:1, (c) $T_{\text{circ}}$:$T_{\text{rad}}$ = 1:0.5, and (d) $T_{\text{circ}}$:$T_{\text{rad}}$ = 0.5:1 for the MVAL and the TVAL specimens. GAG-removal results are from our previous study [23], with sample sizes (MVAL, $n = 7$; TVAL, $n = 6$). . . . . 65

Figure 3-12 Comparison of the percent change between tissues subjected to collagen-, elastin-, and GAG-removal in the stress relaxation behaviors of (a), (b) MVAL, and (c), (d) TVAL specimens. GAG-removal results are from our previous study [23], with sample sizes (MVAL, $n = 7$; TVAL, $n = 6$). . . 66

Figure 4-1 (a) Porcine tricuspid valves dissected to obtain the (b) TV leaflets. A 10x10mm square specimen prepared from the central, belly region of the leaflet and (c) mounted via tined BioRakes to (d) a coupled pSFDI-biaxial testing device. (e) Schematic of the membrane tension ($T$) loading ratios in the biaxial mechanical testing. . . . . 74

Figure 4-2 A schematic diagram of the methods used to acquire (a) the pSFDI-measured collagen fiber angles and (b) the experimentally measured deformation gradient **F** from biaxial testing that were used to (c) predict the collagen fiber orientations from affine fiber kinematics theory. . . . . 78

Figure 4-3 Representative experimentally measured results from TVAL #11. (a) The experimental photo from the pSFDI camera is provided, along with (b) the biaxial mechanical testing results, and (c) the pSFDI-based collagen fiber orientations at the post-preconditioning (PPC) configuration and other applied biaxial tension protocols. Note that the region of interest shown is for the full tissue specimen, while the AFK analysis was only performed for the region delimited by the fiducial markers. . . . . 80
Figure 4-4 Representative experimentally measured results from TVPL #6. (a) The experimental photo from the pSFDI camera is provided, along with (b) the biaxial mechanical testing results, and (c) the pSFDI-based collagen fiber orientations at the post-preconditioning (PPC) configuration and other applied biaxial tension protocols. Note that the region of interest shown is for the full tissue specimen, while the AFK analysis was only performed for the region delimited by the fiducial markers. . . . . 81
Figure 4-5 Representative experimentally measured results from TVSL #10. (a) The experimental photo from the pSFDI camera is provided, along with (b) the biaxial mechanical testing results, and (c) the pSFDI-based collagen fiber orientations at the post-preconditioning (PPC) configuration and other applied biaxial tension protocols. Note that the region of interest shown is for the full tissue specimen, while the AFK analysis was only performed for the region delimited by the fiducial markers. . . . . 82
Figure 4-6 Comparisons of the AFK-predicted and pSFDI-measured collagen fiber orientations for a representative TVAL specimen (TVAL #11) at the (a) PPC deformation (experimental only) and at the peak deformation of various applied biaxial loading states: (b) $T_{\text{circ}}$:$T_{\text{rad}} = 1$:1, (c) $T_{\text{circ}}$:$T_{\text{rad}} = 1$:0.66, (d) $T_{\text{circ}}$:$T_{\text{rad}} = 1$:0.33, (e) $T_{\text{circ}}$:$T_{\text{rad}} = 0.66$:1, and (f) $T_{\text{circ}}$:$T_{\text{rad}} = 0.33$:1. Dashed lines denote the predicted and experimentally measured collagen fiber orientations for some selected pixels, the grayscale gradient represents the absolute error between the predicted and experimental findings, and the black circles represent the positions of the fiducial markers. Histograms denote the probability for the experimental collagen fiber orientations at each five-degree increment. . . . . 87

Figure 4-7 Comparisons of the AFK-predicted and pSFDI-measured collagen fiber orientations for a representative TVPL specimen (TVPL #6) at the (a) PPC deformation (experimental only) and at the peak deformation of various applied biaxial loading states: (b) $T_{\text{circ}}$:$T_{\text{rad}} = 1$:1, (c) $T_{\text{circ}}$:$T_{\text{rad}} = 1$:0.66, (d) $T_{\text{circ}}$:$T_{\text{rad}} = 1$:0.33, (e) $T_{\text{circ}}$:$T_{\text{rad}} = 0.66$:1, and (f) $T_{\text{circ}}$:$T_{\text{rad}} = 0.33$:1. Dashed lines denote the predicted and experimentally measured collagen fiber orientations for some selected pixels, the grayscale gradient represents the absolute error between the predicted and experimental findings, and the black circles represent the positions of the fiducial markers. Histograms denote the probability for the experimental collagen fiber orientations at each five-degree increment. . . . . 88

Figure 4-8 Comparisons of the AFK-predicted and pSFDI-measured collagen fiber orientations for a representative TVSL specimen (TVSL #10) at the (a) PPC deformation (experimental only) and at the peak deformation of various applied biaxial loading states: (b) $T_{\text{circ}}$:$T_{\text{rad}} = 1$:1, (c) $T_{\text{circ}}$:$T_{\text{rad}} = 1$:0.66, (d) $T_{\text{circ}}$:$T_{\text{rad}} = 1$:0.33, (e) $T_{\text{circ}}$:$T_{\text{rad}} = 0.66$:1, and (f) $T_{\text{circ}}$:$T_{\text{rad}} = 0.33$:1. Dashed lines denote the predicted and experimentally measured collagen fiber orientations for some selected pixels, the grayscale gradient represents the absolute error between the predicted and experimental findings, and the black circles represent the positions of the fiducial markers. Histograms denote the probability for the experimental collagen fiber orientations at each five-degree increment. . . . . 89

Figure 5-1 4D transthoracic echocardiographic data from a representative newborn with HLHS (Patient #1): (a) axial plane, (b) sagittal plane, and (c) coronal plane. (d) Illustration of our image segmentation of the TV annulus. . . . 97

Figure 5-2 (a) Visual description of the moving least-squares curve fitting to obtain a smoothed representation of the TV annulus. (b) Schematic of the two diameters of the TV annulus: $D_{\text{SL}}$ and $D_{\text{AP}}$. (c) Illustration of the calculations of the annular height and the annulus bending angle. (d) Representative annulus contours from HLHS Patient #1 at end diastole. . . . . 99

Figure 5-3 Key TV annulus clinical metrics for all newborns with HLHS ($n = 8$) at the selected timepoints over the cardiac cycle (solid red line: the median, the bounding box: the $25^{\text{th}}$ to $75^{\text{th}}$ percentiles, the whiskers: extension between the maximum and minimum non-outlier datapoints). Individual patient data points at each timepoint are visualized with jittering for improved visual clarity. . . . . 103
Figure 5-4 Percentage changes in the TV annulus clinical metrics for the newborns with HLHS ($n = 8$) at the selected timepoints over the cardiac cycle. . . 104
Figure 5-5 Key TV annulus clinical metrics for all healthy newborns ($n = 4$) at the selected timepoints over the cardiac cycle (solid red line: the median, the bounding box: the $25^{\text{th}}$ to $75^{\text{th}}$ percentiles, the whiskers: extension between the maximum and minimum non-outlier datapoints). Individual patient data points at each timepoint are visualized with jittering for improved visual clarity. . . . . 105
Figure 5-6 Percentage changes in the TV annulus clinical metrics for the healthy newborns ($n = 4$) at the selected timepoints over the cardiac cycle. . . . . 106
Figure 5-7 Spatial variations of the computed strain along the TV annulus circumference for a representative HLHS newborn (Patient #1) at the selected timepoints over the cardiac cycle, where the time instant $t_{\text{RVP}_{\text{min}}}$ was chosen as the reference configuration. Note that the $0^\circ$ angle was aligned with the anterior-posterior commissure. . . . . 107
Figure 5-8 Spatial variations of the computed strain along the TV annulus circumference for (a) the studied eight newborns with HLHS ($n = 8$), and (b) the four healthy newborns ($n = 4$) (solid lines: mean, shaded regions: standard error of the mean). Note that the $0^\circ$ angle was aligned with the anterior-posterior commissure. . . . . 108
Figure 5-9 Spatial variations of the computed strain rate along the TV annulus circumference for (a) the studied eight newborns with HLHS ($n = 8$), and (b) the four healthy newborns ($n = 4$) (solid lines: mean, shaded regions: standard error of the mean). Note that the $0^\circ$ angle was aligned with the anterior-posterior commissure. . . . . 109

Figure 5-10 Spatial variations of the computed relative curvature along the TV annulus circumference for (a) the studied eight newborns with HLHS ($n = 8$), and (b) the four healthy newborns ($n = 4$) (solid lines: mean, shaded regions: standard error of the mean). Note that the $0^\circ$ angle was aligned with the anterior-posterior commissure. . . . . 110

Figure 6-1 (a) The geometry of the inflation test. (b) Bidirectional local distance (B-LD) errors for each element of the optimal solution. (c) Contour plot of the objective function and the median (Med.) and interquartile range (IQR) of the top 5% of evaluated BO solutions. . . . . 121

Figure 6-2 Contour plots and finite element meshes of the objective function surfaces considering different amounts of noise generated by a Gaussian function ($N$). Note that the contour surface from **Fig. 6-1** is repeated here with adjusted bounds on the colormap for easier comparisons. The BO solution is shown for the case of $N(0, 0, 02)$ mm. . . . . 123

Figure 6-3 (a) Map of the prescribed regionally varying thicknesses and (b) the corresponding contour surface. (c) The prescribed regionally varying material properties and (d) the corresponding contour surface. . . . . 125

Figure 6-4 (a) The simplified leaflet contact model. (b) The contour plot of the objective function surface and the median (Med.) and interquartile range (IQR) of the top 5% of evaluated BO solutions. (c) The element-wise bidirectional local distance (B-LD) error measurements for the optimal BO solution. (d) The variations in element centroid locations across the $20 \times 20$ grid points. . . . . 126

Figure 6-5 (a) The process for developing the leaflet contact optimization test cases with prescribed leaflet free edge displacements. (b) The contour surface of the objective function when using free-edge leaflet displacements and the median (Med.) and interquartile range (IQR) of the top 5% of evaluated BO solutions. (c) The bidirectional local distance (B-LD) measures for each element of the optimal solution. . . . . 128

Figure 6-6 (a) The valve model used in the forward simulation of the target solution. (b) The contour surface of the objective function and the median (Med.) and interquartile range (IQR) of the top 5% of evaluated BO solutions. (c) Bidirectional local distance (B-LD) measures of each element of the optimal solution (superior view, left; isometric view, right). . . . . 130

Figure 6-7 (a) The image segmentation of an echocardiogram to retrieve the annulus, free edge, and leaflet point clouds. (b) The generated finite element mesh. (c) The dynamic annulus and leaflet free edge boundary conditions: $t_1$ = right ventricle minimum volume; $t_4$ = end diastole. . . . . 132
Figure 6-8 ((a) Top-down and isometric views of the element-wise bidirectional local distance (B-LD) errors and (b) qualitative comparisons with the leaflet point cloud for the optimized TV surface with the 6D synthetic and (c, d) true solutions. Note that for improved visualization a denser finite element mesh was generated than what was used in the real optimization. . . . . 133

Figure 7-1 (a) An image of an excised porcine tricuspid valve that can be used for the pre-strain and valvular measurements. (b) The parameterized finite element model. . . . . 141
Figure 7-2 The reaction force-based three-step procedure for embedding pre-strains into the finite element model. . . . . 142
Figure 7-3 A comparison of the von Mises stresses at the deformed valve configuration for the displacement-based and reaction force-based pre-strain embedding techniques. . . . . 143
Figure 7-4 A potato diagram depicting the different deformation configurations of soft tissues during a standard experimental characterization procedure, and the relationships between the states. . . . . 145
Figure 7-5 (a) TV model based on the average measurements of our cohort of $n = 8$ neonates with HLHS; (b) visualization of the annulus contraction in the finite element simulations; (c) diagram depicting the top-down viewpoint (represented by the dot) and 8 offset viewpoints used to (d) quantify the maximum regurgitation orifice area (all views from the same representative simulation). . . . . 148
Figure 7-6 (a) The *k*-means clustering classification of non-TR and TR groups (note that the natural logarithm of the ROA value is used for better visualization); (b) ROC curves generated from multivariate logistic models using a maximum of 3, 5, or 7 predictor variables; (c) precision-recall curves for each of the multivariate models. . . . . 149

Figure B-1 Bayesian optimization of the Branin function, with contour plots of the residual surface in the five tested exploration ratios ($\xi$). . . . . 166

Figure B-2 Bayesian optimization of the Branin function with added Gaussian noise, with contour plots of the residual surface in the five tested exploration ratios ($\xi$). . . . . 167

## ACKNOWLEDGMENTS

I first want to thank my family for their unwavering love and support throughout this journey. I could not have accomplished even a fraction of the contents of this dissertation without their guidance, and all of the amazingly fun times that kept me sane these last three years—the concerts, the summer pool days, the karaoke nights, and, of course, Mom's above-and-beyond parties. Mom, Dad, Kristen, Jacob, Treyton, Julia, and Ella: I love you, and I can not say thank you enough.

I would also like to express my gratitude for my friends who kept me going. My best friend Lauren, who was always there to listen to me vent and laugh together over a drink; my Ph.D. brothers Sergio, Devin, and Luke, who I annoyed on many an occasion for advice and who made our office the best work environment I could ever ask for; and my other incredible lab mates, Ryan, Allyson, and Keely, who I have been very lucky to become friends with through this experience.

A special thanks goes to Dr. Chung-Hao Lee, who brought me into his lab and guided me from my first days of tissue testing, to the doctoral studies of today. His advice and help has provided me incredible opportunities that I could never have anticipated, and I am forever grateful for it. I would also like to extend my sincerest thanks to my doctoral committee - Drs. Kuang-Hua Chang, Yingtao Liu, Quinggong Tang, and Chenkai Dai for their support.

Finally, I could not have finished this journey without the undying love of my partner Shawn. Through the toughest of times, you were my rock, and you always knew how to pull me up out of my lowest lows. You and our little furry family of Big Boy, Mayonnaise, Janine, and Binx got me out of bed every day and inspired me to do my best. I love you.

To anyone else I could not fit into this one page: thank you.

## ABSTRACT

In this dissertation, the tricuspid valve (TV) is researched from three perspectives — *in vitro* experimental testing, *in vivo* image analysis, and *in silico* modeling.

Starting with the *in vitro* studies, we build upon our previous biaxial mechanical characterization studies to provide a deeper understanding of the microstructure-mechanics relationships. In one study, we performed a three-step experimental procedure for quantifying the mechanical contributions of the collagen and elastin constituents to the bulk tissue function: (i) biaxial testing of the TV leaflets; (ii) treatment of the tissue with an enzyme to remove either the collagen or elastin constituent; and (iii) biaxial testing of the same enzyme-treated tissue to facilitate comparisons within the same specimen. For the collagen-removal testing, we found a greater compliance in the high-tension regime of the stress-strain behaviors in the enzyme-treated tissues, providing experimental evidence of collagen as the primary load-bearing component. Meanwhile, in the elastin-removal testing, we observed a significant increase in tissue stiffness post-treatment, suggesting that the elastin plays a crucial role in the transition between low and high tensions, such as by acting as a regulator of the collagen fiber kinematics. In the next *in vitro* study, we used a polarized light-based imaging modality in conjunction with biaxial testing to evaluate the affine fiber kinematics (AFK) assumptions for the TV leaflets. We found that the AFK theory generally underpredicted the fiber reorientations subject to the equibiaxial loading, with larger errors occuring when the tissue was subjected to the applied non-equibiaxial loading. Furthermore, larger AFK errors were observed with increasing collagen fiber reorientations, suggesting the AFK theory is better suited for relatively smaller fiber reorientations.

As a next step in the TV-focused research, we focused on quantifying the *in vivo* mechanics of the TV, with specific emphasis on a congenital condition called hypoplastic left heart syndrome (HLHS), in which underdevelopment of the left side of the heart causes signifi-

cantly increased cardiac burden on the right side of the heart. Specifically, we developed a framework for analyzing echocardiograms to analyze the TV annulus mechanics and geometric properties, and performed comparisons of these metrics between newborns with and without HLHS. In this study, we found the HLHS-afflicted TV annulus is larger in circumference, area, and antero-posterior diameter, and becomes more circular and bent during valve closing than its healthy counterpart. From an engineering mechanics perspective, tissue strains did not differ significantly between the cohorts, which may provide an indication that the TV remodels in the HLHS condition to maintain tissue homeostasis throughout the cardiac cycle.

To further progress our understanding of the *in vivo* TV function, we performed *in silico* studies in the context of inverse finite element analysis. Specifically, we performed an exploratory study to assess how different factors affect the objective function search space. From this exploration, we found that: (i) an exponential-type material model yields a valley of nearly equivalent solutions; (ii) that the presence of noise in the comparison data (e.g., image-segmented point cloud data) can increase the width of this valley; and (iii) that a novel "leaflet free-edge displacement" boundary condition provides a more desirable optimization search space than the typical *in vivo*-emulating scenario where the chordae tendineae are simulated. Along with this novel idea for simulating the TV closing, we also provided a demonstration of the use of Bayesian optimization for solving the inverse analysis problem in computationally tractable manner.

Overall, the research performed in this dissertation provides significant progress in three major areas of interest for understanding tricuspid valve function. Firstly, refined understandings of the microstructure-mechanics relationships and the collagen fiber kinematics will lead to the development of more accurate constitutive model forms. Secondly, the *in vivo* TV annulus image analysis framework can be used to perform long-term studies of valve function to understand tissue development in both healthy and diseased scenarios. Finally, the developed *in silico* analysis methods provide the next steps for fully realizing patient-specific treatments via simulation frameworks.

# VITA

## Honors and Awards

| | |
|---|---|
| Gallogly College of Engineering Dissertation Excellence Award (OU) | 2022-2023 |
| Frank Chuck Memorial Scholarship (OU) | 2022-2023 |
| 2nd Place, Ph.D.-Level Student Paper Competition, Summer Biomechanics, Bioengineering, and Biotransport Conference | 2022 |
| 3rd Place for the Best Paper Award, the 40th AIAA/ASME Regional Symposium | 2021 |
| Finalist for the M.S.-Level Student Paper Competition, Summer Biomechanics, Bioengineering, and Biotransport Conference | 2020 |
| NSF Graduate Research Fellowships Program | 2020-2023 |
| 3 Minute Thesis (3MT) Competition – Top 10 Finalist (OU) | 2020 |
| Finalist for the B.S.-Level Student Poster Competition, Summer Biomechanics, Bioengineering, and Biotransport Conference | 2019 |
| Thomas Milam, Sr., Endowed Fellowship | 2019-2020 |
| Mechanical Engineering Capstone, Best Presentation (3rd Place) (OU) | 2019 |
| OU Honors College Most Outstanding Project Grand Prize | 2019 |
| Donna Shirley Engineering Award | 2018 |
| Outstanding Junior in the OU School of Aerospace and Mechanical Engineering | 2018 |
| ASME Central Oklahoma Scholarship | 2018 |
| Undergraduate Research Opportunity Program (OU) | 2018 |
| Mentored Research Fellowship (OU) | 2018 |

## Publications

1. **Ross CJ**, Mir A, Burkhart HM, Holzapfel GA, and Lee C-H, "Tricuspid Valve Regurgitation in Hypoplastic Left Heart Syndrome: Current Insights and Future Perspectives," *Journal of Cardiovascular Development and Disease*, 10(3), 111. (IF=4.415). DOI: 10.3390/jcdd10030111

2. **Ross CJ**, Miyake BA, Marsh HR, Bryant PR, Lee C-H, and Barreiro GC, "The Lasso Suture: Ex Vivo Testing of an Alternative to the High-Tension Deep Dermal Stitch," *Plastic and Reconstructive Surgery*, 2023. (IF=5.169). DOI: 10.1097/prs.0000000000010391

3. Laurence DW, **Ross CJ**, Hsu M-C, Mir A, Burkhart HM, Holzapfel GA, and Lee C-H, "Benchtop Characterization of the Tricuspid Valve Leaflet Pre-Strains," *Acta Biomaterialia*, 152, 321-334, 2022. (IF=10.633). DOI: 10.1016/j.actbio.2022.08.046

4. You H, Zhang Q, **Ross CJ**, Lee C-H, Hsu M-C, and Yu Y, "A Physics-Guided Neural Operator Learning Approach to Model Biological Tissues From Digital Image Correlation Measurements," *Journal of Biomechanical Engineering*, 144(12): 121012, 2022. (IF=1.899). DOI: 10.1115/1.4055918.

5. Fitzpatrick DJ, Pham K, **Ross CJ**, Hudson LT, Laurence DW, Yu Y, and Lee C-H, "Ex Vivo Experimental Characterizations for Understanding the Interrelationship Between Tissue Mechanics and Collagen Microstructure of Porcine Mitral Valve Leaflets," *Journal of the Biomedical Behaviors of Biomedical Materials*, 134, 105401, 2022. (IF=4.042). DOI: 10.1016/j.jmbbm.2022.105401

6. You H, Zhang Q, **Ross CJ**, Lee C-H, and Yu Y, "Learning Deep Implicit Fourier Neural Operators (IFNOs) with Applications to Heterogenous Material Modeling," *Computational Methods in Applied Mechanical Engineering*, 398, 115296, 2022. (IF=6.588). DOI: 10.1016/j.cma.2022.115296

7. Liu L-W, Lee C-H, Aggarwal A, Liao Y-K, Chao C-H, **Ross CJ**, "Viscoelastic Modelling of Tricuspid Valve Chordae Tendineae Tissue," *Applied Mathematical Modeling*, 105, 648-669, 2022. (IF=5.336). DOI: 10.1016/j.apm.2021.12.028

8. **Ross CJ**, Trimble EJ, Johnson E, Hsu M-C, Baumwart R, Jolley MA, Mir A, Burkhart HM, and Lee C-H, "A Pilot Investigation of the Tricuspid Valve Annulus in Newborns with Hypoplastic Left Heart Syndrome," *Journal of Thoracic and Cardiovascular Surgery Open*, 10, 324-339, 2022. DOI: 10.1016/j.xjon.2022.02.015

9. Lee C-H, Laurence DW, **Ross CJ**, and Hudson LT, "Advances in Experimental and Computational Biomechanics of the Tricuspid Heart Valve," Solid (Bio)mechanics: Challenges of the Next Decade, 213-243, 2022, Gerhard Sommer, Kewei Li, Daniel Ch. Haspinger, Raymond W. Ogden.

10. **Ross CJ**, Laurence DW, Echols AL, Babu AR, Tinting G, Duginski GA, Johns CH, Mullins BT, Casey KM, Laurence KA, Amini R, Fung K-M, Mir A, Burkhart HM, Wu Y, Holzapfel GA, and Lee C-H, "Effects of Enzyme-Based Removal of Collagen and Elastin Constituents on the Biaxial Mechanical Responses of Porcine Atrioventricular Heart Valve Anterior Leaflets," *Acta Biomaterialia*, 135, 425-440, 2021. (IF=10.633). DOI: 10.1016/j.actbio.2021.08.043

11. **Ross CJ**, Mullins BT, Hillshafer CE, Mir A, Burkhart HM, Lee C-H, "Evaluation of Affine Fiber Kinematics in Porcine Tricuspid Valve Leaflets using Polarized Spatial Frequency Domain Imaging and Planar Biaxial Testing," *Journal of Biomechanics*, 123, 110475, 2021. (IF=2.789). DOI: 10.1016/j.jbiomech.2021.110475

12. Fisher H, Woolard P, **Ross CJ**, Kunkel R, Bohnstedt BN, Liu Y, and Lee C-H, "Thermomechanical Data of Polyurethane Shape Memory Polymer: Considering Varying Compositions," *Data in Brief*, 32, 106294, 2020. DOI: 10.1016/j.dib.2020.106294

13. Hudson LT, Jett SV, Kramer KE, Laurence DW, **Ross CJ**, Towner RA, Baumwart R, Lim KM, Mir A, Burkhart HM, Wu Y, and Lee C-H, "A Pilot Study on Linking Tissue Mechanics with Load-Dependent Collagen Microstructures in Porcine Tricuspid Valve Leaflets," *Bioengineering*, 7(2), 60, 2020. (IF=5.046). DOI: 10.3390/bioengineering7020060

14. **Ross CJ**, Hsu MC, Baumwart R, Mir A, Burkhart HM, Holzapfel GA, Wu Y, and Lee C-H, "Quantification of Load-Dependent Collagen Fiber Reorientations in the Chordae-Leaflet Insertion Region of Atrioventricular Heart Valves," *Biomechanics and Modeling in Mechanobiology*, 1-19, 2020. (IF=3.623), DOI: 10.1007/s10237-020-01379-4

15. **Ross CJ**, Zheng J, Liang M, Wu Y, and Lee C-H, "Mechanics and Microstructure of the Atrioventricular Heart Valve Chordae Tendineae: A Review," *Bioengineering*, 7, 25, 2020. (IF=5.046). DOI: 10.3390/bioengineering7010025

16. **Ross CJ**, Laurence DW, Hsu M-C, Baumwart R, Zhao YD, Burkhart HM, Mir A, Holzapfel GA, Wu Y, and Lee C-H, "Mechanics of Porcine Heart Valves Strut Chordae Tendineae Investigated as a Leaflet-Chordae-Papillary Muscle Entity," *Annals of Biomedical Engineering*, 1-12, 2020. (IF=4.219). DOI: 10.1007/s10439-020-02464-6

17. Duginski GA, **Ross CJ**, Laurence DW, Johns CH, and Lee C-H, "An Investigation of the Effect of Freezing Storage on the Biaxial Mechanical Properties of Excised Porcine Tricuspid Valve Anterior Leaflets," *Journal of the Mechanical Behavior of Biomedical Materials*, 101: 103438, 2020. (IF=4.042). DOI: 10.1016/j.jmbbm.2019.103438

18. **Ross CJ**, Laurence DW, Richardson J, Babu AR, Evans LE, Beyer EG, Childers RC, Wu Y, Towner RA, Fung K-M, Mir A, Burkhart HM, Holzapfel GA, and Lee C-H, "An Investigation of the Glycosaminoglycan Contribution to Biaxial Mechanical Behaviors of Porcine Atrioventricular Heart Valve Leaflets," *Journal of the Royal Society Interface*, 16(156), 20190069, 2019. (IF=4.293). DOI: 10.1098/rsif.2019.0069

19. **Ross CJ**, Laurence DW, Wu Y, and Lee C-H, "Biaxial Mechanical Characterization of Atrioventricular Heart Valves," *Journal of Visualized Experiments*, 146: e59170, 2019. (IF=1.400). DOI: 10.3791/59170

20. Kramer KE, **Ross CJ**, Laurence DW, Babu AR, Wu Y, Towner RA, Mir A, Burkhart HM, Holzapfel GA, and Lee C-H, "An Investigation of Layer-Specific Tissue Biomechanics of Porcine Atrioventricular Valve Anterior Leaflets," *Acta Biomaterialia*, 96: 368-384, 2019. (IF=10.633). DOI: 10.1016/j.actbio.2019.06.049

21. Lee C-H, Laurence DW, **Ross CJ**, Kramer KE, Babu AR, Johnson EL, Hsu M-C, Aggarwal A, Mir A, Burkhart HM, Towner RA, Baumwart R, and Wu Y, "Mechanics of the Tricuspid Valve-From Clinical Diagnosis/Treatment, In-Vivo and In-Vitro Investigations, to Patient-Specific Biomechanical Modeling," *Bioengineering*, 6(2), 47, 2019. (IF=5.046). DOI: 10.3390/bioengineering6020047

22. Laurence DW, **Ross CJ**, Jett SV, Johns CH, Echols AL, Baumwart R, Towner RA, Liao J, Bajona P, Wu, Y, and Lee C-H, "An Investigation of Regional Variations in the Biaxial Mechanical Properties and Stress Relaxation Behaviors of Porcine Atrioventricular Heart Valve Leaflets," *Journal of Biomechanics*, 83: 16-27, 2019. (IF=2.789). DOI: 10.1016/j.jbiomech.2018.11.015

23. Laurence DW, **Ross CJ**, Jett SV, Johns CH, Echols AL, Baumwart R, Towner RA, Liao J, Bajona P, Wu Y, and Lee C-H, "Regional Biaxial Mechanical Data of the Mitral and Tricuspid Valve Anterior Leaflets," *Data in Brief*, 24, 103961, 2019. DOI: 10.1016/j.dib.2019.103961

## Presentations

1. **Ross CJ**, Mir, A., Burkhart, H.M., and Lee, C.-H., "The Lasso Stitch: Evaluation of the Uniaxial Tensile Mechanics and Clinical Advantages of a Novel Suturing Technique for High-Tension Wound Repair in Plastic Surgery" 9$^{th}$ World Congress of Biomechanics, Virtual, July 10-14, 2022.

2. **Ross CJ**, Mir, A., Burkhart, H.M., and Lee, C.-H., "Tricuspid Valve Annulus Mechanics And Geometry In Newborns With Hypoplastic Left Heart Syndrome," Summer Biomechanics, Bioengineering and Biotransport Conference (SB$^3$C), Cambridge, MD, June 20-23, 2022.

3. **Ross CJ**, Mir, A., Burkhart, H.M., and Lee, C.-H., "Tricuspid Valve Annulus Mechanics in Newborns with Hypoplastic Left Heart Syndrome," Biomedical Engineering Society (BMES) Annual Meeting, Virtual, October 6-9, 2021.

4. **Ross CJ**, Mir, A., Burkhart, H.M., and Lee, C.-H., "Evaluation of Affine Fiber Kinematics in Porcine Tricuspid Valve Leaflets," Summer Biomechanics, Bioengineering and Biotransport Conference (SB$^3$C), Virtual, June 14-18, 2021.

5. **Ross CJ**, Mir, A., Burkhart, H.M., and Lee, C.-H., "Evaluation of the Tricuspid Valve Annulus Mechanics in Newborns with Hypoplastic Left Heart Syndrome Using 4D Echocardiograms," Oklahoma ASME/AIAA Symposium, Oklahoma State University, Virtual, April 3, 2021 – received the 3$^{rd}$ Place Best Presentation.

6. **Ross CJ**, Mir, A., Burkhart, H.M., Wu, Y., and Lee, C.-H., "Contributions of Porcine Heart Valve Leaflet Microstructure to Stress-Stretch Behaviors of Chordae Tendineae Groups," Biomedical Engineering Society (BMES) Annual Meeting, Virtual, October 14-17, 2020.

7. **Ross CJ**, Mir, A., Burkhart, H.M., Wu, Y., and Lee, C.-H., "Quantification of Load-Dependent Collagen Fiber Reorientations in the Chordae-Leaflet Insertion Region of Atrioventricular Heart Valves," Summer Biomechanics, Bioengineering and Biotransport Conference ($SB^3C$), Virtual, June 17-20, 2020.

8. **Ross CJ**, Mir, A., Burkhart, H.M., Wu, Y., and Lee, C.-H., "Contributions of Porcine Heart Valve Leaflet Microstructure to Stress-Stretch Behaviors of Chordae Tendineae Groups," Biomedical Engineering Society (BMES) Annual Meeting, Philadelphia, PA, October 16-19, 2019.

9. **Ross CJ**, Laurence, D.W., Yan, Z.D., Hsu, M.-C., Baumwart, R.D., Wu, Y., and Lee, C.-H., "Investigations of the Chordae Tendineae: Mechanical Properties of Porcine Atrioventricular Heart Valves," Summer Biomechanics, Bioengineering and Biotransport Conference (SB3C), Seven Springs, PA, June 25-28, 2019.

10. **Ross CJ**, and Lee, C.-H., "An Investigation of the Contributions of the Porcine Atrioventricular Heart Valve Leaflet Microstructure to Organ-Level Mechanical Behaviors," OU Undergraduate Research Day, The University of Oklahoma, Norman, OK, April 6, 2019.

11. **Ross CJ**, Mir, A., Burkhart, H.M., and Lee, C.-H., "An Investigation of the Mechanical Properties of the Chordae Tendineae of Porcine Atrioventricular Heart Valves," OU-OUHSC Biomedical Engineering Symposium, The University of Oklahoma Health Sciences Center, Oklahoma City, OK, March 29th, 2019.

12. **Ross CJ**, and Lee, C.-H., "Development of A Novel Mechanical Testing Procedure for Investigations of Chordae Mechanical Properties of the Tricuspid Heart Valve," OU Biomedical Engineering Student Affairs Symposium, The University of Oklahoma, Norman, OK, April 27, 2018.

13. **Ross CJ**, and Lee, C.-H., "Development of A Novel Mechanical Testing Procedure for Investigations of Chordae Mechanical Properties of the Tricuspid Heart Valve," Okla-

homa ASME/AIAA Symposium, Oklahoma Christian University, Oklahoma City, OK, April 14, 2018.

14. **Ross CJ**, and Lee, C.-H., "Development of A Novel Mechanical Testing Procedure for Investigations of Chordae Mechanical Properties of the Tricuspid Heart Valve," OU Undergraduate Research Day, The University of Oklahoma, Norman, OK, April 7, 2018.

15. **Ross CJ**, and Lee, C.-H., "Investigations of the Mechanical Properties of Chordae Tendineae of Atrioventricular Heart Valves," National Conference on Undergraduate Research (NCUR), University of Central Oklahoma, Edmond, OK, April 4-7, 2018.

16. **Ross CJ**, Wu, Y., and Lee, C.-H., "Development of A Novel Mechanical Testing Procedure for Investigations of Chordae Mechanical Properties of the Tricuspid Heart Valve," OU-OUHSC Biomedical Engineering Symposium, The University of Oklahoma Health Sciences Center, Oklahoma City, OK, March 30th, 2018.

17. **Ross CJ**, and Lee, C.-H., "Development of a Procedure for Quantification of the Mechanical Properties of Chordae Tendineae of the Atrioventricular Heart Valves," Oklahoma Research Day, Northwestern Oklahoma State University, Alva, OK, March 9, 2018.

# 1 INTRODUCTION

## 1.1 Motivation

The tricuspid valve (TV) of the right-side heart has been historically referred to as the "forgotten valve", but due to nearly a decade of dedicated research this nickname may now be considered a misnomer. These research efforts span a breadth of topics — biaxial mechanical testing, *in-silico* models, and microstructural imaging. From these studies, it is now widely understood that the soft tissue leaflets of the TV are a four-layered structure composed of collagen, elastin, glycan groups, and valvular interstitial cells, which are responsible for the nonlinear, exponential-like stress-strain biaxial tensile behaviors. These leaflet characteristics are similar to those of the mitral valve (MV) in the left-side heart, with some key distinctions making the tricuspid valve unique: (i) the TV leaflets are thinner due to a less dense collagen structure; and (ii) the TV leaflets are generally more extensible than their MV counterparts. Computationally, the *in-silico* investigations of the TV have elucidated the changes in biomechanics metrics in the presence of valvular regurgitation mechanisms, such as papillary muscle displacement indicating more pronounced changes in the leaflet stresses and strains. Altogether, these studies greatly improve our current understanding of the TV function in healthy and simulated disease scenarios, providing progress towards improved TV-specific therapies (e.g., prosthetic valves mimicking native tissue function, simulation-guided surgeries, etc.). To make further progress for these clinical tools, it becomes necessary to continue these research efforts and better understand the biomechanics of the TV in diseased conditions. Specific to this dissertation, part of our focus is turned towards improving the collective understanding of a congenital heart defect known as hypoplastic left heart syndrome (HLHS).

HLHS is a condition affecting $1$ out of every $3,841$ babies born in the United States each year, and is characterized by an underdeveloped left-side heart, including an undersized

aorta or a non-developed mitral valve. The ideal treatment for this congenital condition is a heart transplant, however the supply of donor organs for infants is extremely limited. As an alternative to heart transplantation, HLHS-afflicted infants undergo a three-stage palliative cardiac procedure during their first $2-3$ years of life to create a single-ventricle system. During the staged palliative surgeries the presence of TR is a major risk factor for inter-stage mortality and is associated with poor long-term outcomes. Recent studies have shown that $\sim$10% of HLHS patients develop new onset TR at the Norwood (Stage-I) operation and another 27% acquire significant TR during the later palliation stages. Due to significant TR, 25% of HLHS patients will require TV surgical repair in their lifetime. The prior research efforts have examined the TV biomechanical and clinical attributes in adult populations; however, the existing adult TV biomechanics findings and knowledge may not directly translate to pediatric HLHS patients. Despite the severity of TR and moderate prevalence of HLHS, there are gaps in knowledge that prevent a complete understanding of the effects of the congenital heart defect on the TV biomechanics. For example, the TV may maladapt to the unique single ventricle configuration, including changes in the microstructural properties or the heart valve dynamics and geometry, resulting in the subsequent TR; however, the microstructure-mechanics relationships and in the TV leaflets have not been fully examined. Such information is crucial to advance the current treatment of TR in HLHS (i.e., valvular repair), including the development of high-fidelity simulations for individualized risk assessment. Thus, there are emerging needs to better understand the TV biomechanics, which may be relevant to HLHS for the long-term goal of improving TR prognosis during the staged palliation.

## 1.2 Objective and Scope

Improving the current understandings of TR is a multi-factorial issue, including changes in the tissue biomechanics and alterations in the heart valve geometry. For example, changes in the collagen, elastin, or glycosaminoglycan mass fractions in response to the increased pressure loading in the single ventricle system could manifest as a profoundly different heart valve closing behavior; however, the effects of these alterations have not been effectively quantified in the existing literature. Additionally, the collagen fiber kinematics of the TV leaflets are imperative to the accurate computational modeling of heart valve closing. Thus, these gaps in knowledge motivate *the first specific aim of this dissertation*: to perform experimental investigations for the TV leaflets that enhance the current understanding of the microstructure-mechanics relationships. In addition to improved experimental knowledge

on the TV, it is also important to understand the fundamental changes in the heart valve behaviors in the unique HLHS condition that may lead to the subsequent development of TR. This motivates *the second specific aim of this work*: to perform non-invasive image-based analysis of the tricuspid valve geometry and biomechanics in HLHS-afflicted newborns. Finally, the development of high-fidelity, accurate simulation tools for clinical use with this population requires identifying an efficient method for inversely determining the material behaviors of the soft tissues (i.e., leaflets, chordae). Therefore, *the third specific aim of this work* is to perform *in silico* studies to build a foundation for the inverse analysis problem.

**Specific Aim 1: Perform experimental characterizations of the TV leaflets for improved microstructure-mechanics relationships understanding.**

Porcine TV leaflets will be experimentally characterized to answer two primary questions: (1) *How does collagen and elastin insufficiency affect the bulk TV leaflet mechanics?* (2) *Can the collagen fiber kinematics of the TV leaflets be effectively modeled using the traditional affine fiber kinematics theory?* To answer the first question, TV leaflets will be biaxially tested before and after enzymatic removal of either the collagen or elastin microstructural components to monitor changes in the leaflet biomechanics within the same specimen. In the second study, healthy TV leaflets will be biaxially tested and imaged using polarized light imaging to quantify the load-dependent changes in collagen fiber orientation. These experimentally obtained collagen fiber reorientations will then be compared with the predictions from the affine fiber kinematics theory to determine if the model simplification holds for the TV leaflets.

**Specific Aim 2: Conduct image-based analysis of the HLHS-afflicted TV to quantify the geometry and biomechanics.**

From an enrolled HLHS patient cohort in the Oklahoma Children's Hospital, 4D (3D + time) full volumetric echocardiographic (echo) imaging data will be obtained from neonates with and without HLHS. Image segmentation will be performed in 3D Slicer for the subsequent analysis of the clinical (geometric) and biomechanical (3D shape and mechanical deformation) metrics of the TV annulus. The segmented point cloud geometries will be analyzed to quantify the tissue strains and geometric factors (e.g., diameters). Key differences in the TV associated with HLHS will be determined through statistical comparisons of the quantities between the two groups. This *in vivo* analysis of the annulus will form the foundation for a full-valve analysis pipeline.

### Specific Aim 3: Develop finite element analysis tools for simulation of the TV closing in HLHS

Herein, we develop an inverse finite element analysis framework for the TV closing. In this aim, the complex inverse analysis problem for the TV is investigated through an exploratory analysis of simulation test cases: (i) inflation (i.e., punch) testing; (ii) simplified leaflet contact; and (iii) an idealized tricuspid valve geometry closing. In each test case, the objective function surface is generated for an improved understanding of the proper approach to solving the inverse problem. Additionally, a novel boundary condition application method for simulating tricuspid valve closing will be proposed that may improve the convergence and accuracy of optimization solvers. We will also demonstrate a novel implementation of Bayesian optimization within the inverse finite element analysis framework. Altogether, this study will provide a foundation for holistic *in silico* analysis of the TV in HLHS.

# 2 BACKGROUND AND LITERATURE REVIEW


2.1 The Tricuspid Valve, Tricuspid Regurgitation, and Hypoplastic Left Heart Syndrome . . . . . 5
2.2 Tricuspid Valve Biomechanics . . . . . 6
2.2.1 Leaflet Morphology and Microstructure . . . . . 6
2.2.2 Tissue Biomechanics . . . . . 7
2.2.3 Microstructural Quantification for the TV Leaflets . . . . . 17
2.2.4 Simulation of Tricuspid Valve Function . . . . . 20
2.2.5 Inverse Analysis of Tricuspid Valves . . . . . 22
2.3 Hypoplastic Left Heart Syndrome . . . . . 23
2.3.1 Tricuspid Regurgitation as a Predictor of Mortality . . . . . 25
2.3.2 Identified Indicators of TR in HLHS . . . . . 27
2.4 Lacking Knowledge and Future Perspectives . . . . . 33
2.4.1 Proposed Research in Tricuspid Valve Leaflet Biomechanics . . 34
2.4.2 Propose Studies for Improving the Understanding of HLHS . . 35
2.4.3 An Improved Understanding of TR — Engineering Insights . . . 35
2.5 Structure of the Dissertation . . . . . 36


## 2.1 The Tricuspid Valve, Tricuspid Regurgitation, and Hypoplastic Left Heart Syndrome

The tricuspid valve (TV) regulates unidirectional blood flow through the right-side heart by cyclic coaptation of the anterior, septal, and posterior leaflets (AL, SL, and PL, respectively). These leaflets are connected to the surrounding myocardium and cardiac tissue through the ring-shaped annulus, and are further supported by the string-like chordae tendineae that affix the leaflets to the papillary muscles of the lower chamber (**Fig. 2-1(a)**). Should any

of these subvalvular components become irregular or dysfunctional, such as in the case of tissue calcification, the blood flow through the valve may become bidirectional. This reversed blood flow from the right ventricle to the right atria during the TV closing is aptly named tricuspid regurgitation (TR). TR can be sub-classified into two categories: primary TR ($8-10\%$ of all TR cases) is considered as conditions that directly affect the TV apparatus, such as congenital abnormalities or myxomatous degeneration; secondary TR is described as when the regurgitant flow is due to another condition, such as right ventricular dilation or left-side heart disease [1]. Regardless of the root cause, TR is a common finding in echocardiography, and is approximated to affect $70-90\%$ of the adult population, albeit the majority of these cases are benign, trace TR [2]. Meanwhile, clinically relevant TR is present in approximately $\sim 4\%$ of adults $75+$ years of age [3]. The presence of moderate-to-severe TR has a significant impact on patient prognosis: one-year survival was reported as $90.3\%$ with mild TR, $78.9\%$ with moderate TR, and $64.9\%$ with severe TR [4]. In addition, TR is a self-perpetuating condition and worsens over time [5]. For example, annular dilation can perpetuate as a maladaptation in response to pulmonary hypertension, resulting in progressive increases in TR severity over time [6]. The development and progression of TR is especially dangerous in populations with a comorbidity, such as congenital heart defects. Of specific interest in this dissertation, pediatric patients with a condition known as hypoplastic left heart syndrome (HLHS) are at an especially high risk for early mortality in the presence of TR (**Fig. 2-1(b)**). To this end, researchers have performed studies to better understand the structure and function of the tricuspid valve in both healthy and diseased scenarios, and to understand the indicators and mechanisms of TR in HLHS.

Herein, the review of the current state of the TV, TR, and HLHS research is structured into two primary sections: (1) a summary of the TV biomechanics literature; and (2) a review of the current understanding of TR in HLHS. Then, the gaps in the existent research will be described, laying the foundation for the objectives of this dissertation.

## 2.2 Tricuspid Valve Biomechanics

### 2.2.1 Leaflet Morphology and Microstructure

Morphologically, the TV leaflets consist of four distinct layers, from the atrial to the ventricular surfaces: the atrialis, spongiosa, fibrosa, and ventricularis layers (**Fig. 2-2(a)**). Microstructurally, these leaflets contain a surface layer of endothelial cells and embedded valvular interstitial cells (VICs) within the extracellular matrix (ECM), dispersed through-

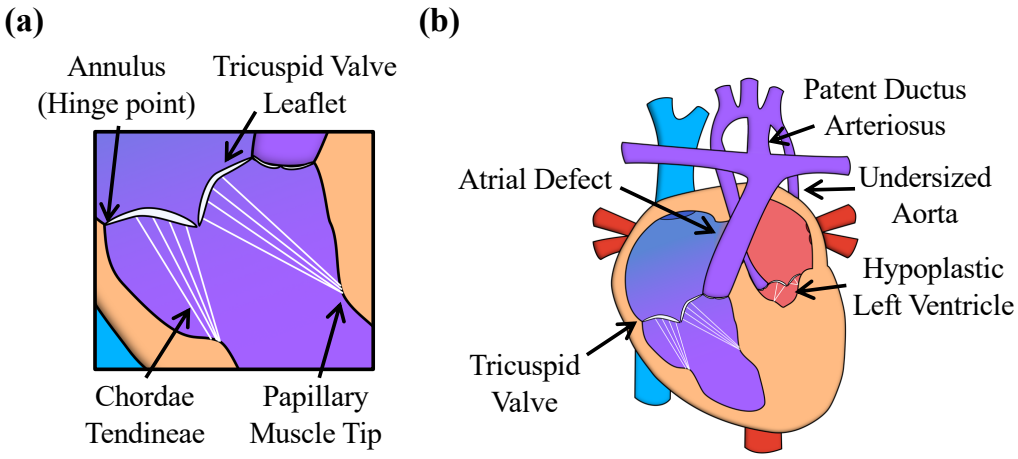


**Figure 2-1** (a) Overview of the tricuspid valve anatomy and (b) the characteristics of hypoplastic left heart syndrome (HLHS).

out the four layers. The ECM has three primary components: collagen, elastin, and glycosaminoglycans (GAGs), each of which provides unique contributions to the mechanical behaviors of the TV leaflets. For example, the collagen fibers are the main load-bearing component and primarily found in the fibrosa layer, with loose fibers in the atrialis and ventricularis layers [7–11]. The unloaded collagen fibers are found in a crimped state with a predominant orientation to the circumferential direction of the tissue [7, 8, 12]. During loading, these fibers then uncrimp, elongate, and reorient as the leaflet undergoes deformation to bear the cardiac loading (**Fig. 2-2(b)**). Meanwhile, the elastin fibers are primarily found within the ventricular and atrialis layers and are responsible for providing elasticity and flexibility to the tissue, allowing the leaflets to return to their *in vivo* stress-free geometry [8, 12, 13]. Finally, the GAGs are the polar proteins that primarily compose the spongiosa layer, but are also found throughout the tissue, mediating the collagen and elastin through fiber cross-linking [8, 10, 12]. These microstructural components are interconnected with the organ-level tissue responses, and as such many researchers have focused on characterizing the mechanical and microstructural properties of the TV leaflets.

### 2.2.2 Tissue Biomechanics

Two approaches have been employed to characterize the mechanical behavior of the TV leaflets. The first is planar biaxial mechanical testing in which orthogonal tensile loads are applied to the tissue specimen using sutures or thin tines [14]. Our lab has extensively used

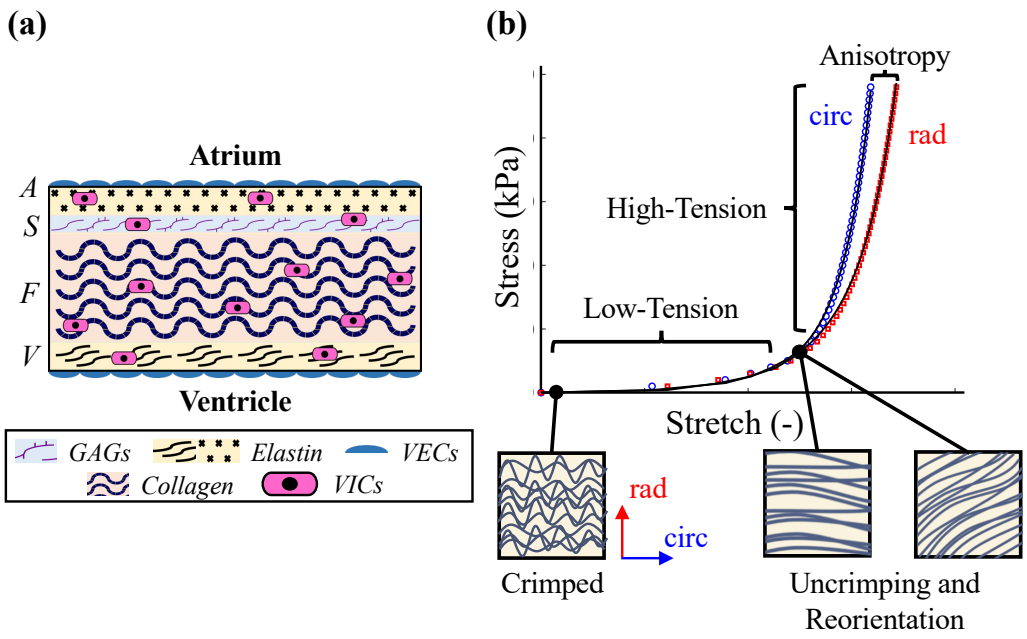


**Figure 2-2** (a) Schematic of the leaflet microstructure, depicting the extracellular matrix (ECM) and four morphologically distinct layers (from the atrium to the ventricle), i.e., the atrialis (A), the spongiosa (S), fibrosa (F), and ventricularis (V). (b) Visualization of collagen fiber transformational changes during biaxial tensile loading.

this experimental method to characterize the planar biaxial mechanical responses of the TV leaflet tissues, which provide useful information for developing TV-specific constitutive models under the hyperelasticity framework [15]. One inherent limitation of this testing method is the lack of mimicking the *in vivo* loading environment for the tissue. Conversely, the second characterization approach utilizes an *in vivo* animal model [16] or an *in vitro* testing apparatus that emulates ithe in-body conditions [17]. This approach provides richer information of the *in vivo* functioning environment of the TV. The following review focuses primarily on the studies from our lab on the TV leaflet tissue biomechanics, and briefly reviews the studies that maintained the entire TV apparatus within an *in vitro* or *in vivo* biomechanical characterization pipeline.

### Planar Biaxial Mechanical Characterizations

Mechanical characterizations of the TV leaflets were first provided by Heyden *et al*. (2015) [18], where the authors performed a survey of the mechanical properties for the leaflet tissues from all four cardiac heart valves. Since then, Khoiy *et al*. (2016) [19] provided the pioneering biaxial mechanical characterization of porcine TV leaflets. Their results highlighted the nonlinear and anisotropic mechanical responses for all the three TV leaflets. Interestingly, each leaflet had its distinct mechanical behavior, as later confirmed by Meador *et al*. (2020) [20] and Pham *et al*. (2017) [21] for ovine and human TVs, respectively. TV leaflet-specific mechanical responses stem from the unique microstructural differences, yet the comprehensive understanding of the intricate mechanics-microstructure interrelationship remains elusive.

Recently, our lab expanded these fundamental characterization studies by developing a comprehensive experimental procedure, *the first of its kind*, to systematically examine the mechanical behaviors of the TV leaflets in response to varied biaxial loading conditions, as well as the time-dependent mechanical response of the tissues [22, 23]. Our investigations using this approach can be generally classified into *bulk-tissue* and *microstructurally focused* characterizations. The former includes characterizations of the loading-rate effect, species differences, and spatial variations in the characterized mechanical properties of the leaflets, while the latter seeks to understand how the microstructural constituents, such as the GAGs or collagen fibers, contribute to the biaxial mechanical properties of the TV leaflets. Collectively, these recent results of our lab have provided an extensive understanding of the mechanical behaviors of the three TV leaflets. The comprehensive biomechanical database

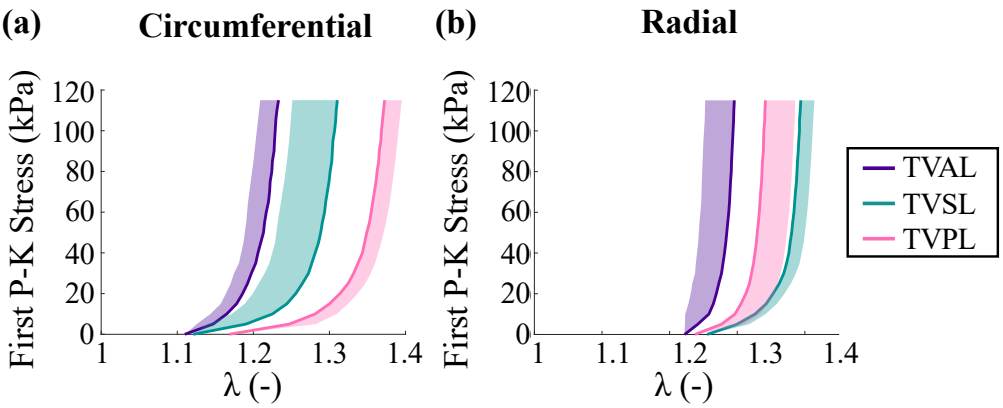


**Figure 2-3** Characterized biaxial mechanical behaviors of the three TV leaflets: stress-stretch data in the tissue's (a) circumferential, and (b) radial directions. Results are presented as mean $\pm$ standard error of the mean (SEM). Piola-Kirchhoff is abbreviated as P-K.

we established is useful for the development of constitutive models for predicting the TV *in vivo* function. Our experimental methods and the key findings of these studies are further elaborated as follows.

**Bulk-Tissue Characterizations** Our lab first aimed to establish a comprehensive biaxial mechanical characterization framework and explore how the strain rate, testing temperature, species, and age influence the observed mechanical behaviors [22, 23]. Like the previous studies [18, 19, 21], we found that the three TV leaflets had distinct, nonlinear and anisotropic mechanical responses (**Fig. 2-3(a)-(b)**). Interestingly, the adult ovine specimens were more compliant than their juvenile counterparts, but stiffer than the adult porcine specimens, indicating species and age are important factors for *in vitro* biomechanical characterizations. Moreover, the mechanical response for all three TV leaflets became stiffer with an increased loading rate, with the differences found to be statistically insignificant. This observation agrees with the typical viscoelastic theory for soft tissues [24]. Finally, the peak radial stretches became larger as the temperature increased, which no obvious microstructural connection was made. Our study provided a fundamental overview of the TV leaflet mechanical responses and explored how several experimental factors influence the observed mechanical behaviors.

The general consensus within the heart valve biomechanics community is to use the central region of the tissue for biaxial mechanical characterizations [19, 25, 26]. This experimental setup is chosen to avoid chordae insertions that may affect the characterized mechanical

properties of the TV leaflet tissues. However, it relies on an assumption that the mechanical properties of the central region accurately represent the entire TV leaflet specimen. Although this assumption may be reasonable for certain applications, no studies have quantified the regionally varying mechanical properties to evaluate the efficacy of this assumption. Laurence *et al*. (2019) [27] used a modified experimental technique to characterize the mechanical properties for six smaller regions of the porcine TVAL. From this study, we, *for the first time*, found that the central regions (i.e., Regions B and E) are more anisotropic compared to the edge regions (i.e., Regions A, C, D, and F) (**Fig. 2-4(a)**). This observation was supported by the quantified *anisotropy index* (AI, defined as the ratio of the peak radial stretch to the peak circumferential stretch). Interestingly, we also found that all the six tissue regions appeared to exhibit similar deformations after the specimen was preconditioned (**Fig. 2-4(b)**). Based on Dr. Y.C. Fung's seminal quasi-linear viscoelasticity theory for soft tissues [24], this post-preconditioning tissue deformation can be viewed as the *in vivo* functioning deformation of the tissue, and our novel findings imply that the assumption of *homogeneous mechanical properties* commonly adopted in heart valve computational modeling is valid, considering the post-preconditioning state as the reference configuration (i.e., the stress-free configuration in the context of continuum mechanics). These observations of our work underscore the importance of the chosen stress-free reference configuration [28], and partially verify the previous assumptions that the mechanical properties of the heart valve leaflets are *spatially homogeneous* [16, 29–31].

In addition, the tissues used in our mechanical characterizations are typically stored in a $-14$°C freezer between dissection and testing. In Duginski *et al*. (2020) [32], our lab sought to understand how this temporary freezer storage may influence the mechanical responses of the TV leaflets, since the existing literature for various tissues (e.g., cartilage, skin or aortic tissues) had conflicting conclusions. In this study, the fresh TVAL specimens were first biaxially characterized using our typical experimental protocols. The tested tissue was then frozen in a $-14$°C freezer for 48 h, and was subsequently tested using the same experimental characterization. Despite the relatively short duration, the freezer storage appeared to make the mechanical response of the leaflet slightly *stiffer* and *more anisotropic*, although we only found a statistically significant difference in the low-tensile mechanical response of the radial tissue direction. This suggests that the short storing period may slightly alter the TV leaflet mechanical response, but in a statistically non-significant manner. Another recent study by Salinas *et al*. (2020) [33] showed opposite trends (i.e., more compliant tissue behaviors) following a freezing period of $1-3$ days at $-80$°C. Thus, it is important to

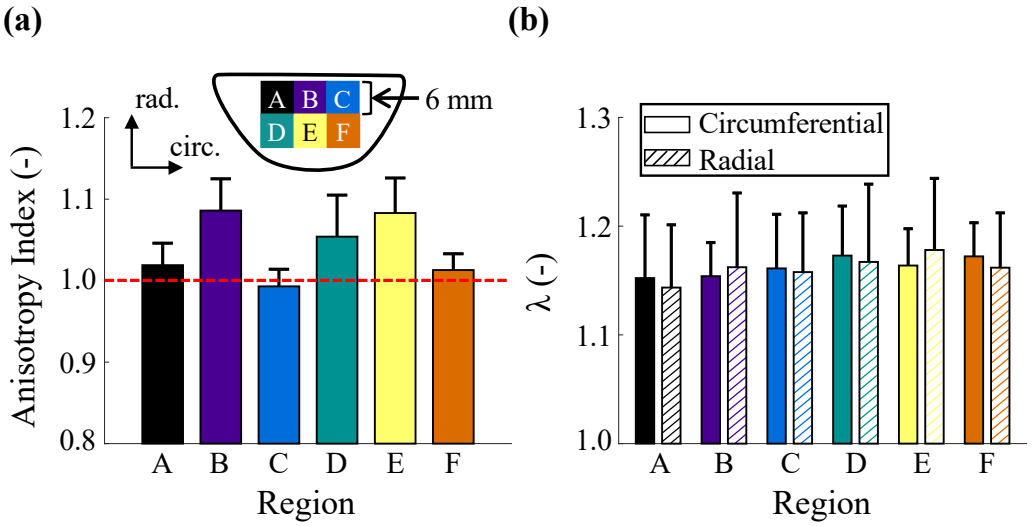


**Figure 2-4** Quantified regional variations in the biaxial mechanical properties of the TVAL: (a) The anisotropy index for the six leaflet regions, and (b) the circumferential (i.e., solid bars) and radial (i.e., patterned bars) tissue deformations for the six regions. Values are in mean $\pm$ SEM.

emphasize that the freezing-storage method for the TV leaflets should be carefully selected, and it is valuable to examine the differences in the characterized tissue mechanical behaviors arising from the selected freezer storage technique.

### Microstructure-Mechanics Relationships

While a general and qualitative understanding of the microstructure-mechanics relationships has been established, the contributions of the microstructure to the mechanical function of the atrioventricular heart valve (AHV) leaflets have not been comprehensively examined. To better quantify the microstructure-mechanics relationships of the individual ECM components, researchers have conducted studies using enzymatic degradation methods to remove the elastin, collagen, or GAGs from the valve tissue prior to the mechanical characterizations. For example, when mechanically testing the *aortic* valve with elastin isolation (i.e., all other ECM constituents were degraded), Vesely (1998) found that the aortic valve cusps shrank in size and were significantly less stiff, suggesting that elastin is naturally under tension within the intact cusp [34]. On the other hand, studies of collagen removal from porcine *aortic* and *pulmonary* valves have shown that: (i) the greater mechanical strains can accelerate collagen catabolism [35]; and (ii) the collagen-deficient aortic/pulmonary cusps had increased proliferation and apoptosis of the interstitial valve cells, increased calcifica-

tion of the cusps, and increased gene expression of disease-related markers [36]. To quantify the mechanical contributions of the GAGs, Lovekamp *et al.* (2006) removed the GAGs enzymatically from porcine aortic valve cusps and found that the GAG-removed tissues had an increase in flexural rigidity of 60% at the flat valve configuration with unchanged flexural rigidity between treated and untreated (control) tissue with increasing curvature of the valve cusps [37]. Recently, Bender *et al.* (2020) used collagen- and elastin degraded porcine mitral valve (MV) leaflets to perform biaxial mechanical testing and microstructural imaging in conjunction with radiofrequency ablation to assess the potential of therapy to restore healthy leaflet function [38]. Their study provided valuable information about the changes in the microstructural architecture of the tissues after the enzyme degradation as well as the limitations of ablation to restore properties of the enzymatically digested tissue in healthy leaflets; however, their study did not show any significant changes in the biaxial tensile (elastic) properties of the tissue after enzymatic removal of collagen or elastin. To supplement these previous studies, we extended the methods for use with the TV leaflets.

**Our Previous Microstructure-Focused Works** Our lab further elucidated the contributions of microstructural constituents to the TV leaflet mechanical responses. Ross *et al*. (2019) [39] used an iterative experimental technique to investigate the role of GAGs in the TV leaflet tissue biomechanics, where the untreated (i.e., control) specimen was biaxially characterized, then treated with an enzyme solution consisting of hyaluronidase and chondroitinase to obtain the treated specimen (**Fig. 2-5(a)**), and finally biaxial characterized. This approach enabled us to understand the differences in the mechanical behaviors, *by using the same single specimen*, considering the removal of $\geq 60\%$ of the GAG content. The deformations of the tissue were larger following the enzyme degradation treatment (**Fig. 2-5(b)-(c)**). Interestingly, we further found that the enzyme degradation-induced discrepancy was primarily attributed to the preconditioning effect. We also conducted stress relaxation tests in the same study, and found a reduced stress relaxation following the removal of the GAGs. This study highlights the intricate contributions of the GAG content to the biaxial mechanical and viscoelastic properties of the TV leaflets.

In Kramer *et al*. (2019) [10], our lab used another experimental method to understand the interrelationship between the tissue mechanics and its underlying microstructure for the TV. This approach utilized a micro-dissection procedure to separate the tissue layers of the TV anterior leaflet and characterize the biaxial mechanical properties of the separated tissue layers. Because the spongiosa layer lacks the structural constituents (such as collagen or elastin

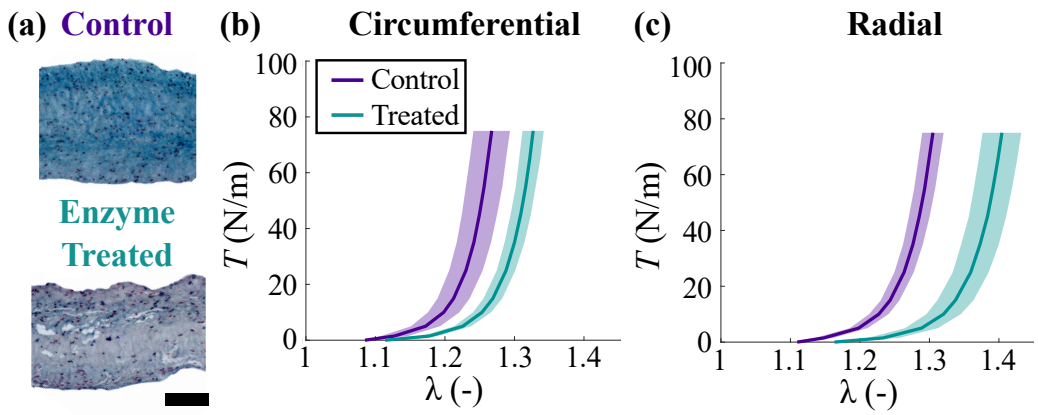


**Figure 2-5** (a) Comparison of the TV leaflet microstructure (*top*) before and (*bottom*) after the enzyme degradation (scale is 200 $\mu$m, Alcian blue stain). Membrane tension vs. stretch responses in the (b) circumferential, and (c) radial directions before and after the enzyme degradation treatment. Results are presented in mean $\pm$ SEM.

fibers) to bear substantial mechanical loading and the ventricularis layer is typically very thin, the TVAL was dissected into two composite layers: namely (i) A/S—the combined atrialis and spongiosa layer; and (ii) F/V—the combined fibrosa and ventricularis layer. These two composite layers were biaxially characterized, and we arrived at two primary observations. First, the tissue deformations with respect to the post-preconditioned configuration were nearly isotropic and much smaller than the anisotropic preconditioning deformations. Second, the A/S and F/V layers had similar tissue deformations with respect to the preconditioned configuration, with most of the differences in the observed mechanical response stemming from preconditioning (**Fig. 2-6**). The latter observation contradicts an assumption that the fibrosa layer behaves similarly to the intact layer; however, similar investigations for the aortic valve leaflets supported our observation and suggested the isotropic behavior of the separated fibrosa is due to the release of inter-layer attachments [40–42]. Although the observations from Kramer *et al*. provided an understanding of the layer-specific biomechanical functions of the TV leaflets, this study did not make a direct comparison of the mechanical properties to the intact leaflet (i.e., before micro-dissection). We are currently refining this experimental technique to provide further information for the future developments of microstructure-informed constitutive models for the TV leaflet tissues.

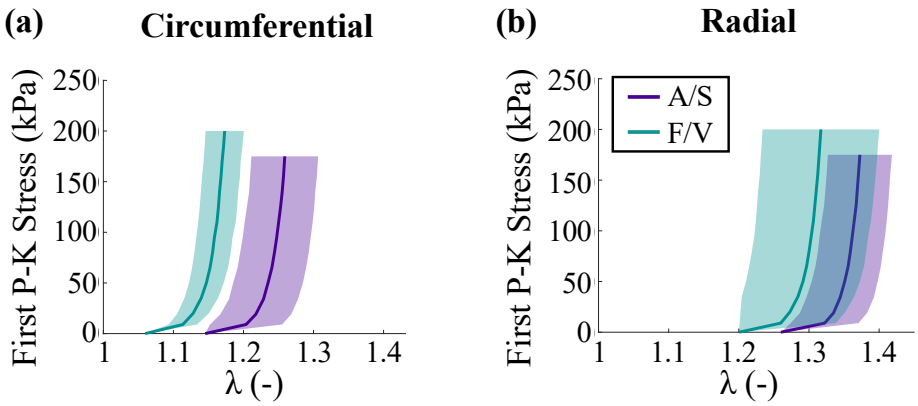


**Figure 2-6** Biaxial mechanical results for the separated tissue layers of the TVAL in the (a) circumferential, and (b) radial directions. Values are in mean ± SEM. Abbreviations: P-K, Piola-Kirchhoff; A/S, atrialis/spongiosa; F/V, fibrosa/ventricularis.

### *In Vitro* and *In Vivo* Characterizations

Previous research efforts to characterize the mechanical properties of the TV leaflets *in vitro* have followed a distinct methodology: excising the TV apparatus and mounting them to a rigid annulus in a ventricular chamber simulator [43]. Although this technique may give insight into the TV leaflet mechanics and coaptation, utilizing a rigid annulus may not be ideal for mimicking the native valve function, primarily due to the dynamic nature of the cardiac valve annulus and the subsequent alterations in the leaflet strain over cardiac cycles. In recent years, significant emphasis has been placed on characterizing the *in vitro* mechanical properties of the TV leaflets by using this type of characterization devices.

Khoiy *et al*. (2016) [44] took the first step towards characterizing the *in vitro* mechanical properties of the TV leaflets by quantifying the dynamic deformations of the TV in a beating porcine heart. This was achieved by implementing an *ex vivo* pump apparatus to simulate the right-sided systolic and diastolic pressures exhibited within the cardiac cycle. The use of this system showed that immediately after the coaptation of the TV leaflets, all the leaflet strain values (i.e., circumferential, areal, and radial) increased rapidly and reached their peak values at the maximum right ventricular pressure. Throughout the cardiac cycle, the maximum principal strain remained evenly distributed throughout the leaflet, increasing until reaching the maximum right ventricular pressure, with the strain values as high as 12%. Overall, the strains were shown to be minuscule during diastole and increased during systole. Heterogeneity in the spatial distribution of the circumferential and radial strains was also

observed for the TV septal leaflet, matching similar trends when the biaxial testing methods are employed. Khoiy *et al*. (2018) [45] later expanded this study in 2018 to investigate the role of the chordae tendineae rupture in the disturbance of annular function and leaflet coaptation. When the chordae tendineae was ruptured, the flow into the right atrium was found to decrease by 26% and the maximum right ventricular pressure decrease by 17%, highlighting the importance of the sub-valvular components in relation to the proper leaflet coaptation and TV function.

Apart from using an intact TV geometry under the *in vitro* apparatus, a deeper understanding of TV leaflet function has been underscored by the recent investigations of the *in vivo* TV leaflet mechanics. Mathur *et al*. (2019) [46] examined the TV leaflet strains in a beating ovine heart, suturing sonomicrometry crystals to the belly and free-edge portions of each TV leaflet, as well as to the TV annulus. A fiducial marker array was constructed for tracking the deformation of the TV leaflets and for calculating the *in vivo* leaflet strains. It was found that the strains are qualitatively different between the belly region and the free edges, with positive strains at systole and little change during diastole in the belly region of each leaflet, whereas the areal and circumferential strains were small at the free edges. Conclusively, no distinct common strain pattern was observed across all the three TV leaflets, although heterogeneity was noted for all strain evaluations (i.e., areal, radial, and circumferential). This study did, however, confirm the anisotropy of the quantified strains within each leaflet, with larger strain in the radial direction than the circumferential direction. Utilizing the technique, Mathur *et al*. (2020) [47] later investigated the effects of the De Vega valvuloplasty on the leaflet tissue mechanics when different degrees of cinching were applied. With each degree of cinching, the De Vega technique reduced the range of motion and angular velocity of the TV anterior leaflet, and, therefore, reduced the areal and radial strains, especially in the belly region of the leaflet. The circumferential strain remained similar throughout each cinching level. These observations concluded that the area strain in the leaflet's belly region was driven by the reduction in radial strains, leading to the reduced chordal tethering (**Table 2-1**). Furthermore, this mechanical interaction resulted in a reduced range of motion for leaflet coaptation. These investigations are integral for understanding their role in leaflet coaptation and mechanics within the native valve after operation.

**Table 2-1** The mean strain values relative to baseline at end-diastole (ED) and end-systole (ES) for each level of De Vega (DV) cinching [46]. Note that each step of DV cinching is $\sim$2 mm of the total annular diameter. Abbreviations: circ, circumferential; rad, radial.

| | DV1 | | DV2 | | DV3 | | DV4 | | DV5 | |
|---|---|---|---|---|---|---|---|---|---|---|
| Strain | ED | ES | ED | ES | ED | ES | ED | ES | ED | ES |
| circ (Mean) | 2.45 | 0.37 | 1.03 | 1.12 | 1.86 | −2.68 | 2.90 | −2.13 | 2.77 | −0.71 |
| circ (STD) | 5.22 | 4.76 | 10.32 | 10.72 | 8.88 | 8.28 | 9.43 | 11.72 | 8.97 | 18.20 |
| rad (Mean) | −3.73 | −1.24 | −0.94 | 1.99 | −6.61 | −8.49 | −0.24 | −9.80 | −2.11 | −12.63 |
| rad (STD) | 13.14 | 5.51 | 10.01 | 14.68 | 11.12 | 9.87 | 21.56 | 14.21 | 22.90 | 16.30 |
| Areal (Mean) | −3.89 | −4.86 | −2.36 | −8.33 | −8.15 | −19.00 | −10.29 | −24.53 | −11.15 | −30.22 |
| Areal (STD) | 17.37 | 16.21 | 20.99 | 20.54 | 20.89 | 21.98 | 37.47 | 32.03 | 28.36 | 36.12 |

### 2.2.3 Microstructural Quantification for the TV Leaflets

In additional to characterization of the mechanical properties of the tricuspid valve leaflets, studies on the mesoscopic quantification of the TV leaflet tissues can further unveil the complex underlying microstructure. Specifically, these observations focus primarily on examining the collagen fiber architecture (CFA) of the TV leaflets, i.e., the reorientation and realignment of the collagen fiber networks in response to the applied mechanical loading [20, 48–50]. Techniques, such as small-angle light scattering (SALS) [51, 52], second harmonic generation (SHG) [53] and two-photon fluorescent microscopy [20], have provided insight to the microstructural components of the TV leaflets. For example, the collagen fibers of the cardiac heart valve leaflets were shown to align predominantly in the circumferential direction in the unloaded state, with varying degrees of fiber dispersion and crimping across different layers of the tissue. In one study, Meador *et al*. (2020) [20] performed a detailed microstructural observation of the three TV leaflets using both two-photon fluorescent microscopy and histological quantification. Each microstructural constituent within the TV, including the collagen fibers, elastin, GAGs, and VICs, was found to be heterogeneously distributed with composition differences between the TV leaflets. Although the constituent composition varied from leaflet to leaflet, the CFA was found to be relatively similar, with fibers primarily oriented in the circumferential direction throughout the thickness direction. Depth-discriminated SHG quantification further suggested that the collagen be organized as individual fibers in the atrialis layer with both radial and circumferential orientations, before organizing into higher-order sheets in the fibrosa/ventricularis layers with a distinct circumferential orientation. Although these studies do not quantify the load-dependent changes

in the CFA, the microstructural quantification has improved our understanding of collagen organization and composition within the TV leaflets.

In order to bridge this gap in the understanding of the dynamic nature of the CFA, our lab utilized polarized spatial frequency domain imaging (pSFDI) to quantify the load-dependent changes in the tissue's CFA for the three TV leaflets [54]. This technique relies on the polarization-dependent, diattenuating properties of collagen fibers, allowing the quantification of the directional-dependence of the CFA and the degree of optical anisotropy (DOA). Another important aspect of this technique is the ability of the pSFDI system to quantify the collagen microstructures in a non-destructive manner, and, therefore, we can avoid the use of optical clearing solutions and fixatives that are known limitations for other collagen imaging modalities such as small-angle light scattering [55, 56]. Our key findings suggest that the TV leaflets displayed an initial collagen fiber orientation in the circumferential direction at the unloaded state, and that the majority of the crimped fibers rotate towards the radial direction before the applied biaxial tensions reached the asymptotic regime of the stress-strain curve (**Fig. 2-7(a)-(b)**). Afterwards, the fibers were straightened, exhibiting the low-force linear regime, which contributed to a better spatial alignment of the collagen fiber networks. More notably, this higher spatial alignment, indicating by the largest changes in the degree of optical anisotropy (DOA) compared to the unloaded state, was found to be the most prominent under radially dominant loading (i.e., $T_{circ}$:$T_{rad}$=0.5:1) (**Fig. 2-7(b)**). On the other hand, the non-equibiaxial loading demonstrated a shift of the collagen fibers towards the direction of the dominant applied loading, yielding an increase of DOA following fiber reorientation. Quantifying these collagen microstructural changes for the TV leaflets shed light on the future developments of microstructure-informed constitutive models, which can be used to better understand complex heart valve diseases. Furthermore, this method could be useful for testing affine fiber kinematics theory, as elaborate in the next subsection.

### Collagen Fiber Kinematics

The collagen fibers in the AHV leaflets are naturally crimped with a preferential alignment to the circumferential tissue direction [8, 12]. As loading is applied to the tissue, the collagen fibers reorient towards the primary loading direction, which contributes to the low-stress "toe-region" of the stress-stretch behaviors. After reorientation, the fibers uncrimp and elongate, which manifests as the high-stress, asymptotic regime. The collagen fiber kinematics form the basis of many constitutive models, but there remains no consensus

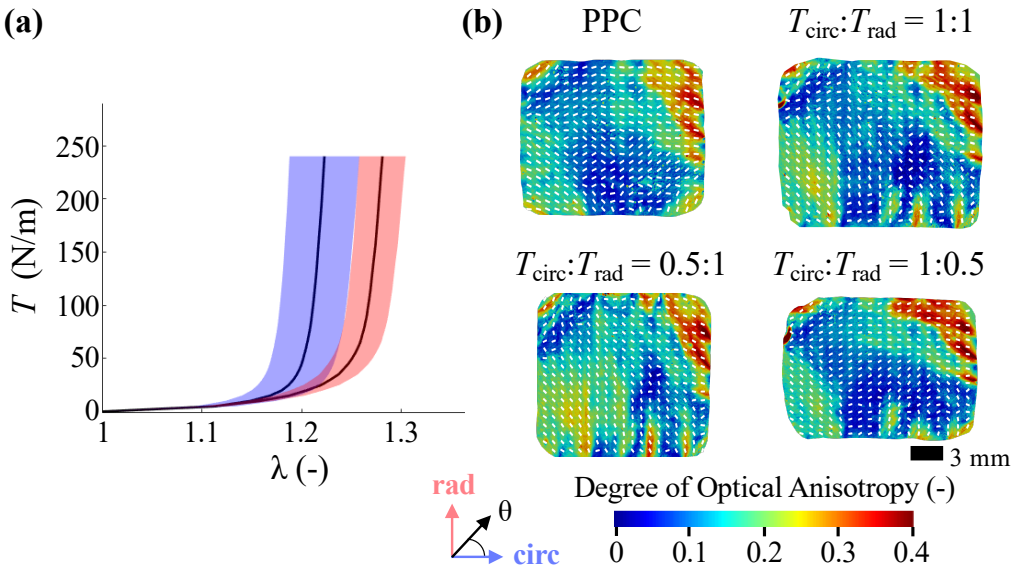


**Figure 2-7** Quantification of the load-dependent collagen fiber architecture for a representative TVAL specimen using our integrated opto-mechanical instrument: (a) applied membrane tension vs. tissue stretch in the tissue circumferential (blue) and radial (red) directions and (b) results of collagen fiber orientation (dashed lines) and degree of optical anisotropy (DOA, in colormaps).

on how the collagen model should be formulated: some AHV leaflet models are based on affine fiber kinematics (AFK) [50, 57–60], while others include the non-affine fiber kinematics (non-AFK), especially when tissue viscoelasticity is critical [61–63]. Herein, AFK is defined as a homogeneous deformation in which the fibers, usually considered as straight fibers without crimp, follow the tissue-level deformation (e.g., parallel fibers in the reference configuration map to parallel fibers in the deformed configuration) [64]. On the other hand, non-AFK is characterized by fibers undergoing inhomogeneous deformations that do not follow the macroscopic tissue deformation, potentially caused by shear deformations or fiber elongation and uncrimping.

Previous studies on soft tissue biomechanics have shown that the use of the AFK theory must be validated on a per-tissue basis. This is exemplified by the finding of a prior study that a modified AFK theory is required for the mitral valve leaflets [50], while other studies of tendons or small intestinal submucosa have noted the AFK theory to be invalid, especially in cases of large strain [65–68]. Moreover, some researchers have noted the *in vitro* tissue testing conditions could affect the observed fiber kinematics. For example, some studies of soft tissues, such as liver, skin, and arteries, conducted bulge/inflation testing and noted minimal fiber reorientations [65, 69], while other studies have performed uniaxial testing of tendons and observed significant fiber reorientations and non-AFK behaviors [65, 66, 70]. It has also been suggested that interactions between collagen fibers and the nonfibrous matrix could play a role in the accuracy of the AFK assumption. Specifically, a stiffer nonfibrous matrix could result in more non-AFK behaviors as the fibers cannot easily reorient [71]. These previous findings from other tissues motivate a work to be presented in this dissertation to validate this assumption for the tricuspid valve leaflets.

### 2.2.4 Simulation of Tricuspid Valve Function

*In silico* simulations enable connections between tissue-level mechanical behaviors and *in vivo* valvular function of the TV. Prior studies have simulated the TV function to understand patient-specific healthy TV mechanical environment [72, 73], explore the impact of papillary muscle displacements on the TV function [74], assess the potential of the MitraClip for restoring healthy TV function [75], or evaluate the performance of a new contact algorithm [76]. Interested readers are referred to our recent review article of these *in silico* studies for more information [11].

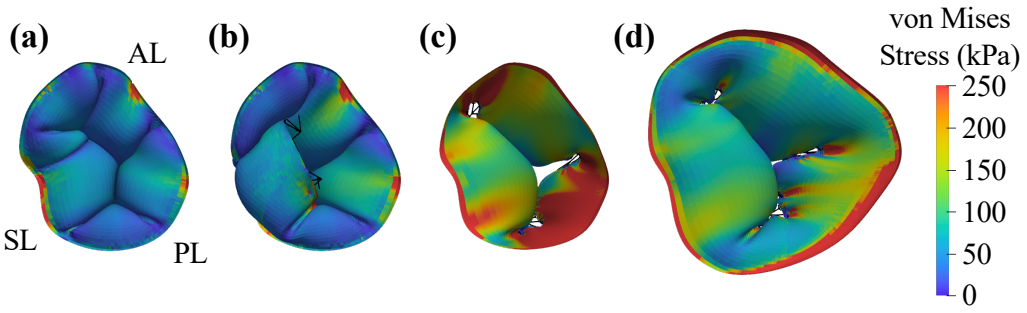


**Figure 2-8** Finite element simulation results for the (a) healthy, and the diseased TVs: (b) chordae rupture, (c) combined flattened annulus and papillary muscle displacement, and (d) combined flattened annulus and annulus dilation. Abbreviations: AL, anterior leaflet; PL, posterior leaflet; SL, septal leaflet.

Our lab has recently provided the first comprehensive *in silico* assessment of how the TV pathologies influence the TV function in Laurence *et al*. (2020) [77]. In brief, the TV geometry from Kamensky *et al*. (2018) [76] was used in finite element analysis to simulate the TV function, considering four pathological scenarios: pulmonary hypertension, annular dilation, papillary muscle displacement, and rupture of the chordae tendineae. Our simulation results underscored the effects of each valvular pathology on the TV function, for example, how tricuspid regurgitation could arise from annulus dilation, papillary muscle displacement, and/or the rupture of the chordae tendineae (**Fig. 2-8**). Additional quantitative analyses, based on our *in silico* TV simulations, led to three key observations. First, the geometry metrics, such as the tenting area or the coaptation height, depended on which two TV leaflets were in contact. This has important clinical implications, because there is uncertainty regarding which two leaflets are visualized for the clinical quantification of these metrics [78]. Second, the isolated scenario of papillary muscle displacement led to TR, suggesting this pathology may be a new target for clinical intervention rather than considering only the annulus dilation as a TR indicator. Third, the chordae tendineae attached to the TV anterior or septal leaflets may be more important to ensure the proper valve closure. Moreover, the leaflet stresses increased for all four pathological scenarios, which may trigger the cellular biosynthetic response and lead to altered leaflet morphology. This pilot *in silico* study has provided, *for the first time*, the simulation-guided assessment of TV pathologies. However, significant improvements and extensions are warranted to translate our model to the real clinical applications, such as a more precise description about the *in vivo* motions of the TV annulus or papillary muscles.

### 2.2.5 Inverse Analysis of Tricuspid Valves

Inverse finite element analysis (iFEA) is a non-invasive method for predicting the biomechanical properties of soft tissues *in vivo* and creating digital reconstructions of organ function; however, this is a computationally expensive problem with many hurdles to be cleared before clinical use.

iFEA has been used to predict the heart valve tissue properties using *ex vivo* beating heart apparatuses, *in vivo* animal models, or human *in vivo* medical imaging data. A particular advantage of *ex vivo* studies is the ability to validate the iFEA framework using benchtop experiments. For example, Abassi *et al.* (2016) performed iFEA for a bioprosthetic semi-lunar valve using a camera-equipped *ex vivo* pulse duplicator system and validated the predicted tissue material properties using biaxial mechanical testing [79]. Aggarwal *et al.* (2016) took a different approach, utilizing *ex vivo* data to develop a realistic semi-lunar valve model and study the effects of the individual components of iFEA on the resulting predictions [80].

As for the iFEA studies using *in vivo* animal models, the use of surgically implanted sonocrystals allows for more accurate measurements of the motions of the valve than can typically be performed with medical imaging techniques. In general, the majority of these iFEA studies are performed for *individual leaflets*, rather than the full valve apparatus, and are performed either by: (i) constructing a finite element mesh for the area delimited by the sonocrystal markers with boundary conditions applied to the edges of the geometry [81–83]; or (ii) digitally reconstructing the full leaflet with the corresponding chordae attachments and displacement/pressure boundary conditions [84, 85]. Lee *et al.* (2014, 2017) analyzed a central region of the sonocrystal-tracked ovine mitral valve anterior leaflet and noted that a fiber-based structural model yielded the most accurate reconstruction of the *in vivo* tissue displacements [81, 83], similar to what was later found in the aforementioned semi-lunar valve study [80]. Interestingly, another study analyzing the ovine mitral valve anterior leaflet suggested that the leaflet strains *in vivo* may not initiate the high-stiffness tissue behaviors, however this may be due to the use of an orthotropic linear elastic form [84]. The same authors also suggest iFEA may be challenging because the leaflets are active structures (e.g., interstitial cells) with transient stiffening behaviors [85]. Another challenge for iFEA was identified by Rausch *et al.* (2013), where they found differences of up to 4 orders of magnitude for the predicted tissues stiffness between models with 0% and 30% applied pre-strain [82].

In the final category of studies, the human *in vivo* heart valve computational models, in contrast, are typically performed with constitutive model parameters from biaxial testing data [86, 87]. While some of these studies have shown reasonable accuracy in simulating the true *in vivo* valve deformations, the majority of existent patient-specific FEA models do not make comparisons between the displacements in the simulated and *in vivo* leaflet surfaces [88, 89]. Interestingly, an alternative approach to the *in vivo* iFEA problem has been proposed by optimizing the chordae tendineae topology and pre-tensions to achieve agreement with the *in vivo* geometry of the mitral valve [21]. It is worth noting, however, that the leaflet properties will not be patient-specific in this context.

## 2.3 Hypoplastic Left Heart Syndrome

Hypoplastic left heart syndrome is a congenital heart defect characterized by underdevelopment of left heart components, including an underdeveloped or undeveloped left ventricle and mitral valve and/or an undersized aorta. Other possible features include a patent ductus arteriosus and a septal-atrial opening, both of which contribute to an oxygenated-deoxygenated blood mixture for systemic perfusion. Taken together, these key features of HLHS inhibit proper blood flow and require surgical correction almost immediately after birth.

This congenital heart defect has attracted increasing attention over the past two decades (**Fig. 2-9**) [90–92]. Of those studies, there is a subset of articles dedicated to the understanding of the debilitating comorbidity of tricuspid regurgitation, which is particularly dangerous in this pediatric population. Great progress has also been made in distinguishing TR and non-TR cohorts and in determining the risk indicators for TR in HLHS. Moving forward, it will prove valuable to summarize these works and identify TR indicators that have have been unanimously agreed upon, as well as those that are controversial and require further research, and to present studies that will improve our understanding of the TV dysfunction in HLHS.

Current standard practice for the treatment of HLHS, first proposed by Norwood *et al.* (1980), involves three palliative (i.e., non-curative) cardiac surgeries performed within the $1.5-3$ years of the patient's life with the overarching goal of incrementally creating a functioning single ventricular system (**Fig. 2-10**) [93, 94]. In the Stage I (Norwood) surgery, performed at $1$ to $2$ weeks of age, the surgeon establishes an unobstructed blood flow be-

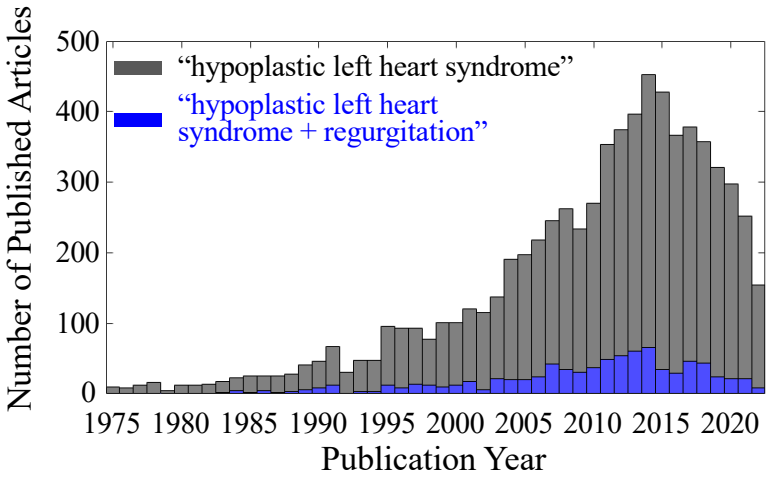


**Figure 2-9** Number of citations per year with the search term "hypoplastic left heart syndrome" (*gray bars*), superimposed with the subset of citations with the search term "hypoplastic left heart syndrome regurgitation" (*blue bars*) (Data courtesy of Lens).

tween the right ventricle (RV) and the aorta, enlarge the opening of the atrial septum, and inserts a shunt to the pulmonary artery from either the aorta or the RV [93, 95].

Then Stage II (i.e., Glenn procedure) is performed at $3-6$ months of age, diverting about half of the pulmonary blood flow for passive circulation by rerouting the superior vena cava directly to the pulmonary artery [96, 97]. Finally, in Stage III (Fontan) surgery, performed at $1.5-3$ years of age, the surgeon renders the pulmonary blood flow completely passive through a conduit connecting the inferior vena cava to the pulmonary artery, using a fenestration to the right atrium made to act as a pop-off valve [98, 99]. This staged palliation has resulted in a significantly improved mortality, with $87-95\%$ of patients surviving up to $20$ years or more after Stage III operation [100–102]. However, TR still represents a challenging risk factor and worsens the quality of life of these infants as they progress into childhood and adulthood.

Specifically, TR is present in up to $25\%$ of all patients with HLHS undergoing staged palliation, which can result in early mortality or require additional risky, invasive TV repair surgeries (e.g., annuloplasty or valvuloplasty) [103–106]. Of the TR-afflicted patients who receive a TV repair, $22\%$ to $48\%$ will need a second TV repair or a total heart transplant within $5-10$ years after the first valve repair operation [107–109]. Despite the clear clinical implication of TR in HLHS, to date there is no consensus on the guidelines or strategies

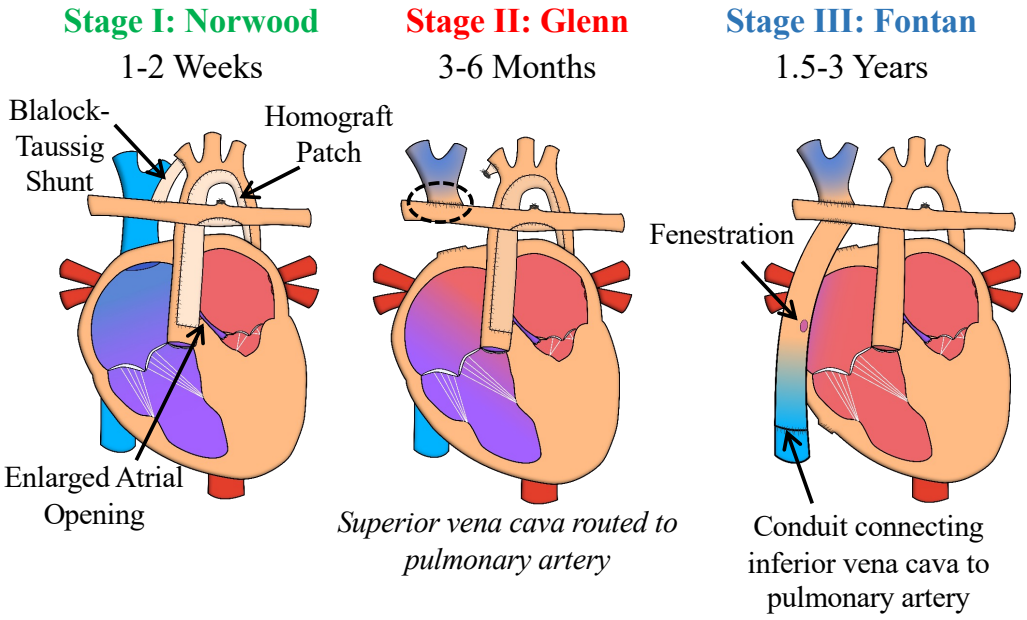


**Figure 2-10** Overview of the timeline and surgical corrections for the three-stage cardiac palliative surgeries in HLHS.

to manage this comorbidity (i.e., valve regurgitation) during the three-stage palliative surgeries, due to limited research to support the creation of such guidelines. Therefore, a special area of research has been devoted to understanding the indicators and mechanisms of TR in newborns with HLHS.

### 2.3.1 Tricuspid Regurgitation as a Predictor of Mortality

Historically, there have been mixed results as to whether TR was an indicator of early mortality in patients with HLHS. In the period just after the advent of palliative procedure, researchers found that TR was not a significant indicator of early mortality [110–112]. In other studies, TR has even been considered as a contra-indicator for surgical palliation and a predestined early mortality [113–115]. From the perspective of inter-stage periods, Barber *et al.* (1988) found that TR is a significant survival factor in inter-Stage I—II period ($\sim$35% survival for moderate/severe TR) [103], while other researchers later contradicted this claim and did not believe that inter-stage TR is a significant risk factor [116–119]. Variations in the consideration of TR as a mortality risk extended to the post-Fontan periods. For example, Chang *et al.* (1991) found TR to be an indicator for post-palliation mortality [120] and others found that TR did not significantly affect survival [121, 122]. The variations in findings may be explained by a few reasons: (i) some studies were performed shortly after

the introduction of the palliative procedure, when early mortality might be due to the surgeon's lack of experience; (ii) in some cases, the statistical analysis may have been biased (e.g., patients organized into groups that could potentially lead to a desired outcome); and (iii) patient selection bias and/or differences in hospital policies may affect study outcomes, such as Mosca *et al.* (2002) admitting an aggressive policy of performing valvuloplasty for all but mild or traceless TR may have skewed their finding that TR was not a mortality risk [121]. Furthermore, the widespread use of valvuoplasty in Mosca's cohort might indicate that more aggressive treatments do not significantly affect post-Fontan TR-related mortality, and it would be beneficial to confirm this in a future study [121].

In more modern studies, pre-Norwood TR has been clearly associated with increased mortality post-Norwood: an odds ratio (OR) of $2.8\ [1.3{-}6.2]$ at $95\%$ confidence interval (CI) [123]. The risk of early onset TR was also demonstrated by Sugiura *et al.* (2014) where they found that patients with TR in the initial palliation stage had a significantly poorer survival time than those who had developed TR in later palliative stages ($42.9\%$ vs. $92.9\%$ at $5$ years, respectively) [107]. Carlo *et al.* (2011) came to similar conclusions that the presence of TR on a pre-Glenn echocardiogram was associated with mortality in the interval between Stages II-III ($55\%$ attrition rate, together with a hazard ratio (HR) of $6.02\ [1.56-23.24]$ $95\%$ CI), however, the presence of TR in the echocardiogram "post-Glenn" was not recognized as a significant indicator of attrition ($27\%$ vs. $5\%$ for with TR and without TR, respectively) [124]. Overall, it is clear that with continued improvements and surgeons' experience in performing palliative surgery, TR has been considered a significant mortality risk factor, particularly for HLHS patients who develop TR at an earlier age.

### Failure of TV Repair and Recurrence of TR

To address TR, TV repair (typically via valvuloplasty [104, 121]) is performed either concomitant with a palliative phase or during the inter-stage period. TV intervention significantly improves the $5$-year survival rates ($52.1\%$ vs. $23.3\%$ for with and without surgical repair, respectively) [107]. However, $33\%$ of these patients suffer a *recurrent* TR within $5$ years of the initial repair [107]. In addition, it was found that patients who received TV repair concomitant with Stage I (aorta reconstruction) had sub-optimal outcomes at an $8$-year follow-up compared to control (non-TR) patients: (i) transplant-free survival rates, $41\%$ and $75\%$ for concomitant TV repair vs. no TR, and (ii) (re-)intervention-free survival rates, $33\%$ and $83\%$ for concomitant TV repair vs no TR [125]. It is clear that TV interventions for the

HLHS-afflicted heart require additional research to improve intermediate and long-term patient outcomes [126]. As a possibility, an improved understanding of the patient-specific characteristics associated with successful repairs could be beneficial for the refinement of current surgical guidelines. In particular, it was found that successful TV repair associated with the Norwood procedure is related with pre-operative anatomical and functional features: smaller dimensions of the lateral annulus, annular area, and mid-width of the RV, higher anterior leaflet excursion, and presence of anterior leaflet prolapse—the primary TR mechanism as opposed to other causes such as leaflet tethering [125]. Future studies along these lines may reveal further trends in TV apparatus related to desired repair outcomes and lead us to patient-targeted surgical guidelines, such as the suggestion of concomitant vs inter-stage repair or a specific TV repair technique.

### 2.3.2 Identified Indicators of TR in HLHS

The mortality and risk associated with TR motivates efforts to understand the mechanisms and indicators of comorbidity, which will provide insight to guide and improve surgical management of newborns with HLHS. Additionally, it proves valuable to identify the predictors of TR onset for HLHS patient risk assessment and risk stratification. Here, we summarize some key findings from the recent literature, including geometric differences, structural abnormalities, ventricular mechanics, and surgical decisions that may be associated with TR onset.

#### Geometric Differences in TR and Non-TR Cases

Using routine echocardiography and image segmentation techniques, in-depth analyses of the valvular geometry have become a promising way to understand the differences between HLHS patients with TR and without TR. For example, Nguyen *et al.* (2019) analyzed TV geometry in post-Fontan patients and found patients with TR had a significantly greater change in the annulus area (16.4% vs. 9.3%), circumference (10.5% vs. 4.1%), and in septo-lateral diameter (10.7% vs. 5.7%) during the cardiac cycle compared to those without TR [127]. These changes were also found to vary regionally, with all but the septal annulus quadrant showing significant changes in these geometric quantities. A multivariate logistic regression model also revealed the mid-systolic anterior papillary muscle angle (OR $= 2.49$ $[1.34 - 4.65]$ 95% CI) and the maximum septo-lateral diameter (OR $= 1.73$ $[1.12 - 2.68]$ 95% CI) as key metrics related to TR [127]. Future studies conducted in a similar manner will be beneficial to better understand the identified mechanisms of TR identified in previ-

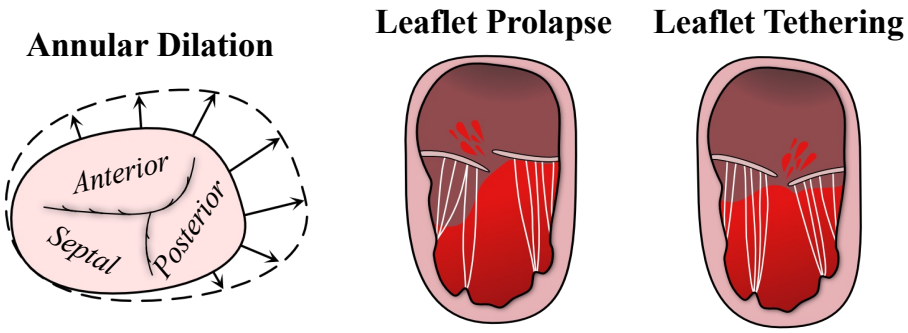


**Figure 2-11** Outlining the predominant mechanisms of tricuspid regurgitation in HLHS.

ous work, including the structural anomalies (e.g., leaflet tethering or annular dilation), as discussed next.

### Structural Anomalies as Mechanisms of TR

Structural anomalies of the TV are primary contributors to TR in neonates and throughout the palliative series [113]. In the pre-Norwood period, the most common valvular abnormalities associated with TR include annular dilation, leaflet tethering, and chordae shortening [107, 125, 128–130] (**Fig. 2-11**). Similar TR mechanisms have been identified in the inter-Stage I-II period along with other additional abnormal features such as leaflet prolapse caused by a flattened annulus and a smaller septal/anterior leaflet area [107, 129, 131, 132]. These findings were repeated in patients analyzed after post-Glenn, with the primary TR-associated factors found as a dilated annulus (total annular area $Z$-score, $6.34 \pm 2.70$; lateral dimension $Z$-score, $4.07 \pm 1.70$; and antero-posterior dimension $Z$-score, $3.74 \pm 1.95$), as well as anterior leaflet prolapse [133]. Other investigators also noted a narrowing of the leaflets (OR $= 5.8$ $[1.2 - 28.9]$ 95% CI) and annular dilation (OR $= 4.1$ $[1.0 - 16.7]$ 95% CI) identified as risk factors for TR after Stage II (the Glenn) palliation [134].

After the Fontan operation, patient cohorts were analyzed to determine short- to long-term abnormalities associated with TR. Even before Stage I, the metrics were associated with moderate to severe TR and a lower survival rate post-Fontan: a greater TV tethering volume ($0.86 \pm 0.60\,\text{mL/m}^2$ vs. $0.54 \pm 0.40\,\text{mL/m}^2$: TR vs. non-TR) and annular bending angle ($155.6 \pm 8.9^\circ$ vs. $150.3 \pm 9.2^\circ$: TR vs. non-TR) [130]. Larger tethering volume correlated with leaflet area (Pearson correlation factor $r = 0.736$), annular area ($r = 0.651$), right ventricular diastolic area ($r = 0.347$), and change in right ventricular fractional area ($r = -0.387$). In another work, leaflet tethering was also correlated with right ventricular end-

systolic areas ($r = 0.421$), RV sphericity index ($r = 0.516$), and the angle between the anterior papillary muscle and the ventricular midline ($r = 0.316$) [131]. Similar results were reported by Ono *et al.* (2020), noting additional factors attributable to TR: prolapse of the anterior leaflets ($52\%$ of patients), restriction of the septal leaflets ($50\%$ of patients), annulus dilation ($48\%$ of patients), and cleft of the anterior leaflet ($21\%$ of patients) [109].

### Discrepancy in Findings with a Longitudinal Cohort

The majority of the above studies were conducted without accounting for patient-specific changes in their statistical analysis (i.e., paired samples) that might affect the identified TR-related trends and mechanisms. This is exemplified in the study by Colen *et al.* (2018), in which they attempted to determine compensatory adaptations of the TV during the pre-Glenn period using a longitudinally tracked cohort [135]. Although they confirmed that TR is associated with larger prolapse volumes and a more flattened and larger annulus, they found that significant TR is associated with *larger* leaflet areas. Interestingly, leaflet coaptation was not significantly different in TR vs non-TR groups, and they believe this to be evident for maladaptation of the TV by excessive growth – a theory they have replicated and further explored in a piglet model [131, 136]. The inconsistencies in these findings may be due to the improved experimental design, which used measurements *from the same patient* pre-Norwood and pre-Glenn, in contrast to conflicting data in other works [129]. In the future, prospective studies of this type will provide better insight into the functional changes in TV during palliation periods that can lead to the development, progression, and worsening of TR.

**Summary of Primary Structural Findings** Overall, annulus dilation and leaflet prolapse or tethering are unanimously recognized as the primary mechanisms of TR in the HLHS demographic. Furthermore, the geometry of the RV also correlates with the onset of TR—the topic elaborated in **Section 2.3.2**. It should also be emphasized that the differences in results from these studies may be due to the use of unpaired vs paired statistical analysis designs, and additional research may be beneficial to confirm whether tracking patient-specific trajectories is a more accurate method (see **Section 7.2.3**). In addition, discrepancies between studies may also be due to the limitations of echocardiographic technology, particularly in previous work, as discussed in the following subsection.

**Discrepancies in Echocardiographic Findings** Echocardiographic imaging is a relatively inexpensive, non-invasive (or minimally invasive) imaging modality that is effective in diagnosing valvular disease, but there is a possibility of misdiagnoses. For example, the primary and secondary mechanisms of TR could be misidentified as demonstrated by Bharucha *et al.* (2013) [134]. In this work, the surgeons identified annular dilation and leaflet dysplasia as the primary TR mechanisms during surgery, while echocardiogram radiologists overwhelmingly reported only leaflet prolapse. Similar discrepancies in echocardiogram-based evaluation and interpretation can be found in the literature describing the location of the regurgitant jet. For example, using 3D echocardiography as a baseline Mah, *et al.* (2021) demonstrated that 2D imaging had lower sensitivity and a poorer accuracy compared to 3D imaging [137]. They observed that in pre-Glenn patients, the primary jet was in the center of the valve (70% of patients), whereas 2D echo analysis identified the antero-septal commissure as the most common (a finding similar with other 2D imaging work [133]). In a later study analyzing pre- and post-Fontan groups, they found that the center of the valve and the antero-septal commissure were equally common jet locations (45% and 48% of patients, respectively), revealing a temporal difference in the jet position [132, 137]. Clearly, 3D echocardiography is more recommended for correct valve diagnoses, but the resolution of these images may need to be improved to reduce inter-study discrepancies. In addition, guidelines for echocardiogram-based clinical evaluation of TR in HLHS patients could improve diagnostic accuracy, e.g., researchers have advocated detailed temporal analyses of the vena contract and proximal isovelocity surface measurements to ensure a more accurate and reliable grading of TR severity.

### Ventricular Mechanics and Its Relation to TR

The TV and the RV structurally and functionally related, and the dysfunction of the RV can also make an important contribution to the development of TR [138]. From a functional point of view, mechanical dyssynchrony and inhomogeneous contractions of the RV have been identified in the neonatal stage as mechanisms for the occurrence and recurrence of TR [134, 139]. At the same time, the presence of TR can impair the RV function, as noted by Bellsham-Revell *et al.* (2013) who found that the presence of TR increases the indexed end-diastolic volume by 16 mL, on average [140]. RV dysfunction is also influenced by the hypoplastic condition of the left side of the heart, with one study reporting reduced basal-septal RV strains in HLHS patients with a visibly developed left ventricle [141]. There are conflicting reports on whether this hypoplasia is associated with TR: in one study, re-

searchers identified severe underdevelopment of the left-side heart associated with TR in the post-Glenn period [142], while others found this trend in the post-Norwood period [129, 141]. From a geometric perspective, greater RV (i.e., apex-to-base length, diastolic area, etc.) was associated with TR throughout the palliative series [107, 125, 130], i.e., the enlarged RV causes lateral papillary muscle displacement and consequently results in leaflet tethering and TR [128, 129]. In conclusion, the function of the RV and TV is clearly closely related, and it is worth exploring RV repair options as a supplement or alternative to traditional TV repairs for HLHS patients undergoing staged palliative surgery.

### Surgical Decisions and Potential Impacts on TR

During palliative procedures, decisions made during the surgery can affect the development of TR. For example, pre-surgical planning can have a major impact on long-term mortality and outcomes; the type of shunt used in the Norwood procedure can affect TR development; and alternative procedures or modifications of each palliation stage may improve or worsen the patient's subsequent condition. Here we review the potential impact of these decisions at each stage of the palliation.

**Fetal Diagnoses and Pre-Surgical Planning** With recent advances in echocardiographic technology, HLHS and TR can be detected as early as fetal development [143–145]. Prenatal HLHS diagnosis has been associated with a lower incidence of TR [146, 147]. However, it is likely that these findings are subject to patient selection bias. Despite this potential limitation, prenatal diagnosis can improve surgical management of HLHS through prophylactic interventions after birth and pre-planned surgical treatments [146, 148], or in some cases fetal interventions and HLHS/TR prevention strategies such as balloon dilation [149], maternal hyperoxygenation [150] or aortic valvuloplasty [151]. Preoperative management of HLHS may also affect the development of TR, with one study reporting that neonates without mechanical ventilation were at greater risk of developing TR [152].

**Norwood: Shunt Selection** During the Norwood procedure, a shunt is used to reconstruct the aorta to increase blood flow to the lungs, and the type of shunt used may vary based on clinician's preference. The two main shunt types seen clinically are the Blalock-Taussig shunt (BTS) and the right ventricle-to-pulmonary artery shunt (RVPAS). The BTS connects the innominate artery or the right subclavian artery (i.e., the first branch of the artery from the aorta) to the pulmonary artery, and Asaki *et al.* (2014) found that the size of the BTS

had a significant impact on the rate of TR prior to the second palliation stage: $3.5$ mm shunt, $36\%$ of patients; $3.0$ mm shunt, $7\%$ of patients (OR $7.3$ $[1.4-38]$ $95\%$ CI) [153]. Comparing BTS and RVPAS, some researchers have found that RVPAS reduces short-term inter-stage mortality and TR [154], while others found no significant differences in short-term mortality between the shunt types [155]. However, in the long term, a meta-analysis found that the two shunt types achieved comparable survival in the period between Stages II and III and up to $6$ years post-Fontan [156]. This was also evident in a post-Fontan follow-up analysis, although BTS recipients had higher TR values [157]. Based on these clinical studies, it is possible that there are long-term complications with the RVPAS that cause this ultimate equivalent performance, such as pulmonary artery stenosis and shunt re-interventions. In addition, it is possible that the optimal shunt device or method has yet to be found.

**Alternatives to the Norwood Procedure** The hybrid procedure was proposed as an alternative to the Norwood procedure, with the overall goal of avoiding neonatal open-heart surgery in infants. In this procedure, a stent is placed via transcatheter in the patent ductus arteriosus, and the pulmonary arteries are connected by an open-chest procedure to balance the pulmonary and systemic blood flow [158–160]. When comparing the hybrid operation with the traditional Norwood procedure, it was found that the development of the TR does not differ significantly [161, 162]. It was also found that the functional indices of RV and TV were not significantly improved in the hybrid procedure and therefore the benefits of adopting this hybrid procedure are not clearly demonstrated [162]. Further investigation is needed to determine whether any of the variations of the Norwood procedure (e.g., the Sano modification using the RVPAS) or other alternatives have clear long-term clinical advantages [163].

**Stage II (Glenn) Operation** During the Glenn operation, certain surgical decisions may be related to the onset of TR in the pre-Fontan period. For example, it has been observed that recipients of a TV repair at the time of the Glenn surgery have a higher risk of death [164]. Another study also examined the use of a bidirectional superior cavopulmonary anastomosis during the Glenn procedure and found that there was an insignificant difference in the development or severity of occurrence of TR [165]. However, patients who develop TR after surgery have a higher risk of adverse late effects (OR $= 16.5$ $[4.4-62.6]$ $95\%$ CI) [166]. In some HLHS-specialized centers, the hemi-Fontan procedure is performed instead of the Glenn procedure, facilitating the connection of the superior vena cava to the pulmonary artery with a homograft patch, as opposed to a translocation of the artery to simplify the

later Fontan operation [167]. So far it has been established that the hemi-Fontan procedure is hardly associated with TR [168] and shows similar results to the Glenn in the short term procedure [169]. Future long-term studies may further demonstrate the benefits or undesirable consequences of these Stage II procedures.

### Mechanisms of Post-Repair Recurrent TR

In addition to the decisions made during the palliation stages, the method of TV repair can also influence the recurrence of TR. Annuloplasty was predominantly used in one patient cohort and it was found that the repair significantly improved leaflet coaptation lengths, reduced partial change in RV area and diastolic area, and improved the grade of TR (reduced from $3.1$ to $1.7$ on a $0.0-4.0$ scale) [170]. It has also been shown that preserving RV function in TV repair prevents severe TR recurrence [106, 139, 171]. It is worth noting that the TV repair can deteriorate the RV function immediately, but long-term improvements are observed such as reduced RV dimensions [104, 106, 107, 170]. In addition, repair beyond an annuloplasty predicts poor prognosis (e.g., mortality) [139]. Other risk factors $5$ years after TV repair were analyzed using multivariate analysis: (i) risk factors for mortality—lower weight at time of repair (HR $= 0.74$ $[0.55-0.99]$ $95\%$ CI); (ii) risk factors for re-operation—intervention before Stage II (HR $= 5.51$ $[1.063-29.62]$ $95\%$ CI) and lower weight at initial TV repair (HR $= 0.77$ $[0.63-0.95]$ $95\%$ CI); and (iii) risk factor for TV replacement—pre-Stage II intervention (HR $= 36.92$ $[2.17-629.63]$ $95\%$ CI). Unsuccessful TV repair can also be associated with the presence of posterior leaflet prolapse and septal leaflet tethering [131]. Overall, it is clear that TV repair can be beneficial in preserving RV function and that patients requiring neonatal TV repair typically have poor outcomes. In future studies, analysis of concomitant repair could be beneficial as it is believed that TV intervention prior to RV dysfunction can improve survival in HLHS patients [106, 171, 172].

## 2.4 Lacking Knowledge and Future Perspectives

To date, there is a great amount of research that has been performed in both TV leaflet biomechanics, and in understanding the HLHS condition. To supplement this information, additional research efforts are needed on both fronts. On one hand, the TV biomechanics information is incomplete with regards to the microstructure-mechanics relationships and the use of AFK theory. On the other hand, the research from an engineering perspective could be massively beneficial for a deeper understanding of HLHS and the development of

clinically relevant tools. These gaps in knowledge motivate the present dissertation research work, and these needed advancements are briefly described below.

### 2.4.1 Proposed Research in Tricuspid Valve Leaflet Biomechanics

Overall, our laboratory has conducted several studies to quantify the biomechanical properties of the TV tissues, along with the groundbreaking works from other laboratories. Despite these efforts, there are still gaps in knowledge that must be filled to complete the picture of the TV leaflet properties.

#### Collagen and Elastin Microstructure-Mechanics Relationships

Previously, we performed an enzymatic removal of the GAGs from the MV and TV leaflets [39], and a logical continuation of this study is to extend the methods for quantifying the contributions of collagen and elastin to the bulk tissue mechanical properties. As an additional benefit of performing such a study, previous researchers have not fully elucidated the contributions of collagen or elastin to tissue viscoelastic properties—properties that have been the subject of many previous characterization studies [25, 173–176] and viscoelastic model formulations [173, 174, 177]. Also, despite the advances in understanding the collagen and elastin microstructure-mechanics relationships for the semilunar valves, enzymatic removal methods have not been used in the same manner for the elastin and collagen constituents in the AHV leaflets, which have a different ECM organization.

#### Evaluation of Affine Fiber Kinematics Theory

The existent studies on affine fiber kinematics theory suggest that tissue-specific studies are required to verify this modeling simplification. While a prior study has been performed to evaluate the AFK of the MV leaflets [50], the TV leaflets undergo a lower pressure gradient in the right side of the heart compared to their MV counterpart on the left side of the heart, i.e., 25 mmHg vs. 100 mmHg [19, 178]. Thus, these AHV tissues that have different functional environments may have different microstructural properties and behaviors that necessitate their own AFK-based investigations [10, 22]. Therefore, we require a TV-centric study for improved confidence in using the AFK theory.

### 2.4.2 Propose Studies for Improving the Understanding of HLHS

Although a wide range of research has been conducted to analyze the occurrence or recurrence of TR in HLHS, there are remaining gaps in knowledge that are critical for refining therapy and assessing patient risk. Primarily, the list of potential TR indicators may be incomplete, and additional factors need to be considered by analyzing the tissue biomechanics of the TV apparatus.

### 2.4.3 An Improved Understanding of TR – Engineering Insights

To date, the focus of TR-related research has been on the valvular geometric indicators, structural abnormalities or problems with TV repair. These findings can also be leveraged by understanding tissue biomechanics, which could provide valuable insights into the driving mechanisms of TR. For example, excessive tissue strains or stresses, possibly caused by the change in the cardiovascular environment, could indicate future onset of TR due to deviation from a homeostatic strain or stress that is more desirable for whole valve tissue function and valvular interstitial cells. The development of image-based engineering analysis tools and refined computational models is a crucial next step towards a better understanding of the onset of TR in the HLHS population.

#### Non-Invasive Analysis of Tissue Biomechanics

Image-based analysis of the valvular structures is a research area with growing potential as medical imaging techniques advance. Echocardiograms, in particular, have enabled most of the reviewed research, and this routine imaging modality can be used for more advanced, engineering-focused analyses. Therefore, another focus of this dissertation is to lay the groundwork for a non-invasive engineering analysis pipeline for echocardiographic atrioventricular heart valve image data. Specifically, a framework is developed for quantifying the annulus mechanics and geometry, which is demonstrated using the tricuspid valve imaging from patients with hypoplastic left heart syndrome.

**Inverse Modeling** Information about tissue strains and geometry can be obtained using the image-segmented valvular structures, but *in silico* computational modeling, on the other hand, can further predict hemodynamics, tissue material properties and/or stresses of the TV apparatus *in vivo*. For example, computational models were developed to compare the hemodynamic environment using different shunts in the Norwood procedure [179]. Com-

putational models and simulation frameworks in the HLHS demographic are sparse, and existent modeling techniques for the adult mitral and TVs could be adapted for use with the HLHS-afflicted TV to gain new insights into the potential changes in tissue properties that underlie and predict the mechanisms of TR. Of specific interest is the potential for using inverse finite element analysis (iFEA) to predict patient-specific tissue properties and provide high-resolution information on the tissue biomechanics. However, iFEA is currently limited by issues such as non-unique solutions, long computational time (1+ days of runtime), and the need for assumptions about the valve structures (i.e., assuming a chordae attachment map). On top of this, the AHVs pose a unique challenge in iFEA compared to the semi-lunar valves (e.g., complex leaflet buckling and folding), and as such there are limited frameworks developed to solve this problem. While a fully robust iFEA framework may require another decade of research, the first steps towards this potential clinical tool will be made to serve as a foundation for future researchers.

## 2.5 Structure of the Dissertation

The remainder of this dissertation is organized as follows: **Chapter 3**, a quantification of the effects of collagen and elastin deficiency on the biomechanics of AHV leaflets; **Chapter 4**, a pSFDI-based evaluation of affine fiber kinematics theory for the TV leaflets; **Chapter 5**, the development and presentation of a non-invasive, engineering analysis framework for the TV annulus, with a pilot study on newborns with HLHS; and **Chapter 6**, an investigation of the potential for inverse finite element analysis of the TV, demonstrated with echocardiographic data from the newborns with HLHS. The findings from each chapter are then briefly summarized in **Chapter 7**, along with a description of future studies that can further enhance the research performed in this dissertation.

# 3 EFFECTS OF ENZYME-BASED REMOVAL OF COLLAGEN AND ELASTIN CONSTITUENTS ON THE BIAXIAL MECHANICAL RESPONSES OF PORCINE ATRIOVENTRICULAR HEART VALVE ANTERIOR LEAFLETS


3.1 Motivation . . . 38
3.2 Methods . . . 38
3.2.1 Tissue Acquisition and Preparation . . . 38
3.2.2 Biaxial Testing Procedure . . . 38
3.2.3 Enzymatic Treatment for Elastin and Collagen Degradation . . . 40
3.2.4 Histological Assessment of Tissue Constituents . . . 41
3.2.5 Verification of Histological Analysis Methods . . . 42
3.2.6 Tissue Stretch and Stress Calculations . . . 42
3.2.7 Statistical Analyses . . . 45
3.3 Results . . . 45
3.3.1 Histological Results . . . 45
3.3.2 Histology Analysis Verification . . . 48
3.3.3 Thickness Measurements . . . 48
3.3.4 Biaxial Tensile Testing . . . 48
3.3.5 Biaxial Stress Relaxation . . . 53
3.4 Discussion . . . 58
3.4.1 Overall Findings . . . 58
3.4.2 Study Limitations and Future Extensions . . . 68
3.5 Chapter Summary . . . 71

## 3.1 Motivation

The objective of this study is to expand our knowledge of the mechanics-microstructure relationships of the AHVs by quantifying the contributions of elastin and collagen to the biaxial tensile and stress relaxation responses of the MV and TV anterior leaflets through an enzymatic treatment process. The findings from this study will be useful in advancing our knowledge of the biomechanics of AHV tissues. The relationship between tissue mechanics and microstructure, which has been determined from the current studies on elastin and collagen removal, could further support the development of microstructure-informed AHV constitutive models.

## 3.2 Methods

### 3.2.1 Tissue Acquisition and Preparation

Healthy porcine hearts ($80-140\,\text{kg}$, $1-1.5\,\text{yrs}$) were obtained from a USDA-approved slaughterhouse (Chickasha Meat Co., Chickasha, OK) and promptly cleaned of blood clots before being stored in the freezer at $-14°\text{C}$ between one and twenty-one days. Freezer storage was used based on previous studies that showed that the AHV leaflet mechanical response was not significantly affected by short-term freezer storage [32, 33]. After storage, hearts were thawed and the anterior MV leaflet (MVAL) and the anterior TV leaflet (TVAL) were excised and placed back in the freezer until the day of testing. On the day of the mechanical testing, the leaflets were thawed in phosphate-buffered saline (PBS). The MVAL and TVAL samples were then sectioned into $10 \times 10\,\text{mm}$ specimens (**Fig. 3-1(a)**), and the chordae tendineae were trimmed at the point of insertion in the leaflets. Average tissue thicknesses were then obtained by taking three leaflet thickness measurements for each specimen using digital calipers (Westward 1AAU4 with $0.01\,\text{mm}$ resolution, Grainger, Wake Forest, IL). In our earlier work we found a reasonable correspondence between this contact-based caliper approach and the non-contact thickness measurement methods [22]. After specimen preparation, biaxial mechanical tests and enzyme treatments were carried out, as discussed next in the **Sections 3.2.2** and **3.2.3**, respectively.

### 3.2.2 Biaxial Testing Procedure

Biaxial mechanical tests were performed to characterize and compare the mechanical responses of the control and the enzymatically treated tissues. The sequential testing proce-

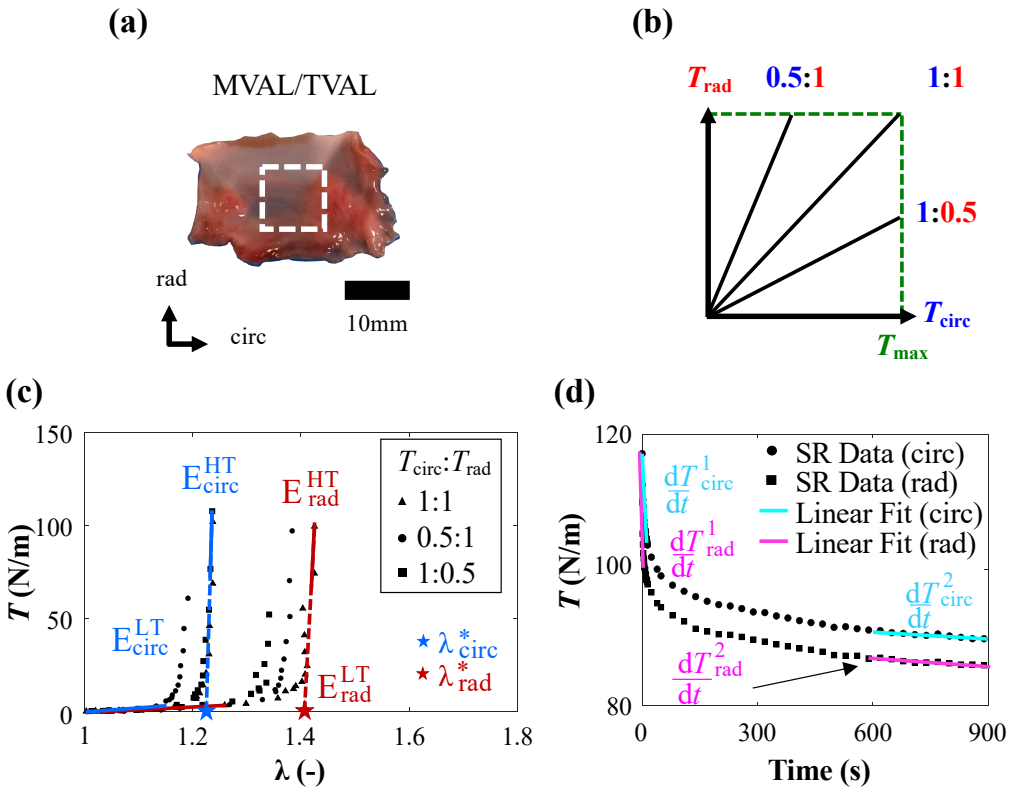


**Figure 3-1** (a) Porcine MVAL and TVAL specimens sectioned to a $10 \times 10$ mm region for (b) biaxial mechanical testing at various ratios of the peak membrane tensions ($T_{\text{circ}}$:$T_{\text{rad}} = 1{:}1$, $0.5{:}1$, and $1{:}0.5$) and for stress relaxation tests ($T_{\text{max}}$ denotes the peak biaxial membrane tension). (c) Parameters quantified from biaxial tension tests, including the tissue stretch $\lambda$, the index of extensibility $\lambda^{*}$, the low-tension modulus $E^{\text{LT}}$, and the high-tension modulus $E^{\text{HT}}$. (d) Parameters quantified from biaxial stress relaxation data, which include the rate of change of membrane tension at the initial and the saturated relaxation regimes, i.e., $\mathrm{d}T^{1}/\mathrm{d}t$ and $\mathrm{d}T^{2}/\mathrm{d}t$, respectively. Note: In (c) and (d) a smaller number of data points are visualized than the actual number of data points analyzed in order to improve visual clarity.

dure was performed as described below: (i) biaxial mechanical testing of the control (untreated) MVAL or TVAL specimens; (ii) enzyme treatment of the specimens in order to degrade a part of the elastin or collagen constituent (see **Section 3.2.3**); (iii) biaxial mechanical testing of the enzymatically treated specimens using the same protocols as in step (i). For the biaxial mechanical characterizations, the tissues were mounted to a commercial biaxial testing system equipped with $1.5\,\mathrm{N}$ load cells (BioTester, CellScale, Canada) using five-tined BioRakes at an effective testing size of $7.5 \times 7.5\,\mathrm{mm}$ for control tissues and $6 \times 6\,\mathrm{mm}$ for enzymatically treated tissues. The tissues were mounted such that the $X$- and $Y$-directions were aligned with the circumferential and radial directions of the tissue, respectively. A surgical pen was then used to apply four fiducial markers to the central third of the tissues for later digital image correlation (DIC)-based quantification of the tissue stretches (see **Section 3.2.6**) [180, 181]. To emulate physiological osmolarity and temperature, the tissues were submerged in a PBS bath heated to $37^{\circ}\mathrm{C}$ during testing.

Following our earlier studies [22, 23, 32], biaxial mechanical testing protocols consisted of a preconditioning step to restore the specimens to their approximate *in vivo* configurations, a displacement-controlled biaxial tensile testing step, and a stress relaxation testing step [182]. In short, during preconditioning the tissues were loaded to a preload of $3\%$ of the targeted membrane tension, followed by a $10$ cycle preconditioning protocol up to the peak biaxial membrane tension $T_{\mathrm{max}}$ of $100\,\mathrm{N/m}$ for the MVAL and $75\,\mathrm{N/m}$ for the TVAL to emulate their respective physiological stresses [19, 25]. After preconditioning, the displacements associated with the maximum applied tension were determined for the three biaxial tension ratios: $T_{\mathrm{circ}}$:$T_{\mathrm{rad}} = 1{:}1,\ 1{:}0.5$, and $0.5{:}1$ (**Fig. 3-1(b)**), and the displacement-controlled biaxial tensile test protocol was carried out with $4$ loading/unloading cycles. Following the biaxial tensile test, a biaxial stress relaxation protocol was performed in which the tissues were stretched to a configuration associated with the peak biaxial membrane tensions $T_{\mathrm{max}}$ and then the displacement held constant for $15\,\mathrm{min}$. Throughout the testing, a CCD camera (The Imaging Source, DMK 41AU02) was used to capture $1280 \times 960$ images at a rate of $5\,\mathrm{Hz}$, while load cell force readings were recorded at a frequency of $15\,\mathrm{Hz}$.

### 3.2.3 Enzymatic Treatment for Elastin and Collagen Degradation

After biaxial testing of the control leaflets, the specimens were enzymatically treated to degrade a portion of the elastin or collagen constituents. For the elastin removal study, the MV and TV leaflets ($n = 18$) were treated in a solution of $60\,\mathrm{Units/mL}$ elastase (Worthington

Biochemical Corp., #002292) and $0.1$ mg/mL trypsin inhibitor (Worthington Biochemical Corp., #003587), while MV/TV tissues ($n = 16$) were treated with collagenase (Worthington Biochemical Corp., #LS004176) at a concentration of $96$ Units/mL for the study of collagen degradation. The tissues were agitated in a thermal shaker (H5000-H MultiTherm Shaker, Benchmark Scientific, Sayreville, NJ) at $37$°C during the enzymatic treatment. After the tissues had been enzymatically treated for the optimal amount of time to remove $> 50\%$ of the constituents, the specimens were rinsed thoroughly with PBS at $4$°C and prepared for further biaxial testing, as described in **Section 3.2.2**.

#### Internal Study for Selecting Enzyme Treatment Time

To determine the optimal enzyme treatment time, we conducted an in-house study for the elastin and collagen removal. In each study, three MVAL and three TVAL specimens were sectioned into nine tissue strips, with one tissue strip serving as control (no treatment) and the remaining eight strips treated in the enzymatic solutions to monitor the progress of the constituent degradation over a period of $120$ min. Every $15$ min one of the strips was removed from the enzyme solution and rinsed with PBS in order to prevent further constituent degradation. After the treatment, the specimens were prepared for histological analyses (see **Section 3.2.4**). The optimal treatment time was determined to be the point in time at which a substantial amount of the desired extracellular matrix (ECM) constituent has been removed while providing adequate experimental time.

### 3.2.4 Histological Assessment of Tissue Constituents

A routine histological analysis was carried out on each strip from the in-house study (see **Section 3.2.3**). Briefly, all tissue strips were fixed for $48$ h in $10\%$ neutral buffer formalin at room temperature. Each slice was then paraffinized and sliced at a thickness of $5-7\,\mu$m using a microtome (Microm HM 355S, Thermo Scientific). The sections were next deparaffinized, rehydrated, placed on a glass slide and stained to visualize the ECM constituents: (i) Masson's trichrome staining (collagen in dark blue), and (ii) Verhoeff elastic-Van Gieson staining (elastin in black).

After staining, a micrograph was taken for each tissue strip using an inverted bright-field microscope (Olympus CKX53) with a 10X objective lens and a 14-megapixel camera. The images were then analyzed using MATLAB (MathWorks, MA) to quantify the change in color intensity of either the elastin or collagen constituents in the stained specimen. The

histology-based quantification of the tissue composition has been shown to be comparable to other constituent quantification techniques such as hydroxyproline assays (a gold standard) in skin tissue [183]. To reinforce use of histology-based techniques, we conducted an in-house verification study using second harmonic generation (SHG) confocal imaging—a microscopy technique commonly used in the previous microstructure-based studies [184, 185]. Based on the results of our in-house study, we decided to analyze the histological micrographs using a color intensity approach. Briefly, a color thresholding was first applied to each micrograph to generate an image that contained only the constituent of interest (i.e., collagen, blue; elastin, purple). Then, the constituent-isolated images were converted to grayscale, and the corresponding pixel intensity distribution was used to obtain the average pixel intensity. In order to finally determine the optimal enzyme treatment time in the intermediate study, the average intensity of the elastin or collagen constituent at each treatment timepoint was compared with the control tissue (untreated) as a percentage reduction in the average pixel intensity, representing the change in constituent composition.

### 3.2.5 Verification of Histological Analysis Methods

To confirm the use of histology-based methods to quantify the constituent degradation, we performed a small in-house study using second harmonic generation imaging. For verification, a TVAL specimen was sectioned into two strips, with one tissue strip serving as a control (untreated) specimen and the second tissue strip being subjected to a $90$ min collagenase treatment. The tissue strips were then prepared using routine histological preparation methods to obtain an unstained $5-7\,\mu$m tissue section. SHG imaging was then performed for each tissue section and the collagen fiber fluorescence signals were recorded. The percentage loss of collagen after enzyme treatment of $90$ min was considered to be the percentage difference in the signal response of the control and enzyme-treated specimens. After SHG imaging, the tissue sections were stained using Masson's trichrome and the constituent degradation was quantified as a change in collagen color (blue) intensity, as described in **Section 3.2.4**. The accuracy of the histology-based analysis was then assessed by comparing the differences in collagen area fractions between the control and enzyme-treated specimens with the percentage of signal loss from SHG imaging.

### 3.2.6 Tissue Stretch and Stress Calculations

We followed our previously developed protocols to calculate the tissue stretches and stresses [22]. In short, the coordinates of the four fiducial markers were determined with

the DIC module in the LabJoy software of the BioTester. A bilinear finite element with four nodes was used from the marker positions to calculate the deformation gradient **F**, based on the previous literature [14, 67, 186], here written in matrix notation as

$$[\mathbf{F}] = [\mathbf{F}(\mathbf{X},t)] = \begin{bmatrix} \sum_{I=1}^{4} B_{XI} u_I(t) & \sum_{I=1}^{4} B_{YI} u_I(t) \\ \sum_{I=1}^{4} B_{XI} v_I(t) & \sum_{I=1}^{4} B_{YI} v_I(t) \end{bmatrix} + \mathbf{I}, \tag{3.2-1}$$

where $B_{XI}$ and $B_{YI}$ are shape function derivatives in the $X$- and $Y$-directions for node $I$, respectively, **I** is the second-order identity tensor, and $u_I(t)$ and $v_I(t)$ are the $X$- and $Y$-displacements at time $t$, respectively. Specifically, the shape functions are those for a single bilinear finite element, i.e.,

$$\begin{aligned} &N_1(\xi,\eta) = \frac{1}{4}(1-\xi)(1-\eta), N_2(\xi,\eta) = \frac{1}{4}(1+\xi)(1-\eta), \\ &N_3(\xi,\eta) = \frac{1}{4}(1+\xi)(1+\eta), \text{ and } N_4(\xi,\eta) = \frac{1}{4}(1-\xi)(1+\eta), \end{aligned} \tag{3.2-2}$$

where $\xi$ and $\eta$ are the coordinates in the parametric domain. Tissue stretches in the circumferential ($X$) and radial ($Y$) directions (i.e., $\lambda_{\text{circ}}$ and $\lambda_{\text{rad}}$) were determined from the principal values of the right Cauchy-Green tensor $\mathbf{C} = \mathbf{F}^{\mathrm{T}}\mathbf{F}$. For quantitative and statistical analyses of the calculated tissue stretches, we further decomposed the total tissue stretches into: (i) the post-preconditioning (PPC) stretch ${}^{1}_{0}\lambda$, defined as the stretch after post-preconditioning ($\Omega_1$) with respect to the undeformed configuration (prior to the preconditioning step) ($\Omega_0$); (ii) the stretch ${}^{2}_{0}\lambda$ between $\Omega_0$ and the maximum tension ($\Omega_2$), where the identity is fulfilled: ${}^{2}_{0}\lambda = {}^{2}_{1}\lambda {}^{1}_{0}\lambda$. In addition, the anisotropy index ($AI$) was used to evaluate the material anisotropy of the tissue, i.e. $AI = {}^{2}_{0}\lambda_{\text{rad}} / {}^{2}_{0}\lambda_{\text{circ}}$.

To calculate the tissue stresses, the membrane tensions $T_{\text{circ}}$ and $T_{\text{rad}}$ were first determined from the force measurements of the load cells and the effective testing length of each specimen. Then, the first Piola-Kirchhoff (1st PK) stress tensor **P** was computed in matrix notation as $[\mathbf{P}] = \text{diag}[P_{\text{cc}}, P_{\text{rr}}] = [T_{\text{circ}}, T_{\text{rad}}]/w$, where $w$ is the measured thickness of the MVAL/TVAL tissue specimen. Other measures of stress, such as the second Piola-Kirchhoff and Cauchy stresses, can then be determined using the classical continuum mechanics text [64, 186, 187].

From the biaxial stress-stretch data we have also determined the low-tension elastic modulus, say $E^{\text{LT}}$, the slope of the stress-stretch curve in the pre-transitional region by using

the first $10-20$ data points of the membrane tension-stretch curve; and the high-tension elastic modulus, say $E^{\mathrm{HT}}$, the slope in the post-transitional region, using the last five data points. In addition, the index of extensibility $\lambda^*$, which is the stretch at the intercept of the extended tangent line of the post-transitional region, was calculated (**Fig. 3-1(c)**) [21, 188, 189].

On the other hand, from the biaxial stress relaxation data, the rate change in the membrane tension reduction was quantified using the initial and saturated slopes ($\mathrm{d}T^1/\mathrm{d}t$ and $\mathrm{d}T^2/\mathrm{d}t$), obtained from a linear fit of the first $5-10$ data points obtained and the last $250-300$ data points (see **Fig. 3-1(d)**). In order to be able to quantitatively assess the shape of the stress-relaxation curve, we have also determined the intersection of the two extended straight lines, which correspond to the initial and the saturated slope and as an indicator for the transition time $T_{\mathrm{trans}}$ between the two stress relaxation regimes. To further extract the information about the stress relaxation time, we also performed a fit to the viscoelastic test results using a standard 3-parameter solid model modified with a fractional-order dashpot, i.e.

$$g(t) = \left[E_0 + E_1 F_\alpha\left(-\frac{t^\alpha}{\tau}\right)\right] u(0), \tag{3.2-3}$$

where $g(t)$ is the force response, $u(0)$ is the constant displacement in the stress relaxation experiment, $E_0$ and $E_1$ are the spring constants, $\eta_1$ is the viscosity of the dashpot, $\alpha$ is the fractional-order parameter controlling the dashpot nonlinearity ($\alpha$=0, spring only; $\alpha$=1, linear dashpot that reduces to the standard *linear* solid model), $F_\alpha(z) = \sum_{k=0}^{\infty} z^k/\Gamma(\alpha k+1)$ is the Mittag-Leffler function, $\Gamma(x)$ is the gamma function, and $\tau = (\eta_1/E_1)^{1/\alpha}$ is the stress relaxation time estimated by this viscoelastic model [190]. The physical meaning of the parameters of this fractional viscoelastic model can be interpreted as follows: $E_0 + E_1$ represents the instantaneous stress at $t = 0$; $E_0$ represents the long-term (asymptotic) stress when $t \to \infty$; $\alpha$ denotes the range of the elastic-viscous response (or spring-dashpot order) (i.e., $\alpha = 0$: a fully elastic response, and $\alpha = 1$: a fully viscous response); and $\tau$ is inversely proportional to the degradation rate of the stress relaxation decay. This fitting was carried out with an in-house differential evolution optimization program [191] taking into account a residual error tolerance of $10^{-3}$.

### 3.2.7 Statistical Analyses

All results are presented as the mean $\pm$ standard error of the mean (SEM). Outliers were determined as any value that were removed more than three scaled median absolute deviations from the median. To determine the appropriate statistical test to compare the biaxial tensile and stress relaxation results between the control and the enzymatically treated specimens, the normality of the data was checked by means of quantile-quantile plots. Due to non-normally distributed data, we performed a two-tailed, paired-sample Wilcoxon signed-rank test to assess the *intrinsic nature* of the experiments. Comparisons were made between the median values of the parameters of the control group and the treated group. The null hypothesis was that the differences between the control group and the treated group had a median value of zero, i.e., the elastin or collagen removal had no statistically significant influence on the tissue mechanics. The parameters compared include: the post-preconditioning stretch ${}^{1}_{0}\lambda$, the stretches ${}^{2}_{1}\lambda$, the peak stretch ${}^{2}_{0}\lambda$, the low-tension modulus $E^{\mathrm{LT}}$, the high-tension modulus $E^{\mathrm{HT}}$, the index of extensibility $\lambda^{*}$, and the initial and saturated slopes of stress relaxation $\dot{T}^{1}$ and $\dot{T}^{2}$, where the overlying dot signifies the time derivative, i.e., $\dot{T} = \mathrm{d}T/\mathrm{d}t$. Note that we did not perform statistical analyses of the fractional viscoelastic model parameters as we did analyses of physical parameters such as stress reduction. For all analyses, differences were considered statistically significant when $p < 0.05$. We also performed a post hoc power analysis of the data acquired and the quantities analyzed, where a higher power value indicates a lower likelihood of false significant $p$-values (i.e., type II error).

## 3.3 Results

### 3.3.1 Histological Results

#### Elastin

The optimal enzyme treatment time for the elastin-removed tissues was determined by the intermediate study. When comparing the enzymatically treated tissue strips with the control, we observed a percent elastin reduction of almost $100\%$ after a treatment of $45$ min in both the MVAL and the TVAL samples. We chose the time interval of $90$ min to ensure that almost all of the elastin has been degraded and to remain consistent with the collagenase-treated tissues. The percentage composition and percentage elastin reduction for the tissue strips at every $15$ min increment can be found in **Table 3-1**, and a representative histological sample from five selected treatment times is shown in **Fig. 3-2**. In the treated MVAL and

**Table 3-1** Quantified area fraction of elastin in three control and elastase-treated MVAL and TVAL tissues from the intermediate study (see **Section 3.2.4**) over a 120 min treatment time. The results are shown as mean±SEM. Note:∼100% elastin reduction for the treated samples indicate almost
traceless elastin components in the histology images. *Only one of the three analyzed specimens contained quantifiable elastin contents.

| | MVAL | TVAL |
|---|---|---|
| Time (min) | Elastin Reduction (%) | Elastin Reduction (%) |
| 0 | - | - |
| 15 | ∼100% | +12.2%* |
| 30 | ∼100% | +14.1%* |
| 45 | ∼100% | ∼100% |
| 60 | ∼100% | ∼100% |
| 75 | ∼100% | ∼100% |
| 90 | ∼100% | ∼100% |
| 105 | ∼100% | ∼100% |
| 120 | ∼100% | ∼100% |

TVAL specimens, the elastin reduction reached ∼100%, indicating that all of the elastin present in the tissue was removed by the elastase treatment.

### Collagen

When we compared each enzyme-treated tissue strip with the control, we observed a percentage collagen reduction of $20.0 \pm 6.3\%$ after a treatment of 15 min, $39.6 \pm 5.2\%$ after a treatment of 45 min, and $46.2 \pm 17.2\%$ after a treatment of 90 min for the TVAL specimen. For each MVAL tissue strip, there was a percent reduction in collagen of $37.4 \pm 5.1\%$ after a treatment of 60 min, $46.2 \pm 17.2\%$ after a treatment of 90 min, and $43.6 \pm 13.2\%$ after a treatment of 120 min. From this in-house study, we chose a treatment time of 90 min for both leaflets for consistency and to keep the overall experimental procedure to a reasonable time (i.e., less than 8 h for each specimen test set). The compositions and reductions of collagen at each increment of 15 min are given in **Table 3-2**, and the representative histology is shown in **Fig. 3-3**.

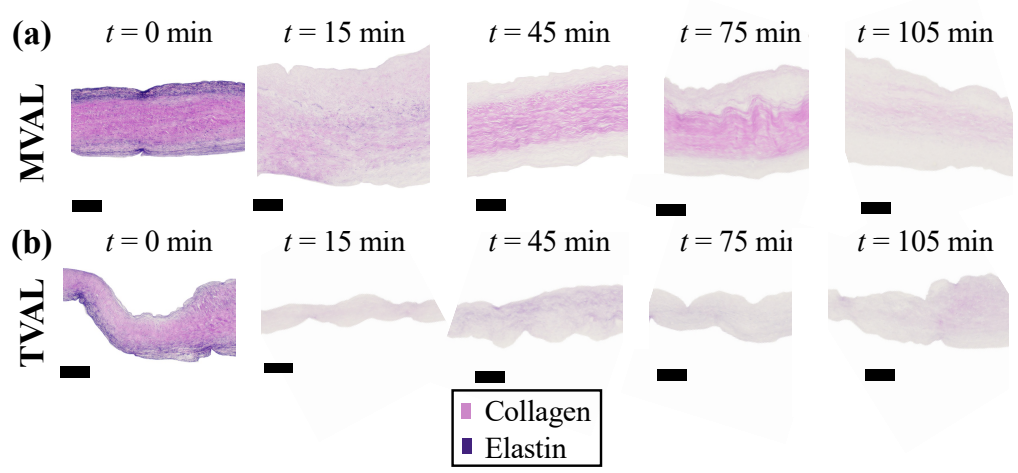


**Figure 3-2** Verhoeff-Van Gieson-stained histological images demonstrating the progression of the elastin constituent removal for: (a) MVAL (representative specimen) and (b) TVAL (representative specimen) at various enzyme treatment time point. Scale bars = 200 $\mu$m. The quantified constituent degradation at each analyzed point in time can be found in **Table 3-1**.

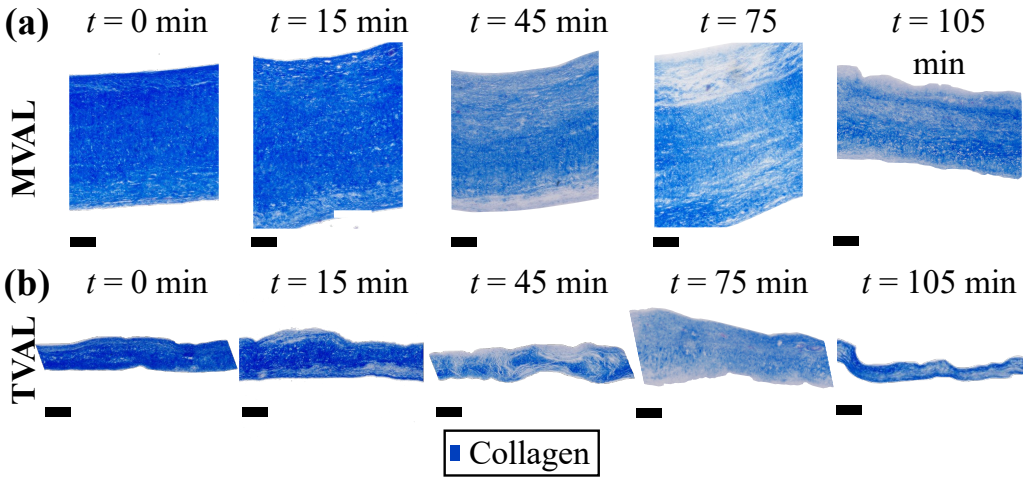


**Figure 3-3** Masson's trichrome-stained histological images demonstrating the progression of the collagen constituent removal for: (a) MVAL (representative specimen) and (b) TVAL (representative specimen) at various enzyme treatment time points. Scale bars = 200 $\mu$m. The quantified constituent degradation at each analyzed point in time can be found in **Table 3-2**.

**Table 3-2** Quantified area fraction of collagen in three control and collagenase-treated MVAL and TVAL tissues from the intermediate study (see **Section 3.2.3**) over a 120 min treatment time. The results are shown as mean±SEM.

| | MVAL | TVAL |
|---|---|---|
| Time (min) | Collagen Reduction (%) | Collagen Reduction (%) |
| 0 | - | - |
| 15 | $0.0 \pm 2.5\%$ | $20.0 \pm 6.3\%$ |
| 30 | $25.8 \pm 11.3\%$ | $10.9 \pm 6.7\%$ |
| 45 | $31.8 \pm 12.5\%$ | $39.6 \pm 5.2\%$ |
| 60 | $17.4 \pm 5.0\%$ | $37.4 \pm 5.1\%$ |
| 75 | $42.2 \pm 2.2\%$ | $43.9 \pm 13.9\%$ |
| 90 | $46.3 \pm 3.6\%$ | $46.2 \pm 17.2\%$ |
| 105 | $37.0 \pm 14.1\%$ | $43.0 \pm 13.3\%$ |
| 120 | $32.8 \pm 17.4\%$ | $43.6 \pm 13.2\%$ |

### 3.3.2 Histology Analysis Verification

On SHG confocal imaging, comparing the control and the 90 min collagenase-treated TVAL tissue strips, we observed a 76.4% decrease in collagen fluoresence signal. In the meantime, in the histology-based analysis of the same specimens, we observed a 73.5% decrease in the collagen area fraction (**Fig. 3-4**). The differences in quantified collagen loss suggest that the use of histology-based quantification is fairly consistent with the SHG imaging modality. It is also worth noting that in both experiments, *the same tissue section* was used in both SHG confocal imaging and histology analysis, ensuring that comparisons between SHG and histological quantification are made at an equivalent level.

### 3.3.3 Thickness Measurements

We found no statistically significant difference in the measured tissue thickness between the control and the elastase-treated tissues. Also, no statistically significant change in tissue thickness was found after collagen degradation.

### 3.3.4 Biaxial Tensile Testing

The biaxial testing results are presented in two separate subsections for the collagen- and elastin-removed specimen.

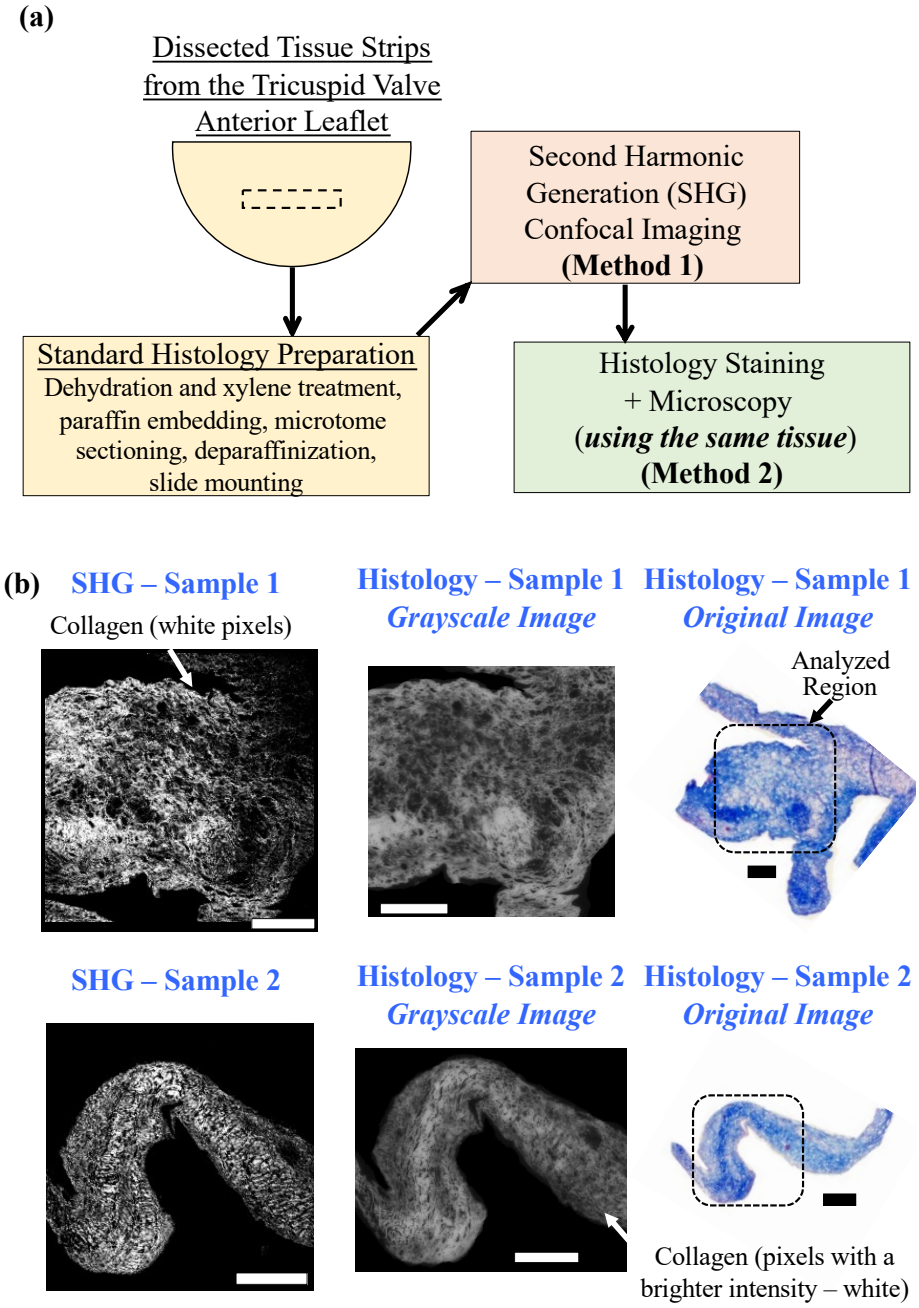


**Figure 3-4** (a) Overview of the second harmonic generation imaging-based procedure to (b) verify the color deconvolution methods used to quantify the constituent area fractions in histological micrographs. Scale bars = 200 $\mu$m.

### Elastin Deficiency

The results of the biaxial mechanical tests of the control and elastin-deficient tissues are summarized in **Figs. 3-5** and **3-6**, respectively. The results of the biaxial tests suggest the following observations:

(i) Stretches of the MVAL and TVAL specimens were significantly reduced by nearly 100% elastin removal, especially in the radial direction.

(ii) Elastin deficiency causes significant increases in the low- and high-tension tissue stiffness.

(iii) Elastase-based enzymatic removal of elastin reduces tissue anisotropy, i.e., in the $AI$: MVAL, $-13.2\pm3.3\%$ change ($p = 0.005$); TVAL, $-20.3\pm4.8\%$ change ($p = 0.002$).

Particularly under equibiaxial loading ($T_{\text{circ}}$:$T_{\text{rad}} = 1$:1) the MVAL specimens showed a statistically significant decrease in stretch between the control tissue and the treated tissue: $-7.5 \pm 1.8\%$ for ${}^{2}_{1}\lambda_{\text{circ}}$ ($p = 0.002$), and $-12.8 \pm 2.1\%$ for ${}^{2}_{1}\lambda_{\text{rad}}$ ($p < 0.001$). On the other hand, the TVAL specimens showed a significant decrease in radial tissue stretch: $-9.7 \pm 3.8\%$ for ${}^{2}_{1}\lambda_{\text{rad}}$ ($p = 0.008$). The tissue stretch values for the other two load ratios ($T_{\text{circ}}$:$T_{\text{rad}} =$ 0.5:1, and 1:0.5) showed a similar decreasing trend (**Fig. 3-5**). From the derived biaxial test parameters (**Fig. 3-6**), the moduli $E^{\text{LT}}$ and $E^{\text{HT}}$ showed previously insignificant changes for MVAL and TVAL under equibiaxial loading before and after the removal of elastin. However, we observed significant decreases in the moduli under *non-equibiaxial* loading, which suggests that elastin removal induces changes in the directional coupling of the tissue (**Fig. 3-6**). In addition, $\lambda^{*}_{\text{rad}}$ decreased under equibiaxial loading: MVAL, $-16.2 \pm 3.0\%$ ($p < 0.001$), and TVAL $-20.2 \pm 4.1\%$ ($p = 0.001$). Similar changes in the extensibility index were observed under non-equibiaxial loading scenarios (**Fig. 3-6**).

### Collagen Deficiency

The results of the biaxial mechanical tests of the control and collagen-deficient MVAL and TVAL are summarized in **Figs. 3-7** and **3-8**. The biaxial test results suggest the following key observations:

(i) Collagen deficiency leads to a significant decrease in the stiffness at the high-tension range during non-equibiaxial loading, especially in the case of the MVAL specimens.

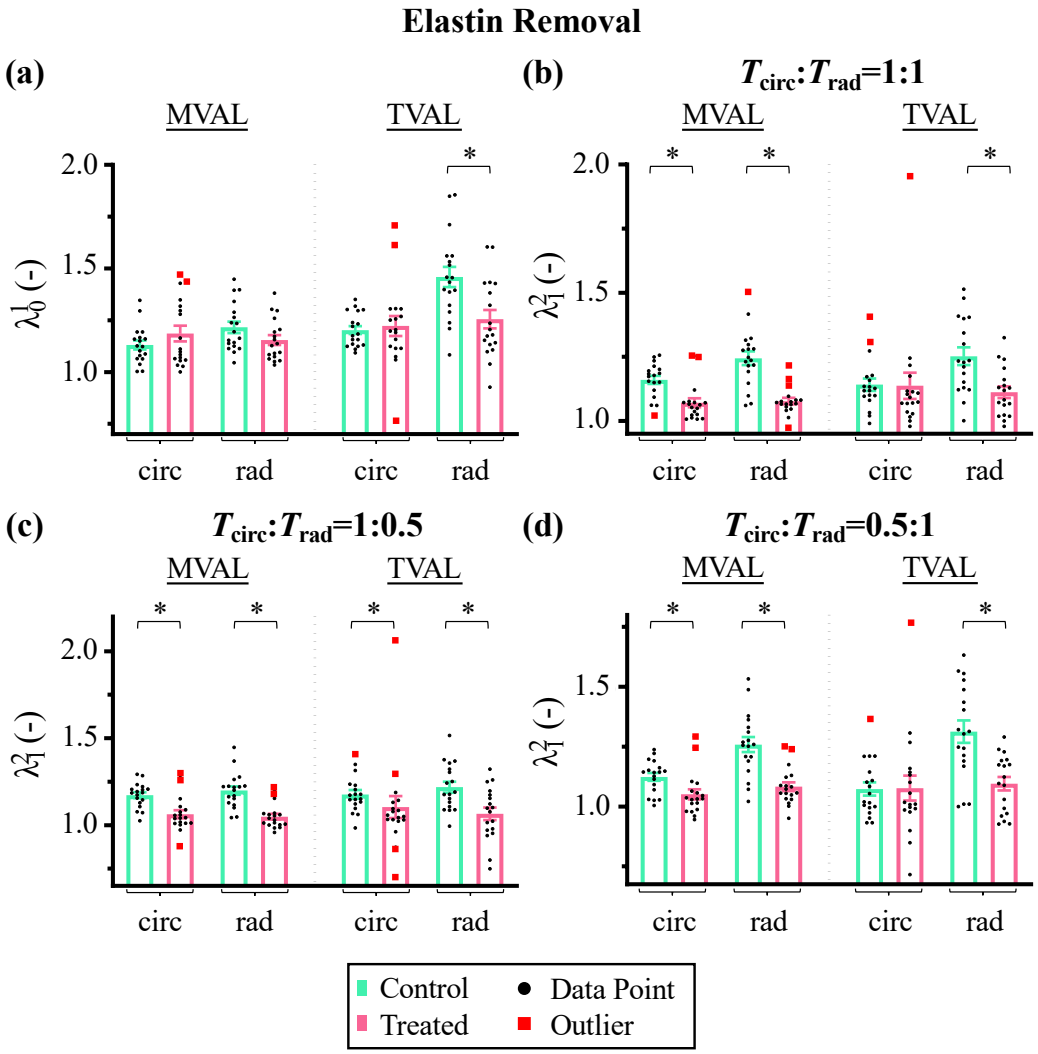


**Figure 3-5** (a) Preconditioning stretch ${}_{0}^{1}\lambda$ of the control (–C) and elastase-treated (–T) MVAL and TVAL specimens. Stretch ${}_{1}^{2}\lambda$ of the MVAL and TVAL specimens at the three biaxial tensions protocols: (b) $T_{circ}$:$T_{rad} = 1{:}1.$, (c) $T_{circ}$:$T_{rad} = 1{:}0.5$, and (d) $T_{circ}$:$T_{rad} = 0.5{:}1$ ($n = 18$). * denotes statistically significant ($p < 0.05$).

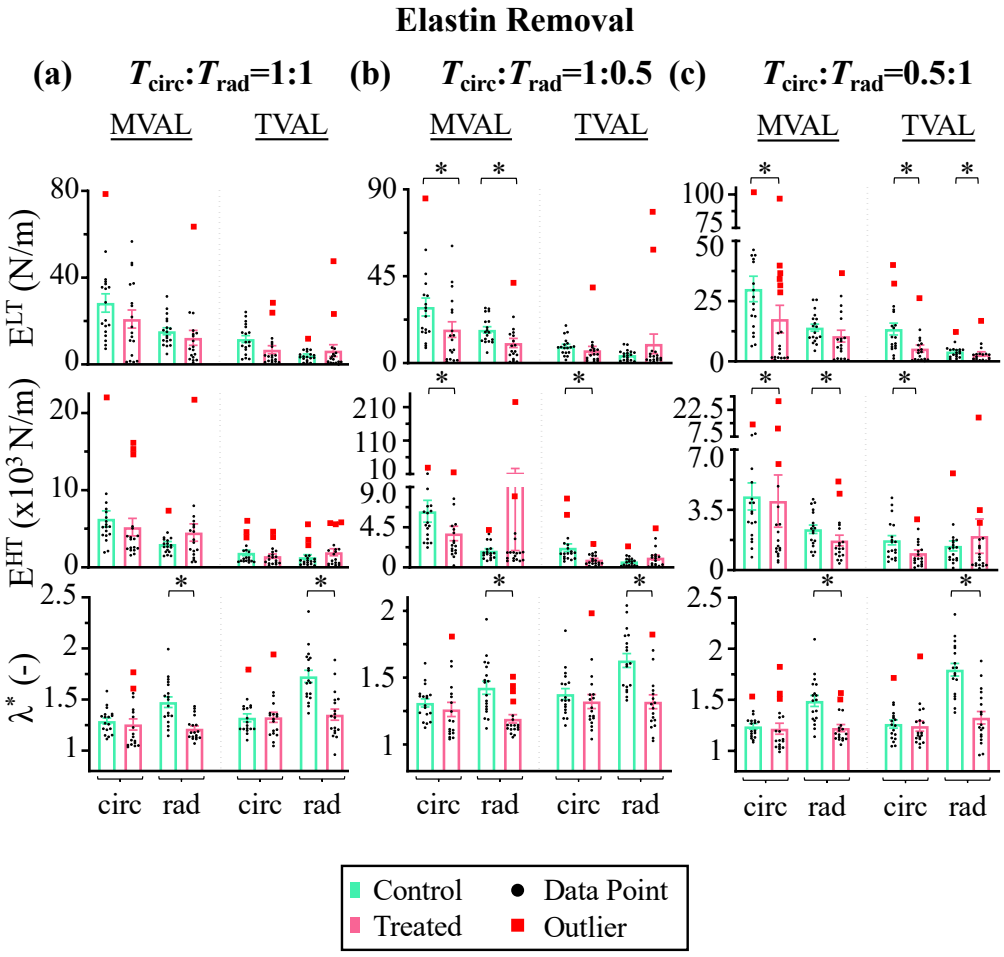


**Figure 3-6** Comparison of (a) the low-tension modulus $E^{LT}$, (b) high-tension modulus $E^{HT}$, and (c) the index of extensibility $\lambda^*$ between the control (–C) and elastase-treated (–T) MVAL and TVAL tissue specimens ($n = 18$) with three different biaxial tensions ($T_{circ}$:$T_{rad}$ = 1:1, 0.5:1, and 1:0.5). * denotes statistically significant ($p < 0.05$).

(ii) Collagen deficiency significantly influences the anisotropic nature of the TVAL tissue ($-16.9 \pm 7.4\%$ change in the *AI*, $p = 0.039$).

We did not observe any statistically significant differences in tissue stretches (${}^{2}_{1}\lambda$) after collagen removal. However, we found statistically significant increases in the PPC stretch for the TVAL in the circumferential direction (${}^{1}_{0}\lambda_{\text{circ}}$, $13.9 \pm 0.06\%$, $p = 0.006$). Similar trends were shown in the peak stretch (**Fig. 3-7**).

Taking into account the derived parameters under equibiaxial loading, $E^{\text{LT}}$ decreased by $-36.0 \pm 14.4\%$ in the circumferential direction ($p = 0.008$) for the TVAL specimens,, with similar significant changes observed during the non-equibaxial loading scenarios (**Fig. 3-8**). On the other hand, differences in $E^{\text{HT}}$ for MVAL and TVAL were observed during the non-equibiaxial loading scenarios.

### 3.3.5 Biaxial Stress Relaxation

#### Elastin Deficiency

Results from biaxial stress relaxation tests of the control and the elastin-deficient tissue are summarized in **Fig. 3-9**. At each of the points in time analyzed (5, 50, 100, 250, 500, and 900 s) there was a statistically significant increase in the percentage reduction in stress reduction in both the circumferential and radial directions for the MVAL and TVAL specimens (**Fig. 3-9(a)**,**(b)**). For the initial and saturated slopes of the stress relaxation for the MVALs, we observed a significant decrease between the control and the treated tissues: $-25.0 \pm 6.6\%$ for $\dot{T}^{1}_{\text{circ}}$ ($p = 0.004$), $-29.2 \pm 6.7\%$ for $\dot{T}^{1}_{\text{rad}}$ ($p = 0.005$), $-66.8 \pm 3.7\%$ for $\dot{T}^{2}_{\text{circ}}$ ($p < 0.001$), and $-62.5 \pm 4.8\%$ for $\dot{T}^{2}_{\text{rad}}$ ($p < 0.001$). On the other hand, we observed similar trends in the saturated slopes for the TVALs: $-69.3 \pm 3.9\%$ for $\dot{T}^{2}_{\text{circ}}$ ($p < 0.001$), and $-64.1 \pm 6.5\%$ for $\dot{T}^{2}_{\text{rad}}$ ($p < 0.001$). The elastin-removed MVAL also had a significantly slower transition to the asymptotic stress part of the curve after enzyme treatment: an increase of $T_{\text{trans}}$ by $27.1 \pm 10.2\%$ for the circumferential direction ($p = 0.031$), and an increase of $t_{\text{trans}}$ by $102.8 \pm 18.4\%$ for the radial direction ($p < 0.001$). In contrast, the TVAL had a faster transition: a decrease of $-37.3 \pm 7.1\%$ ($p < 0.001$) in the circumferential direction and a decrease of $-26.1 \pm 9.4\%$ in the radial direction ($p = 0.031$). These results indicated that the enzymatic removal of elastin resulted in a decrease in both the overall stress reduction and the initial and saturated slopes, suggesting the critical role of elastin in the viscoelastic behavior of MVAL and TVAL tissues.

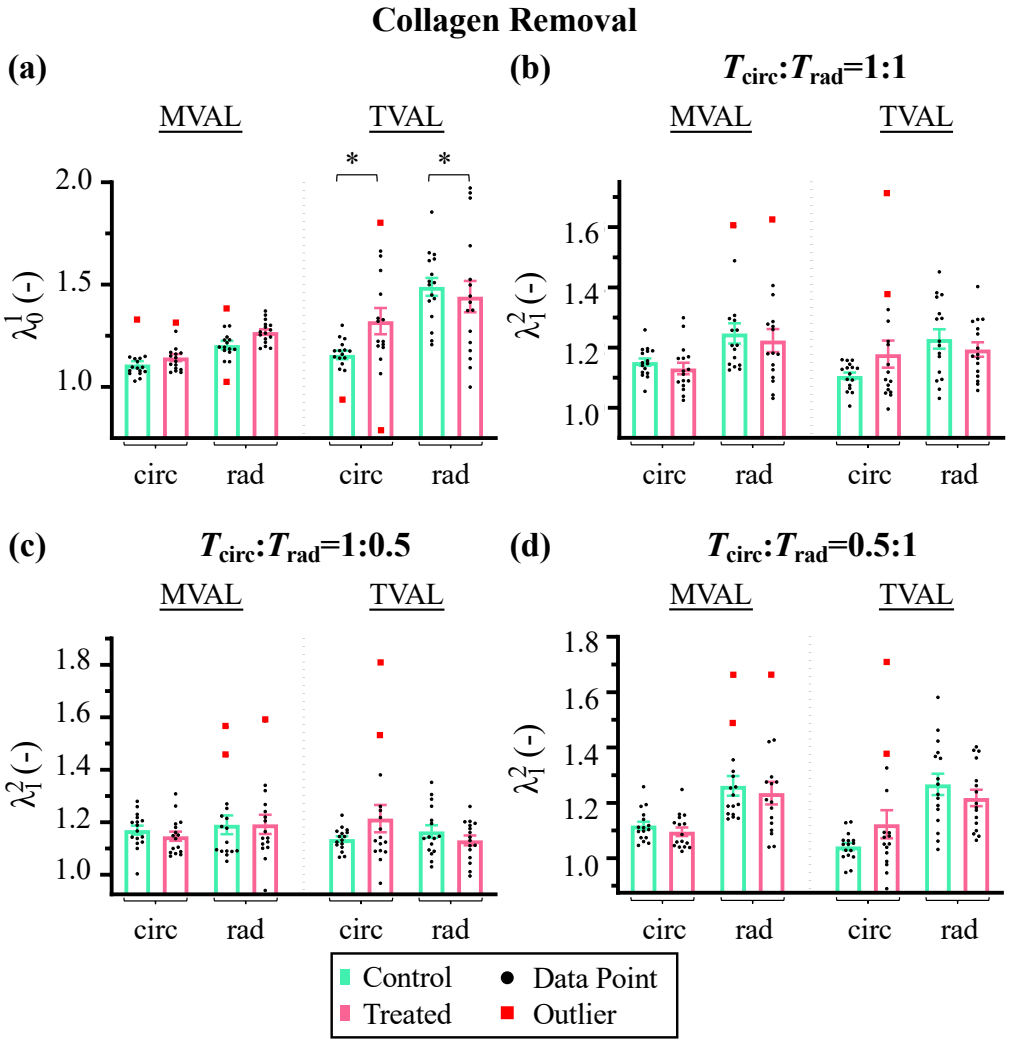


**Figure 3-7** (a) Preconditioning stretches ${}_0^1\lambda$ of the control (–C) and collagenase-treated (–T) MVAL and TVAL specimens. Stretches ${}_1^2\lambda$ of the MVAL and TVAL specimens at the three biaxial tensions protocols: (b) $T_{circ}$:$T_{rad}$ = 1:1, (c) $T_{circ}$:$T_{rad}$ = 1:0.5, and (d) $T_{circ}$:$T_{rad}$ = 0.5:1 ($n = 16$). * denotes statistically significant ($p < 0.05$).

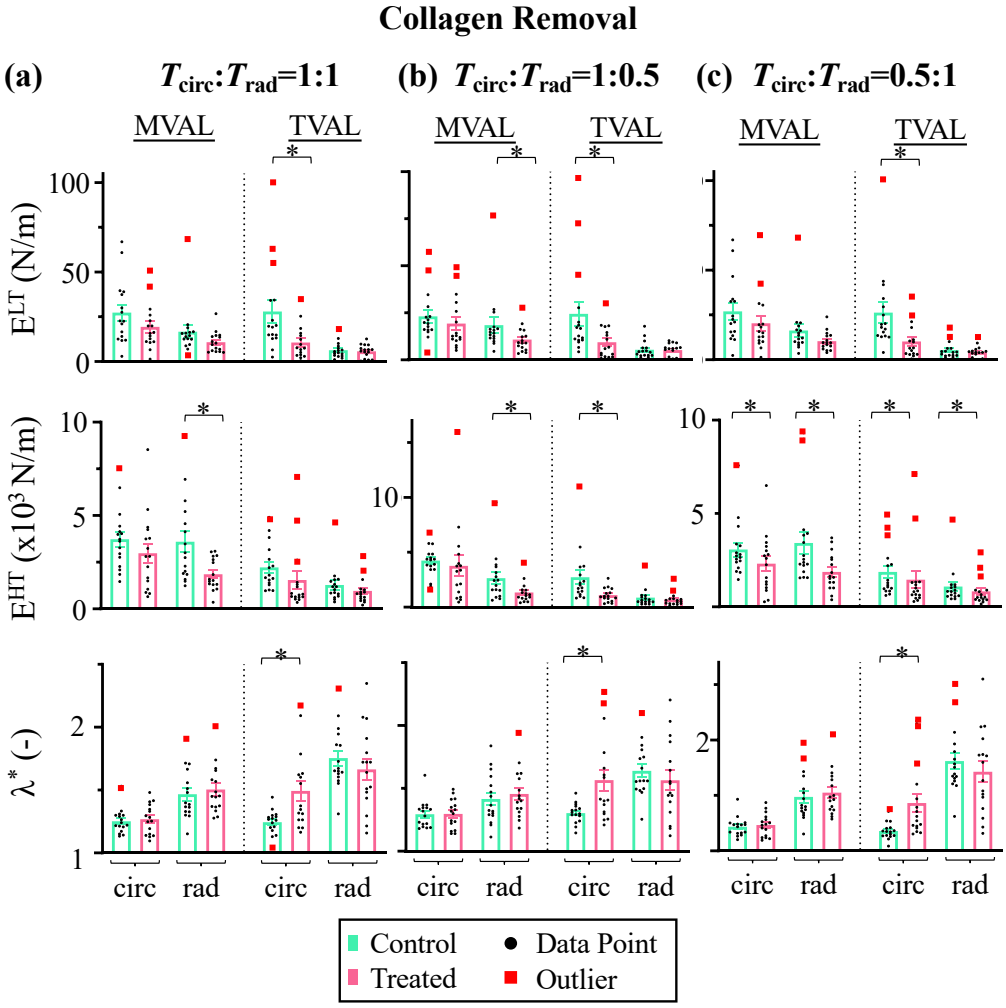


**Figure 3-8** Comparisons of: (a) the low-tension modulus $E^{\mathrm{LT}}$, (b) the high-tension modulus $E^{\mathrm{HT}}$, and (c) the index of extensibility $\lambda^*$ between the control (–C) and the collagenase-treated (–T) MVAL and TVAL tissue specimens ($n = 16$) with three different biaxial tensions ($T_{\mathrm{circ}}$:$T_{\mathrm{rad}} = 1{:}1$, $0.5{:}1$, and $1{:}0.5$). * denotes statistically significant ($p < 0.05$).

In addition, the fitting results of the 3-parameter fractional viscoelastic model of the specimens with elastin removal can be found in **Appendix A**. In general, we found that the elastin-removed MVAL tissues exhibited a greater asymptotic stress decay than the control tissues ($E_0$: $19\%$ and $49\%$ decreases in the tissue's circumferential and radial directions, respectively). We also observed a tendency towards more elastic behavior with respect to $\alpha$ (i.e., $9\%$ and $25\%$ increases in the two directions of the tissues), while $\eta_1$ decreased ($59\%$ and $50\%$ decreases in the circumferential and radial directions, respectively), which indicates a less viscous behavior. Finally, we also observed a larger stress decay (i.e., an increase in the total stress decay of $45\%$ and $43\%$ in both directions) based on changes in the parameter $\tau$, which is inversely correlated with the decay rate. Similar trends were also observed for the TVAL tissues.

### Collagen Deficiency

The results of the biaxial stress relaxation tests of the control and collagen-deficient tissues are summarized in **Fig. 3-10**. At each of the analyzed time points ($5$, $50$, $100$, $250$, $500$, and $900$ s) there was a statistically significant increase in the total stress decay in both tissue directions for the MVAL and TVAL specimens (**Figs. 3-10(a)**,**(b)**). For the initial slope of the stress decay of the MVAL specimens we observed statistically significant decreases in the radial direction: $\dot{T}^1_{\text{rad}}$, $-20.8 \pm 8.3\%$ ($p = 0.034$). For the saturated slope $\dot{T}^2$, there were significant decreases in the radial direction of $-31.5 \pm 9.2\%$ ($p = 0.005$). In contrast, significant changes in both tissue directions were observed in the TVAL specimens: circumferential $-25.2 \pm 9.9\%$ ($p = 0.011$), and radial $-24.3 \pm 9.9\%$ ($p = 0.026$). We also found statistically significant increases in the time to transition between the initial and saturated stress slopes for the MVAL tissues: circumferential $96.3 \pm 24.2\%$ increase ($p = 0.006$); radial $182.3 \pm 33.0\%$ increase ($p = 0.002$). These results indicated that collagen removal resulted in a decrease in both stress reduction and saturated slopes, indicating the unique effect of collagen deficiency on the viscoelastic behavior of the MVAL and TVAL tissues.

In addition, the fitting results of the 3-parameter standard solid model are provided in **Appendix A**. We found decreases in the $E_0$ parameters after collagenase treatment for both MVAL and TVAL of $\sim 50\,\%$ on average in both tissue directions, suggesting a lesser degree of asymptotic stress decay in collagen-deficient tissues. Meanwhile, the viscous vs. elastic MVAL and TVAL responses remained relatively unchanged after collagenase treatment, with only a $0 - 5\%$ in $\alpha$ for both tissue directions. The changes in $\eta_1$ were remarkable,

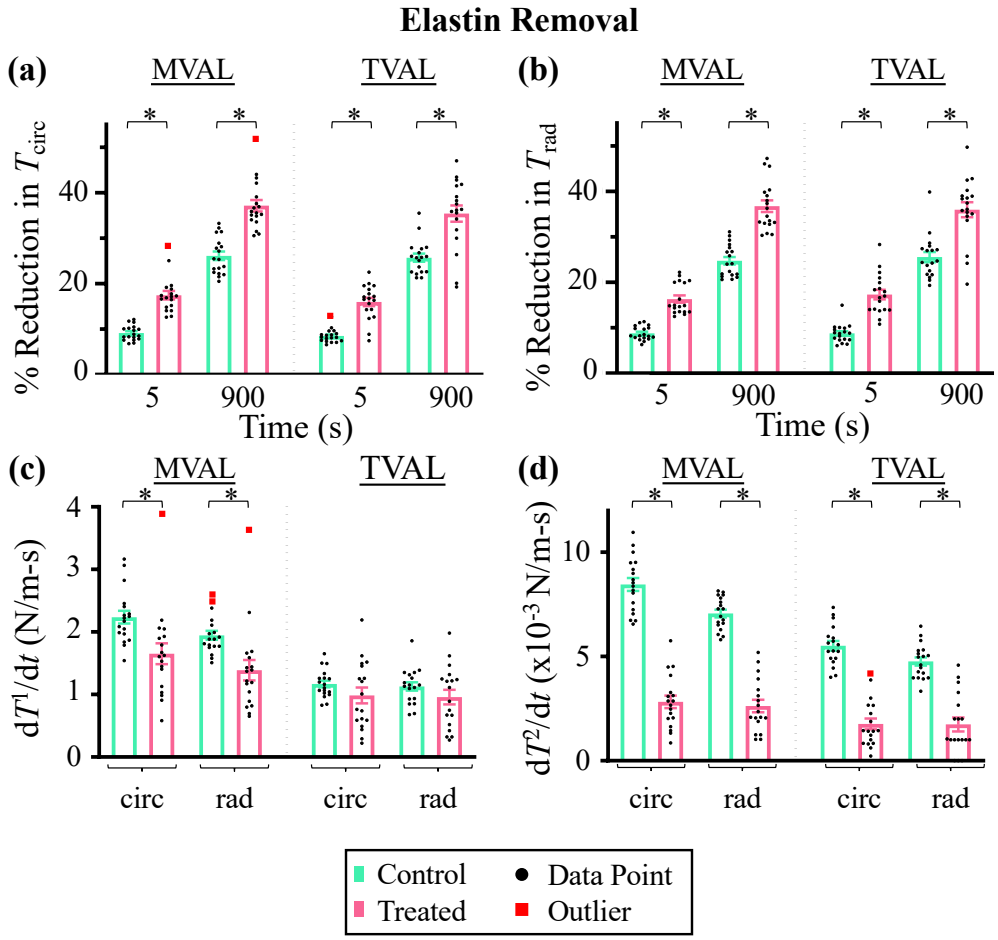


**Figure 3-9** Stress relaxation results of the control (–C) and elastase-treated (–T) MVAL and TVAL tissue specimens ($n = 18$). Membrane tension reduction in (a) the circumferential direction, and (b) the radial direction, and (c) the initial and (d) the saturated slopes of the stress relaxation reduction behavior. * denotes statistically significant ($p < 0.05$).

however, with average decreases of $25-40\%$ for the tissues in both directions, suggesting more elastic tissue behaviors. Finally, $\tau$ was reduced by an average of $\sim 15\%$ after collagen removal, indicating a higher stress decay rate.

## 3.4 Discussion

### 3.4.1 Overall Findings

The most important results of this study are: (i) We have quantified the effects of enzyme removal on the biaxial tensile properties, whereby collagen-deficient tissue has a lower slope in high-tensile behavior and elastin-deficient tissue is stiffer. This quantification and the novel experimental technique could be useful in predicting the disease-related changes in the ECM constituents that are closely related to heart valve tissue mechanics. (ii) Collagen carries the main high-tension loading, while elastin supports the high- and low-stress valve function. This was demonstrated by the observed decrease in the high-tension elastic modulus for the collagen-removed tissues and the decrease in high- and low-tension moduli for the elastin-removed tissues. This information is valuable in refining the constitutive models that describe the essential relationship between tissue mechanics and microstructure. (iii) A better understanding of how collagen and elastin deficiency changes the viscoelastic properties of tissue through stress relaxation tests: a greater stress reduction in the initial and saturated stress-relaxation behavior. In addition, the collagen- and elastin-removed MVAL tissues had a slower transition from initial stress reduction to asymptotic stress relaxation, while the elastin-removed TVAL tissues had a faster transition, as with $t_{\text{trans}}$. These results give an insight into the changes in tissue stress states *in vivo* in the case of microstructural changes caused by AHV disease.

In the literature on the biomechanics of the heart valves, researchers previously examined the biomechanical role of the ECM components in semilunar valve leaflets from porcine animals by selectively removing GAGs, elastin, or collagen via enzymes [34–37]. However, none of these earlier studies examined the mechanical properties of the *atrioventricular* valve leaflets before and after enzymatic removal of collagen or elastin in the same specimen. In the present study, we have, *for the first time*, quantified the biomechanical role of the collagen and elastin in the AHV leaflets, which enables a better insight into the microstructure-mechanics relationships. In addition, we made comparisons with our previous work, in which we carried out a similar enzymatic removal-based mechanical characterization of the GAGs from the AHV leaflets. These comparisons allow us to get a com-

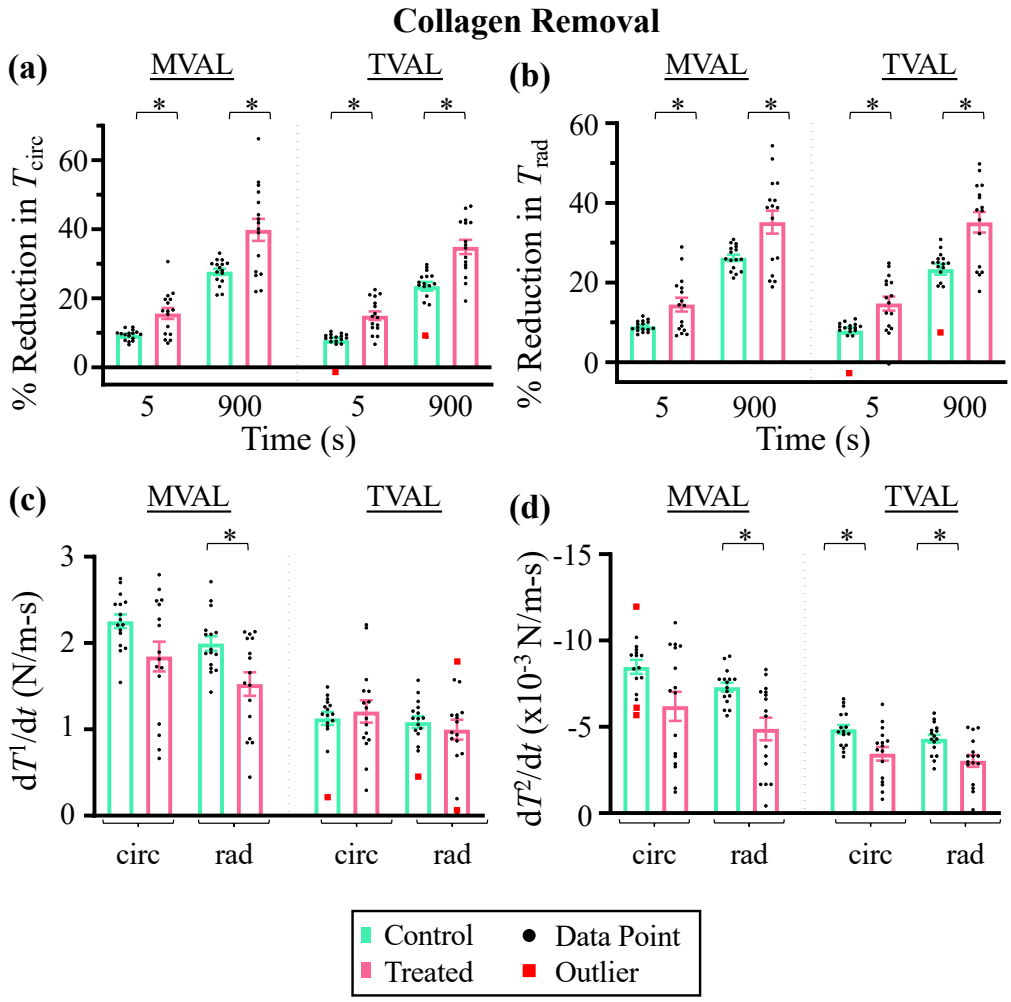


**Figure 3-10** Stress relaxation results of the control (–C) and collagenase-treated (–T) MVAL and TVAL tissue specimens ($n = 16$). Membrane tension reduction in: (a) the circumferential direction, (b) the radial direction, and (c) the initial and (d) the saturated slopes of the stress relaxation reduction behavior. * denotes statistically significant ($p < 0.05$).

plete picture of the microstructural contribution to tissue mechanics. Of particular interest are the quantified changes in tissue behavior when removing ECM constituents in order to determine the microstructure-specific parameters of model forms, such as the Lee-Sacks model [192] or the meso-scale structural constitutive model [184]. These disease-reflecting model parameters could be valuable for simulating the future state of the MV or TV of a patient with degenerative valve disease, whereby the predicted condition of the patient can be used to optimize valve surgery and thus improve the therapeutic outcome.

### Tissue Stretch of Elastin- and Collagen-Deficient AHV Leaflets

In the tissues treated with elastase, almost all MVAL and TVAL specimens showed a significant decrease in stretch in both tissue directions under all three biaxial tension ratios (**Fig. 3-5**). These results are to be expected because nearly 100% of the elastin has been removed from elastase-treated tissues and elastin is the main factor in helping the AHV leaflet withstand and recover from elastic deformation [8]. These results are similar to an earlier mechanical characterization study for the elastase-degraded aorta tissue, in which the tissue became more extensible after 6 h of enzyme exposure [193].

On the other hand, the collagenase-treated samples showed no significant stretch changes in the MVAL specimens, and only one quantity with a significant change was found in the TVAL specimens (**Fig. 3-7**). In contrast, an earlier study of the contribution of collagen to tissue extensibility indicated that a decrease in collagen content would lead to a decrease in tissue stiffness [194]. The difference in our results may be due to the different testing schemes because (i) the previous study used a uniaxial testing protocol for the MV tissue strips, which may not fully capture the coupling between tissue directions; (ii) the machine cross-head displacements were used in the previous study to quantify tissue properties compared to a more representative optical strain tracking approach in our study; and (iii) the analysis of the microstructure components by histology was absent from their work. In comparison with another study by Balguid *et al.* (2007) it was found that the tissue became stiffer with increasing collagen-collagen cross-link concentration in human aortic valve cusps [195]. Our study can confirm these results, as in the present study we removed collagen from the AHV leaflets and changed the underlying cross-links, which led to increased tissue stretching. In addition, previous work by Bender *et al.* (2020) showed that collagenase-treated MV porcine leaflets retained a similar collagen fiber architecture after

degradation, which may explain our observation of the numerical changes (albeit statistically insignificant) in tissue stretch after collagen removal [38].

### Elastic Moduli of Elastin- and Collagen-Deficient AHV Leaflets

By analyzing the high-tension and low-tension moduli, we were able to further elaborate on the contributions of collagen and elastin to the tissue mechanical response. In the specimens with elastin deficiency, the high-tension and low-tension moduli decreased with non-equibiaxial loading (**Fig. 3-6(b)**,**(c)**) compared to equibiaxial tensions (**Fig. 3-6(a)**). The changes in the low-tension modulus were similarly observed in a previous study that performed uniaxial testing of AV cusps after elastase treatment [176]. For the collagen-deficient specimens, the high-tension modulus showed significant decreases, especially during the radially dominant loading ($T_{\text{circ}}$:$T_{\text{rad}} = 0.5$:1, **Fig. 3-8(a)**), while the low-tension reamined largely unaffected apart from the circumferential direction of the TVAL tissue (**Fig. 3-8(b)**). These observed trends provide experimental support for previous theories that collagen is responsible for carrying the majority of the high-stress mechanical behaviors [184, 196] while elastin is primarily responsible for the low-stress mechanical behavior and tissue elasticity at high tensile loading [184, 197, 198].

To work this out, Zhang *et al.* [184] developed a meso-scale constitutive model of the MV leaflets and found that the high-tension modulus best represented the collagen contributions to the mechanical response of the tissue, while the low-tension modulus could better describe the elastin contributions. In another study, Vesely [34] analyzed the role of elastin in the mechanical response of the semilunar valve leaflets and observed that the elastin played an important role in facilitating proper crimping and uncrimping of the collagen fibers that are exposed to cyclic loading. Although Vesely analyzed the semilunar valves, we showed in our study that the roles of collagen and elastin for the AHVs can be similar. Their results can help explain why the high-tension modulus for the elastin-removal tests had some significant changes – by removing elastin in the MVAL and TVAL specimens can disrupt the collagen/elastin interactions, which could inhibit collagen fiber crimping and uncrimping actions.

### Material Anisotropy in Enzymatically Treated AHV Leaflet Tissues

In addition to the holistic approach by comparing the tissue mechanics between control and enzymatically treated leaflets, we also tried to understand how the experimental procedure

affected the direction-dependent tissue responses. When analyzing the anisotropy index parameter ($AI$) we observed that the tissues became for both the MVAL and TVAL specimens became more isotropic after elastin removal, while only the TVAL after after the collagen removal became more isotropic. The more isotropic nature of the elastin-removed, collagen-organized tissues may be a counter-intuitive observation. The *mechanical* anisotropy of soft tissues is a complex, multi-factorial phenomenon. Possible factors for the more isotropic behavior are: (i) a non-uniform initial dispersion of the collagen fiber network, which leads to a more isotropic behavior [199]; (ii) breaking the intrinsic connections between the elastin and collagen structures that can contribute to tissue anisotropy [34]; (iii) the removal of elastin, which creates voids in the extracellular matrix that can interfere with the normal uncrimping and reorientation effects of collagen fibers; and (iv) the intertwining of the fibers [200]. The changes in the direction-dependent tissue mechanics after enzyme treatment were also demonstrated in the extensibility index $\lambda^*$. For the elastin-removed tissues, we observed significant changes in $\lambda^*$ for the radial direction of the MVAL and TVAL specimens (**Fig. 3-6(c)**). This suggests that the reorientation and realignment of radially oriented elastin fibers can have a greater influence on the mechanical responses of the tissue than the circumferentially oriented elastin fibers. The change in $\lambda^*$ in the circumferential direction of the TVAL was significant for the collagen removal (**Fig. 3-8(c)**). This means that the collagen fibers in the TVAL specimens have a preferred orientation to the circumferential direction, which is disrupted by the enzyme treatment. This information is valuable in understanding the changes associated with valvular diseases as myxomatous or rheumatic valves that can cause collagen production or turnover problems that affect the overall direction-dependent tensile and/or viscoelastic behavior [201, 202].

### Stress Relaxation for Elastin- and Collagen-Deficient AHV Leaflets

From the stress relaxation testing of the collagen- and elastin-removed leaflets, we observed that the enzyme treatment had pronounced effects on the viscoelastic properties (**Figs. 3-9** and **3-10**). In all scenarios the percentage reduction of the total stress decay was increased significantly. This was similar to the finding of an earlier study in which collagenase degradation of AV and PV cusps was carried out, in which an increase in collagenase concentration led to an increased total relaxation of the tissue [203]. This finding provides a useful experimental insight into the time-dependent behavior of the tissues and how they are influenced by changes in the ECM components, which have not previously been observed for the AHV leaflets.

We were also able to derive model parameters for the elastin- and collagen-removed leaflets. Elastin-removed leaflets showed a greater initial stress decay, lower asymptotic stress decay behavior, and an increase in the overall stress decay rate after enzyme treatment (as can be seen in $E_0$, $E_1$, and $\tau$). At the same time, the tissues treated with elastase showed a more elastic behavior in contrast to the more viscous behavior of the untreated tissues (as demonstrated by the increased $\alpha$ values). Meanwhile, collagen-removed tissues showed very similar behavior. These results provide information on how microstructural changes, e.g., in degenerative heart valve disease, can affect the homeostatic stress state of the tissue. For example, during systolic valve closing, stress relaxation occurs in the leaflets, which are exposed to high pressure over a long period of time. Our results indicate that the tissues with altered elastin or collagen content can experience a significantly greater stress decay during high-pressure coaptation, which theoretically leads to disease-related remodeling [204]. The quantified difference in viscoelastic behavior can be helpful for therapeutic design in order to optimally restore the homeostatic tissue stress. Our results serve to develop and refine the microstructurally informed constitutive models in the literature with future applications for understanding tissue growth, development, and remodeling [52, 60].

### Comparison: Collagen-, Elastin-, and GAG-Deficient AHV Leaflets

To create a more complete picture of the biomechanical contributions of each constituent to the leaflet biaxial tensile properties, we compared the results of this study with our previous GAG removal study [23]. A comparison of the percentage change in tissue stretch before and after enzymatic degradation shows that elastin-deficient tissues showed the greatest change after degradation for all three biaxial tension protocols—a $15.2\%$ difference compared to the $7.0\%$ and $3.3\%$ differences for collagen- and GAG-deficient tissues, respectively (**Fig. 3-11**). In addition, elastin removal showed a decrease in tissue extensibility, GAG deficiency showed increased tissue extensibility, and collagen removal showed inconsistent changes in tissue stretch after treatment. Our experimental results show the unique contributions of the microstructural constituents to the overall tensile behavior of the tissue. Although we could not directly quantify the intricate mechanical coupling relationships between the microstructure components, our results suggested that the collagen fibers, GAGs, and the non-fibrous ECM provide the stiffness to counteract the extensibility of the elastin. Future studies would include the quantification of the coupled behavior of the ECM constituents, e.g., how the hydrophilic GAGs act as a lubricating mediator between the collagen and elastin components and enable a microstructural reorganization under loading.

Comparing the stress relaxation response of the tissues before and after enzymatic removal, both the collagen- and elastin-deficient tissues showed an increased total stress decay behavior, while the GAG-deficient leaflets demonstrated a decreased total stress decay behavior. In addition, in all three scenarios the removal of the ECM component resulted in statistically significant changes to the viscoelastic properties. Furthermore, the collagen- and elastin-deficiencies had a larger impact on the viscoelastic properties of the AHV leaflets compared to the GAG deficiency. Visual comparisons of the changes in the PPC stretch, the stretch, and the stress relaxation are shown in **Figs. 3-11** and **3-12**.

The enzymatic treatment of the MVALs and TVALs produced different changes in the observed mechanical behavior. These discrepancies can be attributed to the differences in the underlying morphology and microstructure between the two atrioventricular heart valves. While no studies have been done to directly compare the morphology of the two AHVs, previous researchers have compared the aortic and pulmonary valves (i.e., the two semilunar valves). From these studies it was found that the collagen-rich fibrosa makes up a greater proportion of the tissue thickness in the aortic cusps than in the pulmonary cusps ($\sim$20% larger) [205]. These differences in the layered structure and the corresponding microstructural constituents can also be reflected in the AHV leaflets: the MVAL, which contains a larger collagen composition than the TVAL, cannot be easily destroyed by enzymatic treatment. This postulation could explain the greater differences in tissue stretch after collagen removal in the TVAL than in the MVAL as we have observed in the present work. Regarding the variations in leaflet mechanics after elastin removal, there are no studies to date that quantify the elastin content between the two AHVs or the two semilunar valves, which limits a microstructure-informed theory of the differences observed in our study. From the studies by Scott and Vesely (1996) on the elastin morphology of the aortic cusps, it is clear that the elastin and collagen components are closely connected and that elastin can take different forms (amorphous sheets and fibers of varying densities) [206]. Perhaps the larger stretches of the MVAL after elastase treatment could be explained by potential differences in elastin morphology between the two AHVs; however, this must be systematically investigated in a future study.

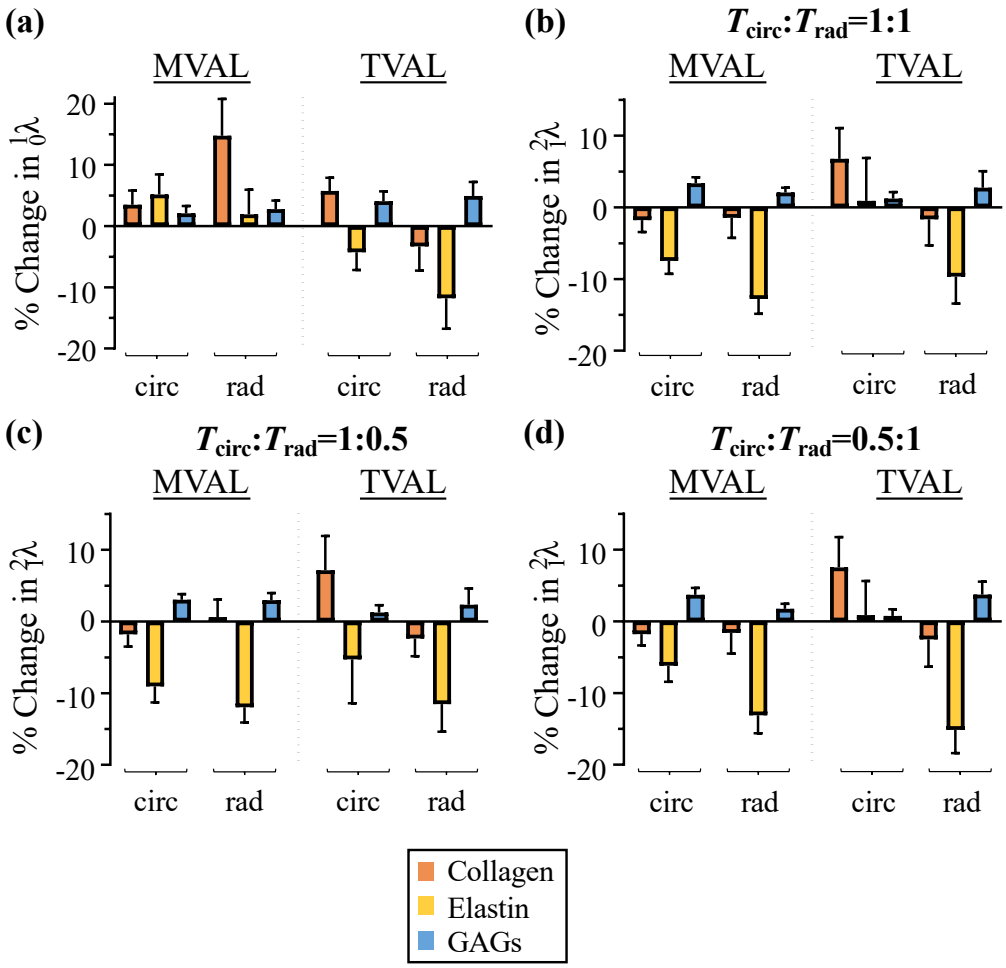


**Figure 3-11** Comparisons of the percent change between tissues subjected to collagen-, elastin-, and GAG-removal with: (a) the preconditioning stretch $^{1}_{0}\lambda$, and the stretch $^{2}_{1}\lambda$ at the three biaxial tension protocols: (b) $T_{\text{circ}}$:$T_{\text{rad}} = 1{:}1$, (c) $T_{\text{circ}}$:$T_{\text{rad}} = 1{:}0.5$, and (d) $T_{\text{circ}}$:$T_{\text{rad}} = 0.5{:}1$ for the MVAL and the TVAL specimens. GAG-removal results are from our previous study [23], with sample sizes (MVAL, $n = 7$; TVAL, $n = 6$).

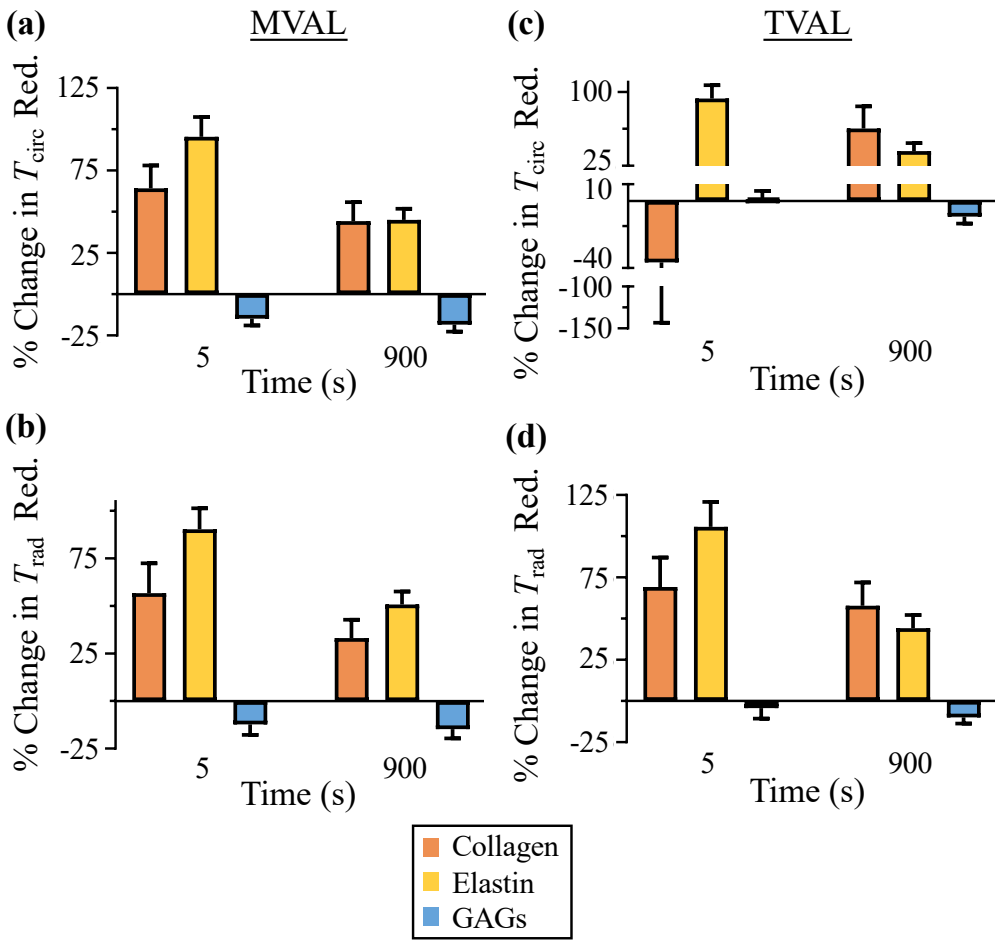


**Figure 3-12** Comparison of the percent change between tissues subjected to collagen-, elastin-, and GAG-removal in the stress relaxation behaviors of (a), (b) MVAL, and (c), (d) TVAL specimens. GAG-removal results are from our previous study [23], with sample sizes (MVAL, $n = 7$; TVAL, $n = 6$).

### Preliminary Analysis: Changes in Collagen Fiber Architecture Due to Enzyme Treatment

In addition to understanding the effects of enzyme-based degradation on the biaxial tensile and viscoelastic properties, it is also of interest to quantify the changes in the load-dependent re-orientation of the collagen fibers. For this purpose, we carried out a preliminary analysis of these microstructural changes with an in-house set of instruments for polarized spatial frequency domain imaging (pSFDI). The entire imaging process is very beneficial as no tissue fixatives are required, which means that the collagen fiber architecture can be quantified under various loading conditions. This pSFDI collagen microstructure imaging technique uses the polarization-dependent light intensity response of the collagen fibers to predict the orientations on a pixel-by-pixel basis. For details on the imaging technology and the data analysis method see [54, 207].

We applied this collagen imaging modality to five ($n = 5$) MVAL and TVAL specimens for both the collagen- and elastin-removed tissues and evaluated the changes in the re-orientation of the collagen fibers in the central region of the specimen, as delimited by the fiducial markers in order to avoid any extreme boundary distortions due to the tine insertions or the applied load. Here we have analyzed the change in the median fiber angle between the equibiaxial (reference) and non-equibiaxial loading states in order to gain an insight into the changes in the fiber rotations after the enzyme treatment. In addition, we analyzed the changes in the interquartile range (IQR) to develop an understanding of the changes in the fiber splay (i.e., the alignment of the fiber groups around the median fiber angle). The changes for the individual specimens are given in **Tables 3-3** and **3-4** as the median fiber angles and the corresponding IQR, respectively.

In the TVAL samples without elastin, we observed a reduced re-orientation of the collagen fibers and a reduced IQR compared to the control specimens. In contrast, the elastin-removal MVAL specimens showed mainly increased re-orientations and decreased changes in the IQR. The reduced changes in the IQR for MVAL and TVAL may indicate that the collagen fibers rotate in larger, collective fiber groups in the absence of elastin, while the network in the control specimens has more freedom of rotation. This assumption can be further confirmed by our observation of the increased tissue stiffness after elastin removal in the TVAL specimens. The differences in the fiber reorientation behavior for each leaflet after

elastin removal also indicate a leaflet-specific variance in the kinematics of the collagen fibers.

On the other hand, for the collagen-removed specimens, the TVAL showed an increased fiber reorientation, while the MVAL specimens showed a reduced fiber reorientation, which provided further evidence of significant differences in the ECM of each leaflet. For the IQR, both the MVAL and TVAL specimens showed mainly increased changes, suggesting that collagen deficiency leads to less grouped fiber network rotations in both leaflets.

### 3.4.2 Study Limitations and Future Extensions

There are several limitations in the present study. First, there is a possibility that the enzymes used in this study could damage the non-targeted ECM components (e.g., degrading elastin due to collagenase). After a quantitative examination of the stained tissue strips from the interim study, however, we observed, on average, minimal changes in the non-targeted ECM components after the enzyme treatment ($< 25\%$), also due to regionally different ECM densities. Second, while porcine hearts are very similar to human hearts in size, structure, and function hearts [208], the results of this study may not be immediately applicable to human applications. Third, due to staining quality difficulties from a commercial supplied, it was not possible to perform a histological analysis on every sample. Although we controlled many of the factors that would affect the histological results of our study (e.g., lighting, section thickness, staining, etc.). Because of the inherent nature of the experimental technique the potential for small variations in quality between the tissues still exists.

We also recognize the potential damage to constituents caused by freezer storage. However, we only observed constituent degradation and made comparisons between control (untreated) and enzyme-treated tissues, while no intermediate freezer storage was used during any of our mechanical experiments and enzyme treatments. Finally, other possible limitations include the use of two different effective testing regions, the use of a contact-based thickness measurement tool, a limited number of loading ratios, and a relatively short stress relaxation protocol. For more details on these limitations and how we have addressed them, see our previous works [22, 23, 32].

Future extensions may include testing the same specimen at multiple time points (e.g., 30, 60, 90, and 120 min) of constituent degradation. This study would provide even more insight into how the mechanical response of the tissue changes as increasing amounts of the target

**Table 3-3** Quantified median fiber angle and half of the interquartile range (IQR) for control (–C) and elastin-removed (–T) MVAL and TVAL specimens ($n = 5$), as obtained from polarized spatial frequency domain imaging. Half of the IQR is reported for easier interpretation of the results. Note that the $0^\circ$ reference angle corresponds to the tissue's circumferential (circ) direction.

| | | MVAL | | | | | |
|---|---|---|---|---|---|---|---|
| ID | Condition | $T_{\text{circ}}$:$T_{\text{rad}} = 1$:1 | | $T_{\text{circ}}$:$T_{\text{rad}} = 1$:0.5 | | $T_{\text{circ}}$:$T_{\text{rad}} = 0.5$:1 | |
| | | Median | 0.5*IQR | Median | 0.5*IQR | Median | 0.5*IQR |
| 1 | –C | 72.0° | 4.7° | 72.1° | 4.5° | 72.5° | 5.7° |
| | –T | 72.0° | 3.7° | 72.7° | 3.6° | 68.8° | 5.4° |
| 2 | –C | 90.4° | 6.6° | 89.4° | 6.3° | 89.6° | 6.8° |
| | –T | 91.3° | 3.0° | 88.8° | 3.3° | 90.2° | 3.5° |
| 3 | –C | 33.6° | 34.4° | 24.6° | 16.2° | 23.2° | 9.5° |
| | –T | 18.5° | 36.7° | 81.9° | 36.3° | 15.0° | 35.9° |
| 4 | –C | 46.1° | 6.2° | 49.1° | 5.9° | 34.7° | 11.4° |
| | –T | 96.9° | 6.3° | 94.4° | 6.3° | 98.6° | 8.3° |
| 5 | –C | 30.6° | 11.2° | 37.0° | 10.8° | 23.26° | 16.2° |
| | –T | 173.9° | 17.6° | 168.4° | 23.3° | 174.1° | 12.7° |
| | | TVAL | | | | | |
| ID | Condition | $T_{\text{circ}}$:$T_{\text{rad}} = 1$:1 | | $T_{\text{circ}}$:$T_{\text{rad}} = 1$:0.5 | | $T_{\text{circ}}$:$T_{\text{rad}} = 0.5$:1 | |
| | | Median | 0.5*IQR | Median | 0.5*IQR | Median | 0.5*IQR |
| 1 | –C | 47.1° | 9.6° | 51.3° | 8.4° | 40.3° | 10.8° |
| | –T | 75.0° | 13.8° | 80.1° | 9.1° | 57.3° | 14.6° |
| 2 | –C | 83.0° | 10.6 ° | 98.9° | 10.6° | 10.8° | 77.9° |
| | –T | 172.6° | 19.8° | 175.8° | 9.0° | 171.0° | 16.7° |
| 3 | –C | 96.6° | 40.7° | 107.6° | 4.4° | 30.2° | 10.5° |
| | –T | 121.8° | 4.0° | 117.6° | 4.8° | 122.8° | 4.7° |
| 4 | –C | 46.9° | 10.5° | 57.0° | 5.1° | 29.2° | 4.2° |
| | –T | 72.9° | 3.3° | 75.4° | 2.9° | 61.9° | 4.7° |
| 5 | –C | 53.2° | 8.0° | 55.1° | 7.7° | 48.4° | 8.9° |
| | –T | 19.7° | 15.7° | 20.0° | 18.1° | 14.9° | 12.4° |

**Table 3-4** Quantified median fiber angle and half of the interquartile range (IQR) for control (–C) and elastin- and collagen-removed (–T) MVAL and TVAL specimens ($n = 5$), as obtained from polarized spatial frequency domain imaging. Half of the IQR is reported for easier interpretation of the results. Note that the $0^\circ$ reference angle corresponds to the tissue's circumferential (circ) direction.

| | | MVAL | | | | | |
|---|---|---|---|---|---|---|---|
| ID | Condition | $T_{\text{circ}}$:$T_{\text{rad}} = 1$:1 | | $T_{\text{circ}}$:$T_{\text{rad}} = 1$:0.5 | | $T_{\text{circ}}$:$T_{\text{rad}} = 0.5$:1 | |
| | | Median | 0.5*IQR | Median | 0.5*IQR | Median | 0.5*IQR |
| 1 | -C | 17.5° | 13.4° | 145.2° | 36.7° | 20.9° | 16.1° |
| | -T | 59.3° | 3.4° | 59.7° | 2.8° | 55.9° | 23.7° |
| 2 | -C | 14.6° | 5.6° | 20.6° | 5.6° | 10.2° | 4.3° |
| | -T | 73.8° | 3.2° | 74.4° | 3.5° | 73.3° | 3.2° |
| 3 | -C | 80.6° | 2.9° | 90.4° | 2.4° | 79.7° | 4.5° |
| | -T | 82.5° | 2.6° | 82.1° | 2.6° | 81.6° | 2.8° |
| 4 | -C | 6.1° | 4.2° | 178.9° | 7.7° | 7.8° | 3.2° |
| | -T | 178.9° | 7.5° | 177.7° | 8.5° | 0.1° | 7.8° |
| 5 | -C | 104.8° | 7.10° | 99.0° | 6.1° | 168.7° | 77.4° |
| | -T | 119.2° | 6.4° | 110.7° | 3.6° | 117.2° | 3.9° |

| | | TVAL | | | | | |
|---|---|---|---|---|---|---|---|
| ID | Condition | $T_{\text{circ}}$:$T_{\text{rad}} = 1$:1 | | $T_{\text{circ}}$:$T_{\text{rad}} = 1$:0.5 | | $T_{\text{circ}}$:$T_{\text{rad}} = 0.5$:1 | |
| | | Median | 0.5*IQR | Median | 0.5*IQR | Median | 0.5*IQR |
| 1 | -C | 84.5° | 31.4° | 90.7° | 5.7° | 73.1° | 25.0° |
| | -T | 47.2° | 6.0° | 53.6° | 7.0° | 36.4° | 4.9° |
| 2 | -C | 88.8° | 42.2° | 93.4° | 18.2° | 43.5° | 42.6° |
| | -T | 83.8° | 34.7° | 92.4° | 32.7° | 29.8° | 17.0° |
| 3 | -C | 63.6° | 29.0° | 71.5° | 15.6° | 11.3° | 19.7° |
| | -T | 31.7° | 28.5° | 58.0° | 26.1° | 18.9° | 6.9° |
| 4 | -C | 13.4° | 3.0° | 13.1° | 2.8° | 12.7° | 4.0° |
| | -T | 5.4° | 6.7° | 8.1° | 5.4° | 1.2° | 6.8° |
| 5 | -C | 67.5° | 34.8° | 86.1° | 15.9° | 21.9° | 8.9° |
| | -T | 26.3° | 57.3° | 79.8° | 39.7° | 10.6° | 54.8° |

constituent are removed, mimicking the effects of progressive disease states, that alter the ECM of the tissue. In addition, we carried out a tension-based stress-relaxation test setup in the present study, in which each specimen was subjected to a certain strain during the viscoelastic characterization in order to identify differences due to the removal of the constituents. In future work it may be advantageous to carry out the stress-relaxation test with a strain-based setup that targets the *in vivo* MVAL/TVAL strains [16, 46]. While no stress relaxation-specific preconditioning was typically carried out in previous studies [25, 35], future work could be done to investigate the repeatability of the stress relaxation behavior with multiple repetitions for the AHV leaflets.

## 3.5 Chapter Summary

In this study, we provided experimental insight into the contributions of collagen and elastin to the mechanical properties of MVAL and TVAL before and after the enzymatic removal of each constituent. The findings from the present study can be used to inform the development of tissue-engineered heart valves that mimic the native tissue microstructure. Studies on tissue-engineered heart valves can use the presented microstructure-mechanics relationships to guide the development of scaffolds with appropriate constituents to achieve the desired properties. In addition, the mechanical properties of the resulting tissue-engineered construct could be compared to the properties of native tissues as well as the collagen-, elastin-, or GAG-deficient tissues in order to fine-tune the development process of tissue-engineered heart valves [209]. These findings can also be used to develop microstructure-informed computational models of AHVs that can be used to better understand heart valve biomechanics, as well as tissue growth and remodeling. These computational modeling works can also be useful in refining current surgical repair techniques such as annuloplasty rings or valvuloplasty, which could avoid adverse tissue overstresses and remodeling that ultimately lead to recurrent regurgitation. Ultimately, these results provide an understanding of the effects of elastin and collagen deficiencies on the mechanical properties of the AHV leaflets. The improved understanding is useful to relate the changes in valve closing behavior to certain heart valve diseases. For example, the myxomatous heart valve exhibits gradual disruption and fragmentation of elastin and collagen fibers [210], and our results and experiments can be used to elucidate the changes in the leaflet mechanics as the disease progresses.

# 4 EVALUATION OF AFFINE FIBER KINEMATICS IN PORCINE TRICUSPID VALVE LEAFLETS USING POLARIZED SPATIAL FREQUENCY DOMAIN IMAGING AND PLANAR BIAXIAL TESTING


4.1 Motivation . . . 73
4.2 Methods . . . 73
4.2.1 Tissue Acquisition and Preparation . . . 73
4.2.2 Biaxial Mechanical Testing . . . 74
4.2.3 Quantification of the Load-Dependent Changes in Collagen Fiber Architecture . . . 75
4.2.4 Application of the Affine Fiber Kinematics Theory . . . 76
4.2.5 Statistical Analysis . . . 77
4.3 Results . . . 77
4.3.1 Biaxial Mechanical Properties of the Tricuspid Valve Leaflets . . . 77
4.3.2 Experimentally Measured Collagen Fiber Architectures . . . 79
4.3.3 Evaluation of the AFK Predictivity . . . 79
4.4 Discussion . . . 86
4.4.1 Differences in Experimental and Predicted Collagen Fiber Reorientations . . . 86
4.4.2 Considerations for Constitutive Modeling Using Affine Fiber Kinematics . . . 90
4.4.3 Limitations and Future Extensions . . . 91
4.5 Chapter Summary . . . 91

## 4.1 Motivation

In this work, we provide a *first-of-its-kind* evaluation of the AFK assumption for the tricuspid valve leaflets using an integrated biaxial testing-polarized spatial frequency domain imaging (pSFDI) device. The non-destructive collagen fiber imaging technique enabled quantification of the load-dependent changes in the CFA of the TV leaflets, which were then compared to the predictions of the AFK theory to evaluate the viability in capturing the collagen fiber reorientations. Unlike previous studies using small-angle light scattering [211, 212], our approach is beneficial as the pSFDI modality does not require tissue fixation, allowing for the observation of collagen fiber reorientations and fiber kinematics within the same tissue specimen. Additionally, the biaxial testing scheme was rarely performed in the previous AFK-based experiments for the mitral valve leaflets and the other tissues [21, 50], and thus, our findings could be helpful for understanding differences in collagen fiber kinematics under different experimental testing conditions. The results of this work will be useful for a refined understanding of AFK in the TV leaflets and for future refinement of accurate microstructure-informed constitutive models and TV simulations.

## 4.2 Methods

The tissue acquisition and biaxial testing methodology used in this study is similar to the methods presented in **Section 3.2.1**. For the sake of brevity, the reader is referred to that previous writing, and the key differences in the present study are highlighted herein.

### 4.2.1 Tissue Acquisition and Preparation

The tissues were acquired as per the previous chapter, with the key differences being in the tissue preparation. After dissecting the leaflets from the porcine hearts (**Fig. 4-1(a)**), the specimens were further sectioned to obtain a $10 \times 10$ mm specimen from the central, belly region of the leaflet (**Fig. 4-1(b)**). The square specimens were then mounted to a commercial biaxial testing device (CellScale, Canada) via tined BioRakes (**Fig. 4-1(c)**), with the tissue's circumferential (circ) and radial (rad) directions aligned with the $X$- and $Y$-directions of the BioTester, respectively. The biaxial testing device was further equipped with an in-house pSFDI device (**Fig. 4-1(d)**), which was used in the quantification of the CFAs of the TV leaflet specimens (see **Section 4.2.3**). Once the tissues were mounted to the biaxial testing system, glass beads were used to construct a $2 \times 2$ fiducial marker array in the center of the specimen for later tissue strain calculation based on digital image correlation [22, 23].

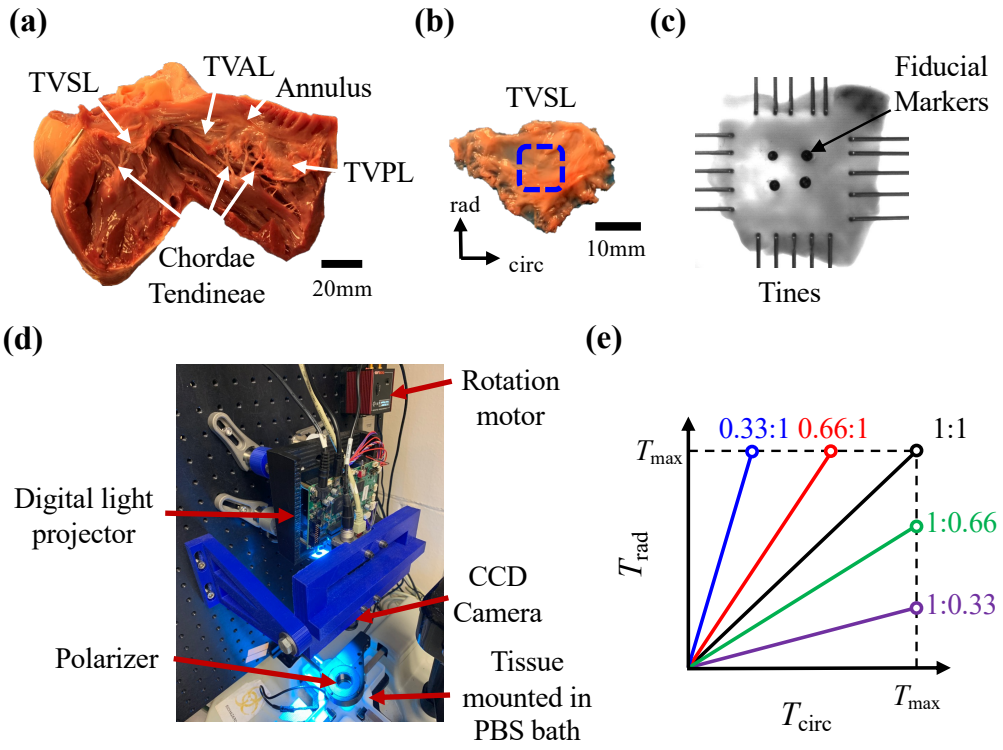


**Figure 4-1** (a) Porcine tricuspid valves dissected to obtain the (b) TV leaflets. A 10x10mm square specimen prepared from the central, belly region of the leaflet and (c) mounted via tined BioRakes to (d) a coupled pSFDI-biaxial testing device. (e) Schematic of the membrane tension ($T$) loading ratios in the biaxial mechanical testing.

Tissues were then submerged in a 32 °C phosphate-buffered saline bath to emulate the physiological temperature. A temperature level slightly lower than body temperature (37 °C) was used to avoid previously observed issues related to polarizer fogging in the pSFDI portion of the experiment [54, 207].

### 4.2.2 Biaxial Mechanical Testing

Biaxial mechanical testing was performed following our established protocols [22, 27]. First, tissues were preconditioned through ten equibiaxial loading/unloading cycles to a targeted membrane tension of 50 N/m to emulate the physiologic loading of the valve leaflets [19]. After preconditioning, tissue specimens were then biaxially loaded with varying ratios of biaxial tensions: $T_{circ}$:$T_{rad}$ = 1:1, 0.66:1, 0.33:1, 1:0.66, and 1:0.33 (**Fig. 4-1(e)**). Each loading ratio was repeated for 4 loading/unloading cycles to ensure repeatability of the stress-strain behaviors, and the final loading cycle was used for tissue stress-stretch

analysis. Throughout testing, the load cell readings were recorded and images were captured by a CCD camera at 5 Hz. After biaxial testing was completed, the pSFDI component of the integrated instrument was used to quantify the load-dependent CFAs of the TV leaflet specimens [54, 207].

### 4.2.3 Quantification of the Load-Dependent Changes in Collagen Fiber Architecture

To quantify the changes in the load-dependent CFA, an in-house pSFDI device was used (**Fig. 4-1(d)**). This device has been used in previous works from our laboratory, and the reader is referred to the pSFDI theory and details about the experimental procedure [54, 207]. Briefly, the imaging modality relies on the polarization-dependent diattenuating properties of collagen fibers to quantify the collagen fiber orientations. The imaging sequence contains:

- A digital light projector casting incident light through a polarizer and onto the specimen at an angle $\theta_{\text{polarizer}}$.
- The polarized light reflected off of the specimen with an intensity $I$.
- The reflected light passing back through the polarizer at the angle $\theta_{\text{polarizer}}$ and an image captured by a CCD camera.

The sequence is repeated for $\theta_{\text{polarizer}} = 0^\circ - 180^\circ$ at $5^\circ$ increments. Then, the light intensity-$\theta_{\text{polarizer}}$ response of the tissue was fit with a three-term Fourier series,

$$I = \gamma_0 + \gamma_2 \cos[2(\theta_{\text{fiber}} - \theta_{\text{polarizer}})] + \gamma_4 \cos[4(\theta_{\text{fiber}} - \theta_{\text{polarizer}})], \tag{4.2-1}$$

where $\gamma_0$ represents the mean light intensity, and $\gamma_2$ and $\gamma_4$ are the coefficients representing the optical anisotropy. The experimentally measured fiber angle $\theta_{\text{fiber}}$ was determined as the $\theta_{\text{polarizer}}$ corresponding to the peak reflected light intensity $I$. Furthermore, the determined Fourier coefficients were then used to quantify the degree of optical anisotropy (DOA):

$$\text{DOA} = \frac{\gamma_2 + \gamma_4}{\gamma_0 + \gamma_2 + \gamma_4}. \tag{4.2-2}$$

The DOA is an optically based metric that describes the level of preferential fiber alignment along $\theta_{\text{fiber}}$. Note that $\theta_{\text{fiber}}$ and the DOA were calculated on a pixel-by-pixel basis, offering a

detailed representation of the spatially varying CFA of the TV leaflets. The pSFDI sequence was repeated at the post-preconditioning (PPC) configuration and at the deformation associated with the peak loading of each biaxial tension protocol to obtain the fiber orientations at the unloaded ($\theta_{\text{PPC}}$) and loaded configurations ($\theta_{\text{exp}}$), respectively. The reorientations of the collagen fibers were quantified via $\theta_{\text{reorient}} = \theta_{\text{exp}} - \theta_{\text{PPC}}$, where a positive $\theta_{\text{reorient}}$ indicates a counterclockwise rotation, and a negative $\theta_{\text{reorient}}$ indicates a clockwise rotation.

### 4.2.4 Application of the Affine Fiber Kinematics Theory

Evaluation of the validity of the AFK theory requires the use of two components of our experimental measurements: (i) the unloaded fiber orientation $\theta_{\text{PPC}}$ and (ii) the deformation gradient **F**. During post-processing of the acquired pSFDI information, we selected the region of interest for the AFK analysis to be within the $2 \times 2$ fiducial marker array, as the fiber kinematics would be more realistic than in the fibers near the tine insertion. The selected region of interest was further discretized into an isoparametric $100 \times 100$ grid of query points based on the isoparametric mapping concept in the context of finite element methods (**Fig. 4-2(a)**, [213]). For each query point, $\theta_{\text{PPC}}$ and $\theta_{\text{exp}}$ were determined by a Euclidean distance-based weighting of the 25 nearest points:

$$\theta_j = \frac{\sum_{k=1}^{25} w_k \theta_k}{\sum_{k=1}^{25} w_k}, \tag{4.2-3}$$

where $\theta_j$ represents the fiber angle of the $j^{\text{th}}$ query point, $\theta_k$ denotes the fiber angle at the $k^{\text{th}}$ pixel within the domain of influence associated with the $j^{\text{th}}$ query point, and $w_k$ represents the weight, calculated as the Euclidean distance from the pixel location $(p, q)$ of the $j^{\text{th}}$ query point: $w_k = \sqrt{(p-p_k)^2 + (q-q_k)^2}$. Then, the unloaded fiber direction vector was constructed as $\mathbf{N}_j = [\cos(\theta_{\text{PPC},j}), \sin(\theta_{\text{PPC},j})]^T$ for the $j^{\text{th}}$ query point in the selected region of interest. Interested readers are referred to [214].

For the deformation gradient **F**, the calculations were made based on the deformation of the fiducial marker array, as tracked via a custom MATLAB program (MathWorks, MA, USA, **Fig. 4-2(b)**; [14, 67]). The pixel locations of the markers in the undeformed, reference ($\Omega_{\text{PPC}}$) configurations and the deformed configurations ($\Omega_t$) were mapped to a parametric

domain, and **F** was constructed as:

$$\mathbf{F} = \begin{bmatrix} \frac{\partial x}{\partial X} & \frac{\partial x}{\partial Y} \\ \frac{\partial y}{\partial X} & \frac{\partial y}{\partial Y} \end{bmatrix} = \begin{bmatrix} \lambda_1 & \kappa_1 \\ \kappa_2 & \lambda_2 \end{bmatrix}, \tag{4.2-4}$$

where $X$ and $Y$ represent the undeformed marker locations, $x$ and $y$ denote the deformed marker locations, $\lambda_1$ and $\lambda_2$ are the stretches in the $X$- and $Y$-directions (i.e., circ and rad, respectively), and $\kappa_j$ represents the shear deformations.

Next, the AFK theory was adopted to determine the fiber orientation at each of the applied biaxial loading states:

$$\mathbf{n}_j = \frac{\mathbf{F} \cdot \mathbf{N}_j}{|\mathbf{F} \cdot \mathbf{N}_j|}, \tag{4.2-5}$$

where $\mathbf{n}_j = [\cos(\theta_{\text{pred},j}) \sin(\theta_{\text{pred},j})]^T$ is the deformed fiber orientation associated with the $j^{\text{th}}$ query point (**Fig. 4-2(c)**). To determine the AFK prediction errors, the difference between $\theta_{\text{pred}}$ and $\theta_{\text{exp}}$ was calculated as $\theta_{\text{error}} = \theta_{\text{pred}} - \theta_{\text{exp}}$, where a negative $\theta_{\text{error}}$ corresponds to an *underprediction* of the AFK theory, and a positive $\theta_{\text{error}}$ demonstrates an *overprediction*.

### 4.2.5 Statistical Analysis

$\theta_{\text{pred}}$ and $\theta_{\text{exp}}$ from the $100 \times 100$ *query points* for each of the TV leaflet specimens are reported as the median$\pm$interquartile range (IQR). Quantities for all the specimens, including $\theta_{\text{error}}$ and $\lambda$, are reported as the mean$\pm$standard error of the mean (SEM). To gain insight into the correlation between any two metrics, a Pearson correlation coefficient ($r$) was computed ($r = 1$ indicating a positive linear correlation between the two compared metrics, $r = -1$ signifying a negative linear correlation, and $r = 0$ representing no linear correlation).

## 4.3 Results

### 4.3.1 Biaxial Mechanical Properties of the Tricuspid Valve Leaflets

From the biaxial testing of the three TV leaflets, we observed the typical nonlinear, anisotropic nature of the soft tissues [19, 20, 22, 53]. Experimental images and stress-stretch curves for representative TVAL, TVPL, and TVSL specimens are shown in **Fig. 4-3**, **4-4**, **4-5(a)-(b)**. The average PPC and peak stretches for the five loading scenarios are

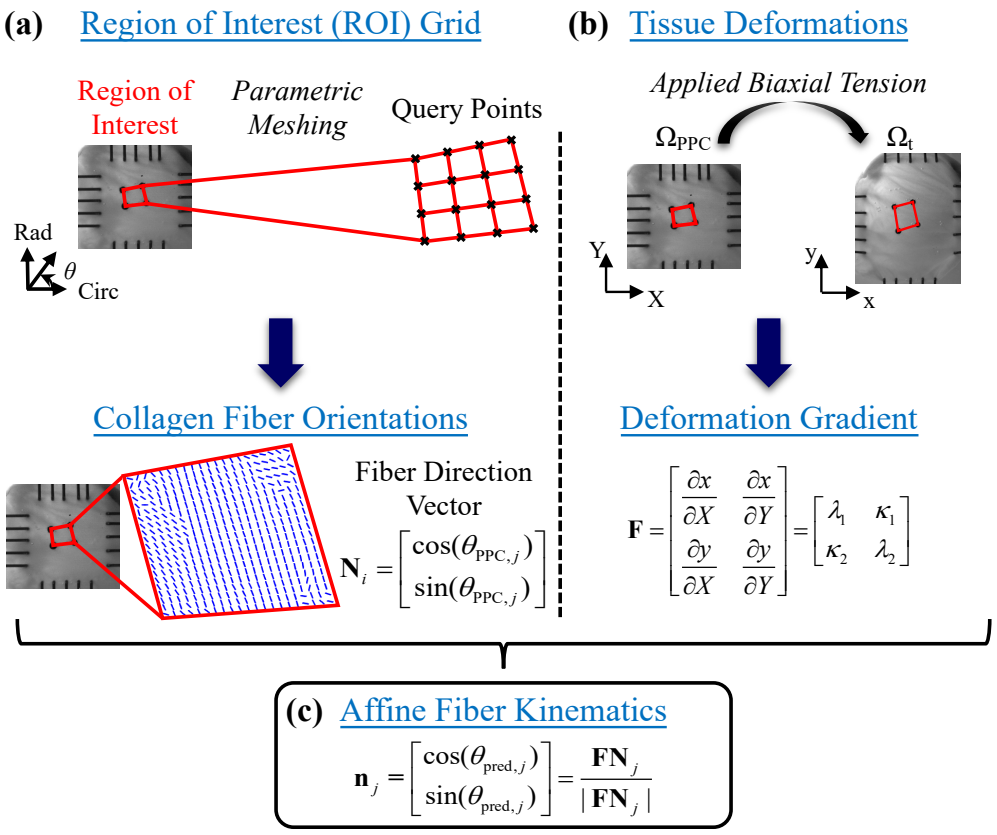


**Figure 4-2** A schematic diagram of the methods used to acquire (a) the pSFDI-measured collagen fiber angles and (b) the experimentally measured deformation gradient **F** from biaxial testing that were used to (c) predict the collagen fiber orientations from affine fiber kinematics theory.

shown in **Table 4-1**. The quantified mechanics for the individual specimens can be found in the original published article [215]. For all the tested specimens, the PPC stretches were: TVAL, $\lambda_{\text{PPC,circ}} = 1.17 \pm 0.03$, $\lambda_{\text{PPC,rad}} = 1.31 \pm 0.05$; TVPL, $\lambda_{\text{PPC,circ}} = 1.17 \pm 0.03$, $\lambda_{\text{PPC,rad}} = 1.36 \pm 0.04$, and TVSL, $\lambda_{\text{PPC,circ}} = 1.17 \pm 0.03$, $\lambda_{\text{PPC,rad}} = 1.32 \pm 0.04$. Under equibiaxial tensions, the tissue stretches were found as: *circumferential*: $1.31 \pm 0.04$ (TVAL), $1.38 \pm 0.07$ (TVPL), $1.49 \pm 0.07$ (TVSL); *radial*: $1.48 \pm 0.06$ (TVAL), $1.62 \pm 0.07$ (TVPL), $1.72 \pm 0.08$ (TVSL). We also observed the TVPL to be the most anisotropic among the three TV leaflets, which was quantified by the anisotropic index=$\lambda_{\text{rad}}/\lambda_{\text{circ}}$: TVAL, $1.13 \pm 0.04$; TVPL, $1.21 \pm 0.07$; and TVSL, $1.16 \pm 0.05$.

### 4.3.2 Experimentally Measured Collagen Fiber Architectures

The pSFDI-quantified CFA results for the TVAL, TVPL, and TVSL specimens as representative of the behavior of all the datasets are shown in **Figs. 4-3(c)**, **4-4(c)**, and **4-5(c)**. The measured CFA results of all three TV leaflets under the applied *equibiaxial loading* are presented in **Tables 4-2**, **4-3**, and **4-4**, while the findings from the applied *non-equibiaxial loading* protocols can be found in the original published article [215]. Generally, an increase in the fiber alignment was observed with increased loading, as exemplified by the DOA; however, there were less drastic changes in the fiber orientation. Specifically, the changes in the fiber orientations between the PPC and the applied equibiaxial loading states were found as: TVAL, $-2.3^\circ \pm 2.7^\circ$; TVPL, $4.4^\circ \pm 3.4^\circ$; and TVSL, $1.5^\circ \pm 2.8^\circ$. In the applied non-equibiaxial loading, we observed more fiber reorientations towards the dominant loading direction (e.g., more circumferential fiber orientations under $T_{\text{circ}}$:$T_{\text{rad}} = 1$:0.33), with greater reorientations occurring with more disproportionate loading in the two directions (e.g., $17.8^\circ \pm 4.0^\circ$ changes under $T_{\text{circ}}$:$T_{\text{rad}} = 0.33$:1 vs. $5.4^\circ \pm 2.3^\circ$ changes under $T_{\text{circ}}$:$T_{\text{rad}} = 0.66$:1).

### 4.3.3 Evaluation of the AFK Predictivity

The vector plots of the experimentally measured and the AFK-predicted fiber orientations for the representative TVAL, TVPL, and TVSL specimens are shown in **Figs. 4-6**, **4-7**, and **4-8**. Comparing the AFK-predicted and the experimental fiber reorientations in the TV leaflets, we observed that the AFK theory generally underpredicted the fiber rotations. Specifically, $\theta_{\text{error}}$ from the applied equibiaxial loading protocol: TVAL, $-1.6^\circ \pm 1.6^\circ$; TVPL, $-2.9^\circ \pm 2.4^\circ$; and TVSL, $-4.6^\circ \pm 1.0^\circ$. We also noted a greater disparity between the AFK theory and the pSFDI-quantified CFA under the applied non-equibiaxial loading. For

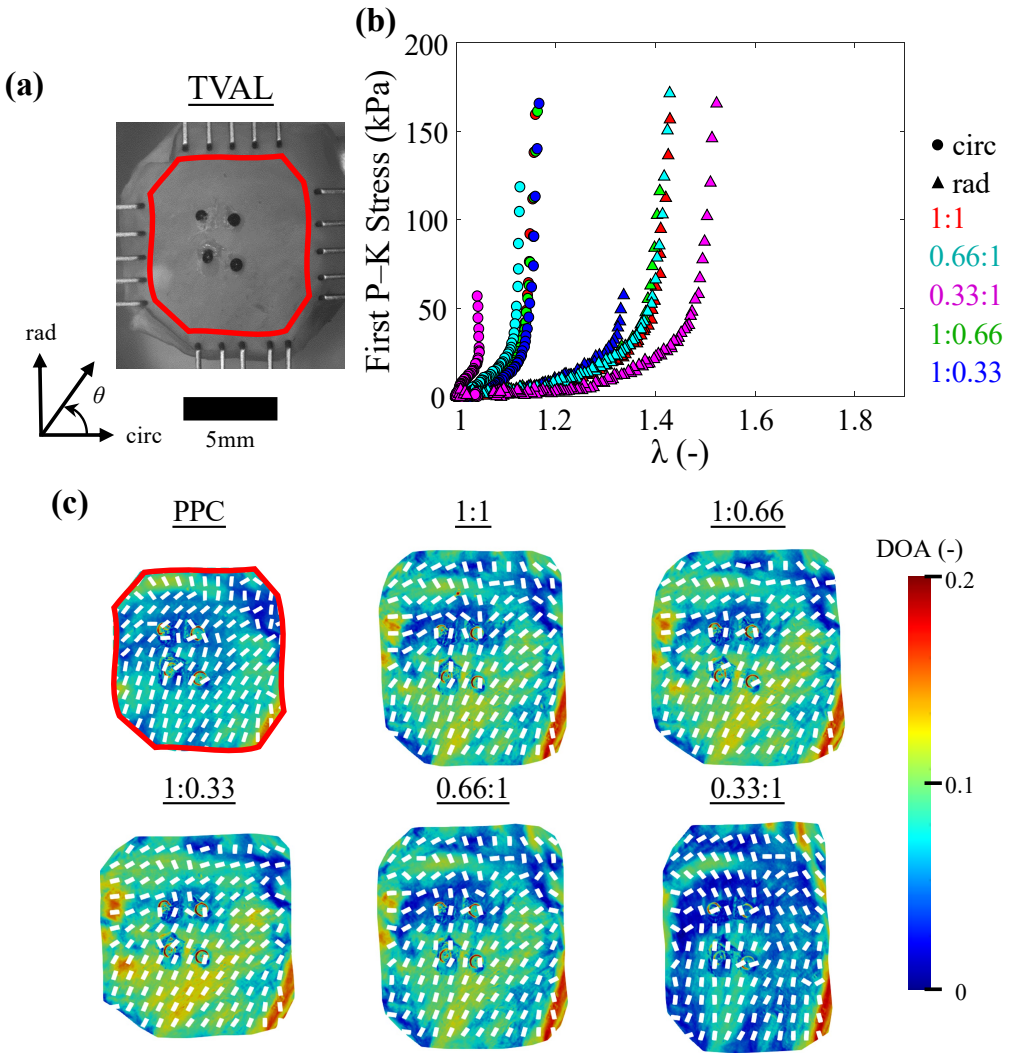


**Figure 4-3** Representative experimentally measured results from TVAL #11. (a) The experimental photo from the pSFDI camera is provided, along with (b) the biaxial mechanical testing results, and (c) the pSFDI-based collagen fiber orientations at the post-preconditioning (PPC) configuration and other applied biaxial tension protocols. Note that the region of interest shown is for the full tissue specimen, while the AFK analysis was only performed for the region delimited by the fiducial markers.

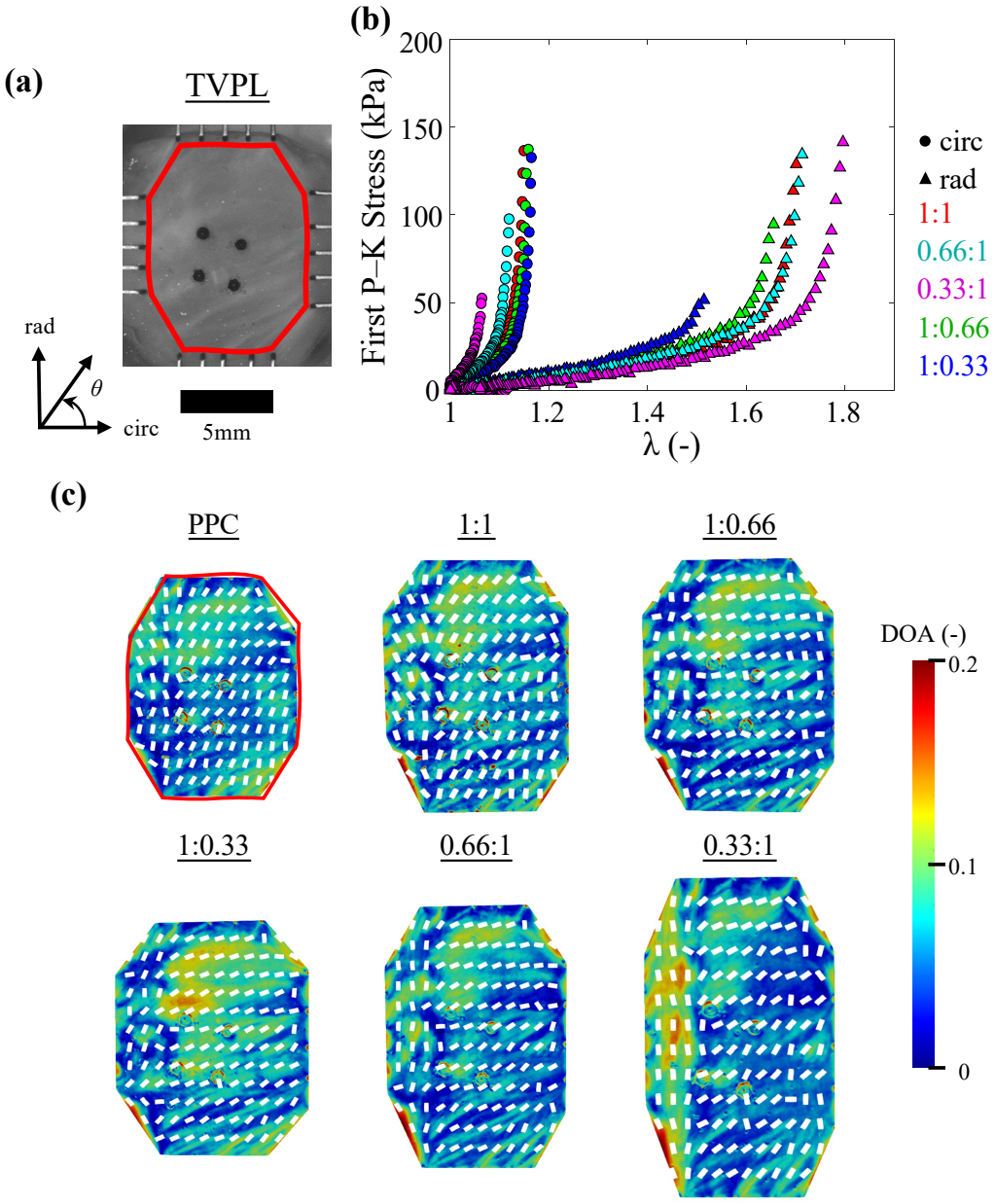


**Figure 4-4** Representative experimentally measured results from TVPL #6. (a) The experimental photo from the pSFDI camera is provided, along with (b) the biaxial mechanical testing results, and (c) the pSFDI-based collagen fiber orientations at the post-preconditioning (PPC) configuration and other applied biaxial tension protocols. Note that the region of interest shown is for the full tissue specimen, while the AFK analysis was only performed for the region delimited by the fiducial markers.

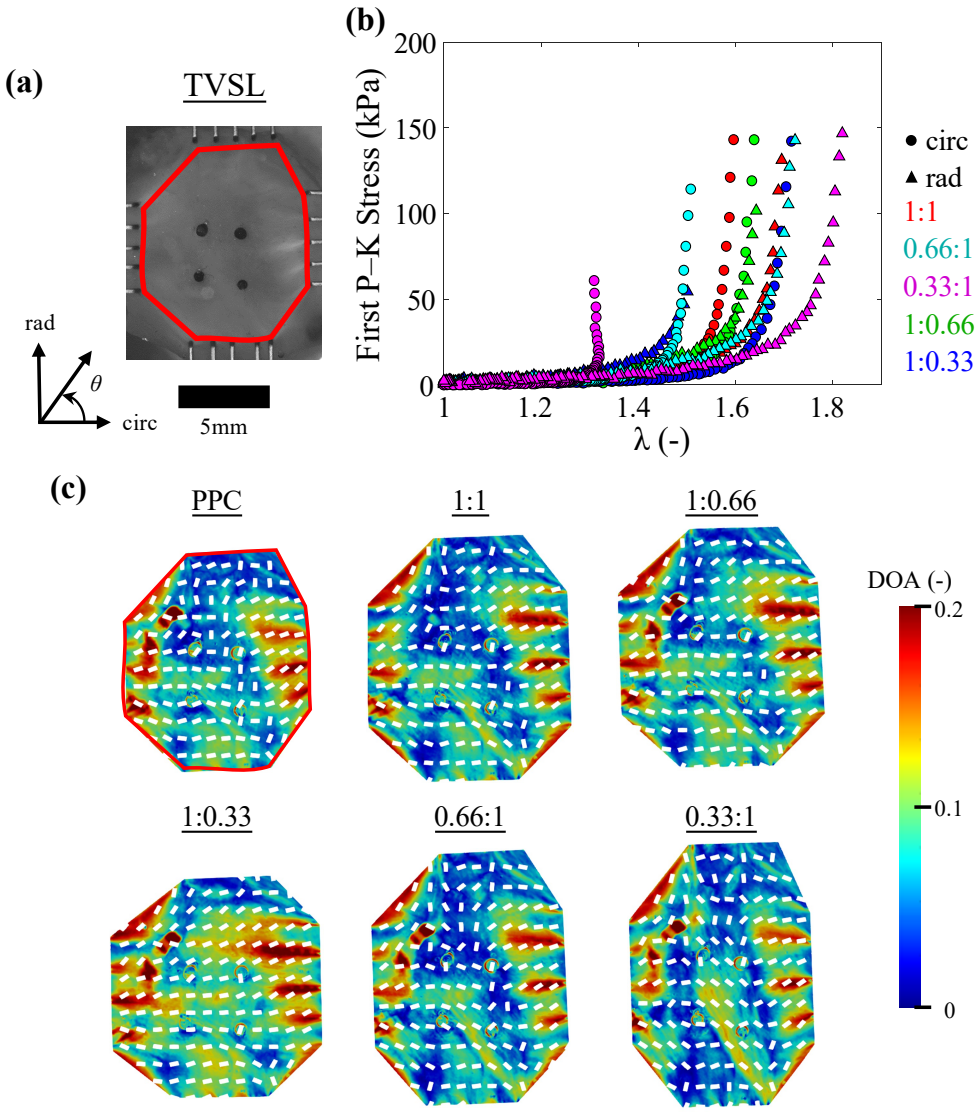


**Figure 4-5** Representative experimentally measured results from TVSL #10. (a) The experimental photo from the pSFDI camera is provided, along with (b) the biaxial mechanical testing results, and (c) the pSFDI-based collagen fiber orientations at the post-preconditioning (PPC) configuration and other applied biaxial tension protocols. Note that the region of interest shown is for the full tissue specimen, while the AFK analysis was only performed for the region delimited by the fiducial markers.

**Table 4-1** The post-preconditioning (PPC) stretches and peak stretches of the TVAL, TVPL, and TVSL specimens under the five applied biaxial tensions ($T_{\text{circ}}$:$T_{\text{rad}}$). Results are presented as the mean±SEM. Abbreviations: circ, circumferential; rad, radial.

| | TVAL | | TVPL | | TVSL | |
|---|---|---|---|---|---|---|
| Loading Protocol | circ | rad | circ | rad | circ | rad |
| PPC | 1.17±0.03 | 1.31±0.05 | 1.17±0.03 | 1.36±0.04 | 1.17±0.03 | 1.32±0.04 |
| 1:1 | 1.31±0.04 | 1.48±0.06 | 1.38±0.07 | 1.62±0.07 | 1.49±0.07 | 1.72±0.08 |
| 1:0.66 | 1.33±0.05 | 1.44±0.06 | 1.40±0.08 | 1.57±0.07 | 1.53±0.07 | 1.65±0.07 |
| 1:0.33 | 1.36±0.05 | 1.33±0.05 | 1.43±0.08 | 1.43±0.06 | 1.58±0.07 | 1.47±0.06 |
| 0.66:1 | 1.27±0.04 | 1.50±0.07 | 1.34±0.07 | 1.64±0.07 | 1.43±0.06 | 1.75±0.08 |
| 0.33:1 | 1.15±0.03 | 1.58±0.08 | 1.25±0.06 | 1.69±0.07 | 1.26±0.05 | 1.85±0.08 |

**Table 4-2** Comparisons of the collagen fiber angle between the pSFDI measurements and AFK predictions at the post-preconditioning (PPC) and peak equibiaxial deformations ($T_{\text{circ}}$:$T_{\text{rad}} = 1$:1) for all TVAL specimens. $\theta_{\text{median}}$ and IQR are provided for the $100 \times 100$ grids considered for each specimen, and the $\theta_{\text{error}}$ between the measured and predicted fiber orientations at the peak deformation are expressed as the mean±SD.

| | PPC | | $T_{\text{circ}}$:$T_{\text{rad}} = 1$:1 | | | | |
|---|---|---|---|---|---|---|---|
| | Measured $\theta_{\text{exp}}$ | | Measured $\theta_{\text{exp}}$ | | Predicted $\theta_{\text{pred}}$ | | $\theta_{\text{error}}$ |
| Specimen ID | Median | IQR | Median | IQR | Median | IQR | |
| 1 | 149.1° | 10.9° | 154.4° | 7.6° | 141.2° | 8.7° | −12.6°±22.9° |
| 2 | 115.4° | 39.5° | 142.5° | 45.2° | 116.3° | 39.9° | −4.5°±21.2° |
| 3 | 38.4° | 21.5° | 40.9° | 11.0° | 38.0° | 19.3° | −6.9°±23.8° |
| 4 | 162.6° | 24.4° | 156.7° | 62.9° | 162.1° | 17.2° | −1.8°±28.2° |
| 5 | 96.5° | 13.5° | 92.2° | 9.5° | 99.8° | 14.7° | −0.3°±12.6° |
| 6 | 111.2° | 11.4° | 114.3° | 10.5° | 113.4° | 11.2° | 0.4°±7.8° |
| 7 | 80.8° | 6.6° | 78.2° | 5.7° | 82.8° | 7.4° | −1.2°±20.8° |
| 8 | 151.5° | 3.5° | 146.5° | 4.1° | 150.5° | 3.7° | 5.0°±12.2° |
| 9 | 141.1° | 43.1° | 144.5° | 30.3° | 141.5° | 43.6° | 5.5°±25.5° |
| 10 | 132.4° | 13.5° | 134.6° | 15.3° | 129.7° | 13.6° | −4.0°±7.5° |
| 11 | 104.9° | 14.7° | 104.7° | 8.6° | 103.1° | 15.1° | 2.4°±13.5° |

**Table 4-3** Comparisons of the collagen fiber angle between the pSFDI measurements and AFK predictions at the post-preconditioning (PPC) and peak equibiaxial deformations ($T_{\text{circ}}$:$T_{\text{rad}} = 1$:1) for all TVPL specimens. $\theta_{\text{median}}$ and IQR are provided for the $100 \times 100$ grids considered for each specimen, and the $\theta_{\text{error}}$ between the measured and predicted fiber orientations at the peak deformation are expressed as the mean$\pm$SD.

| | PPC | | $T_{\text{circ}}$:$T_{\text{rad}} = 1$:1 | | | | |
|---|---|---|---|---|---|---|---|
| | Measured $\theta_{\text{exp}}$ | | Measured $\theta_{\text{exp}}$ | | Predicted $\theta_{\text{pred}}$ | | $\theta_{\text{error}}$ |
| Specimen ID | Median | IQR | Median | IQR | Median | IQR | |
| 1 | 112.6° | 10.0° | 118.4° | 14.7° | 115.2° | 10.4° | $-1.7°\pm16.8°$ |
| 2 | 16.8° | 144.8° | 21.2° | 137.3° | 19.4° | 138.0° | $0.1°\pm20.1°$ |
| 3 | 157.8° | 9.9° | 155.8° | 9.7° | 154.3° | 10.3° | $-2.2°\pm13.6°$ |
| 4 | 124.4° | 21.3° | 121.8° | 21.0° | 123.5° | 20.7° | $2.0°\pm22.6°$ |
| 5 | 136.0° | 11.1° | 94.6° | 77.3° | 134.3° | 11.7° | $-30.8°\pm38.9°$ |
| 6 | 156.6° | 13.3° | 152.2° | 8.2° | 155.4° | 14.2° | $0.0°\pm14.9°$ |
| 7 | 152.2° | 15.0° | 155.5° | 17.6° | 152.3° | 15.0° | $-3.3°\pm20.2°$ |
| 8 | 169.6° | 14.1° | 162.2° | 15.4° | 166.0° | 78.3° | $10.0°\pm20.6°$ |
| 9 | 121.8° | 24.8° | 119.6° | 26.5° | 119.7° | 20.8° | $-6.0°\pm14.6°$ |
| 10 | 132.8° | 31.0° | 136.9° | 34.7° | 128.9° | 28.6° | $-6.7°\pm13.6°$ |
| 11 | 80.1° | 26.0° | 57.9° | 41.1° | 81.9° | 25.6° | $-1.0° \pm -0.9°$ |
| 12 | 136.7° | 24.9° | 142.5° | 28.1° | 136.5° | 25.4° | $-0.9°\pm20.2°$ |
| 13 | 78.5° | 11.7° | 79.9° | 13.6° | 76.5° | 12.1° | $-2.9°\pm12.5°$ |
| 14 | 73.5° | 32.0° | 68.6° | 36.5° | 75.1° | 30.1° | $2.7°\pm14.1°$ |

**Table 4-4** Comparisons of the collagen fiber angle between the pSFDI measurements and AFK predictions at the post-preconditioning (PPC) and peak equibiaxial deformations ($T_{\text{circ}}$:$T_{\text{rad}} = 1$:1) for all TVSL specimens. $\theta_{\text{median}}$ and IQR are provided for the $100 \times 100$ grids considered for each specimen, and the $\theta_{\text{error}}$ between the measured and predicted fiber orientations at the peak deformation are expressed as the mean$\pm$SD.

| | PPC | | $T_{\text{circ}}$:$T_{\text{rad}} = 1$:1 | | | | |
|---|---|---|---|---|---|---|---|
| | Measured $\theta_{\text{exp}}$ | | Measured $\theta_{\text{exp}}$ | | Predicted $\theta_{\text{pred}}$ | | $\theta_{\text{error}}$ |
| Specimen ID | Median | IQR | Median | IQR | Median | IQR | |
| 1 | 113.1° | 23.9° | 123.8° | 32.4° | 114.7° | 22.6° | $-4.9°\pm21.1°$ |
| 2 | 147.1° | 21.0° | 139.0° | 64.0° | 145.9° | 21.3° | $-4.2°\pm19.6°$ |
| 3 | 165.6° | 20.6° | 148.6° | 155.3° | 164.8° | 23.6° | $-6.9°\pm29.0°$ |
| 4 | 8.7° | 99.3° | 10.2° | 7.5° | 9.6° | 94.1° | $-12.2°\pm29.7°$ |
| 5 | 101.4° | 37.8° | 108.3° | 33.8° | 98.1° | 39.5° | $-4.8°\pm15.3°$ |
| 6 | 102.5° | 27.3° | 100.4° | 35.3° | 101.7° | 24.9° | $-8.9°\pm29.5°$ |
| 7 | 124.5° | 49.4° | 102.1° | 74.8° | 126.8° | 40.7° | $-4.4°\pm38.8°$ |
| 8 | 34.1° | 130.8° | 35.6° | 128.7° | 36.0° | 128.0° | $-1.6°\pm24.0°$ |
| 9 | 106.5° | 16.9° | 108.2° | 17.2° | 106.2° | 15.8° | $-1.4°\pm12.6°$ |
| 10 | 15.2° | 14.5° | 14.2° | 14.0° | 16.4° | 14.7° | $-1.0°\pm19.7°$ |
| 11 | 92.4° | 13.9° | 96.8° | 70.6° | 90.3° | 13.3° | $-2.5°\pm47.0°$ |
| 12 | 156.8° | 20.5° | 162.7° | 13.6° | 153.9° | 20.6° | $-2.8°\pm32.9°$ |

example, under $T_{\text{circ}}$:$T_{\text{rad}} = 0.33$:1, $\theta_{\text{error}}$ was found as: $-4.0^{\circ} \pm 4.8^{\circ}$ (TVAL); $-5.0^{\circ} \pm 4.3^{\circ}$ (TVPL), and; $-7.4^{\circ} \pm 4.0^{\circ}$ (TVSL).

## 4.4 Discussion

### 4.4.1 Differences in Experimental and Predicted Collagen Fiber Reorientations

In this study, we have evaluated the AFK theory for the TV leaflets *for the first time* using a biaxial testing-pSFDI approach. We observed that the AFK theory generally underpredicted the rotations of the fibers. To elaborate, weak-to-moderate negative correlations were found between $\theta_{\text{reorient}}$ and $\theta_{\text{error}}$ across all the applied loading scenarios: equibiaxial loading, $r = -0.36$; circumferentially dominant loading, $r = -0.29$ to $0.07$; and radially dominant loading, $r = -0.29$ to $-0.24$. By comparing $\theta_{\text{error}}$ and $\lambda$, we found weak negative correlations under the applied equibiaxial loading (circumferential, $r = -0.17$; radial, $r = -0.02$), while under non-equibiaixal loading the correlation was stronger in the dominant loading direction: circumferentially dominant loading, circumferential direction: $r = -0.27$ to $-0.18$; and radially dominant loading, radial direction: $r = -0.02$ to $-0.32$. The observed trends suggest that increasing collagen fiber reorientations result in an increased magnitude of underpredictions by the AFK theory, which may be further related to the increasing magnitude of the tissue deformations. This trend can be corroborated with a previous vasculature testing study that reported the AFK errors could be associated with excessive tissue deformations [70].

Another explanation for the mispredictions could be related to the direction of applied loading with respect to the preferred fiber orientations. A study by [66] performed uniaxial testing of human supraspinatus tendons and observed that the AFK predictions were less accurate when the loading was applied transverse to the preferred fiber orientation, and when there was a greater dispersion of fibers. We are unable to demonstrate this finding, however, because: (i) in the present study, we performed biaxial testing, and (ii) our pSFDI device quantifies the *optical anisotropy* of the material, which is not a direct measurement of the fiber dispersion. This imaging modality requires more research to be able to quantify the *structural* fiber dispersion. Regardless, it is worth highlighting that we observed a weak correlation between tissue anisotropy, which may be related to the fiber dispersion and $\theta_{\text{error}}$ ($r = 0.15$). Other causes for the AFK mispredictions include the potential for heterogeneous, locally varying affine kinematics [216], the experimental testing conditions inducing vary-

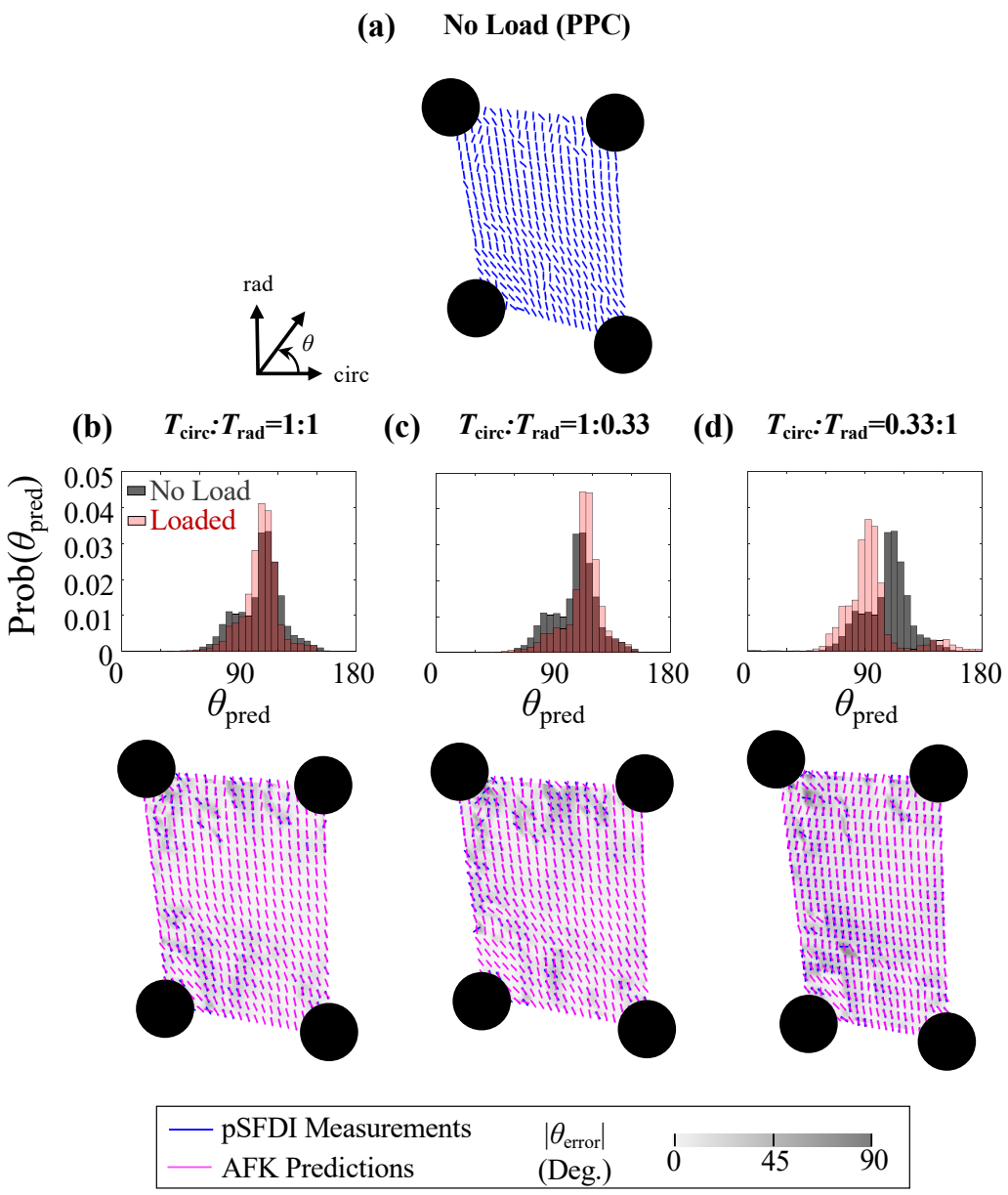


**Figure 4-6** Comparisons of the AFK-predicted and pSFDI-measured collagen fiber orientations for a representative TVAL specimen (TVAL #11) at the (a) PPC deformation (experimental only) and at the peak deformation of various applied biaxial loading states: (b) $T_{circ}$:$T_{rad}$ = 1:1, (c) $T_{circ}$:$T_{rad}$ = 1:0.66, (d) $T_{circ}$:$T_{rad}$ = 1:0.33, (e) $T_{circ}$:$T_{rad}$ = 0.66:1, and (f) $T_{circ}$:$T_{rad}$ = 0.33:1. Dashed lines denote the predicted and experimentally measured collagen fiber orientations for some selected pixels, the grayscale gradient represents the absolute error between the predicted and experimental findings, and the black circles represent the positions of the fiducial markers. Histograms denote the probability for the experimental collagen fiber orientations at each five-degree increment.

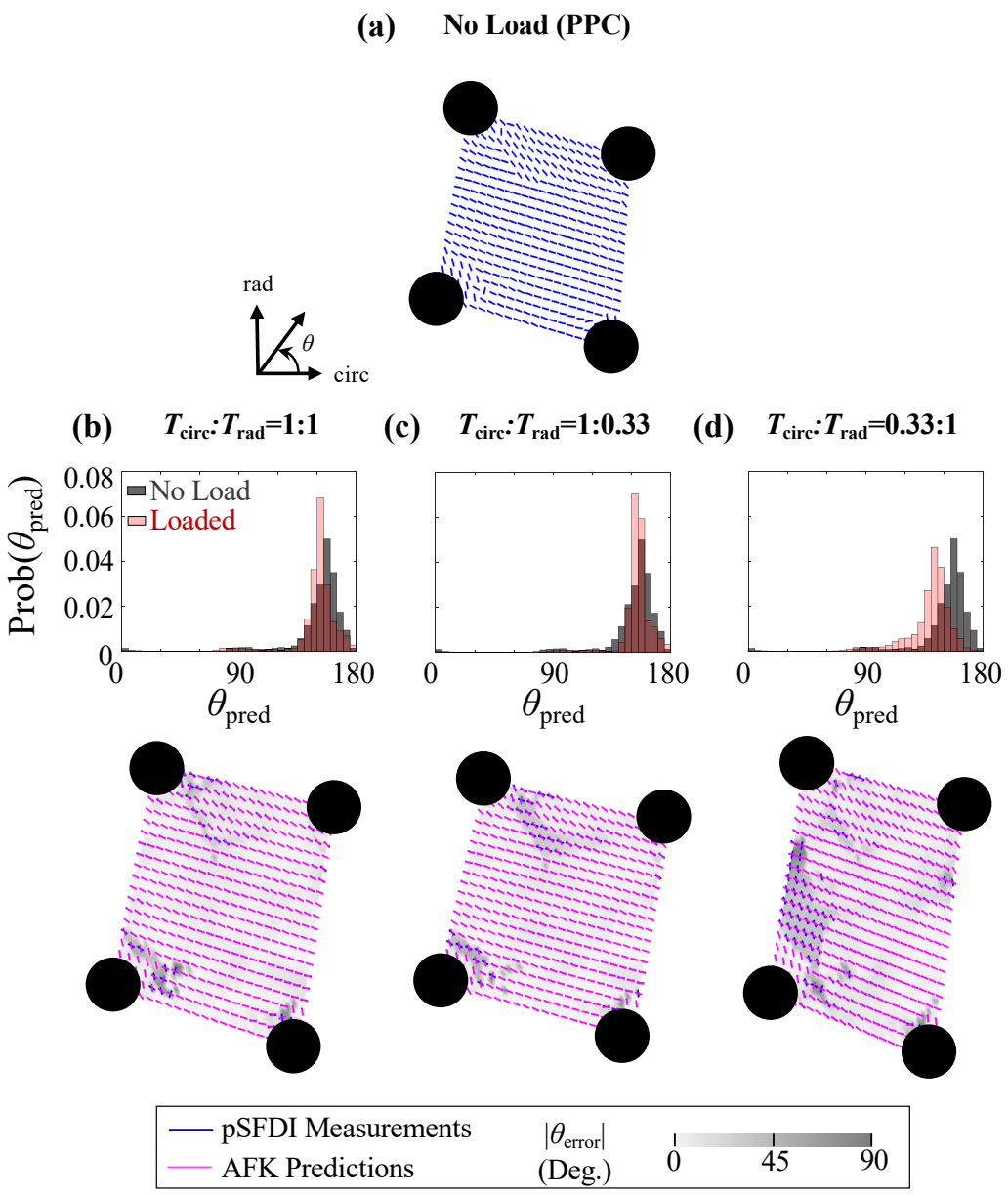


**Figure 4-7** Comparisons of the AFK-predicted and pSFDI-measured collagen fiber orientations for a representative TVPL specimen (TVPL #6) at the (a) PPC deformation (experimental only) and at the peak deformation of various applied biaxial loading states: (b) $T_{circ}$:$T_{rad}$ = 1:1, (c) $T_{circ}$:$T_{rad}$ = 1:0.66, (d) $T_{circ}$:$T_{rad}$ = 1:0.33, (e) $T_{circ}$:$T_{rad}$ = 0.66:1, and (f) $T_{circ}$:$T_{rad}$ = 0.33:1. Dashed lines denote the predicted and experimentally measured collagen fiber orientations for some selected pixels, the grayscale gradient represents the absolute error between the predicted and experimental findings, and the black circles represent the positions of the fiducial markers. Histograms denote the probability for the experimental collagen fiber orientations at each five-degree increment.

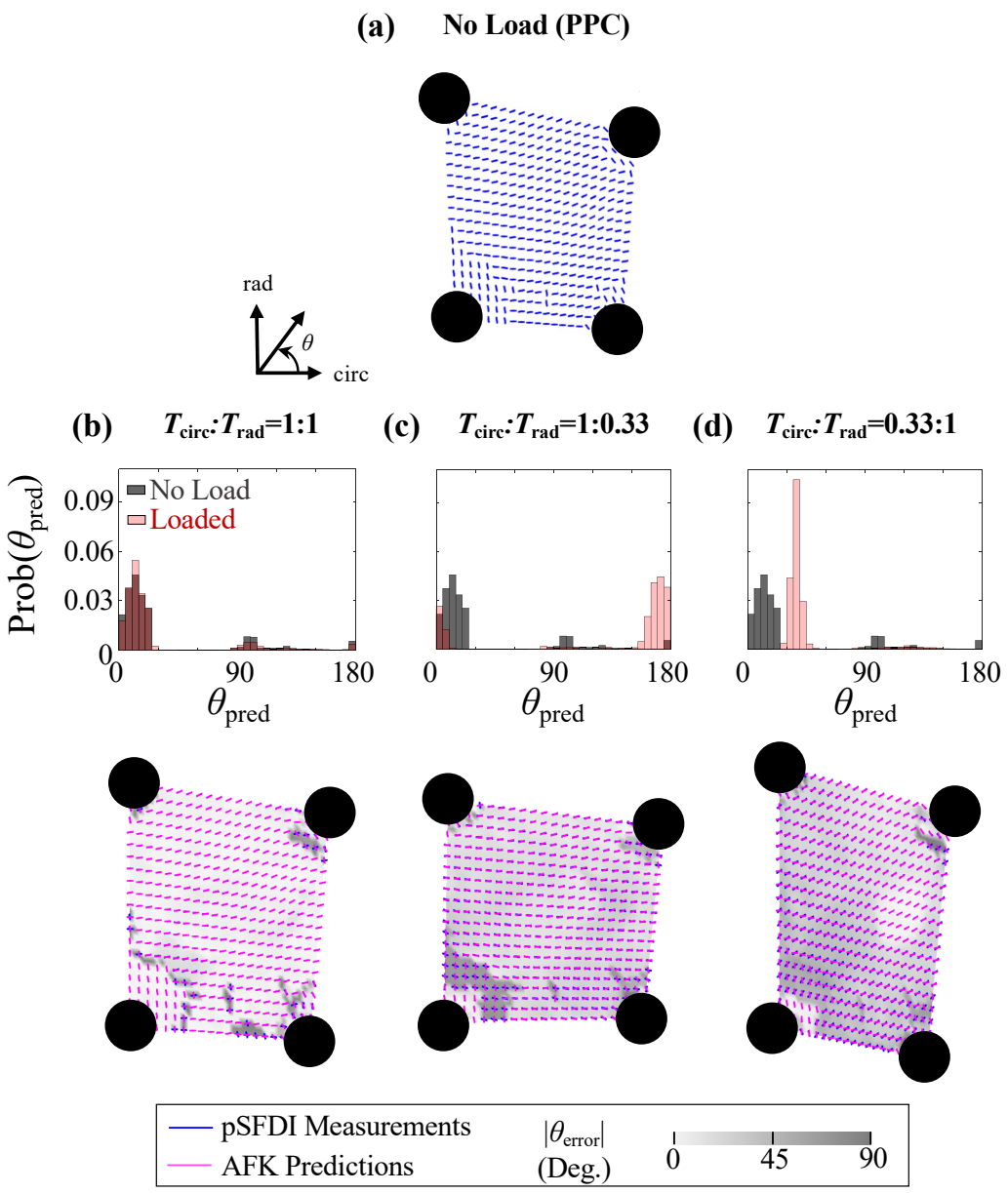


**Figure 4-8** Comparisons of the AFK-predicted and pSFDI-measured collagen fiber orientations for a representative TVSL specimen (TVSL #10) at the (a) PPC deformation (experimental only) and at the peak deformation of various applied biaxial loading states: (b) $T_{circ}$:$T_{rad}$ = 1:1, (c) $T_{circ}$:$T_{rad}$ = 1:0.66, (d) $T_{circ}$:$T_{rad}$ = 1:0.33, (e) $T_{circ}$:$T_{rad}$ = 0.66:1, and (f) $T_{circ}$:$T_{rad}$ = 0.33:1. Dashed lines denote the predicted and experimentally measured collagen fiber orientations for some selected pixels, the grayscale gradient represents the absolute error between the predicted and experimental findings, and the black circles represent the positions of the fiducial markers. Histograms denote the probability for the experimental collagen fiber orientations at each five-degree increment.

ing affine or non-affine fiber kinematics [65], or the fiber crimp causing significant AFK prediction errors [50].

Mispredictions from the AFK theory could also be related to the coupling between the fibers and the nonfibrous matrix. This idea is supported by a fiber-matrix model from [71], in which a more compliant nonfibrous matrix resulted in more fiber reorientations, while a stiffer nonfibrous matrix lead to more fiber stretching. This coupling effect was also observed in the modeling of collagenous gels [217]. The refinement of the AFK assumption based on these intricate non-fibrous matrix interactions requires further experimental and modeling efforts.

### 4.4.2 Considerations for Constitutive Modeling Using Affine Fiber Kinematics

While the exact sources of the errors from the AFK theory are uncertain, the mispredictions should be considered in the formulation of constitutive models. To this end, previous researchers have proposed various improvements to the AFK theory. For example, in the work by [50] performing biaxial testing and small-angle X-ray scattering of two mitral valve leaflets, they observed that including fiber crimp in the AFK theory yielded a more accurate prediction of the fiber reorientations. This correction may not hold for the TV leaflets, however, due to the mechanical and functional differences between the atrioventricular heart valves that could cause a different microstructure, morphology, and CFA (e.g., fibrillar density and dispersion) between the two AHVs. To date, no comprehensive investigation of the TV leaflet microstructure has been performed to confirm this theory, with only one recent study making a qualitative assessment via second harmonic generation [53]. Another AFK theory adjustment was made for the experiments and modeling of gelatin co-gels by including a correction factor to accommodate the AFK errors [218]. The correction factor implementation may be more robust for imaging modalities that cannot quantify fiber crimp, such as the pSFDI method used in the present study.

While a refinement of the AFK theory could provide a more computationally efficient methodology for modeling the collagen fiber behaviors, the incorporation of the non-AFK behaviors could lead to more accurate cardiac simulations and fiber kinematics predictions. In recent literature, there has been increasing focus on modeling non-AFK, and more work should be performed to realize more accurate and computationally inexpensive models, especially for use in modeling the tissue viscoelasticity [61–63, 218, 219]. Furthermore, experimental works should be performed to understand the non-AFK (e.g., fiber uncrimping

together with fiber elongation), such as through small-angle X-ray scattering combined with biaxial mechanical testing or stress-relaxation testing.

### 4.4.3 Limitations and Future Extensions

There are a few limitations of the present work. First, we used the pSFDI modality to determine the CFA of the TV leaflets, and, while the pSFDI modality has been shown to provide accurate quantifications of the collagen fiber orientations [56, 207, 220], there is the potential for mispredictions caused by surface imperfections on the tissue (glue, dust, etc.), or glare in the polarizer. Future studies are warranted to corroborate our results with additional imaging modalities, such as small-angle scattering or multiphoton microscopy. Second, the presented CFA results depict the average collagen fiber orientation through the thickness of the tissue and there could be mispredictions caused by fiber splay. Further investigations could be made using the spatial frequency domain imaging capabilities of the system to obtain quantifications of the CFA at discrete depths of the tissue thickness, allowing for more detailed AFK-based comparisons. Investigations of the regionally varying CFA and AFK mispredictions are further necessitated by previous studies demonstrated highly heterogeneous fiber reorganizations in the aortic valve cusps [221] Additionally, we investigated the AFK assumption for the region within the central third of the tissue using only the deformation gradient obtained from the four fiducial markers. A more refined strain field could yield more accurate AFK results [216]; however, we could not implement a refined strain field without obstructing the view of the tissue for the pSFDI system. Finally, another future study could be performed using the biaxial testing-pSFDI approach to investigate the collagen fiber reorientations in the leaflets during viscoelastic characterizations, as was observed for the aortic valve cusps [222].

## 4.5 Chapter Summary

In this work, we have utilized the pSFDI technique to provide a detailed characterization of the load-dependent changes in the CFA of the three TV leaflets, and compared the experimentally measured fiber orientations to the AFK theory. To our knowledge, this work is *the first of its kind* for evaluating the AFK theory for the TV leaflets, which provides valuable insight for future computational modeling works that rely on AFK-based constitutive forms to describe the leaflet mechanical and microstructural behaviors. Furthermore, another key contribution of this study is the use of biaxial testing to evaluate the AFK assumption, which is limited in the previous literature. The results of this study demonstrate

the need for future experimental work to quantify the fibrous-nonfibrous matrix coupling or the non-AFK, such as crimping and uncrimping. Through an improved understanding of the collagen fiber kinematics in the TV leaflets, computational simulations can be refined for use in research areas such as tissue growth and remodeling to understand how diseases affect the CFA, which in turn impacts tissue mechanics and organ-level valve function.

# 5 NON-INVASIVE GEOMETRIC AND ENGINEERING ANALYSIS OF THE HLHS-AFFLICTED PEDIATRIC TRICUSPID VALVE ANNULUS


5.1 Motivation . . . . . 94
5.2 Methods . . . . . 94
5.2.1 Study Population . . . . . 94
5.2.2 Echocardiogram Imaging and Image Segmentation . . . . . 94
5.2.3 Geometry- and Engineering Mechanics-Based Analyses for the TV Annulus . . . . . 98
5.2.4 Statistical Analysis . . . . . 100
5.3 Results . . . . . 101
5.3.1 TV Annulus Geometric Features in Newborns with HLHS . . . 101
5.3.2 TV Annulus Mechanics for newborns with HLHS . . . . . 102
5.3.3 Differences between Healthy and HLHS-Afflicted Newborns . . 102
5.4 Discussion . . . . . 111
5.4.1 Comparisons between Healthy and newborns with HLHS . . . . 111
5.4.2 Development of Tricuspid Regurgitation in newborns with HLHS . . . . . 112
5.4.3 Comparisons to Previous TV Annulus Biomechanics Studies . . 112
5.4.4 Clinical Relevance and Translatability of the TV Annulus Pipeline . . . . . 113
5.4.5 Limitations and Future Extensions . . . . . 113
5.5 Chapter Summary . . . . . 114

## 5.1 Motivation

While these advancements facilitate a deeper understanding of the geometric abnormalities related to the presence of TR in patients with HLHS, there are currently no biomechanics-focused studies of the TV structures. Mechanical strain, caused by external constraints or loads (in this case due to right ventricular contraction and valve closure), is a geometric measure of deformation, representing the relative displacement between particles in a material body. Understanding the functional strains, together with other engineering mechanics metrics, is crucial for optimizing TV surgical techniques that can ideally prevent TR regression. Specifically, TV interventions, such as valvuloplasty, may be improved to better target the desired tissue homeostatic stress and strain to avoid adverse tissue remodeling and the subsequent disease progression. To this end, we develop a mechanics-based TV annulus analysis pipeline to quantify and systematically analyze the clinical, geometric, and engineering mechanics metrics in HLHS-afflicted TVs. In this pilot study, we use this pipeline to analyze a cohort of eight newborns with HLHS ($n = 8$) and four healthy newborns ($n = 4$), which can lay the foundation for future studies to identify the predictors of TV annulus mechanics associated with TR.

## 5.2 Methods

### 5.2.1 Study Population

This is a single-center study, reviewed and approved by the institutional review board at the University of Oklahoma Health Sciences Center, for a retrospective (IRB#14112) enrollment of patients diagnosed with HLHS from July 2019 to present.

The inclusion criteria for the eight currently enrolled patients wIth HLHS were that they (i) have HLHS, and (ii) have no evidence of moderate or severe TR. Meanwhile, the inclusion criterion for another four *healthy* patients was the absence of cardiovascular disease or defects, and they were imaged for concerns, such as hypoxia or heart murmurs, but presented with normal cardiovascular function. **Table 5-1** summarizes the characteristics of all twelve patients (e.g., birth weight, gestational age).

### 5.2.2 Echocardiogram Imaging and Image Segmentation

Routine 4-dimensional full-volume transthoracic echocardiographic data for a full cardiac cycle was collected in the apical view (coronal scanning plane) using a Philips EPIQ ul-

**Table 5-1** Patient characteristics for the HLHS-afflicted and healthy newborns considered in this study. Note that the diameter of the ascending aorta, RVFAC, and TAPSE scores were not measured in the healthy patients. Abbreviations: TAPSE – tricuspid annular plane systolic excursion; RVFAC – right ventricular fractional area change; MS – mitral stenosis; AoS – aortic stenosis; AoA – aortic atresia.

| **(I) Newborns with HLHS** | | | | | | | | |
|---|---|---|---|---|---|---|---|---|
| ID | Race | Gender | Birth Weight/ Height | Gestational Age | Diameter of Ascending Aorta | TAPSE | RVFAC | HLHS Subtype |
| 1 | Hispanic | Male | 2790 g/ 46 cm | 36 + 0/7 wks | 0.29 cm (z = −3.44) | 8.0 mm | 44% | MS/AoS |
| 2 | Caucasian | Male | 3020 g/ 48.5 cm | 37 + 1/7 wks | 0.20 cm (z = −4.77) | 8.5 mm | 40% | MS/AoA |
| 3 | Caucasian | Male | 3310 g/ 52 cm | 38 + 2/7 wks | 0.16 cm (z = −5.17) | 8.4 mm | 41% | MS/AoA |
| 4 | Caucasian | Male | 3350 g/ 49 cm | 38 + 1/7 wks | 0.23 cm (z = −4.73) | 8.0 mm | 44% | MS/AoS |
| 5 | Caucasian | Male | 3180 g/ 52 cm | 38 + 4/7 wks | 0.32 cm (z = −3.93) | 9.0 mm | 45% | MS/AoS |
| 6 | Unknown | Female | 2700 g/ 49 cm | 39 + 2/7 wks | 0.40 cm (z = −3.07) | 8.0 mm | 43.8% | MS/AoS |
| 7 | Caucasian | Female | 2780 g/ 47.5 cm | 38 + 5/7 wks | 0.18 cm (z = N/A) | 8.5 mm | 37% | MA/AoA |
| 8 | Hispanic | Male | 3350 g/ 47.8 cm | 39 + 1/7 wks | 0.22 cm (z = −4.76) | 6.5 mm | 40% | MA/AoA |
| **(II) Newborns without HLHS** | | | | | | | | |
| ID | Race | Gender | Birth Weight/ Height | Gestational Age | Diameter of Ascending Aorta | TAPSE | RVFAC | HLHS Subtype |
| 9 | Hispanic | Female | 1670 g/ 42.5 cm | 33 + 3/7 wks | N/A | 10.5 mm | 55% | N/A |
| 10 | Hispanic | Male | 3575 g/ 55.5 cm | 40 + 3/7 wks | N/A | 10.7 mm | 45% | N/A |
| 11 | Unknown | Male | 2260 g/ 45 cm | 32 + 5/7 wks | N/A | 8.7 mm | 40% | N/A |
| 12 | Caucasian | Male | 2960 g /50 cm | 39 + 4/7 wks | N/A | 13.3 mm | 62% | N/A |

trasound machine (Philips, NV) equipped with 5 MHz and 7 MHz matrix-array transducers under our IRB approved protocol, where none of the patients were under sedatives/medications during the imaging procedure. The acquired 4D echocardiographic imaging data was converted into a Cartesian DICOM (3DDCM) format in QLAB Cardiac Analysis software (Philips, NV) [223]. The corresponding DICOM files from the patient imaging were then imported to the 3D Slicer software using the SlicerHeart module for definition of the TV annulus using the three standard views—the axial, sagittal, and coronal planes (**Fig. 5-1**) [127, 223, 224]. For the subsequent geometrical and engineering mechanics-based analyses, we defined five key timepoints of interest over the cardiac cycle [16, 224, 225]:

- $\text{RVP}_{\text{min}}$: The TV is open (i.e., leaflets are not in contact), and the right ventricle is at the minimum volume.

- ED: The time instant right before the coaptation of the TV leaflets.

- EIVC: The TV is closed (i.e., TV leaflets are in contact), and the right ventricle is at the maximum volume.

- ES: The TV is closed, and the ventricular volume is at the minimum.

- EIVR: The TV is closed, and the ventricular volume is at the minimum volume without a change in ventricular volume. At each of the above timepoints, the $(X, Y)$ locations of the three commissure regions were first identified on the axial plane, i.e., the AS, the AP, and the PS commissures (**Fig. 5-1(a)**).

Then, the segmentation of the TV annulus was performed within the 3D Slicer software through manual segmentation of the TV leaflet hinge points (**Fig. 5-1(b)**, **(c)**). These leaflet hinge points were identified at every $8^\circ - 9^\circ$ of the TV annulus by rotation of the sagittal plane view about the centroid of the imaging viewpoint (**Fig. 5-1(d)**). Following segmentation, the $(X, Y, Z)$ coordinates of the segmented TV annulus point clouds were exported for the geometry and mechanics analyses. To ensure the consistency and robustness of our overall manual image segmentation, all TV annulus segmentations were performed in consultation with multiple clinicians (e.g., pediatric cardiologist and pediatric cardiac surgeon) at the Oklahoma Children's Hospital and Children's Hospital of Philadelphia.

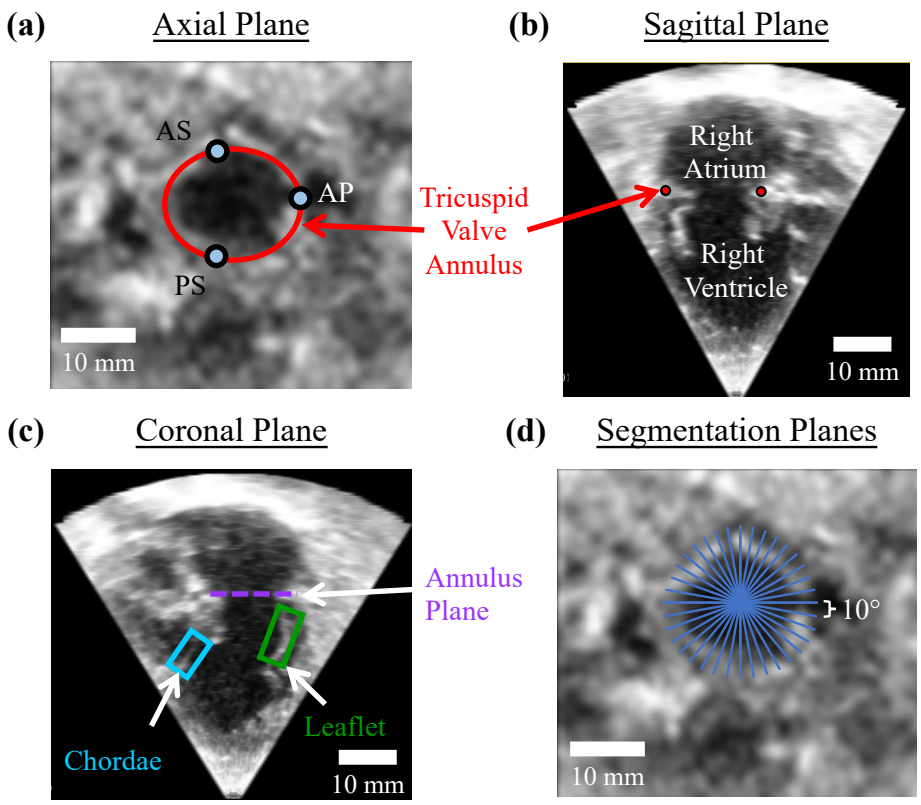


**Figure 5-1** 4D transthoracic echocardiographic data from a representative newborn with HLHS (Patient #1): (a) axial plane, (b) sagittal plane, and (c) coronal plane. (d) Illustration of our image segmentation of the TV annulus.

### 5.2.3 Geometry- and Engineering Mechanics-Based Analyses for the TV Annulus

The $(X,Y,Z)$ coordinates from the TV annulus point clouds were imported to MATLAB (MathWorks, MA). Annulus curve fitting was performed using a moving least-squares algorithm to generate 300 material points to determine geometric measurements: the AP and SL diameters, the annular height, the bending angle, the circumference, the annular area, and the sphericity and biomechanical metrics (e.g., strain, strain rate, and relative curvature). Let $C$ be the TV annulus curve parametrized by the moving least-squares functions in a cylindrical coordinate system $(r,\theta,z)$:

$$C(X,Y,Z) = \left( \sum_{J=1}^{NP} \Psi_J(\theta) r_J, \theta, \sum_{J=1}^{NP} \Psi_J(\theta) z_J \right) \tag{5.2-1}$$

where the TV annulus is represented by $NP$ discrete points associated with their unknown $r_J$ and $z_J$ coordinates and the moving least-squares shape functions $\Psi_J$. The transformation between the cylindrical and Cartesian coordinate systems follows: $X = r\cos\theta$, $Y = r\sin\theta$, and $Z = z$.

According to Belytschko et al. (1996) and Chen et al. (1996), the one-dimensional moving least-squares shape functions are constructed by [226, 227]:

$$\Psi_J(\theta) = \mathbf{H}^T(0)\mathbf{M}^{-1}(\theta)\mathbf{H}(\theta-\theta_J)\phi(\theta-\theta_J;w). \tag{5.2-2}$$

Herein, $\mathbf{H}^T(\theta-\theta_J) = [1, \theta-\theta_J, ..., (\theta-\theta_J^N]$ is the basis function up to a monomial order of $N$, $\phi$ is the window function with a support of $w$, and $\mathbf{M}(\theta)$ is the moment matrix defined as:

$$\mathbf{M}(\theta) = \sum_{K=1}^{NP} \mathbf{H}^T(\theta-\theta_K)\mathbf{H}(\theta-\theta_K)\phi(\theta-\theta_K;w). \tag{5.2-3}$$

In this study, we chose $NP = 9$, a quadratic basis function, i.e., $N = 2$, a cubic B-spline function for $\phi$, and a support of $w = 3.25$ to parametrize the TV annulus curve (i.e., a periodic curve with $\theta = 0^\circ - 360^\circ$) via standard linear least-squares regression with respect to the segmented 3D point cloud data (**Fig. 5-2(a)**). After the fitted curve was obtained, 300 uniformly spaced material points were generated in the $\theta$ coordinate for the subsequent analyses.

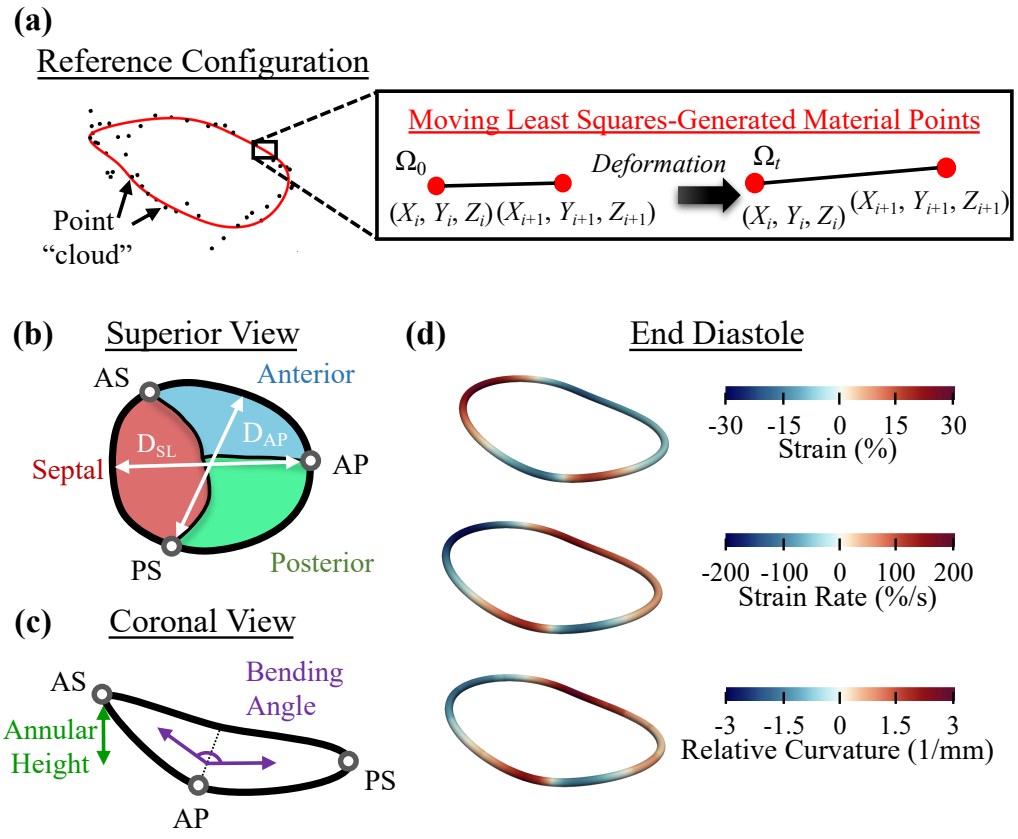


**Figure 5-2** (a) Visual description of the moving least-squares curve fitting to obtain a smoothed representation of the TV annulus. (b) Schematic of the two diameters of the TV annulus: $D_{SL}$ and $D_{AP}$. (c) Illustration of the calculations of the annular height and the annulus bending angle. (d) Representative annulus contours from HLHS Patient #1 at end diastole.

The typical clinical and geometric indices were quantified [228], including: (i) the two primary annulus diameters: the AP diameter $D_{\text{AP}}$ and the SL diameter $D_{\text{SL}}$ (**Fig. 5-2(b)**), (ii) the annular height (**Fig. 5-2(c)**), and (iii) the bending angle which is defined as the angle between the best fit planes of the flat region and the elevated region (**Fig. 5-2(c)**). We also determined other geometry-based metrics of interest, including the circumference, the annulus area, which is approximated by the sum of the area of triangles delimited by any two adjacent material points and the centroid of the annulus curve [45], and the sphericity, which is calculated by $D_{\text{AP}}/D_{\text{SL}}$.

The biomechanical metrics were also determined using the material points from the fitted annulus curve. Herein, we defined $\text{RVP}_{\text{min}}$ as the reference configuration ($\Omega_0$), as it is the timepoint in the cardiac cycle closest to a stress-free reference configuration [82]. The TV annulus strains, associated with each material point $i$ located at $(X_i, Y_i, Z_i)$, were computed by $\epsilon_i = s_i^t/s_i^0$, where $s$ denotes the segment length between two points, and the superscripts $0$ and $t$ denote the reference $\Omega_0$ and deformed states $\Omega_t$, respectively. After the TV annulus strains were determined, the strain rate between any two timepoints $t_1$ and $t_2$ was calculated by $\dot{\epsilon}_i = \delta s_i/\delta t = (s_i^{t_2} - s_i^{t_1})/(t_2 - t_1)$. To further gain insight into the geometry of the dynamic TV annulus, we also calculated the curvature by using the first- and second-order derivatives ($\mathbf{d}^{(1)}$ and $\mathbf{d}^{(2)}$) associated with the annulus curve [229]:

$$\kappa_i = \frac{|\mathbf{d}^{(1)}(X,Y,Z)_i \times \mathbf{d}^{(2)}(X,Y,Z)_i|}{|\mathbf{d}^{(1)}(X,Y,Z)_i|^3}. \tag{5.2-4}$$

In addition, we determined the relative curvature as the difference in curvature between the reference configuration and the subsequent timepoints (i.e., $\kappa_{i,0} - \kappa_{i,t}$). A representative illustration of the spatial variations in the strain, strain rate, and curvature, between EIVC and RVP are shown in **Fig. 5-2(d)**.

### 5.2.4 Statistical Analysis

Normally distributed data was reported as the mean$\pm$standard error of the mean, and non-normal data as the median [the interquartile range]. For comparisons between patients, annular area measurements were first normalized by the body surface area (BSA), while the linear measurements were normalized by $\sqrt{\text{BSA}}$ [127]. Herein, the BSA was estimated using Haycock's formula [230]. Statistical comparisons were performed between the HLHS-afflicted and healthy newborns: normal data via Student's *t*-test (with Welch's correction

in the case of unequal variances), and non-normal data via Wilcoxon rank-sum test. Differences were deemed statistically significant for $p < 0.05$. To analyze trends between the clinical measurements of patient RV function and the TV geometries, we analyzed the Pearson's correlation coefficient ($r$). Note that this study is a pilot investigation, and the statistical comparisons performed provide preliminary insights into the differences between HLHS-afflicted and healthy newborns. Future studies with larger cohorts will be required for more conclusive findings.

## 5.3 Results

### 5.3.1 TV Annulus Geometric Features in Newborns with HLHS

From the geometry perspective, we observed distinct changes in the TV annulus during the cardiac cycle for the newborns with HLHS (**Figs. 5-3, 5-4**). Specifically, $D_{\text{AP}}$ decreased during the leaflet coaptation (EIVC) by $-12.9 \pm 4.0\%$, whereas the trends for $D_{\text{SL}}$ were less consistent, with half of patients demonstrating an increase in $D_{\text{SL}}$ ($6.6\%$ to $45.7\%$), while the remaining patients exhibiting a decreased during EIVC ($-3.6\%$ to $-18.5\%$). These changes were reflected in the sphericity and the annular area. For sphericity, nearly all patients (except Patient #4) had an elliptical annulus shape (sphericity $> 1.0$) at $\text{RVP}_{\text{min}}$, then becoming more circular throughout the cardiac cycle (i.e., sphericity$\approx 1.0$). For annular area, we found decreases between $\text{RVP}_{\text{min}}$ and EIVC for all but one of the patients wIth HLHS ($-42.1\%$ to $-6.8\%$), and a $13.0\%$ increase for Patient #7 who had a restrictive atrial septal defect. In contrast, the circumference remained relatively constant for each patient (variations within $\pm 10\%$ throughout the cardiac cycle).

The bending angle and annular height provide insights into the changes in the out-of-plane "saddleness" of the TV annulus. Specifically, we found the annulus to be flatter in the relaxed state ($\text{RVP}_{\text{min}}$, $166.2°$ [$22.2°$]) and more "bent" at valve closure (EIVC, $143.9°$ [$8.1°$]). We also noted an $8.2 - 87.7\%$ increase in the annular height for 3 out of the 8 newborns with HLHS at EIVC, while the remaining 5 patients showed a decrease in the annular height of $-1.6\%$ to $-36.5\%$. On the other hand, the quantified geometric changes for the healthy newborns are shown in **Figs. 5-5** and **5-6**.

Analyzing the patient RV function data (**Table 5-1**), we observed moderate-to-strong correlations of the RVFAC to the quantified geometric indices: $D_{\text{AP}}$ ($-0.78 < r < -0.44$), $D_{\text{SL}}$ ($-0.75 < r < -0.03$), area ($-0.57 < r < -0.36$), bending angle, ($-0.55 < r < 0.81$),

height ($0.22 < r < 0.67$), and sphericity ($-0.74 < r < 0.22$), whereas the RVFAC was weakly correlated with the mechanical strain and strain rate along with a moderate correlation with the curvature in the septal segment ($0.57 < r < 0.66$). In addition, there were moderate-to-strong correlations between the diameter of the ascending aorta and the annular height ($0.71 < r < 0.86$) and the strain in the posterior segment ($0.36 < r < 0.76$).

### 5.3.2 TV Annulus Mechanics for newborns with HLHS

The spatial variations of the computed annulus strain around the circumference at each of the analyzed timepoints for one representative patient (i.e., Patient #1) are shown in **Fig. 5-7**, whereas the computed annular strain, strain rate, and relative curvature across all patients are presented in **Figs. 5-8**, **5-9**, and **5-10**, respectively. Video animations depicting the annulus shape and strains throughout the cardiac cycle for each patient (HLHS and healthy) can be found online in the published article [231].

From the representative patient, we observed the largest compressive strains in the posterior annulus (a maximum strain of $-8.8\%$ at ED), whereas the anterior segment underwent the smallest strain throughout the cardiac cycle ($< 5\%$ on average). Similarly, across all patients, we found the largest strains in the posterior and septal segments ($-5.7 \pm 2.2\%$ and $-8.7 \pm 3.8\%$ at ED, respectively), and the minimal strain in the anterior segment ($< 5\%$ on average at all selected timepoints). For the strain rate, the largest changes were found at EIVC: posterior segment ($5.2 \pm 63.0\%/\text{s}$), anterior segment ($60.9 \pm 66.6\%/\text{s}$), and septal segment ($-158.8 \pm 96.1\%/\text{s}$). Finally, we observed a maximum change in the relative curvature for the posterior and anterior segments ($\pm 1.0$ mm$^{-1}$), along with a $\pm 2.0$ mm$^{-1}$ curvature change for the septal segment.

### 5.3.3 Differences between Healthy and HLHS-Afflicted Newborns

From the geometric perspective, we noted several key differences between the HLHS and healthy newborns. First, $D_{\text{AP}}$ and the annular circumference were larger for patients wIth HLHS at all five analyzed timepoints ($35-45\%$ and $20-30\%$ larger, respectively; $0.001 < p < 0.040$). Interestingly, however, $D_{\text{SL}}$ was similar between the two groups ($0.074 < p < 0.260$). These trends were similarly reflected in the annular area, wherein the area was significantly larger ($44-65\%$) for the patients wIth HLHS at all timepoints, except EIVC ($0.002 < p < 0.060$). The sphericity was also significantly different between patient subgroups at all timepoints except ED ($0.017 < p < 0.040$). Specifically, the healthy newborns

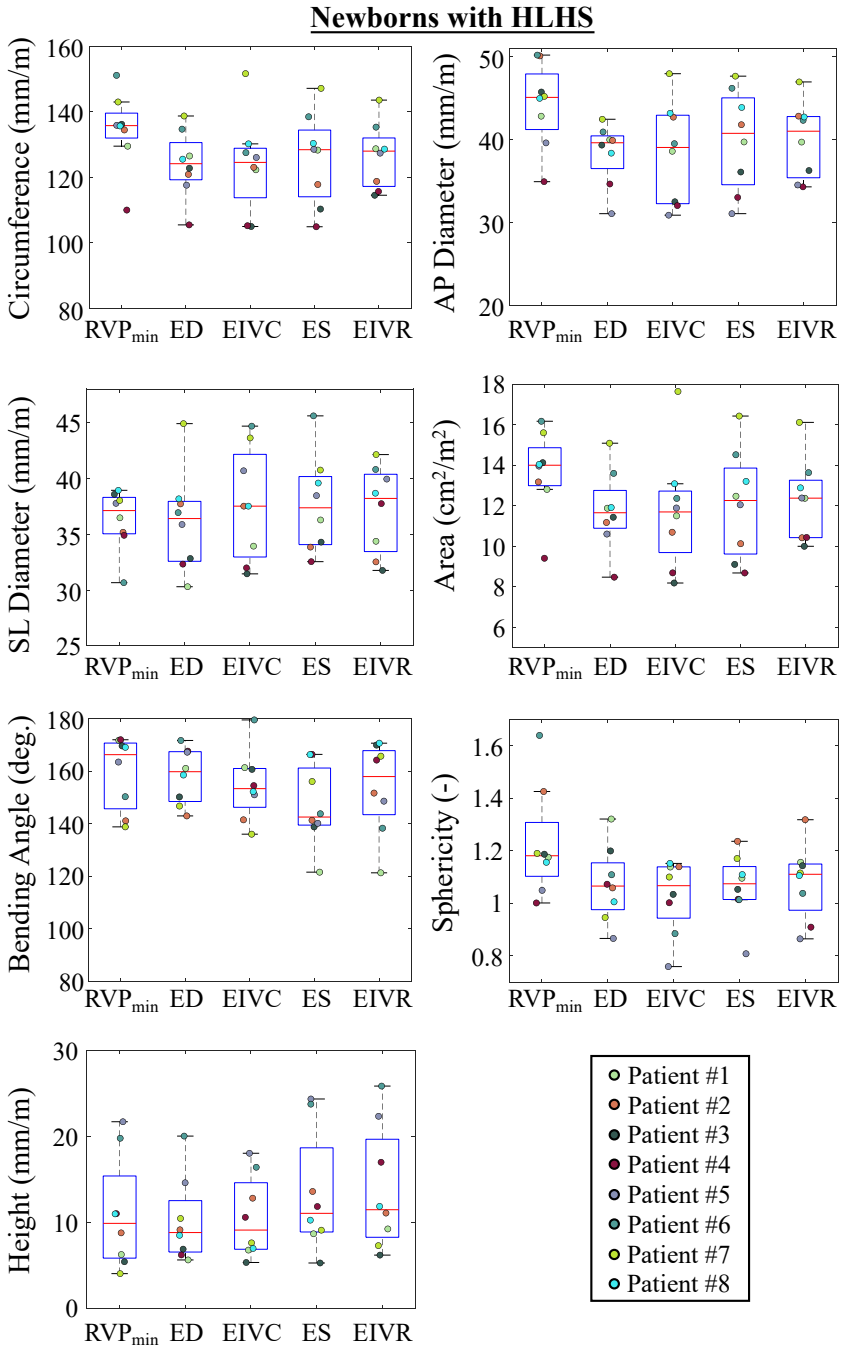


**Figure 5-3** Key TV annulus clinical metrics for all newborns with HLHS ($n = 8$) at the selected timepoints over the cardiac cycle (solid red line: the median, the bounding box: the $25^{th}$ to $75^{th}$ percentiles, the whiskers: extension between the maximum and minimum non-outlier datapoints). Individual patient data points at each timepoint are visualized with jittering for improved visual clarity.

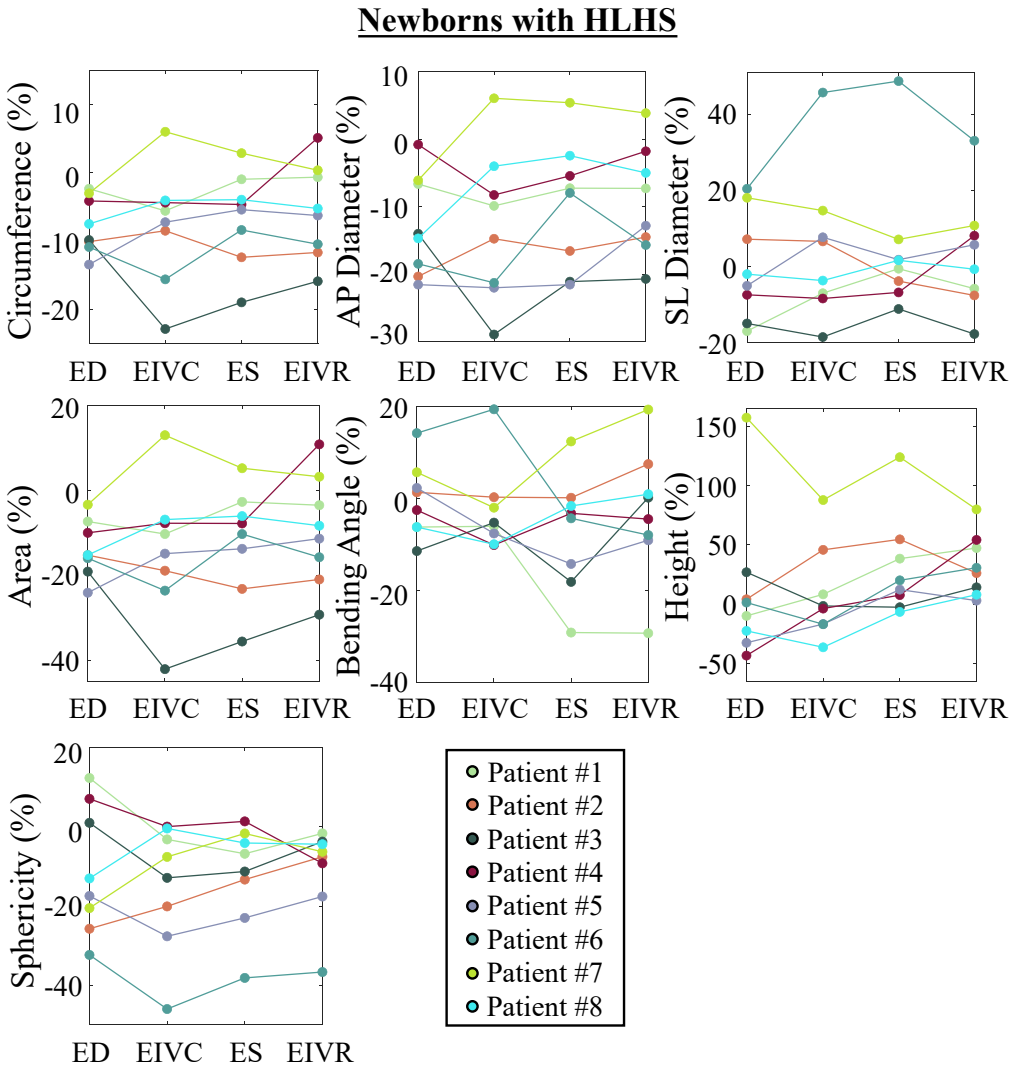


**Figure 5-4** Percentage changes in the TV annulus clinical metrics for the newborns with HLHS ($n = 8$) at the selected timepoints over the cardiac cycle.

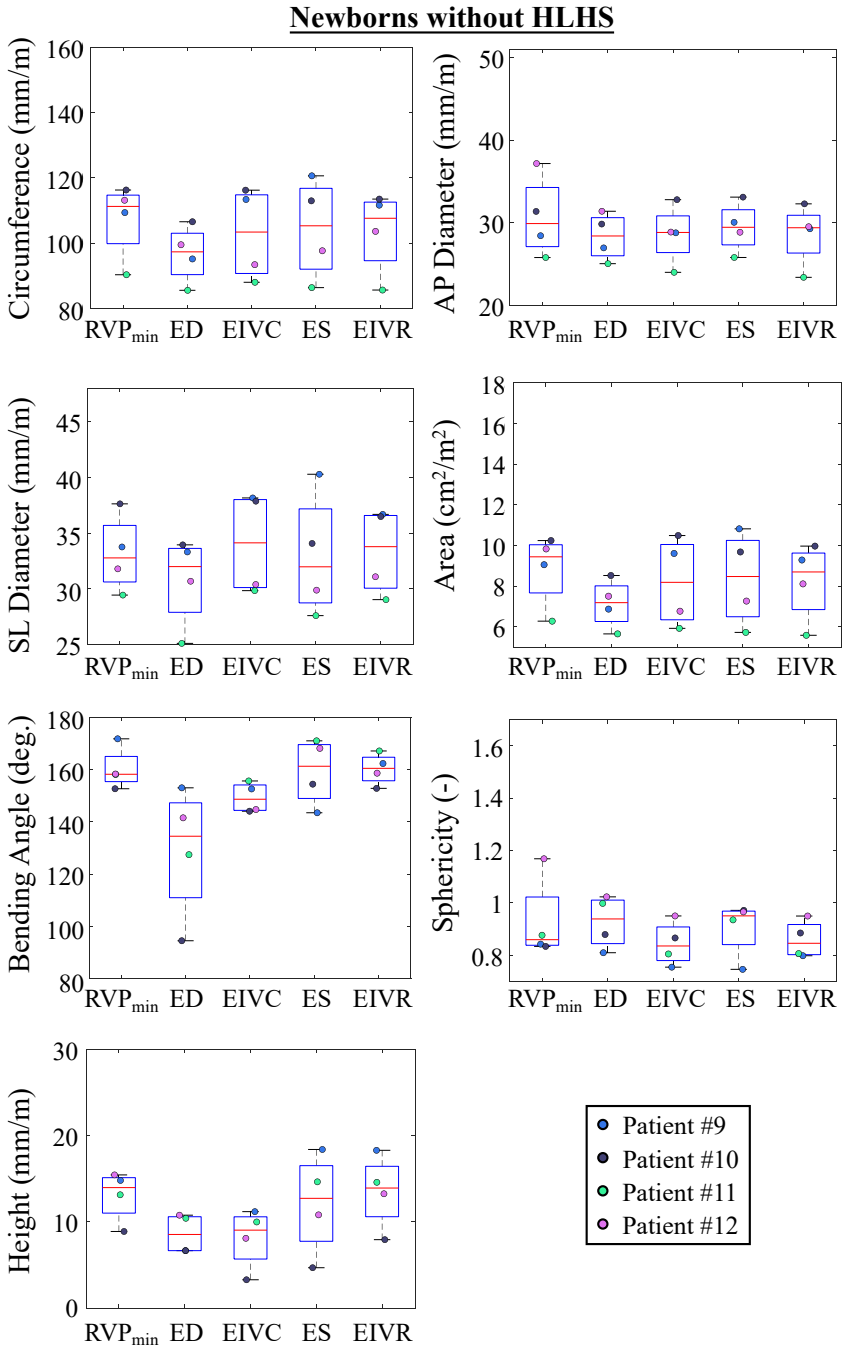


**Figure 5-5** Key TV annulus clinical metrics for all healthy newborns ($n = 4$) at the selected timepoints over the cardiac cycle (solid red line: the median, the bounding box: the $25^{th}$ to $75^{th}$ percentiles, the whiskers: extension between the maximum and minimum non-outlier datapoints). Individual patient data points at each timepoint are visualized with jittering for improved visual clarity.

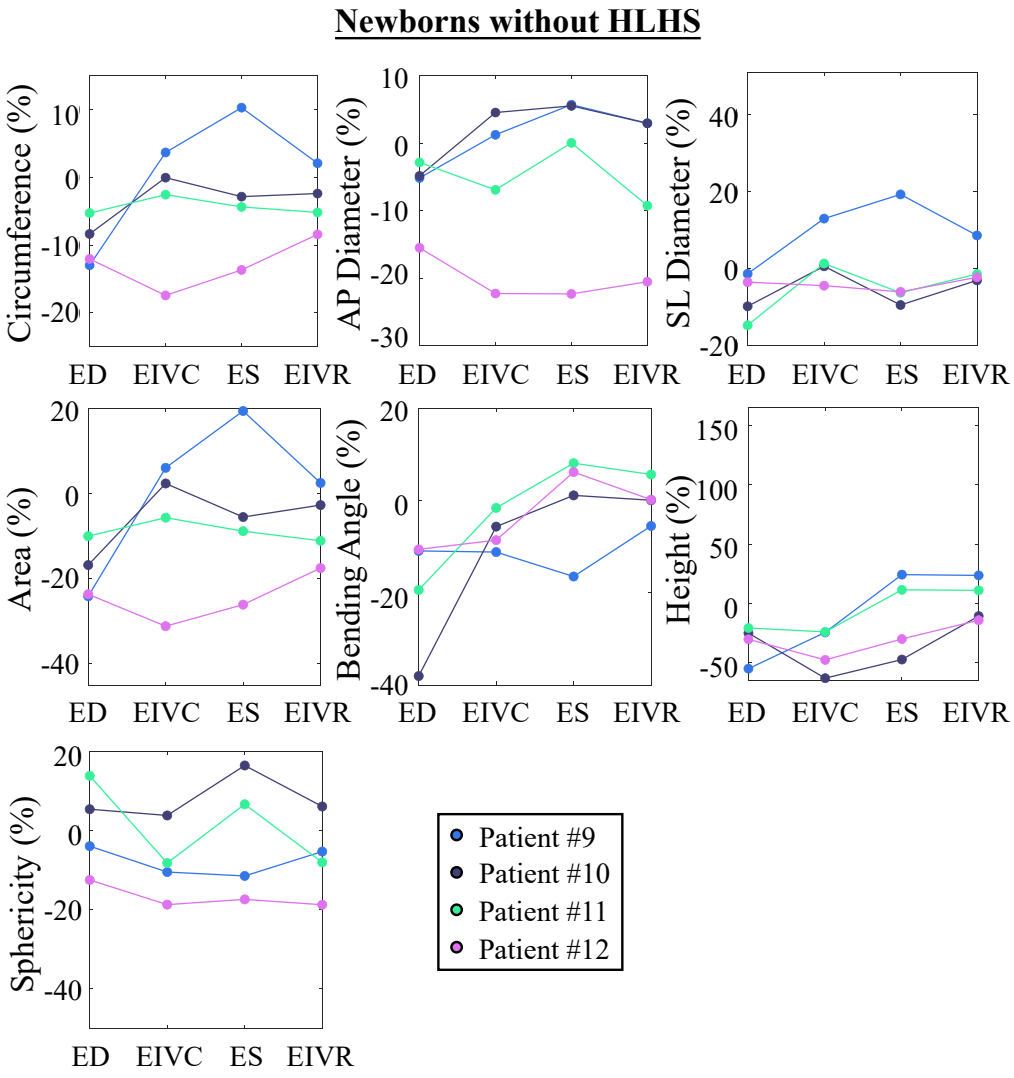


**Figure 5-6** Percentage changes in the TV annulus clinical metrics for the healthy newborns ($n = 4$) at the selected timepoints over the cardiac cycle.

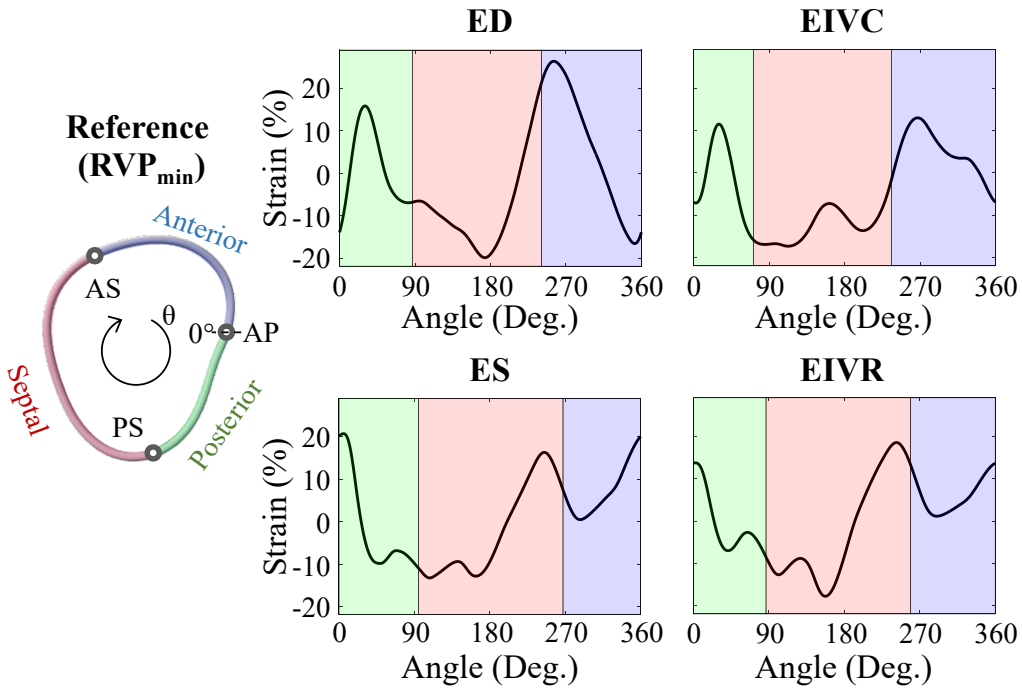


**Figure 5-7** Spatial variations of the computed strain along the TV annulus circumference for a representative HLHS newborn (Patient #1) at the selected timepoints over the cardiac cycle, where the time instant $t_{\mathrm{RVP_{min}}}$ was chosen as the reference configuration. Note that the 0° angle was aligned with the anterior-posterior commissure.

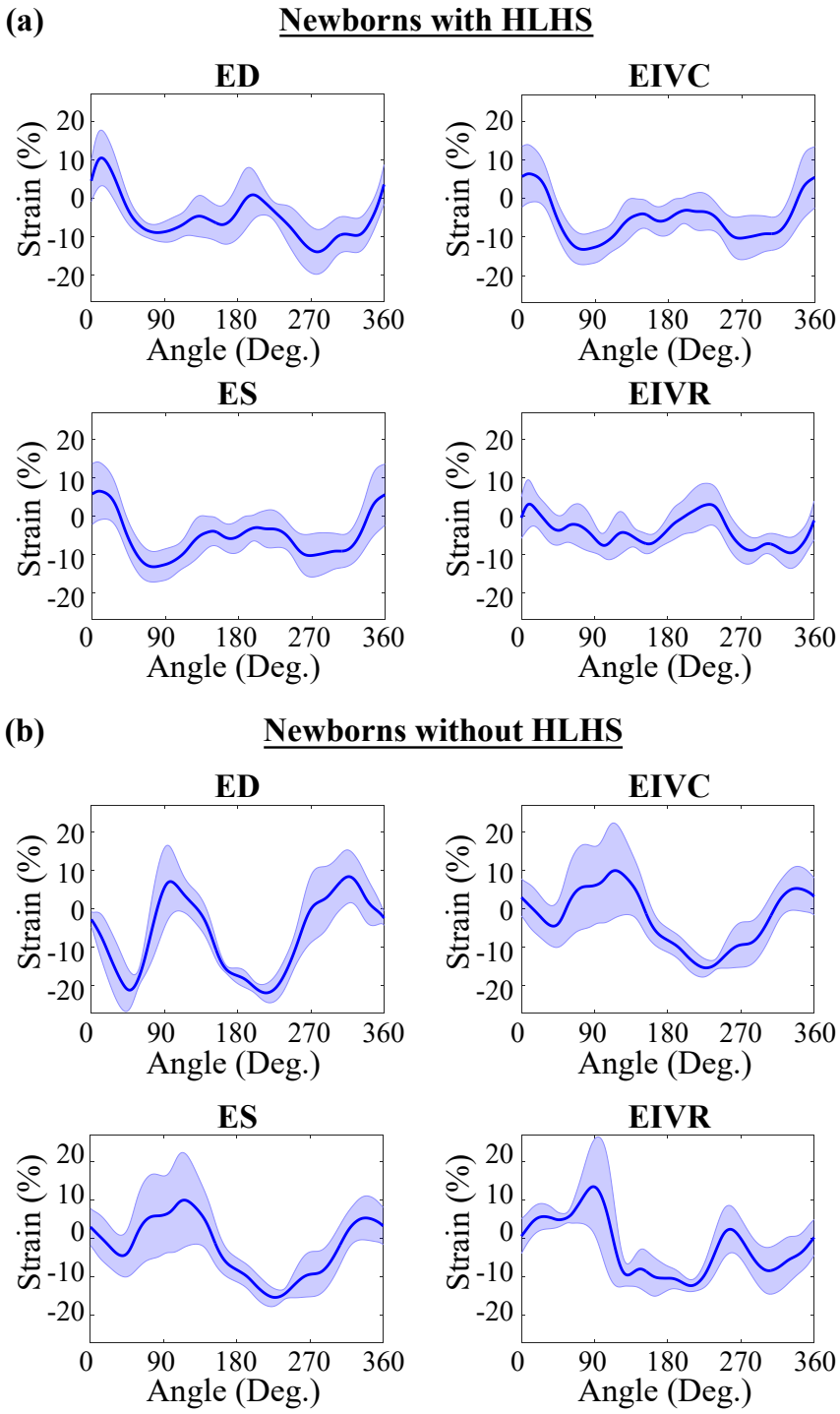


**Figure 5-8** Spatial variations of the computed strain along the TV annulus circumference for (a) the studied eight newborns with HLHS ($n = 8$), and (b) the four healthy newborns ($n = 4$) (solid lines: mean, shaded regions: standard error of the mean). Note that the $0^{\circ}$ angle was aligned with the anterior-posterior commissure.

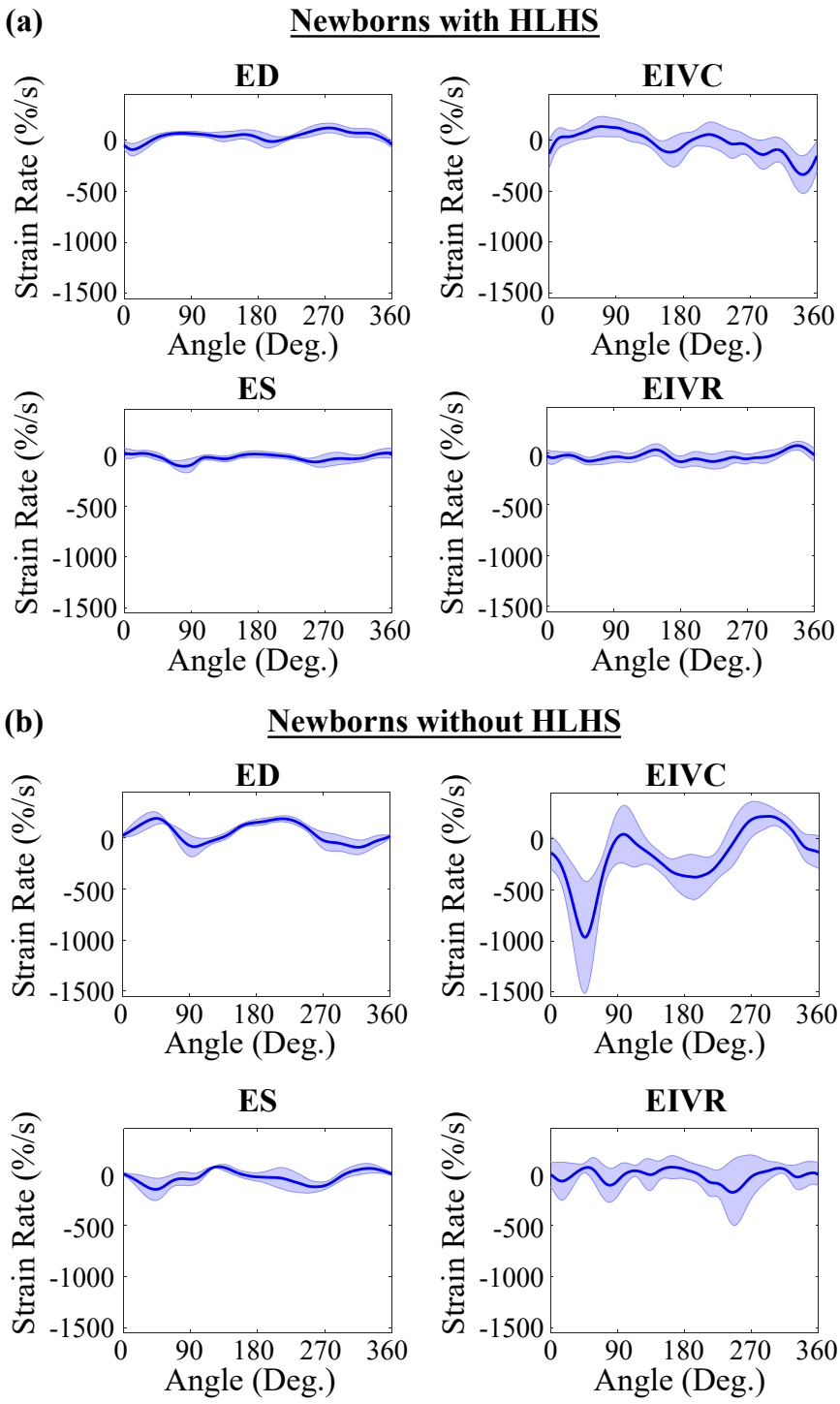


**Figure 5-9** Spatial variations of the computed strain rate along the TV annulus circumference for (a) the studied eight newborns with HLHS ($n = 8$), and (b) the four healthy newborns ($n = 4$) (solid lines: mean, shaded regions: standard error of the mean). Note that the $0^{\circ}$ angle was aligned with the anterior-posterior commissure.

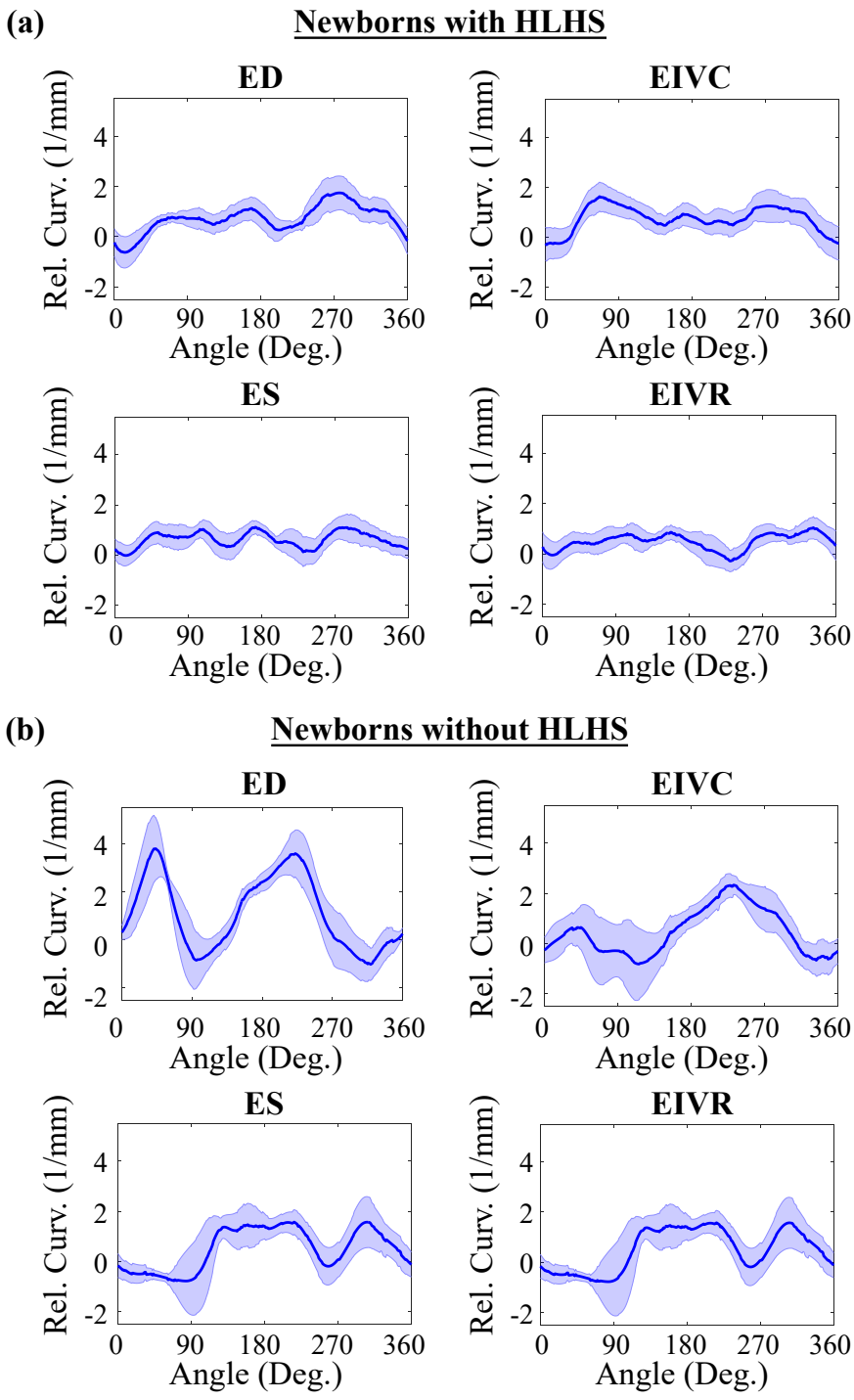


**Figure 5-10** Spatial variations of the computed relative curvature along the TV annulus circumference for (a) the studied eight newborns with HLHS ($n = 8$), and (b) the four healthy newborns ($n = 4$) (solid lines: mean, shaded regions: standard error of the mean). Note that the $0^{\circ}$ angle was aligned with the anterior-posterior commissure.

exhibited an elliptical annulus with the major axis in the $D_{SL}$ direction (i.e., $D_{AP}/D_{SL} < 1$), whereas the patients wIth HLHS had an elliptical annulus at RVP (i.e., $D_{AP}/D_{SL} > 1$) that became more circular during valve closure (i.e., $D_{AP}/D_{SL} \approx 1$).

From the biomechanics standpoint, we did not observe as many significant differences between the HLHS and healthy newborns. For strain, a significant difference was found in the anterior segment (HLHS vs. Healthy): $-0.1 \pm 2.6\%$ vs. $-13.3 \pm 2.9\%$ at ED ($p = 0.010$), and $-1.7 \pm 3.0\%$ vs. $6.8 \pm 0.9\%$ at EIVR ($p = 0.026$). This trend was partially reflected in the larger strain rate of $15\%/s$ at ED for the healthy patients than the newborns with HLHS ($p = 0.011$). For curvature, significant differences were found for the septal segment at EIVC, ES ($p = 0.002$), anterior segment at RVP, ED ($0.008 < p < 0.040$), and posterior segment at EIVC, ED, ES ($0.016 < p < 0.049$).

## 5.4 Discussion

In this study, we presented a novel biomechanics-based framework for the analysis of dynamic valve annuli which we have preliminarily applied to elucidate the TV annular mechanics in HLHS neonates. A complete understanding of the dynamic changes in the TV annulus biomechanics and geometric features will be integral in identifying patient conditions that are related to TR initiation and progression.

### 5.4.1 Comparisons between Healthy and newborns with HLHS

Comparing the HLHS-afflicted and healthy newborns, we observed different annular geometries. Specifically, patients wIth HLHS had a larger circumference, area, and $D_{AP}$ than the healthy cohort, along with different trends in sphericity over the cardiac cycle.

On the other hand, the similarity in annular strain between healthy and patients wIth HLHS could have interesting implications for understanding the remodeling of the TV annulus in this unique congenital condition. For example, the HLHS-afflicted TV may adapt during embryonic developments to maintain similar homeostatic tissue strains as in the healthy (i.e., non-HLHS) scenario. However, future studies are warranted to corroborate this postulation, which could include analyzing in utero echocardiograms of HLHS development. Also, the trends in annular strains could be related to the circumferential strains of the right ventricle, as shown to be similar between healthy and newborns with HLHS [232]. It is worth noting that a previous study indicated that post-Norwood patients wIth HLHS had a

reduced longitudinal strain of the right ventricle compared to the healthy patients, indicating the future development of TR and/or right ventricular dysfunction [233].

### 5.4.2 Development of Tricuspid Regurgitation in newborns with HLHS

Previous investigators shed light on the distinct differences in the TV for newborns with HLHS with and without TR. It has been found that patients wIth HLHS with TR have: (i) a larger annular area, (ii) a lessened change in area during the cardiac cycle (TR, $12\%$ vs. no-TR, $20\%$) [128, 129], (iii) a flatter annulus with a reduced "active bending" ($14^\circ$ vs. $27^\circ$ changes in bending angle, TR vs. no-TR) [128, 135], and (iv) heterogenous annular contractions, whereas in "normal" patients wIth HLHS the contractions are homogenous [127, 128]. While we were unable to enroll any patients wIth HLHS with TR in the present work, we may be able to observe the onset of TV anomalies as we track our patients in a future longitudinal study. For example, Patient #$8$ had smaller changes in the annular area during the cardiac cycle ($3-13\%$) compared to others in the cohort, which may serve as an indicator for potential TR initiation and development.

### 5.4.3 Comparisons to Previous TV Annulus Biomechanics Studies

While we can contextualize our annulus biomechanics findings regarding the previous in vitro animal studies and ex vivo heart pressurization systems, these studies analyze biventricular hearts. Between the biventricular and HLHS-afflicted hearts, the TV has numerous differences: (i) the TV is not designed to function with a circular annulus; (ii) the septal-lateral contraction forces that maintain leaflet coaptation are reduced; and (iii) ventricular dilation can cause papillary muscle shifting and a loss of leaflet coaptation [128]. Considering these differences, we observed strain magnitudes of $\sim 8\%$, on average at each timepoint, which were similar to those reported in other in vivo ovine animal studies using the sonomicrometry technique. For example, Malinowski et al. (2018) incrementally cinched the ovine TV annulus and found annular strains increased from $20\%$ to $40\%$ with increased suturing strengths, whereas another study of the healthy ovine TV annulus observed peak strains of approximately $10\%$ [229, 234]. These findings were similar to another work perfusing ex vivo human hearts to identify peak strains of $\sim 10\%$ [235]. The discrepancy in the observed peak strains may be attributed to the image acquisition methods (i.e., interpolation with $8$ sonocrystal locations vs. $40-45$ segmented locations in the present work), the differences in the ovine and the HLHS-afflicted hearts, or the use of in vivo versus ex vivo experimental methods.

### 5.4.4 Clinical Relevance and Translatability of the TV Annulus Pipeline

The development of this framework lays the foundation for improved patient diagnostics that can be used in refined clinical decisions and surgical planning. Using this pipeline, clinicians can receive the geometric and engineering-based analytics within an hour, demonstrating another benefit of our present work. While we opted to perform manual segmentation, semi-automated or deep learning-based automatic approaches for echocardiogram segmentation of the subvalvular components are a growing field of interest and could further improve the ease of use—a potential future extension [228, 236–238]. With extensions of our TV analysis framework to include the leaflets and ventricle, further information on the unique biomechanics-based indicators can become available for surgical guidance such as the timing of performing valvuloplasty repair.

### 5.4.5 Limitations and Future Extensions

There are a few limitations of the present work. First, we had a limited population size for our pilot investigation, thus our findings are preliminary and should be interpreted in the correct context (i.e., not be applied a larger population). Second, we were unable to identify trends in the development of TR in our HLHS cohort due to the limited available data from our retrospective patient enrollment. Third, there is a potential loss of local landmarks and features in the TV annulus due to the image segmentation technique (i.e., manual point placement or image resolution) or the moving least-squares data fitting and smoothing algorithm. Nonetheless, the circumference changes observed in our study (up to $9\%$ on average) were similar to those reported in the literature [127, 229, 234], ensuring confidence in our analysis technique.

Future work includes investigating the changes in geometry and strains of the TV leaflets and other subvalvular structures, examining right ventricle function, and capturing the longitudinal changes in the TV annulus dynamics in individual patients using follow-up imaging data (e.g., at $8$ weeks vs. $16$ weeks of age, or at Stage II/Stage III palliation) to elucidate the time-evolving indicators of the initiation and progression of TR between the palliation stages. While the present work provides the foundation for understanding the TV annulus in patients wIth HLHS, the occurrence of TR is multifactorial and all subvalvular components can likely contribute to the manifestation of the comorbidity.

## 5.5 Chapter Summary

We have presented a comprehensive patient-specific TV annulus analysis pipeline that is capable of quantifying both the biomechanical and geometric indices, including annular tissue strains from the 4D echocardiograms. We found that newborns with HLHS had annular strains of $8\%$, on average, and a more circular annulus during the heart valve contraction. Additionally, the HLHS annulus was significantly larger than the healthy one, while maintaining similar strains. Application of these techniques to a larger patient cohort in future studies may inform the optimal timing and selection of TV surgical intervention for the challenging HLHS population.

# 6 INVERSE FINITE ELEMENT ANALYSIS OF NONLINEAR MATERIALS USING BAYESIAN OPTIMIZATION FOR APPLICATIONS IN ATRIOVENTRICULAR HEART VALVE SIMULATION


6.1 Motivation . . . 116
6.2 Inverse Finite Element Analysis Approach . . . 116
6.2.1 Objective Function . . . 116
6.2.2 Overview of Bayesian Optimization . . . 117
6.2.3 Implementation of Bayesian Optimization . . . 119
6.2.4 Analysis of Optimization Results . . . 119
6.2.5 Material Modeling . . . 119
6.2.6 Simulation Conditions . . . 120
6.3 Inflation Testing . . . 120
6.3.1 Inflation Simulation Sub-Studies . . . 122
6.4 Leaflet Contact . . . 124
6.4.1 A Novel Approach for iFEA of Leaflet Contact . . . 127
6.5 Idealized Valve Geometry . . . 129
6.5.1 Real Application: Analysis with a Representative Patient with HLHS . . . 129
6.6 Discussion . . . 134
6.6.1 Bayesian Optimization . . . 134
6.6.2 Novel Approach to Inverse Analysis of the Atrioventricular Heart Valves . . . 135
6.6.3 Limitations . . . 136
6.7 Chapter Summary . . . 136

## 6.1 Motivation

To date, the properties of the atrioventricular heart valve leaflets have not been determined *in vivo*, with the exception of the sonocrystal-based animal studies. The translation of iFEA for use with medical imaging data faces many hurdles, including high computational costs associated with simulating leaflet self-contact, difficulties in reconstructing the valve geometry due to limitations in imaging resolution (e.g., chordae are typically too thin to be seen in echocardiograms), and the existence of non-unique solutions limiting the potential use of iFEA-derived material parameters for subsequent simulations of potential treatments. While addressing all of these challenges is well beyond the scope of a single study, in this work, we aim to provide methods useful for progressing iFEA towards clinical translation. Specifically, we propose the use of Bayesian optimization (BO), a derivative-free inverse analysis method, as an efficient method to keep the iFEA computation within a reasonable time. The primary investigations include: (i) an analysis of the residual search space using a synthetic (i.e., user-made) solution; (ii) verification of the BO method using the synthetic solution; and (iii) an application of the BO-iFEA framework to real patient data using echocardiograms from a newborn with hypoplastic left heart syndrome.

## 6.2 Inverse Finite Element Analysis Approach

Three test cases are used: an inflation test, a valve closing considering only the central regions of two leaflets, and an idealized heart valve geometry for iFEA of the full valve closing. Then, we use the BO-iFEA for a patient-specific tricuspid valve geometry to recreate the echocardiogram-derived leaflet surface at the valve closing. For each sub-study, we will present the objective function surface and test the use of Bayesian optimization (BO).

### 6.2.1 Objective Function

Commonly, the goal in medical imaging-based iFEA is to match the shape of the deformed organ between the simulation and the ground truth surface (e.g., image segmentation point cloud data). To this end, we defined the objective function as the minimization of the bidirectional local distance (B-LD) between the element centroids and the comparison point cloud [239]. An overview of the algorithm in the context of the iFEA problem is provided in **Algorithm 1**.

**Algorithm 1** The general algorithm for calculating the bidirectional local distance (B-LD)

Calculate the forward minimum Euclidean distance ($d_{\text{forward,min}}$) from the $i^{th}$ point on the finite element surface $p_{\text{fe},i}$ to all points in the comparison point cloud, $p_{\text{ptc}}$

Calculate the backward minimum Euclidean distance ($d_{backward,min}$) between each $p_{\text{ptc}}$ and all the points on the the finite element surface

Select the $p_{\text{ptc}}$ where $d_{\text{backward,min}}$ is at the current finite element point $p_{\text{fe},i}$

Determine the backward maximum Euclidean distance $d_{\text{backward,max}}$ from the set of identified $p_{\text{ptc}}$.

**if** $d_{\text{forward,min}} > d_{\text{backward,max}}$ **then**

$d_{\text{B-LD},i} = d_{\text{forward,min}}$

**else**

$d_{\text{B-LD},i} = d_{\text{backward,max}}$

**end if**

The B-LD procedure is performed over $i$=1,...,$n$ finite element centroids, with the final objective function value determined as $\mathcal{F}$=$\sum_{i=1}^{n} d_{\text{B-LD},i}$.

### 6.2.2 Overview of Bayesian Optimization

The BO algorithm can be described using the pseudo-code in **Algorithm 2**.

**Algorithm 2** The general algorithm for Bayesian Optimization

Generate a Gaussian prior on the objective function $f(y)$

**while** $i \leq i_{\text{max}}$ or residual $\mathcal{F}_i \leq \mathcal{F}_{\text{threshold}}$ **do**

Select the point $y_i$ such that the acquisition function is maximized

Evaluate $f(y_i)$

Update the posterior probability distribution using observed $f(y_{1:n})$

**end while**

In the BO method the objective function is treated as a "black box" that is fitted with a distribution, which is generally a Gaussian process (GP). [240] First, a prior distribution is created in a generic form for the points ($y$),

$$f(y) \sim N(\mu_0(y), \sigma_0(y)), \tag{6.2-1}$$

where $N$ is the normal (Gaussian) distribution with mean function $\mu_0$ (usually a constant) and covariance function $\sigma_0$ (e.g., the Gaussian kernel). Then, with progressive iterations of the BO solver, we can use the collected data points $y_{1:n}$ with corresponding function values $f(y_{1:n})$ to determine the posterior probability distribution for a prospective point $y_i$ using Bayes' rule:

$$\begin{aligned} &f(y_i)|f(y_{1:n}) \sim N(\mu_n(y_i), \sigma_n(y_i)) \\ &\mu_n(y_i) = \sigma_0(y_i, y_{1:n})\sigma_0(y_{1:n}, y_{1:n})^{-1}(f(y_{1:n}) - \mu_0(y_{1:n})) + \mu_0(y_i) \\ &\sigma_n(y_i) = \sigma_0(y_i, y_i) - \sigma_0(y_i, y_{1:n})\sigma_0(y_{1:n}, y_{1:n})^{-1}\sigma_0(y_{1:n}, y_i). \end{aligned} \tag{6.2-2}$$

At each iteration of the BO routine, the point to be evaluated is determined using an acquisition function that utilizes the GP. Perhaps the most popular acquisition function for BO is the Expected Improvement ($EI$) function, where the value of the prospective points are determined based on the potential improvement of $f(y)$. In a simplified mathematical description, this utility function can be described as:

$$u(y) = \max(f(y_{1:n}) - f(y_i), 0), \tag{6.2-3}$$

where a prospective point is assigned a value of zero if it does not improve $f(y_{1:n})$. The expected utility can then be written as:

$$EI(y) = \begin{cases} (\mu_n(y_{1:n}) - f(y^*) - \xi)\Phi Z + \sigma_n(y_{1:n})\phi Z & \text{if } \sigma_n(y_{1:n}) > 0 \\ 0 & \text{otherwise} \end{cases}, \tag{6.2-4}$$

where $f(y^*)$ is the current optimal observed point, $\xi$ is a tunable hyperparameter to balance exploitation (first summation term) and exploration (second summation term), $\Phi$ and $\phi$ are the cumulative and probability density functions of the GP, respectively, and $Z$ is defined as:

$$Z = \begin{cases} \dfrac{\mu_n(y_{1:n}) - f(y^*) - \xi)}{\sigma_n(y_{1:n})} & \text{if } \sigma_n(y_{1:n}) > 0 \\ 0 & \text{otherwise} \end{cases}. \tag{6.2-5}$$

### 6.2.3 Implementation of Bayesian Optimization

The BO algorithm was implemented using the bayesopt function of MATLAB, with the corresponding acquisition function expected-improvement. In the $EI$ function, the amount of exploration versus exploitation of the solution search space can be tuned using the exploration ratio hyper-parameter, $\xi$, where $\xi$=0.5 represents equal weighting between the search preferences. For our investigations, we used $\xi$ =0.5 based on our findings from an intermediate study and verification of the BO routine, which can be found in **Appendix B**. The Bayesian optimization for all test cases was performed in parallel (Intel Xeon Gold 6136 CPU at 3.00GHz) with the terminating condition of 100 maximum iterations. The number of iterations was chosen to keep computations <1 day, which may be a more clinically desirable feature.

### 6.2.4 Analysis of Optimization Results

Biomechanics-focused iFEA is traditionally performed to find the optimal set of material properties that can describe the mechanical behaviors of the soft tissues being analyzed. In our case analyzing the heart valve leaflets, however, it is likely that without additional information, such as the patient-specific leaflet microstructure, the solution may be non-unique [80, 81]. In the interest of understanding the "uniqueness" of the solution obtained from BO, we propose reporting the median and interquartile range (IQR) of the optimized parameters corresponding to the 95$^{\text{th}}$ percentile of all evaluated $\mathcal{F}$. Using this method of presenting the results, we can determine if a solution is non-unique based upon the IQR — if the IQR is found to be relatively large, it may represent a non-unique solution or a poorly posed optimization problem (e.g., insufficient iterations to explore the search space, many local minima, etc.).

### 6.2.5 Material Modeling

#### Isotropic Lee-Sacks Model

To model the mechanical behaviors of the tricuspid valve (TV) leaflets, we used the Lee-Sacks model. [81] This exponential-type model was selected based on previous studies, and for the use of a two-parameter problem that can be easily visualized using contour surfaces. Specifically, we adopted a modified isotropic Lee-Sacks model, with the strain

energy density form:

$$\psi_{\text{leaflet}} = \begin{cases} \frac{c_0}{2}(I_1-3)+\frac{c_1}{2}(e^{c_2(I_1-3)^2}-1)-\frac{p}{2}(J-1), & \text{if } |I_1-3| \leq (I_1^{\text{ub}}-3) \\ \frac{c_0}{2}(I_1^{\text{ub}}-3)+\frac{c_1}{2}(e^{c_2(I_1^{\text{ub}}-3)^2}-1)-\frac{p}{2}(J-1), & \text{otherwise} \end{cases} \tag{6.2-6}$$

where $c_0$, $c_1$ and $c_2$ are the material parameters, $I_1$ is the first invariant of the right Cauchy-Green tensor ($\mathbf{C} = \mathbf{F}^T\mathbf{F}$, where $\mathbf{F}$ is the deformation gradient), and $p$ is a penalty parameter to enforce the incompressiblity condition (i.e., $J = \det(\mathbf{F}) = 1$). For this hybrid model, the upper bound $(I_1^{\text{ub}} - 3)$ is used to stabilize the material model at non-physiologic stresses ($\geq 1.0$ MPa). For the material parameters, $c_0$ was set as 10 kPa, whereas $c_1$ and $c_2$ were determined from the BO.

#### Chordae Tendineae Model

In the simulation cases involving chordae tendineae, we used a hyperelastic form [81]:

$$\psi_{\text{chordae}} = c_{10}(e^{c_{01}E_{11}}-1), \tag{6.2-7}$$

where $c_{10} = 0.209$ kPa, $c_{01} = 11.65$, and $E_{11} = (1/2)(F_{11}^2 - 1)$ is the Green-Lagrange strain of the chordae.

### 6.2.6 Simulation Conditions

All simulations were performed using ABAQUS Explicit dynamics with a total simulation time of $0.4$ s, a maximum time step of $1 \times 10^{-6}$ s, and adaptive time-stepping.

## 6.3 Inflation Testing

For the inflation test, we generated a $2 \times 2$ mm square geometry with a curvature of 7° that was discretized into 625 equally sized four-node shell elements (S4 in ABAQUS) (**Fig. 6-1(a)**). The nodes on the outside edges of the geometry were pinned while a pressure equivalent to 120 mmHg (i.e., 16 kPa) was applied to the top surface to ensure a large displacement (maximum displacement of $0.45$ mm) of the material. A synthetic solution was then constructed with the arbitrarily selected model parameters $c_1 = 0.209$ kPa and $c_2 = 11.65$. The comparison point cloud for the objective function calculation was then considered as

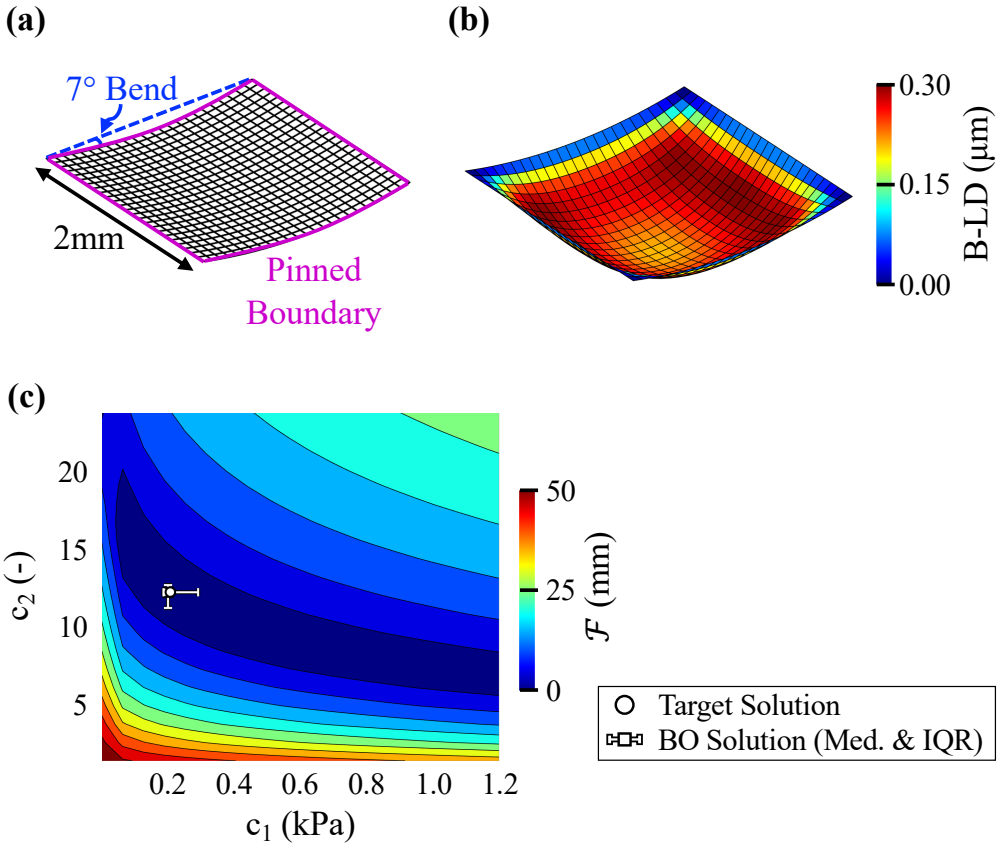


**Figure 6-1** (a) The geometry of the inflation test. (b) Bidirectional local distance (B-LD) errors for each element of the optimal solution. (c) Contour plot of the objective function and the median (Med.) and interquartile range (IQR) of the top 5% of evaluated BO solutions.

the locations of the element centroids at the final deformed configuration of the synthetic solution.

First, we performed a grid search of the objective function space for the synthetic inflation test over a linearly spaced $20 \times 20$ grid within the boundaries $c_1 \in [0.00209, 1.2]$ kPa and $c_2 \in [1.0, 23.0]$. The objective function values (i.e., the residuals) were then used to generate a contour plot for visualization of the parameter search space. In addition, BO was performed within the grid search domain using the settings described in Section 6.2.3.

The error surface for the optimum BO solution is shown in **Fig. 6-1(b)**, while the contour surface with the median and IQR of the top 5% of evaluated BO solutions is shown in **Fig. 6-1(c)**. From the grid search of the baseline inflation test, we found a valley-shaped surface in the objective function, as is expected with exponential-type material models (**Fig. 6-**

**1(c)**) [80]. This valley-shaped function caused minor errors in the final solution from the BO ($\mathcal{F} = 0.22\ [0.17, 0.27]$ mm); however, a larger spread of parameter values was found for the top $5\%$ of BO-evaluated points ($c_1 = 0.202\ [0.188, 0.292]$ kPa, $c_2 = 11.65\ [10.65, 12.10]$). The minimum observed objective function value occurred at iteration 42/100. Interestingly, we also found that the BO routine reconstructed the shape of the valley in the objective function surface.

### 6.3.1 Inflation Simulation Sub-Studies

We also sought to understand the influence of segmentation errors (i.e., noise) and modeling assumptions on the objective surface and optimization convergence.

#### Effects of Noise in the Solution

We generated artificial noise for the synthetic solution of the inflation test by adding randomly sampled values from a Gaussian (normal) distribution to the Cartesian coordinates of the final deformed mesh [241]. The noise-adjusted element centroid locations then served as the comparison point cloud. A range of noise levels were tested using Gaussian distributions with a mean of zero and standard deviations of $0.005$, $0.01$, $0.02$ and $0.03$ mm. We also performed BO for the scenario with a standard deviation noise level of $0.02$ mm.

Testing the effects of additive noise in the inflation test comparison point cloud, we found that an increase in the additive noise (i.e, a larger standard deviation) resulted in a widening of the valley of nearly equivalent solutions (**Fig. 6-2**). The objective function values associated with the synthetic solution at each noise level, in increasing order, were found as $2.28$ mm, $4.78$ mm, $9.03$ mm, and $13.9$ mm. The widening of the valley of nearly equivalent solutions also caused a wider spread of parameter values in the Bayesian optimization performed at the $0.02$ mm noise level ($c_1 = 0.241\ [0.160, 0.498]$ kPa and $c_2 = 11.21\ [9.27, 12.91]$) than in the case without additive noise, however, the range of objective function values were smaller ($\mathcal{F} = 18.20\ [18.20, 18.23]$).

#### Additional Test Cases for Typical Modeling Assumptions

Common atrioventricular heart valve simulation assumptions include prescribing a spatially homogeneous leaflet thickness [242], and spatially homogeneous leaflet material properties [243]. To test the former assumption, we constructed a synthetic solution containing regionally varying thicknesses in the range $[0.1, 0.4]$ mm (**Fig. 6-3(a)**) and gener-

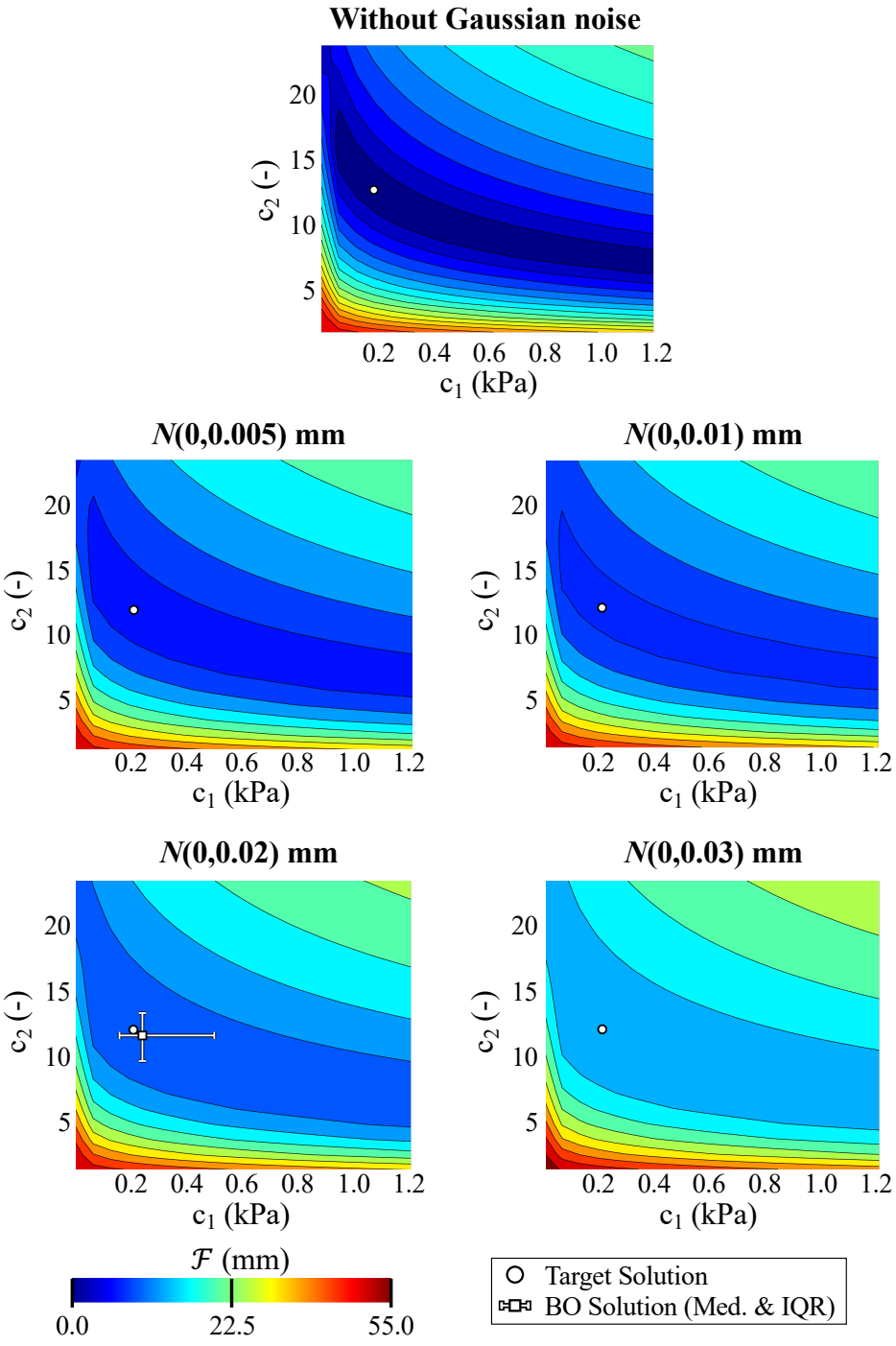


**Figure 6-2** Contour plots and finite element meshes of the objective function surfaces considering different amounts of noise generated by a Gaussian function ($N$). Note that the contour surface from **Fig. 6-1** is repeated here with adjusted bounds on the colormap for easier comparisons. The BO solution is shown for the case of $N(0,0,02)$ mm.

ated a contour surface (**Fig. 6-3(b)**). For the latter assumption, the synthetic solution was constructed by random sampling of material parameter combinations within the ranges $c_1 \in [0.109, 0.309]$ kPa and $c_2 \in [10.65, 12.65]$ (**Fig. 6-3(c)**) and visualized the corresponding errors (**Fig. 6-3(d)**). This range was chosen based on our biaxial testing study of the regional mechanical properties of the tricuspid valve anterior leaflet where we found minimal spatial variations in the stress-stretch behaviors [27].

For the case where the synthetic solution contained regionally varying thicknesses, we found the valley of nearly equivalent solutions to shift towards smaller values of $c_1$ and $c_2$, however the general shape of the valley was not noticeably different (**Fig. 6-3(b)**). This finding suggests that assuming a spatially homogeneous thickness would not significantly affect iFEA. Meanwhile, we observed the opposite trend in the case where the material parameters are heterogeneous in the synthetic solution, with a large shift of the location of the global minima region towards larger values of $c_1$ and $c_2$ (**Fig. 6-3(d)**).

## 6.4 Leaflet Contact

For the next test scenario, we generated a simplified model of the valve closing that only considers the contact between the central regions of two leaflets [244]. By removing the commissural regions from the simulation, we reduce the computational expense of each simulation (i.e., no self-contact) and remove potential problem complexity due to the buckling and folding behaviors of the leaflets in the commissures.

The geometry was constructed as two curved, rectangular geometries, each consisting of 576 four-node shell elements (**Fig.6-4(a)**). To emulate the *in vivo* measurements of the tricuspid valve, the "leaflet" heights and widths were $38$ mm, and $12.7$ mm, respectively, with a leaflet separation distance of $39$ mm [245]. Also, six free edge chordae tendineae were equally spaced around each of the leaflet perimeters stemming $39$ mm from the model origin. The boundary conditions included: (i) pinning the top edge of each leaflet; (ii) applying a pressure of $25$ mmHg to the outside (i.e., "ventricular") surface; and (iii) applying a viscous damping pressure of $5 \times 10^{-6}$ MPa to the inside (i.e., "atrial") surface (**Fig.6-4(b)**). In this sub-study, a $20 \times 20$ grid search and a Bayesian optimization was performed within the domain: $c_1 \in [0.00209, 1.2]$ kPa and $c_2 \in [1.0, 23.0]$.

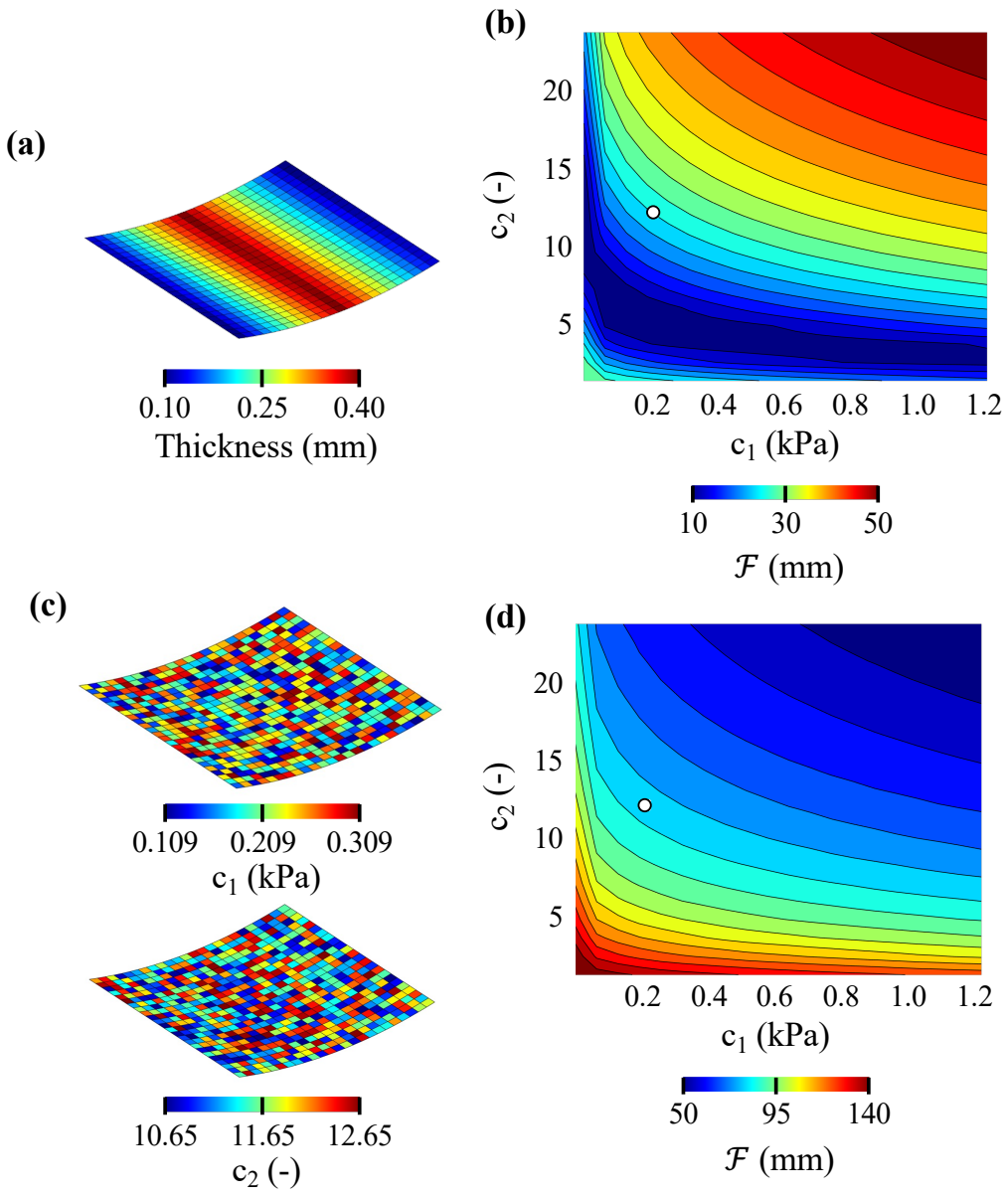


**Figure 6-3** (a) Map of the prescribed regionally varying thicknesses and (b) the corresponding contour surface. (c) The prescribed regionally varying material properties and (d) the corresponding contour surface.

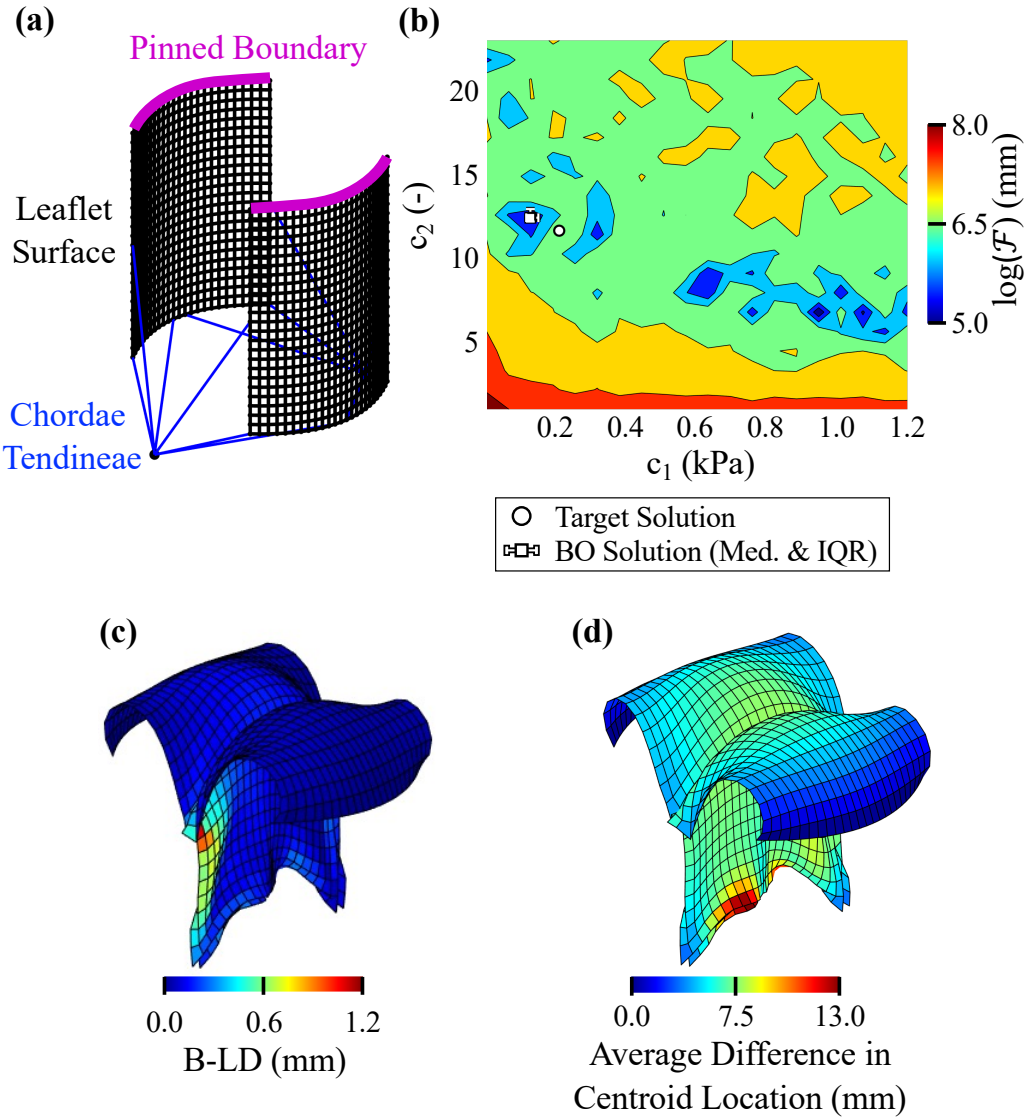


**Figure 6-4** (a) The simplified leaflet contact model. (b) The contour plot of the objective function surface and the median (Med.) and interquartile range (IQR) of the top 5% of evaluated BO solutions. (c) The element-wise bidirectional local distance (B-LD) error measurements for the optimal BO solution. (d) The variations in element centroid locations across the 20 $\times$ 20 grid points.

We found that the objective function was non-smooth (variations of $0 \leq \mathcal{F} \leq 1000\,\text{mm}$) for the leaflet contact scenario (**Fig.6-4(c)**). Despite the non-smooth objective function, the Bayesian optimization retrieved a solution with relatively small error of $237.9\ [211.3, 246.6]\,\text{mm}$ (i.e., average error per element of $0.21\ [0.18, 0.22]\,\text{mm}$). However, the optimized values were found as $c_1 = 0.127\ [0.115, 0.150]\,\text{kPa}$ and $c_2 = 12.43\ [12.19, 12.94]$, and the BO was not able to reconstruct the desired synthetic solution. The variations in the valve closing behaviors with different prescribed model parameters inspired our alternative approach (**Fig. 6-4(d)**).

### 6.4.1 A Novel Approach for iFEA of Leaflet Contact

In an effort to improve optimization performance, we performed a *novel modification* to the iFEA approach for the atrioventricular heart valve leaflets that does not consider the chordae attachments. Instead, a displacement boundary condition is prescribed to the leaflet free edges. This approach has a clinically relevant benefit—the chordae tendineae can not typically be segmented in lower-resolution imaging methodologies, such as echocardiography, and the assumptions regarding chordae topologies or material properties can be avoided.

To test this new approach, we performed a three-step procedure: (i) a forward simulation for the leaflet contact model of known properties in **Section 6.4**; (ii) extraction of the time-varying locations of the leaflet free edge nodes from the synthetic solution; and (iii) generation of a new leaflet contact model *with no chordae attachments*, and the time-varying displacement boundary condition applied to the leaflet nodes at the free edge for use with the BO (**Fig. 6-5(a)**). A $20 \times 20$ grid search and a Bayesian optimization was performed within the search space $c_1 \in [0.00209, 1.2]\,\text{kPa}$ and $c_2 \in [1.0, 23.0]$.

Using the "guided free-edge" approach, we found a smooth, valley-shaped contour surface (**Fig. 6-5(b)**), and minimal errors in the finite element surface (exempting buckling variations at the free edge, **Fig. 6-5(c)**). This more favorable shape of the objective surface resulted in a lower residual value for the optimized Bayesian solution compared to the *in vivo*-emulating model: $\mathcal{F} = 91.1\ [83.6, 93.9]\,\text{mm}$; $c_1 = 0.541\ [0.395, 0.674]\,\text{kPa}$; $c_2 = 8.97\ [8.74, 10.21]$. While the optimized parameter ranges do not contain the synthetic solution, the $61.7\%$ decrease in the objective function value demonstrates the advantage of the revised simulation approach. Additionally, the optimal solution was obtained at iteration $24/100$ in the revised leaflet contact approach, as opposed to iteration $90/100$ in the *in vivo*-emulating approach.

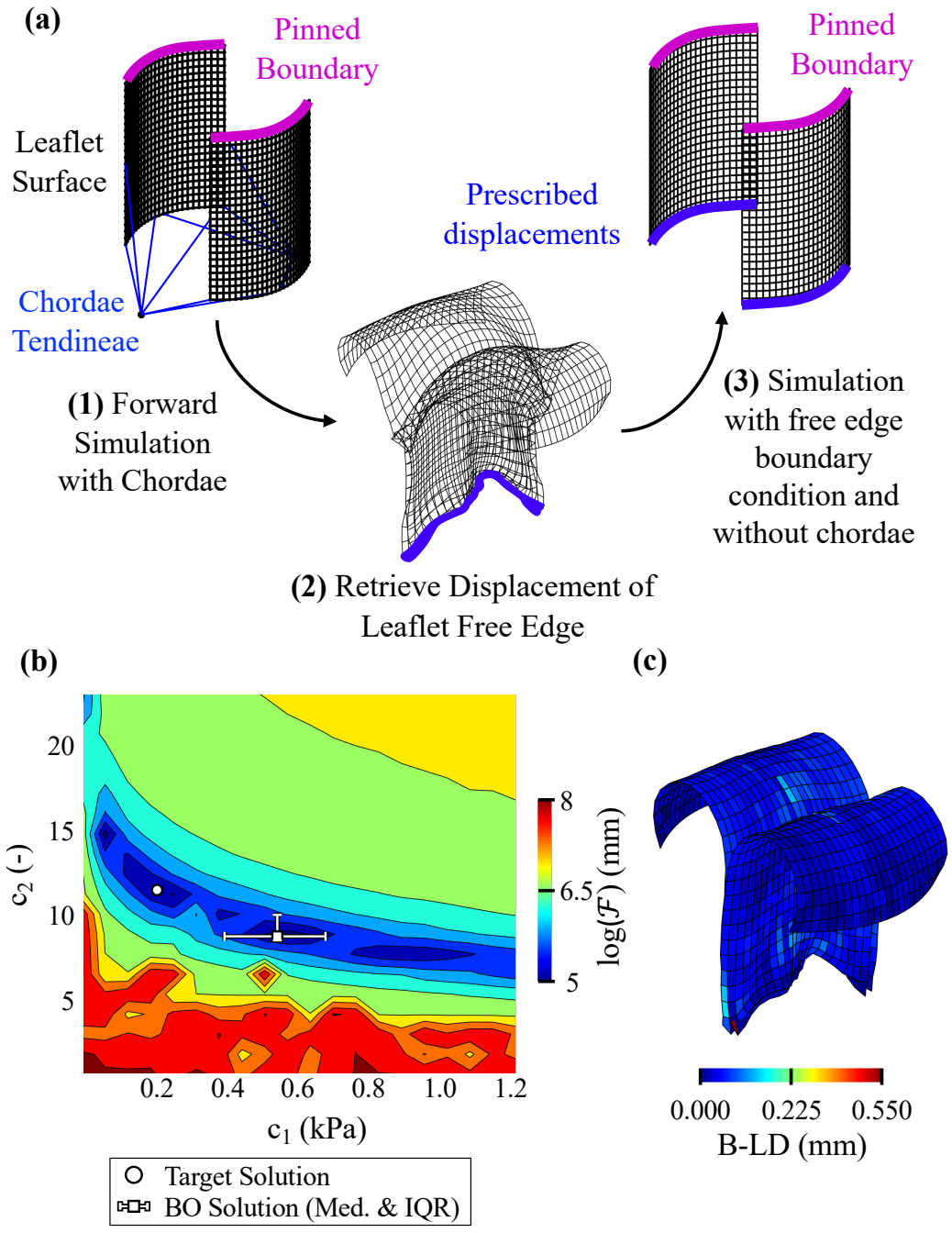


**Figure 6-5** (a) The process for developing the leaflet contact optimization test cases with prescribed leaflet free edge displacements. (b) The contour surface of the objective function when using free-edge leaflet displacements and the median (Med.) and interquartile range (IQR) of the top 5% of evaluated BO solutions. (c) The bidirectional local distance (B-LD) measures for each element of the optimal solution.

## 6.5 Idealized Valve Geometry

For the idealized TV simulation, we used a cylinder-shaped geometry with an elliptical annulus (major diameter, 15 mm; minor diameter, 10 mm), and leaflet and commissure heights of 20 mm and 13 mm, respectively. Briefly, the leaflet free edge contour was generated using a smoothing cubic spline fitted to points generated below the annulus curve at the desired leaflet-to-free edge distances. Then, the annulus and leaflet contours were subdivided circumferentially into $55$ evenly spaced points, and the mesh was constructed, composed of $770$ four-node shell elements with thickness values of $0.4$ mm. The boundary conditions for the model were as follows: (i) a smooth-stepped transvalvular pressure gradient of $25$ mmHg was applied to the ventricular surface of the leaflets over $0.005$ s (simulation time, total simulation duration of $0.4$ s); and (ii) the self-contact of the leaflets was facilitated using the general algorithm in ABAQUS, with a contact penalty stiffness of $0.5$.

For the synthetic solution, we followed the same procedure as in **Section 6.4.1**, where the forward simulation had a simple chordae geometry with papillary muscle tips located below each commissure, and two, single-strand free edge chordae per group. The leaflet free edge displacements were similarly retrieved from the synthetic solution (i.e., material parameters of $c_1 = 0.209$ kPa and $c_2 = 11.65$) (**Fig. 6-6(a)**,**(b)**). Then, a valve model *without chordae* and using the leaflet free edge displacement condition was generated for the $20 \times 20$ grid search and Bayesian optimization within $c_1 \in [0.00209, 1.2]$ kPa and $c_2 \in [1, 23]$.

From the analysis of an idealized TV, we found the presence of a wider and less smooth, valley of nearly equivalent solutions in the objective function surface (**Fig. 6-6(b)**), and the largest element-wise errors in the commissural regions (**Fig. 6-6(c)**). Of specific interest, we found 3 parameter sets that resulted in unstable simulations and the inability to obtain a residual value. From the BO, we found a large range of parameters in the top $5\%$ of evaluated solutions, with a small range of residual values: $c_1 = 1.143$ $[0.660, 1.163]$ kPa; $c_2 = 6.36$ $[5.93, 7.98]$; $\mathcal{F} = 172.4$ $[165.6, 177.6]$ mm. The wide IQR for the parameters is likely caused by the wider shape of the valley, and the variations in tissue folding behaviors in the commissure regions.

### 6.5.1 Real Application: Analysis with a Representative Patient with HLHS

Finally, we analyzed a patient-specific TV geometry obtained from an echocardiogram. In this section, we perform two sub-studies using the patient-specific valve geometry: (i) opti-

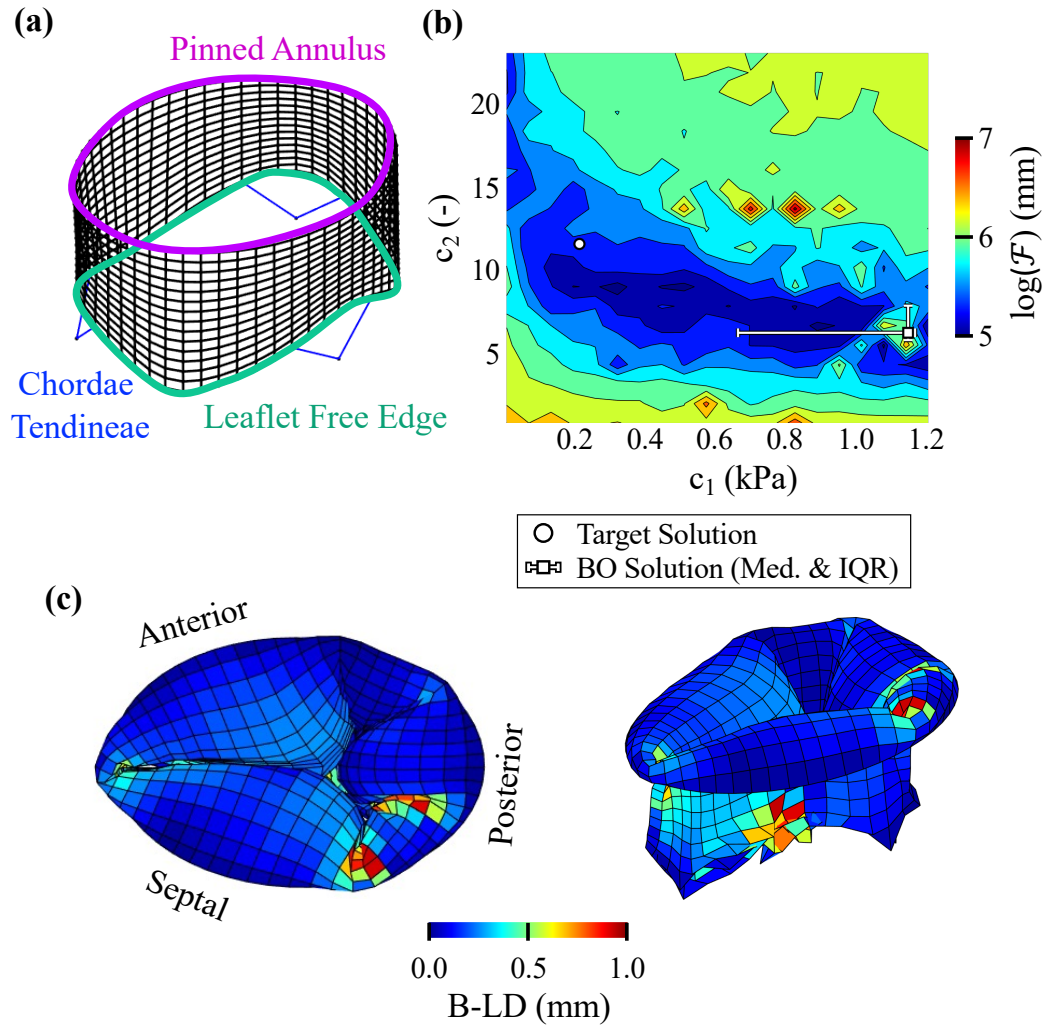


**Figure 6-6** (a) The valve model used in the forward simulation of the target solution. (b) The contour surface of the objective function and the median (Med.) and interquartile range (IQR) of the top 5% of evaluated BO solutions. (c) Bidirectional local distance (B-LD) measures of each element of the optimal solution (superior view, left; isometric view, right).

mization of a 6-parameter, i.e., 6D, problem with a user-prescribed target solution (*synthetic solution*); and (ii) optimization of a 6-parameter problem using the real echocardiogram-derived leaflet point cloud segmentation to recreate the true *in vivo* deformed tricuspid valve surface (*true solution*). In the 6-dimensional (6D) problem, each leaflet has a unique set of $c_1$ and $c_2$, resulting in six parameters to be optimized.

For the valve geometry, 4D echocardiographic imaging data was imported to segmentation software for retrieval of the TV annulus and the free edge at all available imaging time points between the open and closed valve configurations (right ventricular minimum volume and end diastole, respectively) (**Fig. 6-7(a)**). The annulus and leaflet free edge point clouds were fit with a smoothing spline, and the mesh was constructed by linear interpolation between the two contours at the open valve state, resulting in 980 shell elements (**Fig. 6-7(b)**). The three TV leaflets were individually identified based on the commissure locations obtained from the echocardiogram. The annulus and leaflet point clouds at each segmented time instance were used to inform the displacement boundary conditions (**Fig. 6-7(c)**). We also segmented the leaflet surface at the end diastolic state for use in the optimization of the *true solution*.

For the BO, we used a larger search domain because we do not know the true material parameters for the *in vivo* tissues. The 6D synthetic solution was constructed by randomly sampling values within the search domain of $c_1 \in [0.1, 100]$ kPa and $c_2 \in [0.1, 50]$. For the three leaflets, the target parameters were: TVSL, $c_1 = 81.49$ kPa and $c_2 = 45.68$; TVAL, $c_1 = 90.59$ kPa and $c_2 = 31.65$; and TVPL, $c_1 = 12.79$ kPa and $c_2 = 4.97$. The number of maximum BO iterations of the BO was increased to 200.

### Synthetic Solution

For the 6D synthetic solution using the real patient geometry, the optimized parameters were found at iteration $138/200$ as: TVSL, $c_1 = 75.70\ [65.83, 78.26]$ kPa and $c_2 = 40.82\ [38.79, 44.32]$; TVAL, $c_1 = 96.78\ [89.04, 97.70]$ kPa and $c_2 = 23.40\ [22.44, 25.56]$; and TVPL, $c_1 = 26.51\ [23.71, 32.43]$ kPa and $c_2 = 2.94\ [2.30, 3.10]$; $\mathcal{F} = 126.3\ [114.8, 136.4]$ mm (**Fig. 6-8(a)-(b)**). The optimized solution is within the vicinity of the target parameters, with the errors likely being attributed to the existence of a region of near-equivalent solutions in the hyperspace.

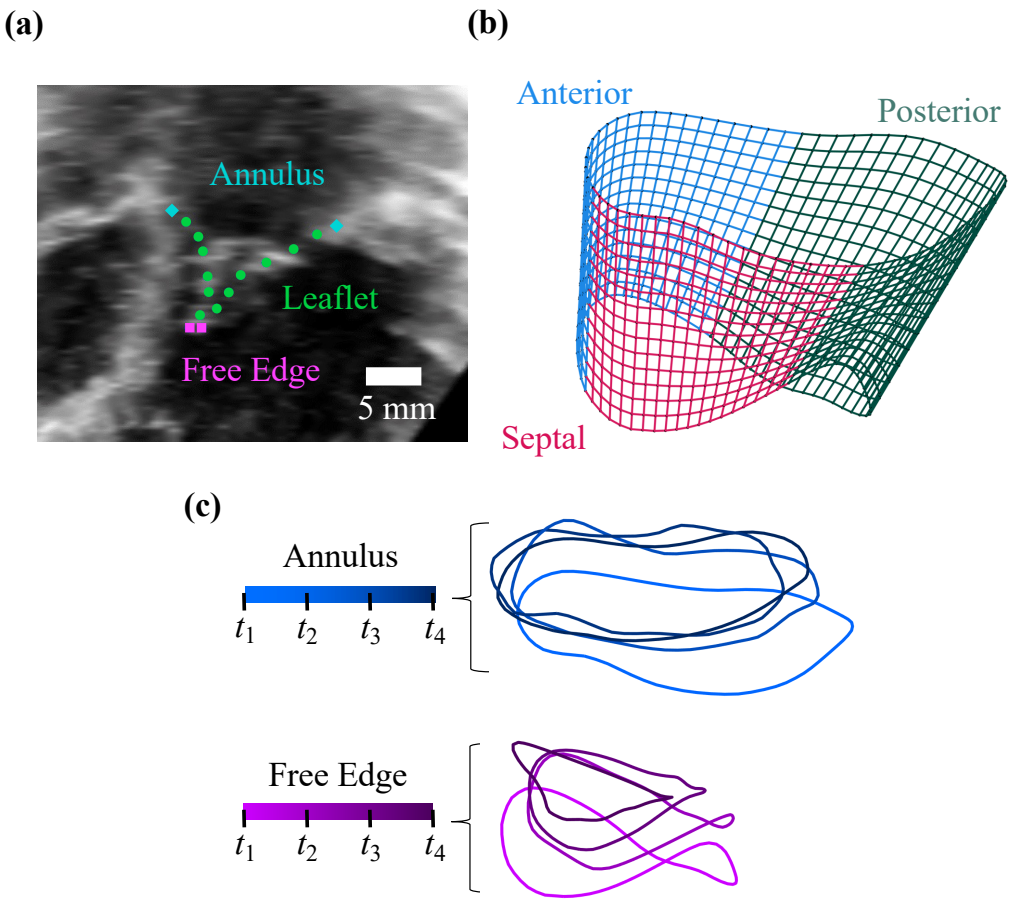


**Figure 6-7** (a) The image segmentation of an echocardiogram to retrieve the annulus, free edge, and leaflet point clouds. (b) The generated finite element mesh. (c) The dynamic annulus and leaflet free edge boundary conditions: $t_1$ = right ventricle minimum volume; $t_4$ = end diastole.

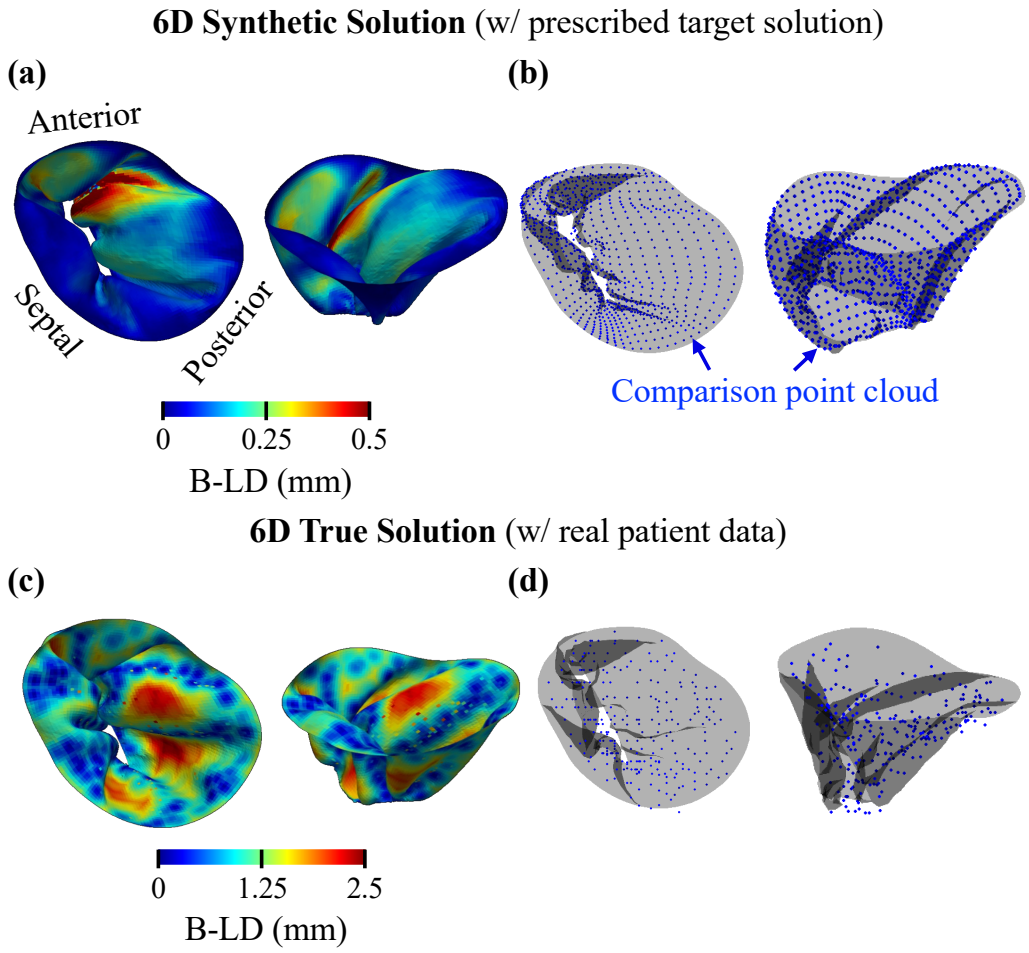


**Figure 6-8** ((a) Top-down and isometric views of the element-wise bidirectional local distance (B-LD) errors and (b) qualitative comparisons with the leaflet point cloud for the optimized TV surface with the 6D synthetic and (c, d) true solutions. Note that for improved visualization a denser finite element mesh was generated than what was used in the real optimization.

### True Solution

In the patient-specific optimization using the real locations of the image-segmented leaflet point cloud, the BO-determined parameters were found at iteration 171/200 as TVSL, $c_1 = 0.77\ [0.27, 1.83]$ kPa and $c_2 = 20.20\ [16.77, 26.14]$; TVAL, $c_1 = 51.08\ [43.35, 72.47]$ kPa and $c_2 = 11.98\ [11.34, 16.75]$; and TVPL, $c_1 = 64.34\ [56.40, 91.80]$ kPa and $c_2 = 24.95\ [21.80, 28.64]$; $\mathcal{F} = 945.7\ [935.5, 949.5]$ mm (**Fig. 6-8(c)-(d)**). The larger objective function value was likely caused by noise in the point cloud stemming from the low-resolution imaging modality. This phenomenon also explains the wider IQR for the optimized parameters, but a more narrow IQR for the objective function as compared to the synthetic 6D problem.

## 6.6 Discussion

We have performed an exploratory analysis of the iFEA problem for the atrioventricular heart valves and provided two major contributions: (i) a *first-of-its-kind* implementation of Bayesian optimization for inverse finite element analysis of the tricuspid valve, and (ii) a novel boundary condition approach to simulating the TV that provides a more desirable optimization search space when using exponential-type material models.

### 6.6.1 Bayesian Optimization

From our test cases, we found that Bayesian optimization is capable of locating the region of the global optima within a reasonable number of iterations in cases with both smooth and non-smooth residual search spaces (all simulations performed in $<$1 day in our laboratory). In the inflation testing case, the synthetic solution was effectively captured within 42 iterations. Meanwhile, in the leaflet contact and the tricuspid valve simulation, the exact solution was not reconstructed; however, the objective function values were reasonable and the obtained solutions were in the local vicinity of the user-prescribed parameter values. We were also able to reconstruct a patient-specific geometry using BO, albeit the solution appeared to converge to a region of equivalent solutions in the hyperspace. Overall, we find these results to be satisfactory for the present study, and the Bayesian optimization can be further improved by using various extensions of the solver.

#### Improvements to BO

In our work, we used a relatively simple implementation of the BO algorithm. Other researchers have further modified BO for improved performance. For example, the BO routine can be parallelized using Thompson sampling as an acquisition function, providing an efficient random sampling method for each of the parallelized processes [246]. More complicated parallelization methods rely on modifying the acquisition functions for batch processing, such as with local penalization or Monte-Carlo methods [247]. In future works, it woudl be valuable to compare the efficiency and accuracy of the different parallel processing schemes for biomechanics-iFEA problems. Another modification to improve BO is using a "dynamic search domain" for solving problems where the ideal search domain is unknown [248]. This method is specifically interesting for the biomechanics-focused iFEA studies, because, while *in vitro* testing of soft tissues may provide an estimate for the ideal search space, phenomena such as pre-strains could change the predicted material parameters by four orders of magnitude [28, 82].

### 6.6.2 Novel Approach to Inverse Analysis of the Atrioventricular Heart Valves

The traditional method of simulating the mitral or tricuspid valve closing from medical image data involves generating a chordae structure that may or may not emulate the true *in vivo* condition. For example, Khaligi *et al.* developed a "functionally equivalent" chordae topology model; however, the implementation may have some shortfalls for *in vivo* data analysis due to inaccuracies in measuring the chordae thicknesses or when simulating the diseased valves [249]. Additionally, determining the material properties of the chordae further complicates, especially when considering the three mechanically distinct types of chordae (i.e., basal, marginal, strut) [53]. While BO could theoretically be used to optimize the chordae and leaflet properties at the same time (BO can solve $\leq$20-dimensional problems), the convergence of the solution may be infeasible or extremely expensive. With these limitations, our question was: *Can we simulate the AHV function without the chordae tendineae?* Thus, we proposed our novel "guided free-edge" approach, which we found to provide faster solution convergence and a smoother objective function surface than the *in vivo*-emulating approach.

The logical next step for our framework is verification using an *ex vivo* heart simulator in conjunction with an excised human, animal, or synthetic AHV. In this scenario, the tissues could be characterized experimentally and compared with the iFEA-predicted material

properties. Also, the images obtained from ultrasound probes can be compared with higher resolution imaging methods to verify the accuracy of the image segmentations.

### 6.6.3 Limitations

This study is not without limitations. First, the material parameters that were obtained for the patient-specific geometry may not be truly representative of the tissue material behaviors due to our "guided free-edge" approach; the chordae material properties may be consequently embedded in the predicted leaflet properties. Consequently, the future patient conditions or therapy outcomes can not be predicted using our framework. Second, the exponential constitutive model causes a valley of nearly equivalent solutions (i.e., non-unique solution). Despite this, a high-resolution iFEA-retrieved digital reconstruction of the valve surface provides rich detail about the geometry and mechanics of the valve, which may be useful in predicting adverse tissue remodeling caused by excessive strains [250], or valvular regurgitation. Finally, in our simulations of the real patient TV, we observed non-physiologic behaviors at the leaflet free edge due to minor errors in the image segmentation and contour smoothing process affecting the prescribed displacements. This issue could likely be remedied by a semi-automated or automated routine that more accurately maintains the leaflet lengths throughout the segmentation process (e.g., contour propagation).

## 6.7 Chapter Summary

Overall, we proposed a novel use of BO that has some advantages over derivative-free or derivative-based solvers. While there are still remaining challenges for inverse analysis of the heart valve structures, BO could be used to obtain information about the leaflet strains and coaptation in a relatively short time frame (each inverse analysis was performed within one day in our laboratory). With continued work in this field, a long-term vision can be realized of a patient-specific framework for the prediction of surgical outcomes and disease progression.

# 7 CONCLUSIONS AND FUTURE WORK

7.1 Summary of the Dissertation . . . . . 137
7.2 Future Investigations . . . . . 139
7.2.1 Incorporation of Pre-Strains . . . . . 139
7.2.2 Non-Invasive Analysis of Tissue Biomechanics . . . . . 144
7.2.3 Statistical Analysis Designs in TR-Related HLHS Research . . 145

## 7.1 Summary of the Dissertation

Herein, the key findings from each chapter are briefly stated.

**Collagen & Elastin Degradation** This study presents, for the first time, a thorough mechanical characterization of the atrioventricular heart valve leaflets before and after enzymatic removal of elastin and collagen. We found that the biaxial tensile properties of an elastin-deficient tissue are stiffer, and the collagen-deficient tissue is more extensible. The fact of elastin supporting low-stress valve function and collagen as the main load-bearing component was evident in a decrease in the low-tension modulus for elastin-deficient tissues and in the high-tension modulus for collagen-deficient tissues. Our quantification and experimental technique could be useful in predicting the disease-related changes in heart valve mechanics. This information obtained from this work is valuable for refining the constitutive models that describe the essential microstructure-mechanics relationship.

**Affine Fiber Kinematics** This study provided a *first-of-its-kind* evaluation of the affine fiber kinematics assumption used for many constitutive models of the tricuspid valve leaflets using a biaxial testing-polarized spatial frequency domain imaging approach. Three

main findings were observed in this study: (i) The affine fiber kinematics theory underpredicted the reorientations of the collagen fibers during biaxial mechanical testing, with greater errors occurring during non-equibiaxial loading scenarios. (ii) There was an observed trend between the magnitude of the collagen fiber reorientations and the magnitude of the error from the affine fiber kinematics theory, suggesting that the modeling assumption may be better suited for relatively smaller fiber reorientations. (iii) The magnitude of tissue deformation was found to be partially correlated to the magnitude of the error from affine fiber kinematics theory, which may imply that the affine kinematics assumption is more appropriate for small tissue deformations. This work also provides a useful contribution to the field of soft tissue biomechanical modeling for refining the current hyperelastic constitutive forms to more accurately predict changes in the collagen fiber architecture and the corresponding macroscopic tissue deformations, which will lead to refinement of tricuspid valve simulations for healthcare diagnostics.

**TV Annulus in HLHS** This study on the mechanics and geometry of the TV annulus provided novel comparisons between the healthy newborns and those with HLHS. Most interestingly, we found that annulus strains were similar between the two groups, despite the presence of a significantly larger annulus area in the patients with HLHS. This finding is interesting, as it supports a working theory that the TV may mal-adapt to the pressure overloading of the right-side heart by increasing in size to preserve a desired homeostatic tissue strain. Other interesting findings from the HLHS cohort were: (i) largest strains generally in the posterior annulus and smallest strains in the septal region; (ii) the HLHS□affected TV annulus is larger in circumference, area, and antero-posterior diameter and becomes more circular and curved during valve closure than its healthy counterpart. Future works along a similar direction for larger cohorts, a longitudinal study, and/or analyzing the TV leaflets could facilitate a refinement of the therapies to be in better compliance with tissue remodeling potentials.

**Inverse Finite Element Analysis** The exploratory study of the iFEA problem for the AHVs yielded two primary contributions: (i) a demonstration of Bayesian optimization, with recommendations on standardized reporting of results (i.e., median and IQR); and (ii) a proposed method for digital reconstruction of the heart valve closing using “free-edge displacement”, rather than an assumed chordae topology. Implementation of the BO to iFEA frameworks could significantly reduce computational time for system convergence, bringing the field a step closer to timely patient-specific simulations. While there are still hurdles

to be cleared before making a full in-clinic implementation of the BO-iFEA method for the AHVs (e.g., resolving the chordae), our findings provide useful insight to the potential pathways to this goal.

## 7.2 Future Investigations

Here, a brief outline of potential avenues of future investigation are detailed, along with some preliminary results from prototyped demonstrations of the methods. These investigations include simulation modeling of tissue pre-strains, non-invasive biomechanics analysis, and statistical modeling for predictive risk assessment in HLHS. Altogether, these studies provide crucial information that will lead to more accurate simulations and the development of patient-specialized predictive frameworks.

### 7.2.1 Incorporation of Pre-Strains

Accurate computational modeling of the soft tissue biomechanics is contingent on the selected constitutive model and the corresponding material parameters, which are built upon our experimentally backed understanding of the tissue biomechanics. While many constitutive models exist and can effectively represent the *in vivo* and *ex vivo* behaviors of the soft tissues, there is a gap in translation for using this information in *in silico* models due to the issue of the tissue pre-strains. To elaborate, the heart valve leaflets contain an inherent pre-strain due to the dynamic *in vivo* cardiac environment. Previous research efforts have been focused on understanding these pre-strains *in vivo* and *in vitro*. In the *in vivo* studies, researchers have used ovine models implanted with sonocrystals and quantified relatively isotropic pre-strains of $32-35\%$ between the *in vivo* and the *in vitro* reference states [31, 251]. Meanwhile, in a previous *in vitro* work from our own laboratory group, we performed a photogrammetry-based full-valve analysis of the tricuspid valve (TV) leaflet pre-strains, and observed compressive areal strains of $3.3\%$, $13.2\%$, and $25.2\%$, on average, for the anterior, septal, and posterior leaflet, respectively [252]. These pre-strains have a profound effect on the quantified material behaviors of the leaflets, including reducing the observed stretches and the mechanical anisotropy (i.e., the ratio of stretches in the two tissue directions). For simulation-focused studies, the pre-strains can have major effects on the simulated valve closing.

In the pre-strain-focused *in silico* studies, researchers have presented methods for embedding the pre-strains to the models, and the effects of pre-strains on the inverse prediction

of the leaflet material properties. For instance, Rausch *et al.* (2013) and Rausch and Kuhl (2013b) used a geometry-based two-step approach for the mitral valve and found that a uniform pre-strain of 30% could cause the inverse-predicted tissue stiffnesses to vary by up to four orders of magnitude [28, 82]. These variations to the predicted tissue stiffnesses were further reflected in a mitral valve leaflet model using sonocrystal-derived *in vivo* ovine data, albeit the variations were not as large [251]. In an alternative approach, Maas *et al.* (2016) presented an iterative framework in which the mechanical behaviors of the soft tissues could be used to predict the *in vivo* pre-strain gradient field [253]. While these works lay the foundation for future studies, these approaches are limited for incorporating *regionally varying* pre-strains, or the analyzed pre-strains are not backed by experimental data. As a first step towards improving the *in silico* understanding of pre-strains, we provide a brief demonstration.

### Demonstration of Potential Finite Element Methods for Pre-Strain Implementation

Overall, the embedding of pre-strains to the model involves the deformation of the finite element mesh from a "shrunken" configuration to the desired, original geometry, and consequently applying a strain to the elements. For our demonstration herein, we utilize a typical method from previous literature [82], along with proposing a new technique. Starting with the approach from previous researchers, we name this the "displacement-based" approach. Note that all simulations were performed with the synthetic solution in the idealized valve simulation settings described in **Chapter 6**, with a targeted homogeneous pre-strain of $20\%$ for the model.

**Displacement-Based Pre-Strains** First, we determined the shrunken valve configuration, using custom MATLAB script to convert the coordinates of the finite element mesh into polar coordinates. Then, the radius and height values of each node were multiplied by the corresponding circumferential and radial strain, respectively. The simulation then proceeded in two steps (**Fig. 7-2**). (Step 1): Then, the displacement of each node was calculated in the Cartesian coordinate and applied to each node to transform the mesh from the shrunken configuration ($\Omega_{\text{shrunken}}$) to the original configuration ($\Omega_{\text{original}}$). Note that here we did not apply any displacement to the papillary muscle tips to ensure the chordae did not cause inadvertent element strains. (Step 2): After restoring the $\Omega_{\text{original}}$ configuration, a smooth-stepped transvalvular pressure gradient of 25 mmHg was applied to the ventricular surface of the leaflets over 0.4 s (simulation time).

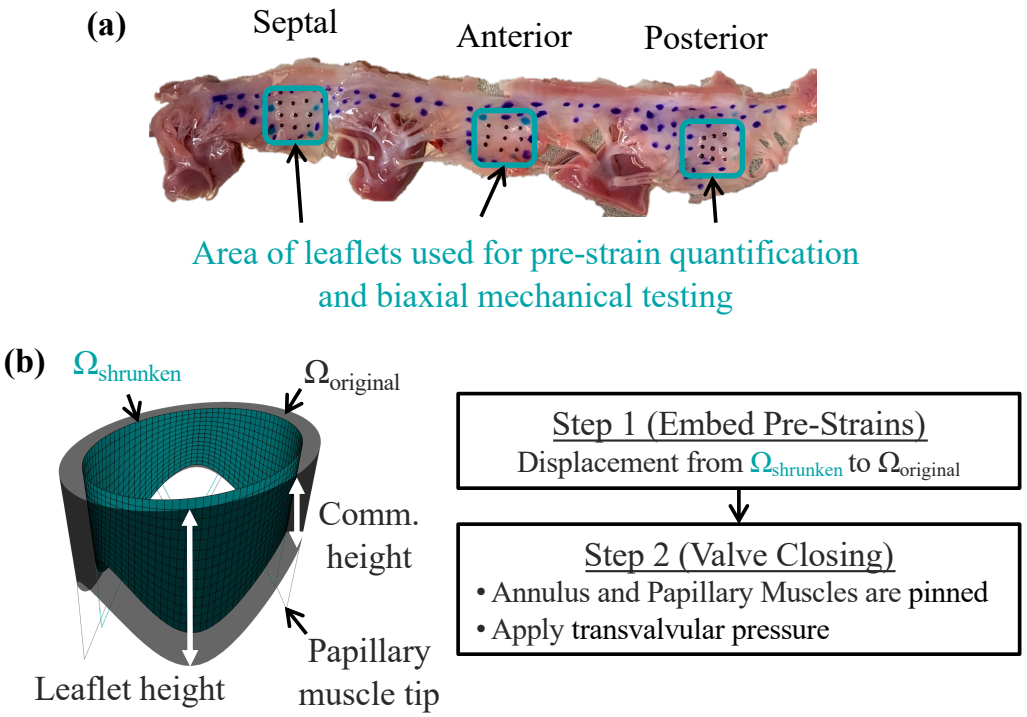


**Figure 7-1** (a) An image of an excised porcine tricuspid valve that can be used for the pre-strain and valvular measurements. (b) The parameterized finite element model.

**New Method: Force-Based Pre-Strains** During our testing, we noted an interesting behavior during the displacement-based embedding of the pre-strains that necessitated additional investigations—when the nodal displacements are removed at the beginning of the Step 2 simulation, the pre-strains may be "released" from the tissue in the absence of additional boundary conditions. Therefore, to verify the use of the displacement-based method for embedding the pre-strains to the finite element model, we developed a novel three-step procedure based on nodal reaction forces that maintains the pre-strains throughout the Step 2 simulation (**Fig. 7-2**). In brief, this technique requires the addition of a "Step 0", in which pre-strains are embedded to the model through the displacement of the finite element mesh, and the nodal reaction forces are retrieved at the final, deformed configuration. Then, in Step 1, rather than using the nodal displacements to embed the pre-strains, we apply the nodal reaction forces to restore the *in vivo*, pre-strained configuration. Then, in Step 2, the reaction forces are maintained while the transvalvular pressure is applied.

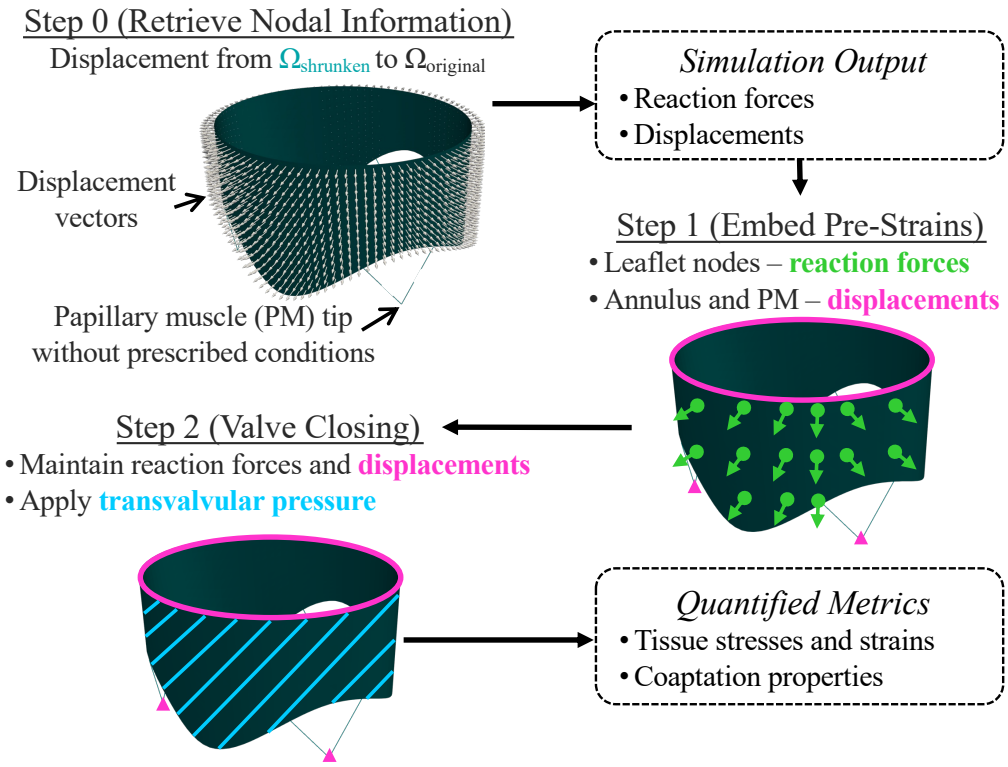


**Figure 7-2** The reaction force-based three-step procedure for embedding pre-strains into the finite element model.

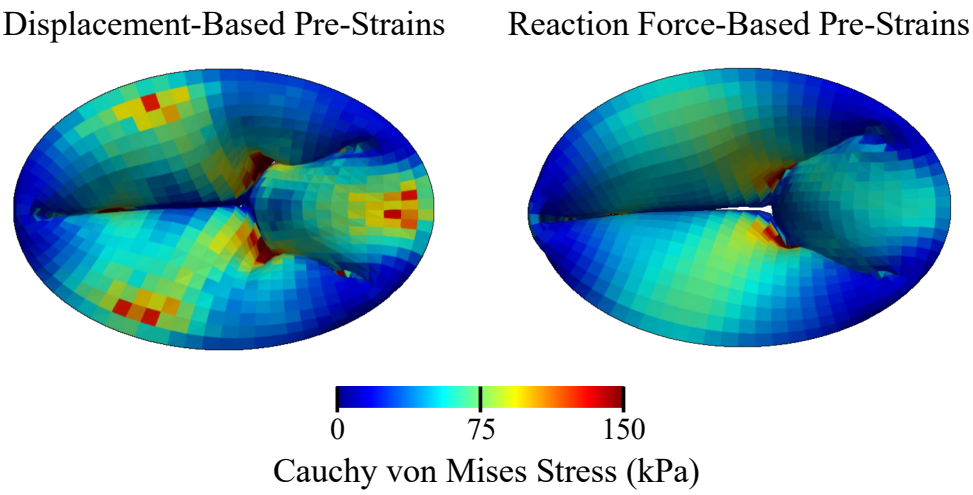


**Figure 7-3** A comparison of the von Mises stresses at the deformed valve configuration for the displacement-based and reaction force-based pre-strain embedding techniques.

### Displacement- vs. Force-based Methods

Comparing the displacement-based and reaction force-based methods of embedding the pre-strains to the finite element model, we found that the displacement-based method resulted in larger predicted von Mises stress values (**Fig. 7-3**). Specifically, the von Mises stresses in the reaction-force model were $9.5 \pm 39.5$ kPa lower than in the displacement-based model (averaged across all elements). However, the differences in element centroid locations between the two methods was relatively low ($1.2 \pm 1.1$ mm, on average), demonstrating the displacement method to predict the closed valve geometry with relative accuracy. The reaction force method comes with drawbacks, however, as numerical instability could be encountered in cases of spatially heterogeneous pre-strains. Regardless, our findings show that there is room for improvement in the methods for embedding pre-strains to heart valve simulations.

**Additional Note: Challenges in Using Experimental Data** Herein, we also quickly highlight issue that are encountered when using experimentally acquired pre-strain data. In our previous study, the TV leaflet pre-strains were experimentally quantified using a photogrammetry approach across different tissue states during a typical biaxial testing procedure [252]. As part of a prototyped study design, we attempted to utilize the quantified biaxial tensile properties and pre-strain data to generate subject-specific heart valve models for a *first-of-its-kind*, benchtop-to-simulation understanding of the pre-strain phenomenon. However, in these attempts we encountered physiologically unrealistic pre-stresses of 500-700 kPa in

the TV leaflets after the Step 1 (pre-strain embedding) simulation, which caused numerical issues and an inability for the valve to close due to the high stiffness tissue behaviors. We believe this issue can be attributed to discrepancies in the description of tissue deformations between various configurations. Specifically, the standard method of *ex vivo* material characterizations may not be compatible with pre-strain focused finite element analysis works, which we elaborate upon in the next subsection.

#### Constitutive Modeling and Preconditioning

As was described in our previous work, it is clear that the standard biaxial testing preconditioning protocol does not effectively restore the tissue configurations from before the dissections were performed [252]. However, determining a preconditioning protocol that would restore the unloaded *in vivo* tissue configuration is challenging, especially when using real patient data as opposed to animal models. This raises questions regarding the proper method for translating *ex vivo* mechanical characterizations to the *in silico* models in a way that best emulates the *in vivo* conditions.

Depending on the research of interest, the elastic deformation gradient may take different forms. For example, in the case of inverse finite element analysis, $\mathbf{F}_{\text{elastic}}$ usually only consists of the applied loading condition (i.e., transvalvular pressure). Meanwhile, in the pre-strain focused works, $\mathbf{F}_{\text{elastic}}$ is composed of both the pre-strain and applied loading deformation gradients (**Figure 7-4**). On the *ex vivo* side, we find the elastic deformation may be only considered as the displacements between the post-preconditioned and peak loading states. However, if we are to use a similar logic as in the pre-strain focused works, then $\mathbf{F}_{\text{elastic,data}}$ may require consideration of the PPC deformations to relate the biaxial peak loading to the *ex vivo* unloaded configuration. Relating the various tissue configurations is a challenging venture that requires additional, careful investigation—perhaps the preconditioning protocol must be subject-specific to properly equate $\Omega_{\text{in-vivo,unloaded}}$ and $\Omega_{\text{ex-vivo,PPC}}$, or the proper elastic deformation gradient formulation could be verified using a living animal-benchtop testing-simulation modeling trifecta approach.

### 7.2.2 Non-Invasive Analysis of Tissue Biomechanics

Image-based analysis of the valvular structures is a research area with growing potential as medical imaging techniques advance. Echocardiograms, in particular, have enabled most of the research examined in this dissertation, and this routine imaging modality can be used

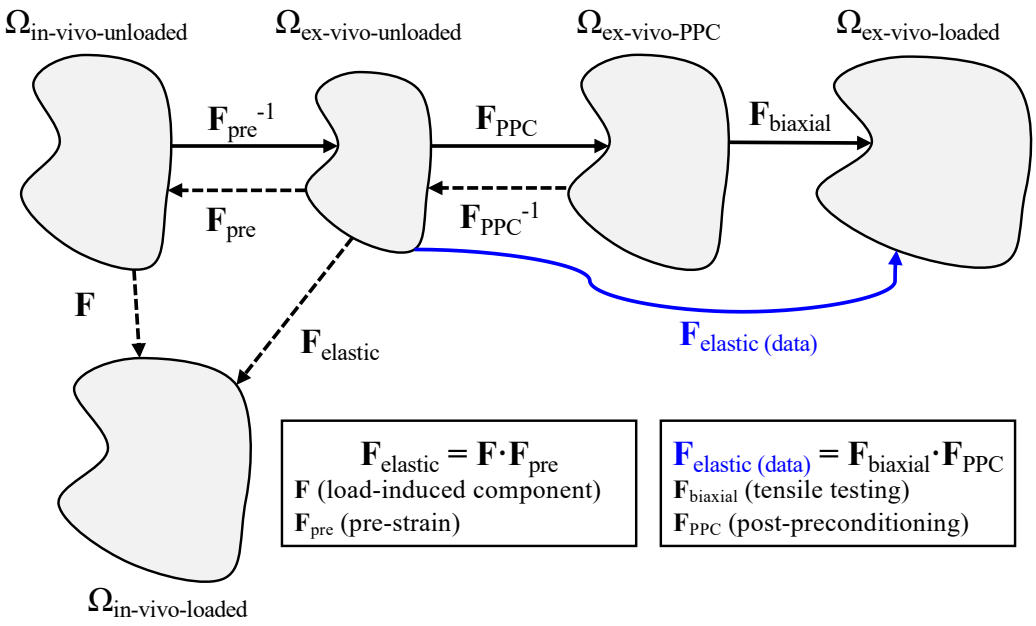


**Figure 7-4** A potato diagram depicting the different deformation configurations of soft tissues during a standard experimental characterization procedure, and the relationships between the states.

for more advanced, engineering-focused analyses. For example, in this dissertation we performed image segmentation of the TV annulus in healthy and HLHS-affected newborns to gain preliminary insight into the main differences in valve function. Future research can be performed in a similar way for the TV leaflets to quantify the strains, curvatures or other biomechanical and geometric factors. In order to enable such an exploration of these dynamic, geometrically complex structures, it can be advantageous to use fully or semi-automated image segmentation methods, such as the recently developed statistical shape modeling technique [254] or deep learning [237, 255]. Through the development and refinement of these engineering-focused and automated image segmentation frameworks, the non-invasive analysis of TV becomes more manageable in the clinical setting, which can eventually lead to a detailed, individualized patient risk assessment, such as the multivariate logistic model in the next subsection.

### 7.2.3 Statistical Analysis Designs in TR-Related HLHS Research

Most of the work reviewed in this dissertation involves analyses of the differences in several recorded measurements and factors between TR and non-TR cohorts relevant to HLHS. Overall, these studies focus on answering the question: *What are the significant differences*

*between HLHS patients with TR and without TR?* While these studies may provide new insights into indicators of TR, a more clinically useful research question exists: *What are the key predictors of TR in the HLHS population during the palliation stages?* To answer this question, another subset of statistical analysis tools must be warranted to obtain the *predictors* of the onset of TR. With more advanced statistical techniques, a predictive model could be developed to determine those patients at risk of TR based on their individual measurements in the clinic. We believe that using multivariate logistic models can lead us to answer the overarching question about the most important TR predictors [256]. To demonstrate the feasibility of this technique, we provide a brief description in the following subsections. In addition to advocating the use of multivariate models, we also briefly discuss the advantages of working with a longitudinally tracked patient cohort, which can more accurately provide the predictors of TR by accounting for patient-specific trajectories.

### Demonstration of Multivariate Logistic Modeling

Using our previously presented HLHS patient cohort [231] (IRB #14112 from the University of Oklahoma Health Sciences Center on 12/8/2021), we constructed a *population-averaged* TV geometry as the baseline for elucidating the mechanisms of TR. In short, we first created a collection of TV geometries covering a range of several key measurements identified as TR indicators in the previous literature: two primary annular diameters, bending angle, three leaflet heights, and area change during TV systolic closure (**Table 7-1**, **Fig. 7-5(a)**). These geometries were then used in our finite element simulation framework using the conditions and simulation specifications detailed in [77]. After the finite element simulation was completed, the simulated TV closing surface was exported and post-processed to quantify the regurgitant orifice area (ROA), which represents TR severity (i.e., the grading of TR). In this procedure, as previously described in [257], the simulated TV surface was projected onto a series of camera viewpoints and the area of the uncoapted region was calculated, using the maximum ROA as a measure of TR severity (**Fig. 7-5(b)**). The diagram in **Fig. 7-5(c)** shows the top-down viewpoint and eight offset viewpoints used to quantify the maximum regurgitation orifice area (**Fig. 7-5(d)**). To categorize patients with severe or non-severe TR, we used *k*-means clustering – an unsupervised classification algorithm (**Fig. 7-6(a)**). Here, we briefly highlight that this TR quantification and classification pipeline can be useful in future work with real patient data for automated bulk data processing.

**Table 7-1** Range of geometric parameters used to construct the pseudo-population for the multivariate logistic modeling demonstration. Note that the mentioned average values are based on our preliminary observations of a cohort of $n = 8$ neonates born with HLHS.

| Geometry Parameter | Parameter Range | Description |
|---|---|---|
| Anterior-Posterior Diameter (mm) | $[20.1, 40.2]$ | $100-200\%$ of the average value for emulating annular dilation |
| Septal-Lateral Diameter (mm) | $[16.5, 33.1]$ | $100-200\%$ of the average value for emulating annular dilation |
| Bending Angle (deg) | $[143.5, 175.4]$ | $\pm 10\%$ of the average value |
| Area Change (%) | [5, 20] | Covering the range described in Section 2.3.2 |
| Septal Leaflet Height (mm) | $[6.6, 19.9]$ | $\pm 50\%$ of the average value |
| Anterior Leaflet Height (mm) | $[7.7, 23.0]$ | $\pm 50\%$ of the average value |
| Posterior Leaflet Height (mm) | $[8.2, 24.5]$ | $\pm 50\%$ of the average value |

With the binary classification performed, we then performed a multivariate logistic regression fit using the LASSO algorithm and a $70/30$ train/test cross-validation data split [258], with the determined coefficients listed in **Table 7-2**. LASSO regression can further be used to find the best $n$ predictors for a multivariate model, which may be useful to determine the trade-off between model simplicity and model accuracy, as visualized by the receiver operating characteristic (ROC) curves (**Fig. 7-6(b)**).

After developing the multivariate model, we also demonstrated the calculation of the key performance metrics, which are crucial for transparency and model assessment. On the one hand, the common performance metrics for predictive models can be summarized into four main categories: (i) *overall performance*, reflecting the differences between the predicted and actual results; (ii) *discrimination*, which describes the effectiveness of the model in distinguishing between events and non-events; (iii) *calibration*, quantifying the agreement between predicted and observed risks; and (iv) *reclassification*, the number of data points that change category with an updated form of the prediction model [259]. On the other hand, the generally adopted assessments for the multivariate logistic models include the *c* statistic (i.e., the area under the ROC curve), sensitivity $SN$ (i.e. the true positive rate), specificity $SP$, and the precision $PREC$. The last three metrics can be determined from the number of true positive $TP$, false positive $FP$, false negative $FN$, and true negative $TN$ cases

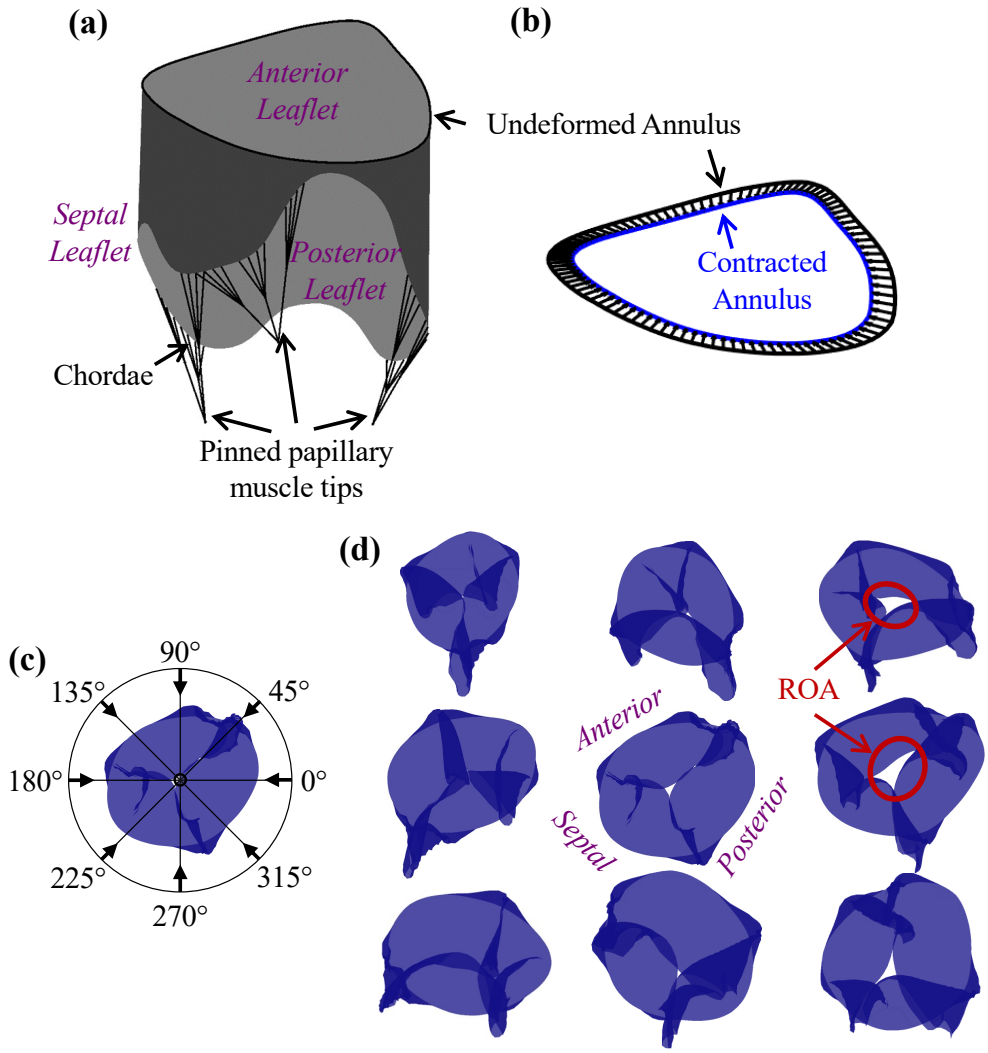


**Figure 7-5** (a) TV model based on the average measurements of our cohort of $n = 8$ neonates with HLHS; (b) visualization of the annulus contraction in the finite element simulations; (c) diagram depicting the top-down viewpoint (represented by the dot) and 8 offset viewpoints used to (d) quantify the maximum regurgitation orifice area (all views from the same representative simulation).

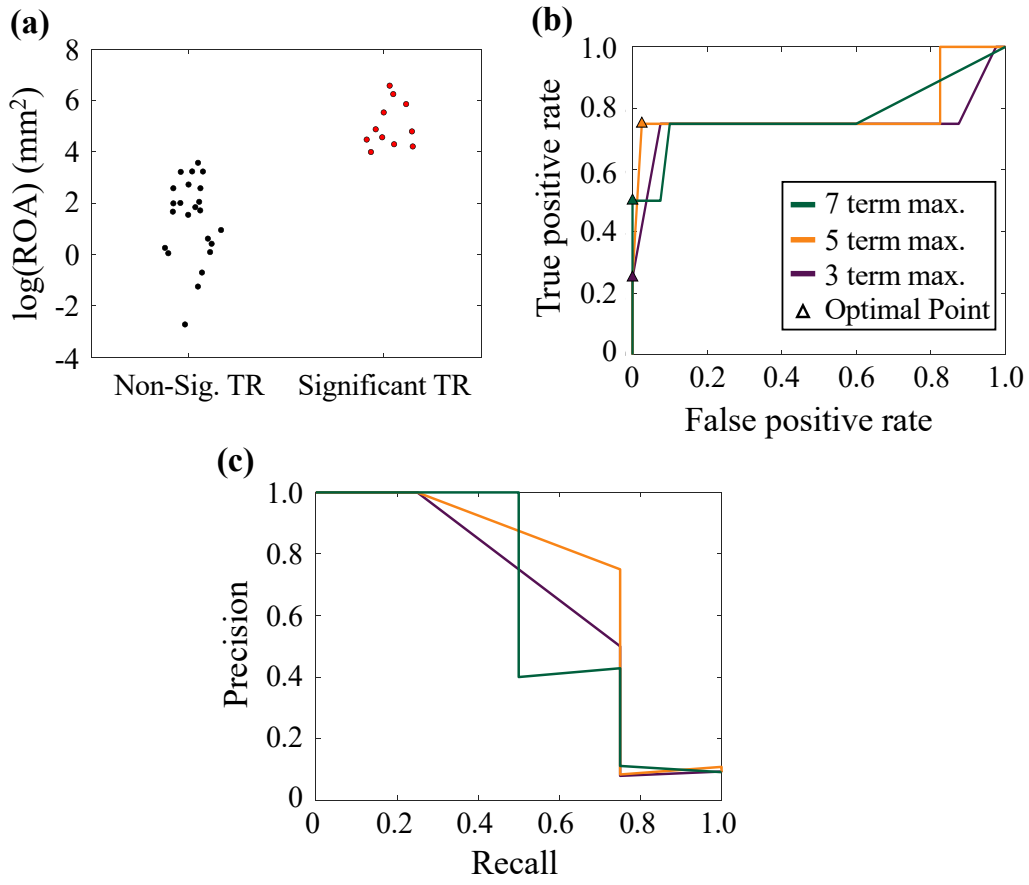


**Figure 7-6** (a) The *k*-means clustering classification of non-TR and TR groups (note that the natural logarithm of the ROA value is used for better visualization); (b) ROC curves generated from multivariate logistic models using a maximum of 3, 5, or 7 predictor variables; (c) precision-recall curves for each of the multivariate models.

**Table 7-2** Coefficients determined for the multivariate logistic models considering 3, 5 or 7 terms, together with the respective area under the curve to assess the model accuracy. It should be noted that the number of parameters was chosen to obtain unique ROC curves to demonstrate the statistical technique.

| Maximum Number of Parameters | 3 | 5 | 7 |
|---|---|---|---|
| Intercept Term | 2.40 | 2.53 | −112.63 |
| Anterior-Posterior Diameter (mm) | 0 | 0.05 | 1.33 |
| Septal-Lateral Diameter (mm) | 0.04 | 0.09 | 1.49 |
| Bending Angle (deg) | 0 | 0 | 0.77 |
| Septal Leaflet Height (mm) | 0 | 0 | 0 |
| Anterior Leaflet Height (mm) | 0 | −0.06 | −1.64 |
| Posterior Leaflet Height(mm) | −0.19 | −0.28 | −3.08 |
| Area Change (%) | −23.06 | −31.48 | −339.19 |
| Area Under the Curve (-) | 0.75 | 0.79 | 0.78 |
| Sensitivity (-) | 0.25 | 0.75 | 0.5 |
| Specificity (-) | 1.00 | 0.98 | 1.00 |

based on the optimal threshold value that balances the $TP$ and $FP$ rates (Fig. 7-5(b)), i.e.

$$\begin{aligned} SN &= \frac{TP}{TP+FN}, \\ SP &= \frac{TN}{TN+FP}, \\ PREC &= \frac{TP}{TP+FP}. \end{aligned} \tag{7.2-1}$$

For the example models developed here, the performance metrics revealed a trade-off between the maximum number of parameters used and the model accuracy, with at least five parameters required for accurate prediction of the pseudo-patient condition. As an alternate measure of model performance (particularly in the case of unbalanced observations for each group), the precision-recall (i.e., precision-sensitivity) graph can be used to visualize the model's ability to discriminate between groups (**Fig. 7-6(c)**).

For comparison with the multivariate model, we also performed statistical comparisons of each measurement between the two groups using Student's $t$-test. From this we found sig-

nificant differences between the two groups for the posterior leaflet height ($p = 0.001$) and the annular area change ($p = 0.001$). Comparing the two statistical modeling approaches, it becomes clear that the metrics that differ significantly from the $t$-tests do not necessarily indicate the measurements needed to accurately predict the onset and development of TR.

In this simple demonstration, we have shown that identifying the *predictors* of TR requires the use of a binary classification technique, such as multivariate logistic regression or support vector machines. By applying the same procedure with real patient data, insights can be obtained to clarify the key indicators of TR. In summary, the multivariate logistic model can be usefully implemented as a supplement to the statistics typically reported in the literature so far and can be helpful to identify the most important TR-related indicators.

### Longitudinal Cohorts and Mixed-Effect Models

In a more statistically rigorous study design, longitudinal statistical modeling can provide even better insight into the mechanisms of TR. As a key example of the benefits of conducting a longitudinal study, Colen *et al.* (2017) found that the leaflet areas *increase* in the presence of TR for their longitudinally tracked, post-Norwood cohort [135], whereas in another non-paired sample study by Takahashi *et al.* (2009) TR was associated with *smaller* leaflet areas [129]. By performing a statistical analysis with repeated measurements of the same patient over time, the findings can be more representative of the underlying phenomena in TR due to the complex, multi-factorial nature of this disease condition. Of all the possible methods, mixed-effect models are the primary model of choice for many statisticians for longitudinal predictive modeling, especially on a patient-specific basis [260–262].

In general, mixed-effect models are a class of powerful statistical modeling techniques that incorporate both the population-averaged trends (i.e., fixed-effects) and the patient-specific variations (i.e., mixed effects). In short, these mixed-effect models have the form

$$y_i(t) = \mathbf{bX} + \mathbf{u}_i\mathbf{Z}_i, \tag{7.2-2}$$

where $y_i(t)$ is the outcome of the $i^{\text{th}}$ patient at time $t$, and $\mathbf{b}$ and $\mathbf{u}_i$ are the coefficients of the fixed-effect parameters $\mathbf{X}$ and the individual-effect parameters $\mathbf{Z_i}$, respectively [260, 261]. Advantages of this statistical modeling technique include: (i) the model can still be applicable to patient dropout data (e.g., early mortality); (ii) patient-specific predictions can become more dependent on individual trends when each follow-up dataset is considered; and (iii)

the time-specific probabilities of TR onset can be determined by implementation with a Cox model. We can therefore use this method in future HLHS research to optimize intervention timing. For example, a prophylactic TV repair concomitant with palliative surgery may be beneficial to proactively correct TR.

## Nomenclature

| Abbreviation | Description |
|---|---|
| $\theta_{\text{exp}}$ | Collagen fiber angle at loaded tissue configuration |
| $\theta_{\text{fiber}}$ | Collagen fiber angle |
| $\theta_{\text{PPC}}$ | Collagen fiber angle at unloaded tissue configuration |
| $\theta_{\text{reorient}}$ | Collagen fiber angle reorientation |
| $\Omega_2$ | Configuration at peak deformation |
| $\Omega_1$ | Configuration at post preconditioning |
| $\Omega_0$ | Configuration at undeformed state |
| $\kappa$ | Curvature or shear deformation |
| $\alpha$ | Dashpot nonlinearity factor |
| $\eta_1$ | Dashpot viscosity |
| $\Omega_i$ | Deformation configuration |
| $\Omega_t$ | Deformed configuration |
| $\xi$ | Exploration ratio |
| $\theta_{\text{error}}$ | Error between AFK-predicted and experimentally measured collagen fiber angle |
| $\gamma$ | Fourier coefficient |
| $\lambda^*$ | Index of extensibility |
| $\mu$ | Mean |
| $E^{\text{HT}}$ | Modulus, high-tension |
| $E^{\text{LT}}$ | Modulus, low-tension |
| $\Psi$ | Moving least squares shape function |
| $\theta_{\text{polarizer}}$ | Polarizer angle |
| $PREC$ | Precision |
| $\Omega_0$ | Reference configuration |
| $\dot{T}^1$ | Slope of stress relaxation, initial |
| $\dot{T}^2$ | Slope of stress relaxation, saturated |
| $E_0$ | Spring constant |

| Abbreviation | Description |
|---|---|
| $E_1$ | Spring constant |
| $\sigma$ | Standard deviation |
| $\epsilon$ | Strain |
| $\psi$ | Strain energy density function |
| $\dot{\epsilon}$ | Strain rate |
| $\tau$ | Stress-relaxation time |
| $\lambda$ | Stretch |
| $\phi$ | Window function |
| A/S | Atrialis/spongiosa |
| AHV | Atrioventricular heart valve |
| AFK | Affine fiber kinematics |
| AI | Anisotropy index |
| AL | Anterior leaflet |
| AoA | Aortic atresia |
| AoS | Aortic stenosis |
| AP | Antero-posterior |
| AS | Antero-septal |
| BLD | Bidirectional local distance |
| BO | Bayesian optimization |
| BSA | Body surface area |
| BTS | Blalock-Taussig shunt |
| **C** | Right Cauchy-Green tensor |
| $c_i$ | Material parameters |
| –C | Control |
| CFA | Collagen fiber architecture |
| CI | Confidence interval |
| $D$ | Diameter |
| $d$ | Distance |
| DIC | Digital image correlation |
| DOA | Degree of optical anisotropy |
| $E_{11}$ | 11-component of strain tensor |
| ECM | Extracellular matrix |
| ED | End diastole |

| Abbreviation | Description |
|---|---|
| $EI$ | Expected improvement |
| EIVC | End isovolumetric contraction |
| EIVR | End isovolumetric relaxation |
| ES | End systole |
| $\mathcal{F}$ | Objective function/residual value |
| **F** | Deformation gradient |
| F/V | Fibrosa/ventricularis |
| $FN$ | False negative |
| $FP$ | False positive |
| GAG | Glycosaminoglycan |
| **H** | Basis function |
| HLHS | Hypoplastic left heart syndrome |
| HR | Hazard ratio |
| $I$ | Polarized light intensity |
| $I_i$ | Invariant of right Cauchy-Green tensor |
| iFEA | Inverse finite element analysis |
| IQR | Interquartile range |
| **M** | Moment matrix |
| MS | Mitral stenosis |
| MV | Mitral valve |
| **n** | Deformed fiber direction vector |
| **N** | Reference fiber direction vector |
| $N$ | Gaussian distribution |
| OR | Odds ratio |
| $p$ | Incompressibility penalty parameter |
| PBS | Phosphate buffered saline |
| PL | Posterior leaflet |
| PPC | Post-preconditioning |
| PS | Postero-septal |
| pSFDI | Polarized spatial frequency domain imaging |
| $r$ | Pearson correlation coefficient |
| ROA | Regurgitant orifice area |
| ROC | Receiver operating characteristic |

| Abbreviation | Description |
|---|---|
| RV | Right ventricle |
| RVFAC | Right ventricular fractional area change |
| RVPAS | Right ventricle-to-pulmonary artery shunt |
| $RVP_{min}$ | Right ventricular minimum pressure |
| SALS | Small angle light scattering |
| SD | Standard deviation |
| SEM | Standard error of the mean |
| SHG | Second harmonic generation |
| SL | Septal leaflet |
| $SN$ | Sensitivity |
| $SP$ | Specificity |
| $T$ | Membrane tension |
| –T | Enzyme-treated |
| $t$ | Time |
| TAPSE | Tricuspid annular plane systolic excursion |
| $TN$ | True negative |
| $TP$ | True positive |
| TR | Tricuspid regurgitation |
| TV | Tricuspid valve |
| $u$ | Utility function |
| VIC | Valvular interstitial cell |

# A FITTED MODEL PARAMETERS FOR THE VISCOELASTIC CHARACTERIZATION OF COLLAGEN- AND ELASTIN-REMOVED TRICUSPID VALVE LEAFLETS

This Appendix provides the additional tables for **Chapter 3**, in which data fitting was performed for the stress-relaxation data from the collagen- and elastin-removed specimens. For convenience, the standard 3-parameter solid model modified with a fractional-order dashpot is repeated, i.e.

$$g(t) = \left[E_0 + E_1 F_\alpha\left(-\frac{t^\alpha}{\tau}\right)\right] u(0), \tag{A.0-1}$$

where $g(t)$ is the force response, $u(0)$ is the constant displacement in the stress relaxation experiment, $E_0$ and $E_1$ are the spring constants, $\eta_1$ is the viscosity of the dashpot, $\alpha$ is the fractional-order parameter controlling the dashpot nonlinearity ($\alpha$=0, spring only; $\alpha$=1, linear dashpot that reduces to the standard *linear* solid model), $F_\alpha(z) = \sum_{k=0}^{\infty} z^k/\Gamma(\alpha k+1)$ is the Mittag-Leffler function, $\Gamma(x)$ is the gamma function, and $\tau = (\eta_1/E_1)^{1/\alpha}$ is the stress relaxation time estimated by this viscoelastic model [190].

**Table A-1** Stress-relaxation parameters for the modified 3-parameter standard solid model for each control (–C) and treated (–T) specimen pair from the elastin-removal study – circumferential direction, MVAL.

| | $E_0$ *(N/mm)* | | $E_1$ *(N/mm)* | | $\alpha$ *(-)* | | $\eta_1$ *(Ns/mm)* | | $\tau$ (s) | | Error (-) | |
|---|---|---|---|---|---|---|---|---|---|---|---|---|
| ID | -C | -T | -C | -T | -C | -T | -C | -T | -C | -T | -C | -T |
| 1 | 0.225 | 0.104 | 0.058 | 0.097 | 0.508 | 0.382 | 0.138 | 0.130 | 5.609 | 2.142 | 2.45E-06 | 6.57E-08 |
| 2 | 0.212 | 0.059 | 0.116 | 0.047 | 0.332 | 0.393 | 0.209 | 0.072 | 5.863 | 2.973 | 4.60E-07 | 1.14E-07 |
| 3 | 0.242 | 0.054 | 0.153 | 0.039 | 0.300 | 0.397 | 0.270 | 0.063 | 6.604 | 3.235 | 6.58E-07 | 8.80E-08 |
| 4 | 0.646 | 0.224 | 0.370 | 0.168 | 0.392 | 0.385 | 0.732 | 0.246 | 5.692 | 2.708 | 2.85E-07 | 2.74E-07 |
| 5 | 0.241 | 0.109 | 0.148 | 0.071 | 0.346 | 0.402 | 0.268 | 0.111 | 5.574 | 3.056 | 6.25E-07 | 1.37E-07 |
| 6 | 0.330 | 0.223 | 0.167 | 0.123 | 0.376 | 0.417 | 0.321 | 0.201 | 5.669 | 3.268 | 4.16E-07 | 1.10E-07 |
| 7 | 0.219 | 0.144 | 0.095 | 0.102 | 0.374 | 0.392 | 0.177 | 0.167 | 5.223 | 3.520 | 3.57E-07 | 1.02E-07 |
| 8 | 0.335 | 0.082 | 0.133 | 0.058 | 0.378 | 0.385 | 0.258 | 0.091 | 5.716 | 3.266 | 5.20E-07 | 9.51E-08 |
| 9 | 0.189 | 0.053 | 0.155 | 0.035 | 0.308 | 0.450 | 0.289 | 0.061 | 7.630 | 3.437 | 3.92E-07 | 7.76E-08 |
| 10 | 0.393 | 0.096 | 0.317 | 0.085 | 0.299 | 0.330 | 0.621 | 0.141 | 9.456 | 4.604 | 5.61E-07 | 9.44E-08 |
| 11 | 0.099 | 0.023 | 0.087 | 0.029 | 0.355 | 0.425 | 0.161 | 0.044 | 5.723 | 2.527 | 3.42E-07 | 8.55E-08 |
| 12 | 0.374 | 0.194 | 0.181 | 0.145 | 0.364 | 0.340 | 0.375 | 0.222 | 7.401 | 3.508 | 4.09E-07 | 2.59E-07 |
| 13 | 0.442 | 0.030 | 0.233 | 0.044 | 0.334 | 0.342 | 0.423 | 0.072 | 5.947 | 4.376 | 4.94E-07 | 8.89E-08 |
| 14 | 0.274 | 0.094 | 0.295 | 0.066 | 0.288 | 0.346 | 0.525 | 0.110 | 7.437 | 4.423 | 5.65E-07 | 6.40E-08 |
| 15 | 0.013 | 0.111 | 0.358 | 0.082 | 0.269 | 0.315 | 0.742 | 0.131 | 14.900 | 4.423 | 2.98E-07 | 8.37E-08 |
| 16 | 0.158 | 0.052 | 0.133 | 0.055 | 0.331 | 0.313 | 0.234 | 0.092 | 5.574 | 5.185 | 2.44E-07 | 2.15E-08 |
| 17 | 0.215 | 0.093 | 0.210 | 0.079 | 0.297 | 0.327 | 0.370 | 0.121 | 6.669 | 3.652 | 4.06E-07 | 5.55E-08 |
| 18 | 0.186 | 0.061 | 0.173 | 0.105 | 0.321 | 0.295 | 0.303 | 0.165 | 5.704 | 4.583 | 4.25E-07 | 9.13E-08 |

**Table A-2** Stress-relaxation parameters for the modified 3-parameter standard solid model for each control (–C) and treated (–T) specimen pair from the elastin-removal study – circumferential direction, TVAL.

| | $E_0$ *(N/mm)* | | $E_1$ *(N/mm)* | | $\alpha$ *(-)* | | $\eta_1$ *(Ns/mm)* | | $\tau$ (s) | | Error (-) | |
|---|---|---|---|---|---|---|---|---|---|---|---|---|
| ID | -C | -T | -C | -T | -C | -T | -C | -T | -C | -T | -C | -T |
| 1 | 0.160 | 0.032 | 0.116 | 0.023 | 0.272 | 0.371 | 0.199 | 0.034 | 7.31 | 2.651 | 1.25E-07 | 8.48E-08 |
| 2 | 0.051 | 0.047 | 0.066 | 0.026 | 0.245 | 0.256 | 0.113 | 0.040 | 9.148 | 5.108 | 2.39E-07 | 1.05E-07 |
| 3 | 0.075 | 0.04 | 0.129 | 0.033 | 0.256 | 0.437 | 0.241 | 0.050 | 11.231 | 2.552 | 2.12E-07 | 1.16E-07 |
| 4 | 0.086 | 0.049 | 0.101 | 0.014 | 0.299 | 0.432 | 0.196 | 0.024 | 9.076 | 3.647 | 1.74E-07 | 3.95E-08 |
| 5 | 0.076 | 0.027 | 0.037 | 0.010 | 0.312 | 0.491 | 0.061 | 0.015 | 4.931 | 2.379 | 2.84E-07 | 5.01E-08 |
| 6 | 0.06 | 0.069 | 0.115 | 0.055 | 0.295 | 0.200 | 0.246 | 0.068 | 13.321 | 2.846 | 1.40E-07 | 5.94E-08 |
| 7 | 0.086 | 0.052 | 0.080 | 0.036 | 0.300 | 0.394 | 0.142 | 0.057 | 6.616 | 3.188 | 2.53E-07 | 1.40E-07 |
| 8 | 0.120 | 0.021 | 0.092 | 0.013 | 0.300 | 0.463 | 0.163 | 0.024 | 6.743 | 3.545 | 1.89E-07 | 4.92E-08 |
| 9 | 0.081 | 0.016 | 0.125 | 0.022 | 0.248 | 0.318 | 0.228 | 0.033 | 11.370 | 3.906 | 2.72E-07 | 5.90E-08 |
| 10 | 0.008 | 0.008 | 0.178 | 0.044 | 0.273 | 0.276 | 0.403 | 0.073 | 19.767 | 6.179 | 2.15E-07 | 4.18E-08 |
| 11 | 0.056 | 0.032 | 0.190 | 0.025 | 0.238 | 0.349 | 0.337 | 0.035 | 11.069 | 2.726 | 2.06E-07 | 5.53E-08 |
| 12 | 0.056 | 0.064 | 0.084 | 0.063 | 0.267 | 0.277 | 0.149 | 0.098 | 8.431 | 4.938 | 4.84E-07 | 1.26E-07 |
| 13 | 0.079 | 0.018 | 0.052 | 0.015 | 0.300 | 0.365 | 0.094 | 0.025 | 7.100 | 3.598 | 1.63E-07 | 6.67E-08 |
| 14 | 0.048 | 0.023 | 0.186 | 0.039 | 0.279 | 0.312 | 0.404 | 0.065 | 16.382 | 5.097 | 1.83E-07 | 8.06E-08 |
| 15 | 0.040 | 0.057 | 0.149 | 0.052 | 0.258 | 0.325 | 0.260 | 0.087 | 8.679 | 4.686 | 1.91E-07 | 8.20E-08 |
| 16 | 0.025 | 0.028 | 0.155 | 0.046 | 0.264 | 0.270 | 0.341 | 0.072 | 20.076 | 5.301 | 1.32E-07 | 2.33E-08 |
| 17 | 0.004 | 0.047 | 0.333 | 0.063 | 0.294 | 0.291 | 0.822 | 0.096 | 21.733 | 4.336 | 1.37E-07 | 9.39E-08 |
| 18 | 0.004 | 0.027 | 0.126 | 0.049 | 0.266 | 0.292 | 0.257 | 0.074 | 14.751 | 4.144 | 2.08E-07 | 5.98E-08 |

**Table A-3** Stress-relaxation parameters for the modified 3-parameter standard solid model for each control (–C) and treated (–T) specimen pair from the elastin-removal study – radial direction, MVAL.

| | $E_0$ *(N/mm)* | | $E_1$ *(N/mm)* | | $\alpha$ *(-)* | | $\eta_1$ *(Ns/mm)* | | $\tau$ (s) | | Error (-) | |
|---|---|---|---|---|---|---|---|---|---|---|---|---|
| ID | -C | -T | -C | -T | -C | -T | -C | -T | -C | -T | -C | -T |
| 1 | 0.11 | 0.039 | 0.101 | 0.030 | 0.238 | 0.452 | 0.165 | 0.046 | 7.835 | 2.543 | 5.79E-07 | 1.12E-07 |
| 2 | 0.076 | 0.049 | 0.036 | 0.032 | 0.332 | 0.377 | 0.066 | 0.049 | 6.452 | 3.154 | 3.66E-07 | 8.84E-08 |
| 3 | 0.109 | 0.034 | 0.064 | 0.039 | 0.299 | 0.391 | 0.115 | 0.064 | 6.973 | 3.485 | 3.53E-07 | 1.09E-07 |
| 4 | 0.236 | 0.217 | 0.112 | 0.171 | 0.395 | 0.389 | 0.209 | 0.255 | 4.915 | 2.783 | 3.43E-07 | 2.59E-07 |
| 5 | 0.187 | 0.066 | 0.098 | 0.040 | 0.356 | 0.411 | 0.165 | 0.064 | 4.366 | 3.235 | 7.63E-07 | 1.16E-07 |
| 6 | 0.104 | 0.049 | 0.070 | 0.029 | 0.306 | 0.414 | 0.126 | 0.049 | 6.688 | 3.444 | 4.41E-07 | 1.32E-07 |
| 7 | 0.081 | 0.048 | 0.065 | 0.033 | 0.294 | 0.366 | 0.112 | 0.052 | 6.298 | 3.405 | 4.13E-07 | 6.26E-08 |
| 8 | 0.115 | 0.145 | 0.057 | 0.087 | 0.313 | 0.364 | 0.098 | 0.139 | 5.604 | 3.685 | 3.09E-07 | 7.93E-08 |
| 9 | 0.097 | 0.046 | 0.073 | 0.023 | 0.306 | 0.490 | 0.134 | 0.050 | 7.517 | 4.795 | 3.80E-07 | 7.78E-08 |
| 10 | 0.092 | 0.027 | 0.079 | 0.016 | 0.280 | 0.377 | 0.145 | 0.028 | 8.686 | 4.200 | 4.34E-07 | 9.77E-08 |
| 11 | 0.075 | 0.038 | 0.061 | 0.029 | 0.343 | 0.449 | 0.112 | 0.045 | 5.963 | 2.633 | 3.91E-07 | 6.70E-08 |
| 12 | 0.136 | 0.084 | 0.086 | 0.055 | 0.325 | 0.380 | 0.178 | 0.089 | 9.200 | 3.629 | 2.83E-07 | 1.60E-07 |
| 13 | 0.130 | 0.013 | 0.070 | 0.024 | 0.307 | 0.345 | 0.121 | 0.041 | 6.072 | 4.822 | 2.89E-07 | 5.77E-08 |
| 14 | 0.050 | 0.023 | 0.122 | 0.023 | 0.248 | 0.346 | 0.214 | 0.042 | 9.495 | 5.591 | 3.81E-07 | 5.19E-08 |
| 15 | 0.070 | 0.053 | 0.149 | 0.068 | 0.296 | 0.311 | 0.317 | 0.114 | 12.748 | 5.119 | 3.19E-07 | 9.89E-08 |
| 16 | 0.123 | 0.029 | 0.102 | 0.035 | 0.315 | 0.320 | 0.179 | 0.060 | 6.006 | 5.385 | 3.75E-07 | 8.45E-08 |
| 17 | 0.149 | 0.050 | 0.115 | 0.043 | 0.306 | 0.352 | 0.201 | 0.075 | 6.289 | 4.951 | 4.27E-07 | 7.66E-08 |
| 18 | 0.061 | 0.028 | 0.148 | 0.080 | 0.252 | 0.272 | 0.252 | 0.123 | 8.357 | 4.758 | 3.75E-07 | 1.27E-07 |

**Table A-4** Stress-relaxation parameters for the modified 3-parameter standard solid model for each control (–C) and treated (–T) specimen pair from the elastin-removal study – radial direction, TVAL.

| | $E_0$ *(N/mm)* | | $E_1$ *(N/mm)* | | $\alpha$ *(-)* | | $\eta_1$ *(Ns/mm)* | | $\tau$ (s) | | Error (-) | |
|---|---|---|---|---|---|---|---|---|---|---|---|---|
| ID | -C | -T | -C | -T | -C | -T | -C | -T | -C | -T | -C | -T |
| 1 | 0.053 | 0.055 | 0.034 | 0.035 | 0.275 | 0.408 | 0.057 | 0.052 | 6.675 | 2.654 | 1.67E-07 | 5.71E-08 |
| 2 | 0.030 | 0.016 | 0.041 | 0.005 | 0.238 | 0.443 | 0.069 | 0.008 | 8.851 | 2.566 | 2.97E-07 | 5.45E-08 |
| 3 | 0.035 | 0.043 | 0.051 | 0.034 | 0.258 | 0.402 | 0.093 | 0.050 | 10.016 | 2.667 | 1.94E-07 | 8.86E-08 |
| 4 | 0.026 | 0.010 | 0.097 | 0.019 | 0.257 | 0.157 | 0.183 | 0.026 | 11.973 | 7.861 | 1.59E-07 | 3.36E-08 |
| 5 | 0.038 | 0.044 | 0.064 | 0.017 | 0.231 | 0.454 | 0.111 | 0.027 | 10.821 | 2.791 | 3.18E-07 | 7.00E-08 |
| 6 | 0.012 | 0.006 | 0.048 | 0.003 | 0.268 | 0.765 | 0.107 | 0.010 | 19.057 | 5.234 | 1.35E-07 | 1.99E-08 |
| 7 | 0.049 | 0.072 | 0.053 | 0.052 | 0.285 | 0.388 | 0.091 | 0.081 | 6.682 | 3.133 | 2.37E-07 | 9.10E-08 |
| 8 | 0.06 | 0.020 | 0.053 | 0.020 | 0.300 | 0.368 | 0.094 | 0.028 | 6.843 | 2.541 | 2.45E-07 | 5.96E-08 |
| 9 | 0.013 | 0.008 | 0.053 | 0.009 | 0.216 | 0.284 | 0.097 | 0.012 | 15.49 | 3.094 | 1.93E-07 | 1.05E-07 |
| 10 | 0.015 | 0.006 | 0.031 | 0.008 | 0.283 | 0.308 | 0.068 | 0.013 | 14.949 | 5.658 | 1.20E-07 | 7.41E-08 |
| 11 | 0.016 | 0.015 | 0.028 | 0.018 | 0.254 | 0.292 | 0.048 | 0.023 | 8.956 | 2.199 | 1.26E-07 | 8.55E-08 |
| 12 | 0.032 | 0.077 | 0.120 | 0.082 | 0.247 | 0.299 | 0.217 | 0.133 | 11.210 | 5.012 | 3.07E-07 | 1.21E-07 |
| 13 | 0.033 | 0.004 | 0.033 | 0.021 | 0.265 | 0.255 | 0.055 | 0.032 | 7.321 | 4.752 | 2.00E-07 | 7.42E-08 |
| 14 | 0.023 | 0.029 | 0.076 | 0.053 | 0.271 | 0.299 | 0.160 | 0.093 | 15.524 | 6.598 | 1.31E-07 | 9.28E-08 |
| 15 | 0.005 | 0.045 | 0.064 | 0.053 | 0.252 | 0.320 | 0.111 | 0.085 | 8.810 | 4.376 | 2.07E-07 | 1.12E-07 |
| 16 | 0.019 | 0.037 | 0.072 | 0.071 | 0.267 | 0.279 | 0.158 | 0.114 | 19.032 | 5.527 | 1.22E-07 | 3.19E-08 |
| 17 | 0.033 | 0.029 | 0.027 | 0.031 | 0.369 | 0.305 | 0.065 | 0.050 | 11.214 | 4.729 | 2.72E-07 | 9.59E-08 |
| 18 | 0.004 | 0.033 | 0.089 | 0.070 | 0.281 | 0.278 | 0.198 | 0.112 | 17.149 | 5.273 | 2.36E-07 | 3.97E-08 |

**Table A-5** Stress-relaxation parameters for the modified 3-parameter standard solid model for each control (–C) and treated (–T) specimen pair from the collagen-removal study – circumferential direction, MVAL.

| | $E_0$ *(N/mm)* | | $E_1$ *(N/mm)* | | $\alpha$ *(-)* | | $\eta_1$ *(Ns/mm)* | | $\tau$ (s) | | Error (-) | |
|---|---|---|---|---|---|---|---|---|---|---|---|---|
| ID | -C | -T | -C | -T | -C | -T | -C | -T | -C | -T | -C | -T |
| 1 | 0.260 | 0.038 | 0.110 | 0.048 | 0.391 | 0.247 | 0.210 | 0.076 | 5.214 | 6.312 | 4.68E-07 | 1.53E-07 |
| 2 | 0.296 | 0.035 | 0.281 | 0.054 | 0.325 | 0.343 | 0.533 | 0.084 | 7.133 | 3.525 | 5.72E-07 | 1.14E-07 |
| 3 | 0.278 | 0.019 | 0.153 | 0.016 | 0.415 | 0.377 | 0.304 | 0.024 | 5.259 | 2.869 | 2.97E-07 | 9.03E-08 |
| 4 | 0.206 | 0.056 | 0.128 | 0.064 | 0.397 | 0.345 | 0.241 | 0.099 | 4.877 | 3.477 | 4.38E-07 | 1.41E-07 |
| 5 | 0.158 | 0.025 | 0.193 | 0.023 | 0.290 | 0.398 | 0.340 | 0.035 | 6.976 | 2.999 | 5.83E-07 | 5.01E-08 |
| 6 | 0.213 | 0.039 | 0.207 | 0.140 | 0.337 | 0.389 | 0.381 | 0.226 | 6.127 | 3.440 | 4.31E-07 | 2.28E-07 |
| 7 | 0.268 | 0.458 | 0.204 | 0.369 | 0.320 | 0.281 | 0.366 | 0.665 | 6.183 | 8.147 | 5.42E-07 | 4.96E-07 |
| 8 | 0.212 | 0.133 | 0.160 | 0.165 | 0.338 | 0.299 | 0.301 | 0.289 | 6.498 | 6.527 | 3.80E-07 | 5.75E-07 |
| 9 | 0.178 | 0.239 | 0.143 | 0.197 | 0.348 | 0.317 | 0.274 | 0.361 | 6.516 | 6.729 | 4.65E-07 | 4.58E-07 |
| 10 | 0.357 | 0.186 | 0.286 | 0.195 | 0.345 | 0.328 | 0.625 | 0.411 | 9.593 | 9.674 | 5.67E-07 | 2.68E-07 |
| 11 | 0.295 | 0.175 | 0.234 | 0.212 | 0.294 | 0.271 | 0.451 | 0.402 | 9.407 | 10.710 | 4.66E-07 | 4.11E-07 |
| 12 | 0.221 | 0.046 | 0.205 | 0.289 | 0.341 | 0.309 | 0.399 | 0.550 | 7.003 | 8.070 | 1.28E-06 | 7.15E-07 |
| 13 | 0.104 | 0.052 | 0.326 | 0.223 | 0.261 | 0.277 | 0.624 | 0.376 | 12.039 | 6.614 | 4.97E-07 | 3.08E-07 |
| 14 | 0.259 | 0.034 | 0.112 | 0.137 | 0.337 | 0.312 | 0.202 | 0.232 | 5.794 | 5.397 | 4.62E-07 | 3.18E-07 |
| 15 | 0.142 | 0.016 | 0.132 | 0.161 | 0.270 | 0.335 | 0.221 | 0.329 | 6.808 | 8.484 | 3.35E-07 | 1.21E-07 |
| 16 | 0.005 | 0.150 | 0.513 | 0.135 | 0.290 | 0.365 | 1.212 | 0.219 | 19.286 | 3.772 | 3.57E-07 | 7.49E-08 |

**Table A-6** Stress-relaxation parameters for the modified 3-parameter standard solid model for each control (–C) and treated (–T) specimen pair from the collagen-removal study – circumferential direction, TVAL.

| | $E_0$ *(N/mm)* | | $E_1$ *(N/mm)* | | $\alpha$ *(-)* | | $\eta_1$ *(Ns/mm)* | | $\tau$ (s) | | Error (-) | |
|---|---|---|---|---|---|---|---|---|---|---|---|---|
| ID | -C | -T | -C | -T | -C | -T | -C | -T | -C | -T | -C | -T |
| 1 | 0.104 | 0.056 | 0.149 | 0.059 | 0.272 | 0.277 | 0.276 | 0.098 | 9.614 | 6.197 | 1.97E-07 | 1.54E-07 |
| 2 | 0.150 | 0.031 | 0.137 | 0.083 | 0.272 | 0.260 | 0.225 | 0.127 | 6.102 | 5.008 | 2.47E-07 | 2.20E-07 |
| 3 | 0.121 | 0.039 | 0.086 | 0.106 | 0.320 | 0.279 | 0.156 | 0.195 | 6.544 | 8.957 | 2.22E-07 | 1.11E-07 |
| 4 | 0.065 | 0.025 | 0.093 | 0.038 | 0.283 | 0.319 | 0.167 | 0.057 | 7.889 | 3.574 | 2.45E-07 | 1.18E-07 |
| 5 | 0.182 | 0.035 | 0.096 | 0.026 | 0.328 | 0.331 | 0.167 | 0.043 | 5.363 | 4.777 | 2.02E-07 | 8.45E-08 |
| 6 | 0.056 | 0.002 | 0.110 | 0.016 | 0.275 | 0.202 | 0.207 | 0.024 | 10.147 | 9.250 | 2.53E-07 | 2.75E-08 |
| 7 | 0.077 | 0.020 | 0.063 | 0.019 | 0.295 | 0.367 | 0.115 | 0.030 | 7.985 | 3.339 | 1.84E-07 | 8.81E-08 |
| 8 | 0.036 | 0.008 | 0.169 | 0.176 | 0.265 | 0.231 | 0.335 | 0.332 | 13.100 | 15.703 | 2.63E-07 | 1.62E-07 |
| 9 | 0.068 | 0.068 | 0.048 | 0.057 | 0.265 | 0.251 | 0.085 | 0.099 | 8.542 | 9.123 | 1.22E-07 | 1.66E-07 |
| 10 | 0.051 | 0.035 | 0.108 | 0.042 | 0.239 | 0.283 | 0.190 | 0.067 | 10.636 | 5.163 | 1.97E-07 | 1.50E-07 |
| 11 | 0.153 | 0.020 | 0.085 | 0.111 | 0.304 | 0.245 | 0.152 | 0.214 | 6.820 | 14.420 | 2.29E-07 | 2.18E-07 |
| 12 | 0.148 | 0.044 | 0.108 | 0.087 | 0.368 | 0.224 | 0.407 | 0.111 | 36.903 | 3.056 | 1.32E-06 | 5.17E-08 |
| 13 | 0.008 | 0.022 | 0.293 | 0.152 | 0.252 | 0.226 | 0.620 | 0.249 | 19.399 | 9.077 | 2.37E-07 | 1.79E-07 |
| 14 | 0.264 | 0.077 | 0.106 | 0.071 | 0.305 | 0.352 | 0.179 | 0.125 | 5.671 | 4.993 | 1.23E-07 | 1.60E-07 |
| 15 | 0.067 | 0.006 | 0.079 | 0.064 | 0.276 | 0.229 | 0.145 | 0.097 | 9.186 | 6.377 | 2.15E-07 | 1.87E-07 |
| 16 | 0.143 | 0.039 | 0.106 | 0.056 | 0.288 | 0.335 | 0.184 | 0.085 | 6.732 | 3.512 | 2.76E-07 | 1.38E-07 |

**Table A-7** Stress-relaxation parameters for the modified 3-parameter standard solid model for each control (–C) and treated (–T) specimen pair from the collagen-removal study – radial direction, MVAL.

| | $E_0$ *(N/mm)* | | $E_1$ *(N/mm)* | | $\alpha$ *(-)* | | $\eta_1$ *(Ns/mm)* | | $\tau$ (s) | | Error (-) | |
|---|---|---|---|---|---|---|---|---|---|---|---|---|
| ID | -C | -T | -C | -T | -C | -T | -C | -T | -C | -T | -C | -T |
| 1 | 0.178 | 0.016 | 0.080 | 0.047 | 0.343 | 0.215 | 0.143 | 0.084 | 5.347 | 14.429 | 3.76E-07 | 1.27E-07 |
| 2 | 0.087 | 0.014 | 0.092 | 0.017 | 0.309 | 0.294 | 0.171 | 0.025 | 7.453 | 3.693 | 3.50E-07 | 8.39E-08 |
| 3 | 0.276 | 0.009 | 0.149 | 0.015 | 0.411 | 0.338 | 0.295 | 0.021 | 5.276 | 2.469 | 3.43E-07 | 7.38E-08 |
| 4 | 0.167 | 0.017 | 0.105 | 0.022 | 0.386 | 0.347 | 0.192 | 0.035 | 4.788 | 3.724 | 5.89E-07 | 1.73E-07 |
| 5 | 0.126 | 0.021 | 0.122 | 0.018 | 0.307 | 0.360 | 0.213 | 0.026 | 6.194 | 2.755 | 5.01E-07 | 1.23E-07 |
| 6 | 0.115 | 0.027 | 0.077 | 0.048 | 0.343 | 0.389 | 0.143 | 0.078 | 6.036 | 3.368 | 3.99E-07 | 1.79E-07 |
| 7 | 0.081 | 0.034 | 0.065 | 0.136 | 0.294 | 0.221 | 0.112 | 0.240 | 6.298 | 13.038 | 4.13E-07 | 6.29E-07 |
| 8 | 0.088 | 0.071 | 0.052 | 0.049 | 0.351 | 0.313 | 0.100 | 0.084 | 6.334 | 5.631 | 3.06E-07 | 2.81E-07 |
| 9 | 0.078 | 0.082 | 0.057 | 0.054 | 0.347 | 0.327 | 0.105 | 0.099 | 6.002 | 6.198 | 3.38E-07 | 2.96E-07 |
| 10 | 0.092 | 0.089 | 0.057 | 0.042 | 0.322 | 0.342 | 0.110 | 0.083 | 7.534 | 7.182 | 3.01E-07 | 1.64E-07 |
| 11 | 0.092 | 0.098 | 0.061 | 0.023 | 0.303 | 0.554 | 0.117 | 0.103 | 8.363 | 14.370 | 4.40E-07 | 1.33E-06 |
| 12 | 0.142 | 0.032 | 0.093 | 0.111 | 0.363 | 0.354 | 0.198 | 0.277 | 7.943 | 13.142 | 9.72E-07 | 8.20E-07 |
| 13 | 0.053 | 0.012 | 0.185 | 0.122 | 0.254 | 0.253 | 0.354 | 0.208 | 12.906 | 8.095 | 4.29E-07 | 2.64E-07 |
| 14 | 0.045 | 0.018 | 0.112 | 0.078 | 0.266 | 0.25 | 0.232 | 0.132 | 15.329 | 7.925 | 1.89E-06 | 2.51E-07 |
| 15 | 0.270 | 0.006 | 0.222 | 0.090 | 0.291 | 0.295 | 0.402 | 0.175 | 7.680 | 9.503 | 3.61E-07 | 2.44E-07 |
| 16 | 0.022 | 0.051 | 0.086 | 0.057 | 0.289 | 0.316 | 0.189 | 0.086 | 15.104 | 3.809 | 1.91E-07 | 1.70E-07 |

**Table A-8** Stress-relaxation parameters for the modified 3-parameter standard solid model for each control (–C) and treated (–T) specimen pair from the collagen-removal study – radial direction, TVAL.

| | $E_0$ *(N/mm)* | | $E_1$ *(N/mm)* | | $\alpha$ *(-)* | | $\eta_1$ *(Ns/mm)* | | $\tau$ (s) | | Error (-) | |
|---|---|---|---|---|---|---|---|---|---|---|---|---|
| ID | -C | -T | -C | -T | -C | -T | -C | -T | -C | -T | -C | -T |
| 1 | 0.040 | 0.024 | 0.031 | 0.016 | 0.280 | 0.284 | 0.053 | 0.026 | 6.733 | 5.885 | 2.30E-07 | 1.01E-07 |
| 2 | 0.045 | 0.015 | 0.029 | 0.017 | 0.314 | 0.317 | 0.048 | 0.026 | 4.988 | 4.044 | 2.18E-07 | 1.39E-07 |
| 3 | 0.041 | 0.012 | 0.033 | 0.026 | 0.305 | 0.276 | 0.059 | 0.045 | 6.942 | 7.618 | 1.54E-07 | 1.38E-07 |
| 4 | 0.024 | 0.014 | 0.062 | 0.018 | 0.263 | 0.395 | 0.111 | 0.028 | 9.113 | 3.082 | 3.18E-07 | 9.06E-08 |
| 5 | 0.071 | 0.001 | 0.039 | 0.017 | 0.323 | 0.214 | 0.066 | 0.024 | 5.090 | 6.182 | 2.41E-07 | 8.84E-08 |
| 6 | 0.013 | 0.002 | 0.054 | 0.001 | 0.233 | 0.927 | 0.098 | 0.010 | 12.228 | 8.880 | 2.37E-07 | 9.17E-09 |
| 7 | 0.055 | 0.026 | 0.049 | 0.023 | 0.293 | 0.406 | 0.090 | 0.035 | 7.941 | 2.813 | 1.63E-07 | 7.91E-08 |
| 8 | 0.025 | 0.042 | 0.034 | 0.039 | 0.285 | 0.268 | 0.062 | 0.067 | 8.284 | 7.446 | 2.43E-07 | 1.67E-07 |
| 9 | 0.006 | 0.006 | 0.063 | 0.071 | 0.208 | 0.199 | 0.114 | 0.127 | 17.209 | 19.15 | 1.54E-07 | 3.13E-07 |
| 10 | 0.026 | 0.012 | 0.030 | 0.016 | 0.268 | 0.305 | 0.052 | 0.026 | 7.689 | 4.827 | 2.16E-07 | 1.41E-07 |
| 11 | 0.062 | 0.009 | 0.036 | 0.056 | 0.289 | 0.233 | 0.065 | 0.108 | 7.662 | 16.909 | 1.73E-07 | 1.50E-07 |
| 12 | 0.276 | 0.054 | 0.046 | 0.024 | 0.581 | 0.576 | 0.328 | 0.121 | 29.516 | 16.305 | 1.49E-06 | 4.47E-07 |
| 13 | 0.029 | 0.024 | 0.050 | 0.072 | 0.277 | 0.243 | 0.099 | 0.121 | 11.870 | 8.174 | 3.49E-07 | 2.86E-07 |
| 14 | 0.067 | 0.014 | 0.017 | 0.055 | 0.532 | 0.264 | 0.063 | 0.085 | 11.666 | 5.465 | 1.02E-06 | 1.07E-07 |
| 15 | 0.029 | 0.002 | 0.038 | 0.041 | 0.252 | 0.245 | 0.067 | 0.071 | 9.283 | 9.113 | 1.92E-07 | 1.43E-07 |
| 16 | 0.074 | 0.032 | 0.069 | 0.044 | 0.268 | 0.330 | 0.116 | 0.069 | 7.057 | 3.802 | 3.16E-07 | 1.66E-07 |

# B VERIFICATION OF BAYESIAN OPTIMIZATION WITH THE BRANIN FUNCTION

We analyzed the effects of $\xi$ and the effects of additive noise on the performance of BO using a common test function—the Branin function. We chose this function due to the valley-shaped solution space and the presence of multiple local minima, which may emulate the worst-case scenario with the real patient tricuspid valve optimization. The Branin function is expressed as:

$$f(x) = a(x_2 - bx_1^2 + cx_1 - r)^2 + s(1-t)\cos(x_1) + s, \tag{B.0-1}$$

where $a = 1$, $b = 5.1/(4\pi^2)$, $c = 5/\pi$, $r = 6$, $s = 10$, and $t = 1/(8\pi)$, and the function is evaluated on the square $x_1 \in [-5, 10]$, $x_2 \in [0, 15]$. The local minima are located at $f(\mathbf{x}^*) = 0.397887$ where $\mathbf{x}^* = (-\pi, 12.275), (\pi, 2.275)$, and $(9.425, 2.475)$. The BO was performed with $\xi = 0.1, 0.2, 0.3, 0.4$, and $0.5$, in scenarios with and without noise added to the Branin function. In this scenario, the noise was added using a Gaussian distribution with a mean of zero and a standard deviation of 1 (i.e., $f(x)_{\text{noise}} = f(x) + N(0,1)$). All optimizations were run for 100 iterations (same as in **Section 6.2.3**) in a non-parallelized scenario to ensure repeatability of the results.

The results of the BO for the Branin function with and without added noise are shown in **Figs. B-1** and **B-2**, respectively. In the scenario without added noise, all three global minima were found across all five tested values of ER. When noise was added to the solution, however, the global minima were not obtained in all scenarios, as evidenced in $ER = 0.2$ and $ER = 0.5$ (only two out of the three global optima found). Regardless, the implementation and efficacy of the BO was successfully demonstrated using this test function.

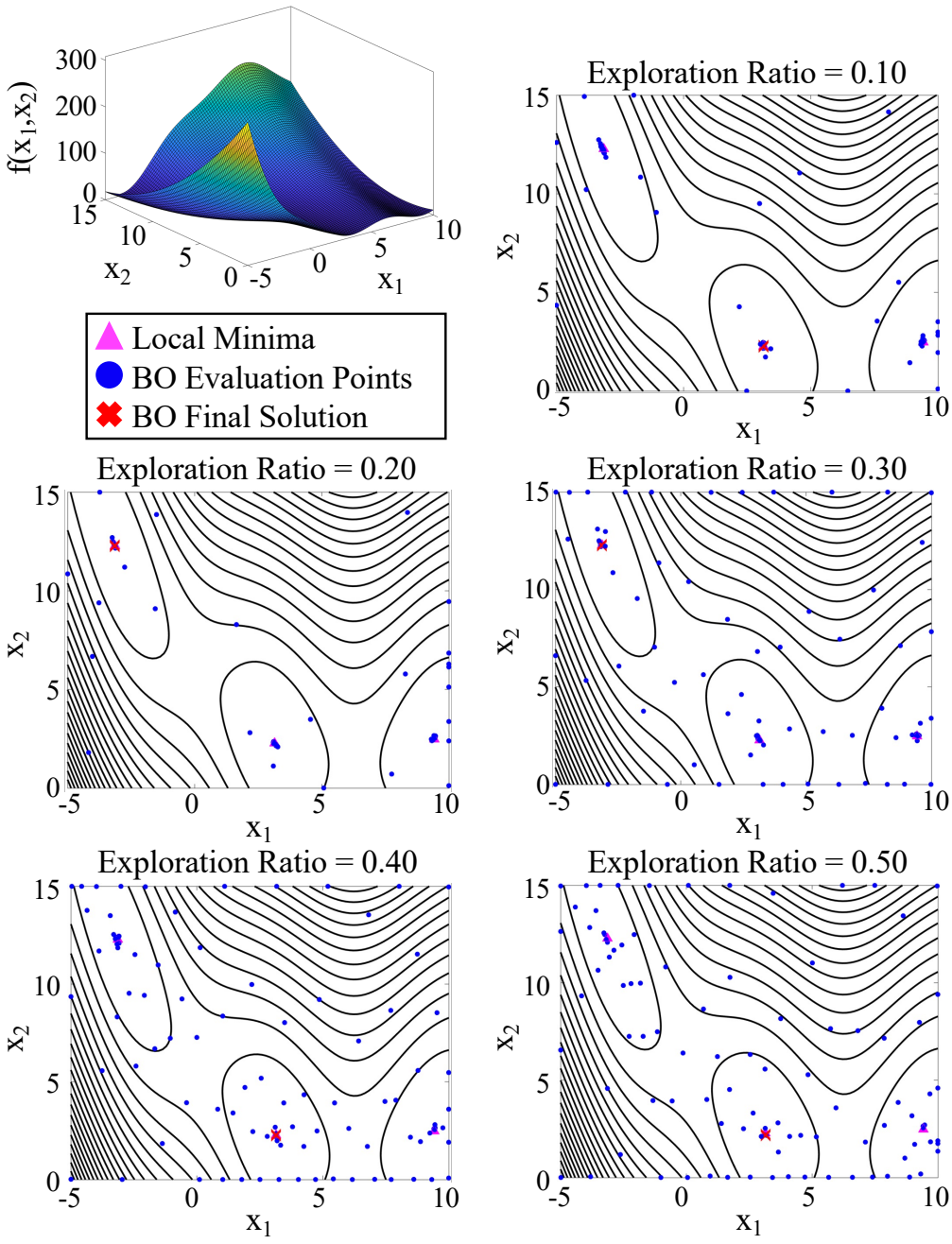


**Figure B-1** Bayesian optimization of the Branin function, with contour plots of the residual surface in the five tested exploration ratios ($\xi$).

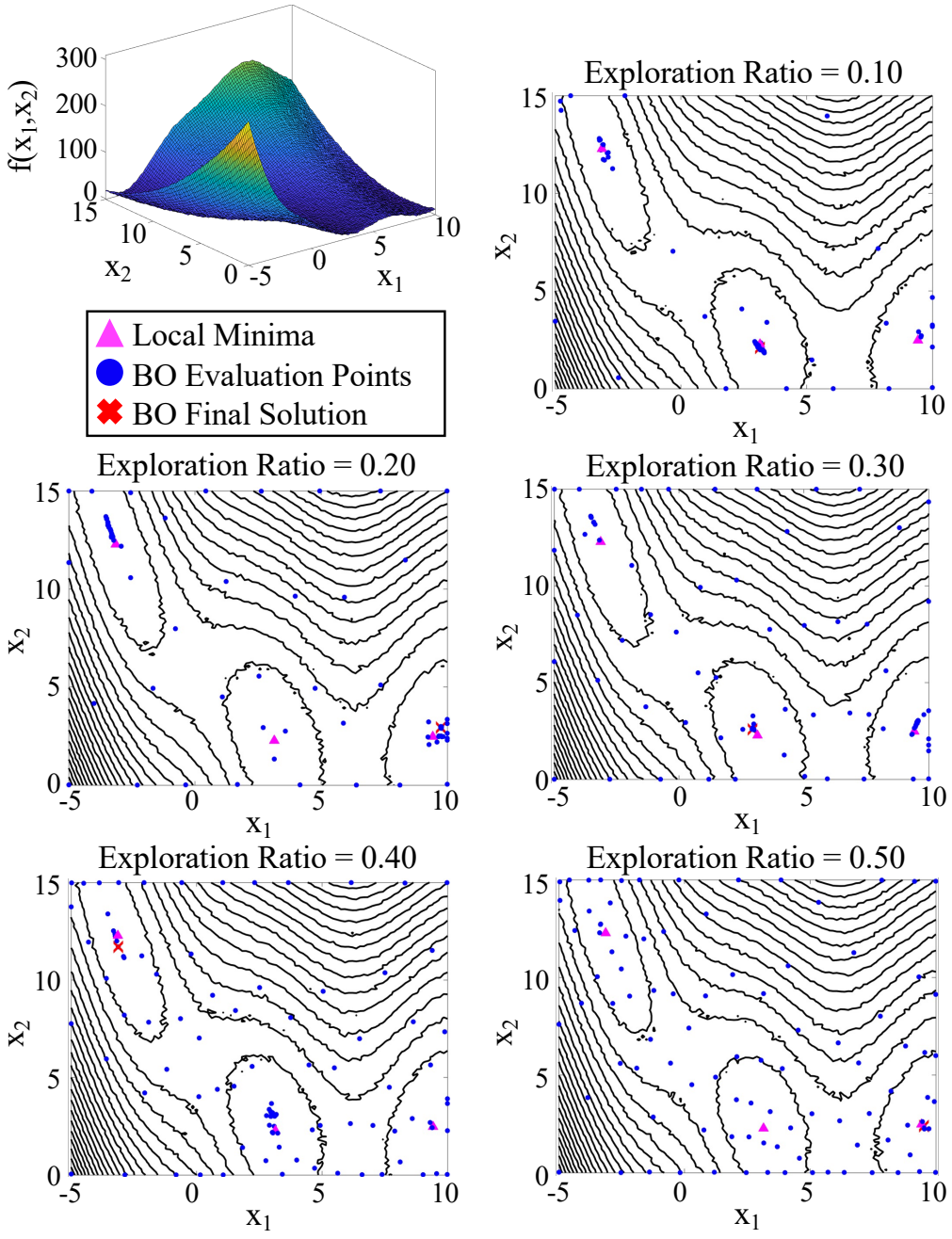


**Figure B-2** Bayesian optimization of the Branin function with added Gaussian noise, with contour plots of the residual surface in the five tested exploration ratios ($\xi$).

## REFERENCES


[1] M. Arsalan, T. Walther, R. L. Smith, and P. A. Grayburn, "Tricuspid regurgitation diagnosis and treatment," *European Heart Journal*, vol. 38, no. 9, pp. 634–638, 2017.

[2] J. P. Singh, J. C. Evans, D. Levy, M. G. Larson, L. A. Freed, D. L. Fuller, B. Lehman, and E. J. Benjamin, "Prevalence and clinical determinants of mitral, tricuspid, and aortic regurgitation (the Framingham Heart Study)," *The American Journal of Cardiology*, vol. 83, no. 6, pp. 897–902, 1999.

[3] Y. Topilsky, S. Maltais, J. Medina Inojosa, D. Oguz, H. Michelena, J. Maalouf, D. W. Mahoney, and M. Enriquez-Sarano, "Burden of tricuspid regurgitation in patients diagnosed in the community setting," *JACC: Cardiovascular Imaging*, vol. 12, no. 3, pp. 433–442, 2019.

[4] J. Nath, E. Foster, and P. A. Heidenreich, "Impact of tricuspid regurgitation on long-term survival," *Journal of the American College of Cardiology*, vol. 43, no. 3, pp. 405–409, 2004.

[5] M. Russo, R. Zilberszac, P. Werner, A. Kocher, D. Wiedemann, M. Schneider, J. Mascherbauer, G. Laufer, R. Rosenhek, and M. Andreas, "Isolated tricuspid valve regurgitation: Old concepts, new insights and innovation," *Journal of Cardiovascular Medicine*, vol. 21, no. 6, pp. 406–414, 2020.

[6] W. D. Meador, M. Mathur, G. P. Sugerman, M. Malinowski, T. Jazwiec, X. Wang, C. M. Lacerda, T. A. Timek, and M. K. Rausch, "The tricuspid valve also maladapts as shown in sheep with biventricular heart failure," *eLife*, vol. 9, e63855, 2020.

[7] L. Gross and M. A. Kugel, "Topographic anatomy and histology of the valves in the human heart," *The American Journal of Pathology*, vol. 7, no. 5, pp. 445–474.7, 1931.

[8] K. S. Kunzelman, R. P. Cochran, S. S. Murphree, W. S. Ring, E. D. Verrier, and R. C. Eberhart, "Differential collagen distribution in the mitral valve and its influence on biomechanical behaviour," *The Journal of Heart Valve Disease*, vol. 2, no. 2, pp. 236–244, 1993.

[9] M. Martin and H.-H. Sievers, "Heart valve macro- and microstructure," *Philosophical Transactions of the Royal Society B: Biological Sciences*, vol. 362, no. 1484, pp. 1421–1436, 2007.

[10] K. E. Kramer, C. J. Ross, D. W. Laurence, A. R. Babu, Y. Wu, R. A. Towner, A. Mir, H. M. Burkhart, G. A. Holzapfel, and C.-H. Lee, "An investigation of layer-specific tissue biomechanics of porcine atrioventricular valve anterior leaflets," *Acta Biomaterialia*, vol. 96, pp. 368–384, 2019.

[11] C.-H. Lee, D. W. Laurence, C. J. Ross, K. E. Kramer, A. R. Babu, E. L. Johnson, M.-C. Hsu, A. Aggarwal, A. Mir, H. M. Burkhar, R. A. Towner, R. Baumwart, and Y. Wu, "Mechanics of the tricuspid valve—-from clinical diagnosis/treatment, in-vivo and in-vitro investigations, to patient-specific biomechanical modeling," *Bioengineering*, vol. 6, no. 2, p. 47, 2019.

[12] M. S. Sacks and A. P. Yoganathan, "Heart valve function: A biomechanical perspective," *Philosophical Transactions of the Royal Society B: Biological Sciences*, vol. 362, no. 1484, pp. 1369–1391, 2007.

[13] M. Misfeld and H. H. Sievers, "Heart valve macro- and microstructure," *Philosophical Transactions of the Royal Society B: Biological Sciences*, vol. 362, no. 1484, pp. 1421–1436, 2007.

[14] M. S. Sacks, "Biaxial mechanical evaluation of planar biological materials," *Journal of Elasticity and the Physical Science of Solids*, vol. 61, pp. 199–246, 2000.

[15] G. A. Holzapfel, *Nonlinear solid mechanics: A continuum approach for engineering science*, 2002.

[16] M. Sacks, Y. Enomoto, J. R. Graybill, W. D. Merryman, A. Zeeshan, A. P. Yoganathan, R. J. Levy, R. C. Gorman, and J. H. G. III, "In-vivo dynamic deformation of the mitral valve anterior leaflet," *The Annals of Thoracic Surgery*, vol. 82, no. 4, pp. 1369–1377, 2006.

[17] J.-P. Rabbah, N. Saikrishnan, and A. P. Yoganathan, "A novel left heart simulator for the multi-modality characterization of native mitral valve geometry and fluid mechanics," *Annals of Biomedical Engineering*, vol. 41, pp. 305–315, 2013.

[18] S. Heyden, A. Nagler, C. Bertoglio, J. Biehler, M. W. Gee, *et al.*, "Material modeling of cardiac valve tissue: Experiments, constitutive analysis and numerical investigation," *Journal of Biomechanics*, vol. 48, no. 16, pp. 4287–4296, 2015.

[19] K. A. Khoiy and R. Amini, "On the biaxial mechanical response of porcine tricuspid valve leaflets," *Journal of Biomechanical Engineering*, vol. 138, no. 10, p. 104 504, 2016.

[20] W. D. Meador, M. Mathur, G. P. Sugerman, T. Jazwiec, M. Malinowski, M. R. Bersi, T. A. Timek, and M. K. Rausch, "A detailed mechanical and microstructural analysis of ovine tricuspid valve leaflets," *Acta Biomaterialia*, vol. 102, pp. 100–113, 2020.

[21] T. Pham, F. Sulejmani, E. Shin, D. Wang, and W. Sun, "Quantification and comparison of the mechanical properties of four human cardiac valves," *Acta Biomaterialia*, vol. 54, pp. 345–355, 2017.

[22] S. V. Jett, D. W. Laurence, R. P. Kunkel, A. R. Babu, K. E. Kramer, R. Baumwart, R. A. Towner, Y. Wu, and C.-H. Lee, "An investigation of the anisotropic mechanical properties and anatomical structure of porcine atrioventricular heart valves," *Journal of the Mechanical Behavior of Biomedical Materials*, vol. 87, pp. 155–171, 2018.

[23] C. J. Ross, D. W. Laurence, Y. Wu, and C.-H. Lee, "Biaxial mechanical characterizations of atrioventricular heart valves," *Journal of Visualized Experiments*, vol. 146, e59170, 2019.

[24] Y.-C. Fung, *Biomechanics: Mechanical Properties of Living Tissues*. Springer Science & Business Media, 2013.

[25] J. S. Grashow, A. P. Yoganathan, and M. S. Sacks, "Biaixal stress–-stretch behavior of the mitral valve anterior leaflet at physiologic strain rates," *Annals of Biomedical Engineering*, vol. 34, pp. 315–325, 2006.

[26] T. Pham and W. Sun, "Material properties of aged human mitral valve leaflets," *Journal of Biomedical Materials Research Part A*, vol. 102, no. 8, pp. 2692–2703, 2014.

[27] D. W. Laurence, C. J. Ross, S. V. Jett, C. H. Johns, A. L. Echols, R. Baumwart, R. A. Towner, J. Liao, P. Bajona, Y. Wu, and C.-H. Lee, "An investigation of regional variations in the biaxial mechanical properties and stress relaxation behaviors of porcine atrioventricular heart valve leaflets," *Journal of Biomechanics*, vol. 83, pp. 16–27, 2019.

[28] M. K. Rausch and E. Kuhl, "On the effect of prestrain and residual stress in thin biological membranes," *Journal of the Mechanics and Physics of Solids*, vol. 61, no. 9, pp. 1955–1969, 2013.

[29] V Prot and B. Skallerud, "Nonlinear solid finite element analysis of mitral valves with heterogeneous leaflet layers," *Computational Mechanics*, vol. 43, pp. 353–368, 2009.

[30] V Prot, B Skallerud, G Sommer, and G. A. Holzapfel, "On modelling and analysis of healthy and pathological human mitral valves: Two case studies," *Journal of the Mechanical Behavior of Biomedical Materials*, vol. 3, no. 2, pp. 167–177, 2010.

[31] R. Amini, C. E. Eckert, K. Koomalsingh, J. McGarvey, M. Minakawa, *et al.*, "On the *in vivo* deformation of the mitral valve anterior leaflet: Effects of annular geometry and referential configuration," *Annals of Biomedical Engineering*, vol. 40, pp. 1455–67, 2012.

[32] G. A. Duginski, C. J. Ross, D. W. Laurence, C. H. Johns, and C.-H. Lee, "An investigation of the effect of freezing storage on the biaxial mechanical properties of excised porcine tricuspid valve anterior leaflets," *Journal of the Mechanical Behavior of Biomedical Materials*, vol. 101, p. 103 438, 2020.

[33] S. D. Salinas, M. M. Clark, and R. Amini, "The effects of -80°C short-term storage on the mechanical response of tricuspid valve leaflets," *Journal of Biomechanics*, vol. 98, p. 109 462, 2020.

[34] I. Vesely, "The role of elastin in aortic valve mechanics," *Journal of Biomechanics*, vol. 31, no. 2, pp. 115–123, 1998.

[35] S. Huang and H. Y. S. Huang, "Biaxial stress relaxation of semilunar heart valve leaflets during simulated collagen catabolism: Effects of collagenase concentration and equibiaxial strain state," *Proceedings of the Institution of Mechanical Engineers. Part H, Journal of Engineering in Medicine*, vol. 229, no. 10, pp. 721–731, 2015.

[36] K. J. Rodriguez, L. M. Piechura, A. M. Porras, and K. S. Masters, "Manipulation of valve composition to elucidate the role of collagen in aortic valve calcification," *BMC Cardiovasc. Disord.*, vol. 14, p. 29, 2014.

[37] J. J. Lovekamp, D. T. Simionescu, J. J. Mercuri, B. Zubiate, M. S. Sacks, and N. R. Vyavahare, "Stability and function of glycosaminoglycans in porcine bioprosthetic heart valves," *Biomaterials*, vol. 27, no. 8, pp. 1507–1518, 2006.

[38] J. M. Bender, W. R. Adams, A. Mahadevan-Jansen, W. D. Merryman, and M. R. Bersi, "Radiofrequency ablation alters the microstructural organization of healthy and enzymatically digested porcine mitral valves," *Experimental Mechanics*, vol. 61, pp. 237–251, 2021.

[39] C. J. Ross, D. W. Laurence, J. Richardson, A. R. Babu, L. E. Evans, E. G. Beyer, Y. Wu, R. A. Towner, K. M. Fung, A. Mir, H. M. Burkhart, G. A. Holzapfel, and C.-H. Lee, "An investigation of the glycosaminoglycan contribution to biaxial mechanical behaviors of porcine atrioventricular heart valve leaflets," *Journal of the Royal Society Interface*, vol. 16, no. 156, p. 20 190 069, 2019.

[40] I. Vesely and R. Noseworthy, "Micromechanics of the fibrosa and the ventricularis in aortic valve leaflets," *Journal of Biomechanics*, vol. 25, no. 1, pp. 101–109, 111–113, 1992.

[41] I. Vesely and A. Lozon, "Natural preload of aortic valve leaflet components during glutaraldehyde fixation: Effects on tissue mechanics," *Journal of Biomechanics*, vol. 26, no. 2, pp. 121–131, 1993.

[42] J. A. Stella and M. S. Sacks, "On the biaxial mechanical properties of the layers of the aortic valve leaflet," *Journal of Biomechanical Engineering*, vol. 129, no. 5, pp. 757–766, 2007.

[43] A. Basu and Z. He, "Annulus tension on the tricuspid valve: An in-vitro study," *Cardiovascular Engineering and Technology*, vol. 7, pp. 270–279, 2016.

[44] K. A. Khoiy, D. Biswas, T. N. Decker, K. T. Asgarian, F. Loth, *et al.*, "Surface strains of porcine tricuspid valve septal leaflets measured in ex vivo beating hearts," *Journal of Biomechanical Engineering*, vol. 138, no. 11, p. 111 006, 2016.

[45] K. A. Khoiy, K. T. Asgarian, F. Loth, and R. Amini, "Dilation of tricuspid valve annulus immediately after rupture of chordae tendineae in ex-vivo porcine hearts," *PLoS One*, vol. 13, no. 11, e0206744, 2018.

[46] M. Mathur, T. Jazwiec, W. D. Meador, M. Malinowski, M. Goehler, H. Ferguson, T. A. Timek, and M. K. Rausch, "Tricuspid valve leaflet strains in the beating ovine heart," *Biomechanics and Modeling in Mechanobiology*, vol. 18, pp. 1351–1361, 2019.

[47] M. Mathur, W. D. Meador, T. Jazwiec, M. Malinowski, T. A. Timek, *et al.*, "Tricuspid valve annuloplasty alters leaflet mechanics," *Annals of Biomedical Engineering*, pp. 2911–2923, 2020.

[48] N. J. B. Driessen, C. V. C. Bouten, and F. P. T. Baaijens, "Improved prediction of the collagen fiber architecture in the aortic heart valve," *Journal of Biomechanical Engineering*, vol. 127, no. 2, pp. 329–36, 2005.

[49] J. Liao, L. Yang, J. Grashow, and M. S. Sacks, "The relation between collagen fibril kinematics and mechanical properties in the mitral valve anterior leaflet," *Journal of Biomechanical Engineering*, vol. 129, no. 1, pp. 78–87, 2007.

[50] C.-H. Lee, W. Zhang, J. Liao, C. A. Carruthers, J. I. Sacks, and M. S. Sacks, "On the presence of affine fibril and fiber kinematics in the mitral valve anterior leaflet," *Biophysical Journal*, vol. 108, no. 8, pp. 2074–2087, 2015.

[51] A. D. Pant, V. S. Thomas, A. L. Black, T. Verba, J. G. Lesicko, *et al.*, "Pressure-induced microstructural changes in porcine tricuspid valve leaflets," *Acta Biomaterialia*, vol. 67, pp. 248–258, 2018.

[52] V. S. Thomas, V. Lai, and R. Amini, "A computational multi-scale approach to investigate mechanically-induced changes in tricuspid valve anterior leaflet microstructure," *Acta Biomaterialia*, vol. 94, pp. 524–535, 2019.

[53] A. Pokutta-Paskaleva, F. Sulejmani, M. DelRocini, and W. Sun, "Comparative mechanical, morphological, and microstructural characterization of porcine mitral and tricuspid leaflets and chordae tendineae," *Acta Biomaterialia*, vol. 85, pp. 241–252, 2019.

[54] L. T. Hudson, S. V. Jett, K. E. Kramer, D. W. Laurence, C. J. Ross, R. A. Towner, R. Baumwart, K. M. Lim, A. Mir, H. M. Burkhart, Y. Wu, and C.-H. Lee, "A pilot study on linking tissue mechanics with load-dependent collagen microstructures in porcine tricuspid valve leaflets," *Bioengineering*, vol. 7, no. 2, p. 60, 2020.

[55] S. Plotnikov, V. Juneja, A. B. Isaacson, W. A. Mohler, and P. J. Campagnola, "Optical clearing for improved contrast in second harmonic generation imaging of skeletal muscle," *Biophysical Journal*, vol. 90, no. 1, pp. 328–339, 2006.

[56] W. Goth, B. Yang, J. Lesicko, A. Allen, M. S. Sacks, and J. W. Tunnell, "Polarized spatial frequency domain imaging of heart valve fiber structure," in *Proceedings of SPIE Volume 9710, Optical Elastography and Tissue Biomechanics III*, vol. 9710, 2016, p. 971 019.

[57] A. Anssari-Benam and A. Bucchi, "Modeling the deformation of the elastin network in the aortic valve," *Journal of Biomechanical Engineering*, vol. 140, no. 1, p. 011 004, 2018.

[58] N. T. Jacobs, D. H. Cortes, E. J. Vresilovic, and D. M. Elliott, "Biaxial tension of fibrous tissue: Using finite element methods to address experimental challenges arising from boundary conditions and anisotropy," *Journal of Biomechanical Engineering*, vol. 135, no. 2, p. 021 004, 2013.

[59] Y. Lanir, "Multi-scale structural modeling of soft tissues mechanics and mechanobiology," *Journal of Elasticity*, vol. 129, pp. 7–48, 2017.

[60] R. Fan and M. S. Sacks, "Simulation of planar soft tissues using a structural constitutive model: Finite element implementation and validation," *Journal of Biomechanics*, vol. 47, no. 9, pp. 2043–2054, 2014.

[61] D. Bianchi, C. Morin, and P. Badel, "Implementing a micromechanical model into a finite element code to simulate the mechanical and microstructural response of arteries," *Biomechanics and Modeling in Mechanobiology*, vol. 19, pp. 2553–2566, 2020.

[62] R. Y. Dhume and V. H. Barocas, "Emergent structure-dependent relaxation spectra in viscoelastic fiber networks in extension," *Acta Biomaterialia*, vol. 87, pp. 245–255, 2019.

[63] C. Morin, S. Avril, and C. Hellmich, "Non-affine fiber kinematics in arterial mechanics: A continuum micromechanical investigation," *Journal of Applied Mathematics and Mechanics / Zeitschrift für Angewandte Mathematik und Mechanik*, vol. 98, no. 12, pp. 2101–2121, 2018.

[64] E. B. Tadmor, R. E. Miller, and R. S. Elliott, *Continuum Mechanics and Thermodynamics: From Fundamental Concepts to Governing Equations*. Cambridge University Press, 2012.

[65] C. Jayyosi, J.-S. Affagard, G. Ducourthial, C. Bonod-Bidaud, B. Lynch, S. Bancelin, F. Ruggiero, M.-C. Schanne-Klein, J.-M. Allain, and K. Bruyère-Garnier, "Affine kinematics in planar fibrous connective tissues: An experimental investigation," *Biomechanics and Modeling in Mechanobiology*, vol. 16, pp. 1459–1473, 2017.

[66] S. P. Lake, D. H. Cortes, J. A. Kadlowec, L. J. Soslowsky, and D. M. Elliott, "Evaluation of affine fiber kinematics in human supraspinatus tendon using quantitative projection plot analysis," *Biomechanics and Modeling in Mechanobiology*, vol. 11, pp. 197–205, 2012.

[67] K. L. Billiar and M. S. Sacks, "A method to quantify the fiber kinematics of planar tissues under biaxial stretch," *Journal of Biomechanics*, vol. 30, no. 7, pp. 753–756, 1997.

[68] T. W. Gilbert, M. S. Sacks, J. S. Grashow, S. L.-Y. Woo, S. F. Badylak, and M. B. Chancellor, "Fiber kinematics of small intestinal submucosa under biaxial and uniaxial stretch," *Journal of Biomechanical Engineering*, vol. 128, no. 6, pp. 890–898, 2006.

[69] C. Cavinato, C. Helfenstein-Didier, T. Olivier, S. R. Du Roscoat, N. Laroche, and P. Badel, "Biaxial loading of arterial tissues with 3D *in situ* observations of adventitia fibrous microstructure: A method coupling multi-photon confocal microscopy and bulge inflation test," *Journal of the Mechanical Behavior of Biomedical Materials*, vol. 74, pp. 488–498, 2017.

[70] C. Cavinato, P. Badel, W. Krasny, S. Avril, and C. Morin, "Experimental characterization of adventitial collagen fiber kinematics using second-harmonic generation imaging microscopy: Similarities and differences across arteries, species and testing conditions," in *Multi-scale Extracellular Matrix Mechanics and Mechanobiology*, Springer, 2020, pp. 123–164.

[71] L. Zhang, S. P. Lake, V. K. Lai, C. R. Picu, V. H. Barocas, and M. S. Shephard, "A coupled fiber-matrix model demonstrates highly inhomogeneous microstructural interactions in soft tissues under tensile load," *Journal of Biomechanical Engineering*, vol. 135, no. 1, p. 011 008, 2013.

[72] M. Stevanella, E. Votta, M. Lemma, C. Antona, and A. Redaelli, "Finite element modelling of the tricuspid valve: A preliminary study," *Medical Engineering & Physics*, vol. 32, no. 10, pp. 1213–23, 2010.

[73] F. Kong, T. Pham, C. Martin, R. McKay, C. Primiano, *et al.*, "Finite element analysis of tricuspid valve deformation from multi-slice computed tomography images," *Annals of Biomedical Engineering*, vol. 46, pp. 1112–1127, 2018.

[74] S. Singh-Gryzbon, V. Sadri, M. Toma, E. L. Pierce, Z. A. Wei, *et al.*, "Development of a computational method for simulating tricuspid valve dynamics," *Annals of Biomedical Engineering*, vol. 47, pp. 1422–1434, 2019.

[75] Y. Dabiri, J. Yao, K. L. Sack, G. S. Kassab, and J. M. Guccione, "Tricuspid valve regurgitation decreases after mitraclip implantation: Fluid structure interaction simulation," *Mechanics Research Communications*, vol. 97, pp. 96–100, 2019.

[76] D. Kamensky, F. Xu, C.-H. Lee, J. Yan, Y. Bazilevs, *et al.*, "A contact formulation based on a volumetric potential: Application to isogeometric simulations of atrioventricular valves," *Computer Methods in Applied Mechanics and Engineering*, vol. 330, pp. 522–546, 2018.

[77] D. W. Laurence, E. L. Johnson, M.-C. Hsu, R. Baumwart, A. Mir, H. M. Burkhart, G. A. Holzapfel, Y. Wu, and C.-H. Lee, "A pilot *in silico* modeling-based study of the pathological effects on the biomechanical function of tricuspid valves," *International Journal for Numerical Methods in Biomedical Engineering*, vol. 36, no. 7, e3346, 2020.

[78] I. Stankovic, A. M. Daraban, R. Jasaityte, A. N. Neskovic, P. Claus, *et al.*, "Incremental value of the en face view of the tricuspid valve by two-dimensional and three-dimensional echocardiography for accurate identification of tricuspid valve leaflets," *Journal of the American Society of Echocardiography*, vol. 27, no. 4, pp. 376–384, 2014.

[79] M. Abbasi, M. S. Barakat, K. Vahidkhah, and A. N. Azadani, "Characterization of three-dimensional anisotropic heart valve tissue mechanical properties using inverse finite element analysis," *Journal of the Mechanical Behavior of Biomedical Materials*, vol. 62, pp. 33–44, 2016.

[80] A. Aggarwal and M. S. Sacks, "An inverse modeling approach for semilunar heart valve leaflet mechanics: Exploitation of tissue structure," *Biomechanics and Modeling in Mechanobiology*, vol. 15, pp. 909–932, 2016.

[81] C.-H. Lee, R. Amini, R. C. Gorman, J. H. Gorman III, and M. S. Sacks, "An inverse modeling approach for stress estimation in mitral valve anterior leaflet valvuloplasty for in-vivo valvular biomaterial assessment," *Journal of Biomechanics*, vol. 47, no. 9, pp. 2055–2063, 2014.

[82] M. K. Rausch, F. A. Tibayan, N. B. Ingels, D. C. Miller, and E. Kuhl, "Mechanics of the mitral annulus in chronic ischemic cardiomyopathy," *Annals of Biomedical Engineering*, vol. 41, pp. 2171–2180, 2013.

[83] C.-H. Lee, W. Zhang, K. Feaver, R. C. Gorman, J. H. Gorman III, and M. S. Sacks, "On the *in vivo* function of the mitral heart valve leaflet: Insights into tissue–interstitial cell biomechanical coupling," *Biomechanics and Modeling in Mechanobiology*, vol. 16, no. 5, pp. 1613–1632, 2017.

[84] G. Krishnamurthy, D. B. Ennis, A. Itoh, W. Bothe, J. C. Swanson, M. Karlsson, E. Kuhl, D. C. Miller, and N. B. Ingels Jr, "Material properties of the ovine mitral valve anterior leaflet *in vivo* from inverse finite element analysis," *American Journal of Physiology: Heart and Circulatory Physiology*, vol. 295, no. 3, H1141–H1149, 2008.

[85] G. Krishnamurthy, A. Itoh, J. C. Swanson, D. C. Miller, and N. B. Ingels Jr, "Transient stiffening of mitral valve leaflets in the beating heart," *American Journal of Physiology Heart and Circulatory Physiology*, vol. 298, no. 6, H2221–H2225, 2010.

[86] Q. Wang and W. Sun, "Finite element modeling of mitral valve dynamic deformation using patient-specific multi-slices computed tomography scans," *Annals of Biomedical Engineering*, vol. 41, pp. 142–153, 2013.

[87] P. Oomen, S. Loerakker, D. van Geemen, J. Neggers, M.-J. Goumans, A. J. van den Bogaerdt, A. J. Bogers, C. V. Bouten, and F. P. Baaijens, "Age-dependent changes of stress and strain in the human heart valve and their relation with collagen remodeling," *Acta Biomaterialia*, vol. 29, pp. 161–169, 2016.

[88] M. Stevanella, F. Maffessanti, C. A. Conti, E. Votta, A. Arnoldi, M. Lombardi, O. Parodi, E. G. Caiani, and A. Redaelli, "Mitral valve patient-specific finite element modeling from cardiac mri: Application to an annuloplasty procedure," *Cardiovascular Engineering and Technology*, vol. 2, no. 2, pp. 66–76, 2011.

[89] C. A. Conti, A. Della Corte, E. Votta, L. Del Viscovo, C. Bancone, L. S. De Santo, and A. Redaelli, "Biomechanical implications of the congenital bicuspid aortic valve: A finite element study of aortic root function from *in vivo* data," *The Journal of Thoracic and Cardiovascular Surgery*, vol. 140, no. 4, pp. 890–896, 2010.

[90] C. I. Tchervenkov, J. P. Jacobs, P. M. Weinberg, V. D. Aiello, M. J. Béland, S. D. Colan, M. J. Elliott, R. C. Franklin, J. W. Gaynor, O. N. Krogmann, *et al.*, "The nomenclature, definition and classification of hypoplastic left heart syndrome," *Cardiology in the Young*, vol. 16, no. 4, pp. 339–368, 2006.

[91] M. Yabrodi and C. W. Mastropietro, "Hypoplastic left heart syndrome: From comfort care to long-term survival," *Pediatric Research*, vol. 81, pp. 142–149, 2017.

[92] A. Saraf, W. M. Book, T. J. Nelson, and C. Xu, "Hypoplastic left heart syndrome: From bedside to bench and back," *Journal of Molecular and Cellular Cardiology*, vol. 135, pp. 109–118, 2019.

[93] W. I. Norwood, J. K. Kirklin, and S. P. Sanders, "Hypoplastic left heart syndrome: Experience with palliative surgery," *The American Journal of Cardiology*, vol. 45, no. 1, pp. 87–91, 1980.

[94] J Maxwell, J. D. Pigott, J. D. Murphy, G. Barber, and W. I. Norwood, "Palliative reconstructive surgery for hypoplastic left heart syndrome," *The Annals of Thoracic Surgery*, vol. 45, no. 2, pp. 122–128, 1988.

[95] S. Sano, K. Ishino, M. Kawada, S. Arai, S. Kasahara, T. Asai, Z. Masuda, M. Takeuchi, and S. Ohtsuki, "Right ventricle–pulmonary artery shunt in first-stage palliation of hypoplastic left heart syndrome," *The Journal of Thoracic and Cardiovascular Surgery*, vol. 126, no. 2, pp. 504–509, 2003.

[96] A. K. Pridjian, A. M. Mendelsohn, F. M. Lupinetti, R. H. Beekman III, M. Dick II, G. Serwer, and E. L. Bove, "Usefulness of the bidirectional Glenn procedure as staged reconstruction for the functional single ventricle," *The American Journal of Cardiology*, vol. 71, no. 11, pp. 959–962, 1993.

[97] M. A. Scheurer, E. G. Hill, N. Vasuki, S. Maurer, E. M. Graham, V. Bandisode, G. S. Shirali, A. M. Atz, and S. M. Bradley, "Survival after bidirectional cavopulmonary anastomosis: Analysis of preoperative risk factors," *The Journal of Thoracic and Cardiovascular Surgery*, vol. 134, no. 1, 82–89.e2, 2007.

[98] F Fontan and E Baudet, “Surgical repair of tricuspid atresia,” *Thorax*, vol. 26, pp. 240–248, 1971.

[99] J. D. Salazar, F. Zafar, K. Siddiqui, R. D. Coleman, D. L. Morales, J. S. Heinle, J. W. Rossano, E. B. Mossad, and C. D. Fraser Jr, “Fenestration during Fontan palliation: Now the exception instead of the rule,” *The Journal of Thoracic and Cardiovascular Surgery*, vol. 140, no. 1, pp. 129–136, 2010.

[100] M. Ono, D. Boethig, H. Goerler, M. Lange, M. Westhoff-Bleck, and T. Breymann, “Clinical outcome of patients 20 years after Fontan operation–effect of fenestration on late morbidity,” *European Journal of Cardio-Thoracic Surgery*, vol. 30, no. 6, pp. 923–929, 2006.

[101] K. N. Pundi, J. N. Johnson, J. A. Dearani, K. N. Pundi, Z. Li, C. A. Hinck, S. H. Dahl, B. C. Cannon, P. W. O’Leary, D. J. Driscoll, and F. Cetta, “40-year follow-up after the Fontan operation: Long-term outcomes of 1,052 patients,” *Journal of the American College of Cardiology*, vol. 66, no. 15, pp. 1700–1710, 2015.

[102] C. Poh and Y d’Udekem, “Life after surviving Fontan surgery: A meta-analysis of the incidence and predictors of late death,” *Heart, Lung and Circulation*, vol. 27, no. 5, pp. 552–559, 2018.

[103] G. Barber, J. G. Helton, B. A. Aglira, A. J. Chin, J. D. Murphy, J. D. Pigott, and W. I. Norwood, “The significance of tricuspid regurgitation in hypoplastic left-heart syndrome,” *American Heart Journal*, vol. 116, no. 6,1, pp. 1563–1567, 1988.

[104] A Reyes 2nd, E. L. Bove, R. S. Mosca, T. J. Kulik, and A. Ludomirsky, “Tricuspid valve repair in children with hypoplastic left heart syndrome during staged surgical reconstruction,” *Circulation*, vol. 96, no. 9 Suppl, pp. II–341–3, 1997.

[105] S. Sano, S.-C. Huang, S. Kasahara, K. Yoshizumi, Y. Kotani, and K. Ishino, “Risk factors for mortality after the Norwood procedure using right ventricle to pulmonary artery shunt,” *The Annals of Thoracic Surgery*, vol. 87, no. 1, pp. 178–186, 2009.

[106] M. Elmi, E. J. Hickey, W. G. Williams, G. Van Arsdell, C. A. Caldarone, and B. W. McCrindle, “Long-term tricuspid valve function after Norwood operation,” *The Journal of Thoracic and Cardiovascular Surgery*, vol. 142, no. 6, 1341–1347.e4, 2011.

[107] J. Sugiura, T. Nakano, S. Oda, A. Usui, Y. Ueda, and H. Kado, "Effects of tricuspid valve surgery on tricuspid regurgitation in patients with hypoplastic left heart syndrome: A non-randomized series comparing surgical and non-surgical cases," *European Journal of Cardio-Thoracic Surgery*, vol. 46, no. 1, pp. 8–13, 2014.

[108] B. Alsoufi, R. Sinha, C. McCracken, J. Figueroa, F. Altin, and K. Kanter, "Outcomes and risk factors associated with tricuspid valve repair in children with hypoplastic left heart syndrome," *European Journal of Cardio-Thoracic Surgery*, vol. 54, no. 6, pp. 993–1000, 2018.

[109] M. Ono, B. Mayr, M. Burri, N. Piber, C. Röhlig, M. Strbad, J. Cleuziou, A. Hager, J. Hörer, and R. Lange, "Tricuspid valve repair in children with hypoplastic left heart syndrome: Impact of timing and mechanism on outcome," *European Journal of Cardio-Thoracic Surgery*, vol. 57, no. 6, pp. 1083–1090, 2020.

[110] V. A. Starnes, M. L. Griffin, P. T. Pitlick, D. Bernstein, D. Baum, K. Ivens, and N. E. Shumway, "Current approach to hypoplastic left heart syndrome: Palliation, transplantation, or both?" *The Journal of Thoracic and Cardiovascular Surgery*, vol. 104, no. 1, pp. 189–195, 1992.

[111] K. Hoshino, K. Ogawa, T. Hishitani, R. Kitazawa, and R. Uehara, "Hypoplastic left heart syndrome: Duration of survival without surgical intervention," *American Heart Journal*, vol. 137, no. 3, pp. 535–542, 1999.

[112] S. Weinstein, J. W. Gaynor, N. D. Bridges, G. Wernovsky, L. M. Montenegro, R. I. Godinez, and T. L. Spray, "Early survival of infants weighing 2.5 kilograms or less undergoing first-stage reconstruction for hypoplastic left heart syndrome," *Circulation*, vol. 100, pp. II–167–II–170, 1999.

[113] P. Lang and W. I. Norwood, "Hemodynamic assessment after palliative surgery for hypoplastic left heart syndrome," *Circulation*, vol. 68, no. 1, pp. 104–108, 1983.

[114] J. Helton, B. Aglira, A. Chin, J. Murphy, J. Pigott, and W. Norwood, "Analysis of potential anatomic or physiologic determinants of outcome of palliative surgery for hypoplastic left heart syndrome," *Circulation*, vol. 74, no. 3 Pt 2, pp. I70–6, 1986.

[115] V. Hraška, M. Nosál, P. Sỳkora, V. Soják, M. Šagát, and P. Kunovskỳ, "Results of modified Norwood's operation for hypoplastic left heart syndrome," *European Journal of Cardio-Thoracic Surgery*, vol. 18, no. 2, pp. 214–219, 2000.

[116] R. A. Jonas, D. D. Hansen, N. Cook, and D. Wessel, "Anatomic subtype and survival after reconstructive operation for hypoplastic left heart syndrome," *The Journal of Thoracic and Cardiovascular Surgery*, vol. 107, no. 4, pp. 1121–1128, 1994.

[117] J. M. Forbess, N. Cook, S. J. Roth, A. Serraf, J. E. Mayer Jr, and R. A. Jonas, "Ten-year institutional experience with palliative surgery for hypoplastic left heart syndrome: Risk factors related to stage I mortality," *Circulation*, vol. 92, pp. 262–266, 1995.

[118] J. Hirsch, R. Ohye, E. Devaney, C. Goldberg, and E. Bove, "The lateral tunnel Fontan procedure for hypoplastic left heart syndrome: Results of 100 consecutive patients," *Pediatric Cardiology*, vol. 28, pp. 426–432, 2007.

[119] D. A. Hehir, T. E. Dominguez, J. A. Ballweg, C. Ravishankar, B. S. Marino, G. L. Bird, S. C. Nicolson, T. L. Spray, J. W. Gaynor, and S. Tabbutt, "Risk factors for interstage death after stage 1 reconstruction of hypoplastic left heart syndrome and variants," *The Journal of Thoracic and Cardiovascular Surgery*, vol. 136, no. 1, 94–99.e3, 2008.

[120] A. C. Chang, P. E. Farrell Jr, K. A. Murdison, J. M. Baffa, G. Barber, W. I. Norwood, and J. D. Murphy, "Hypoplastic left heart syndrome: Hemodynamic and angiographic assessment after initial reconstructive surgery and relevance to modified Fontan procedure," *Journal of the American College of Cardiology*, vol. 17, no. 5, pp. 1143–1149, 1991.

[121] R. S. Mosca, T. J. Kulik, C. S. Goldberg, R. P. Vermilion, J. R. Charpie, D. C. Crowley, and E. L. Bove, "Early results of the Fontan procedure in one hundred consecutive patients with hypoplastic left heart syndrome," *The Journal of Thoracic and Cardiovascular Surgery*, vol. 119, no. 6, pp. 1110–1118, 2000.

[122] J. W. Gaynor, N. D. Bridges, M. I. Cohen, W. T. Mahle, W. M. DeCampli, J. M. Steven, S. C. Nicolson, and T. L. Spray, "Predictors of outcome after the Fontan operation: Is hypoplastic left heart syndrome still a risk factor?" *The Journal of Thoracic and Cardiovascular Surgery*, vol. 123, no. 2, pp. 237–245, 2002.

[123] P. Shamszad, T. A. Gospin, B. J. Hong, E. D. McKenzie, and C. J. Petit, "Impact of preoperative risk factors on outcomes after Norwood palliation for hypoplastic left heart syndrome," *The Journal of Thoracic and Cardiovascular Surgery*, vol. 147, no. 3, pp. 897–901, 2014.

[124] W. F. Carlo, K. E. Carberry, J. S. Heinle, D. L. Morales, E. D. McKenzie, C. D. Fraser Jr, and D. P. Nelson, "Interstage attrition between bidirectional Glenn and Fontan palliation in children with hypoplastic left heart syndrome," *The Journal of Thoracic and Cardiovascular Surgery*, vol. 142, no. 3, pp. 511–516, 2011.

[125] I. Wamala, K. G. Friedman, M. Y. Saeed, K. Gauvreau, L. Gellis, M. Borisuk, A. Kaza, S. Emani, P. J. Del Nido, and C. W. Baird, "Tricuspid valve repair concomitant with the Norwood operation among babies with hypoplastic left heart syndrome," *European Journal of Cardio-Thoracic Surgery*, vol. 62, no. 4, ezac033, 2022.

[126] J. S. Son, A. James, C.-P. S. Fan, L. Mertens, B. W. McCrindle, C. Manlhiot, and M. K. Friedberg, "Prognostic value of serial echocardiography in hypoplastic left heart syndrome," *Circulation: Cardiovascular Imaging*, vol. 11, no. 7, e006983, 2018.

[127] A. V. Nguyen, A. Lasso, H. H. Nam, J. Faerber, A. H. Aly, A. M. Pouch, A. B. Scanlan, F. X. McGowan, L. Mercer-Rosa, M. S. Cohen, *et al.*, "Dynamic three-dimensional geometry of the tricuspid valve annulus in hypoplastic left heart syndrome with a Fontan circulation," *Journal of the American Society of Echocardiography*, vol. 32, no. 5, 655–666.e13, 2019.

[128] M. Nii, V. Guerra, K. S. Roman, C. K. Macgowan, and J. F. Smallhorn, "Three-dimensional tricuspid annular function provides insight into the mechanisms of tricuspid valve regurgitation in classic hypoplastic left heart syndrome," *Journal of the American Society of Echocardiography*, vol. 19, no. 4, pp. 391–402, 2006.

[129] K Takahashi, A Inage, I. Rebeyka, D. Ross, R. Thompson, A. Mackie, and J. Smallhorn, "Real-time 3-dimensional echocardiography provides new insight into mechanisms of tricuspid valve regurgitation in patients with hypoplastic left heart syndrome," *Circulation*, vol. 120, pp. 1091–1098, 2009.

[130] S. Kutty, T. Colen, R. B. Thompson, E. Tham, L. Li, C. Vijarnsorn, A. Polak, D. T. Truong, D. A. Danford, J. F. Smallhorn, *et al.*, "Tricuspid regurgitation in hypoplastic left heart syndrome: Mechanistic insights from 3-dimensional echocardiography and relationship with outcomes," *Circulation: Cardiovascular Imaging*, vol. 7, no. 5, pp. 765–772, 2014.

[131] S. Shigemitsu, K. Mah, R. B. Thompson, J. Grenier, L. Q. Lin, A. Silmi, M. V. R. Beigh, N. S. Khoo, and T. Colen, "Tricuspid valve tethering is associated with residual regurgitation after valve repair in hypoplastic left heart syndrome: A three-

dimensional echocardiographic study," *Journal of the American Society of Echocardiography*, vol. 34, no. 11, pp. 1199–1210, 2021.

[132] K. Mah, N. S. Khoo, B.-J. Martin, M. Maruyama, S. Alvarez, I. M. Rebeyka, J. Smallhorn, and T. Colen, "Insights from 3D echocardiography in hypoplastic left heart syndrome patients undergoing TV repair," *Pediatric Cardiology*, vol. 43, pp. 735–743, 2022.

[133] V. Bautista-Hernandez, D. W. Brown, H. Loyola, P. O. Myers, M. Borisuk, J Pedro, and C. W. Baird, "Mechanisms of tricuspid regurgitation in patients with hypoplastic left heart syndrome undergoing tricuspid valvuloplasty," *The Journal of Thoracic and Cardiovascular Surgery*, vol. 148, no. 3, pp. 832–840, 2014.

[134] T. Bharucha, O. Honjo, N. Seller, C. Atlin, A. Redington, C. A. Caldarone, G. Van Arsdell, and L. Mertens, "Mechanisms of tricuspid valve regurgitation in hypoplastic left heart syndrome: A case-matched echocardiographic–surgical comparison study," *European Heart Journal–Cardiovascular Imaging*, vol. 14, no. 2, pp. 135–141, 2013.

[135] T. Colen, S. Kutty, R. B. Thompson, E. Tham, A. S. Mackie, L. Li, D. T. Truong, M. Maruyama, J. F. Smallhorn, and N. S. Khoo, "Tricuspid valve adaptation during the first interstage period in hypoplastic left heart syndrome," *Journal of the American Society of Echocardiography*, vol. 31, no. 5, pp. 624–633, 2018.

[136] L. Q. Lin, S. Hatami, J. Y. Coe, T. M. Colen, C. Sergi, R. Thompson, E. S. Di Martino, W. Herzog, Z. A. Sara, D. H. Freed, *et al.*, "A novel right ventricular volume and pressure loaded piglet heart model for the study of tricuspid valve function," *Journal of Visualized Experiments*, no. 161, e61251, 2020.

[137] K. Mah, N. S. Khoo, E. Tham, M. Yaskina, M. Maruyama, B.-J. Martin, S. Alvarez, N. Alami, I. M. Rebeyka, J. Smallhorn, *et al.*, "Tricuspid regurgitation in hypoplastic left heart syndrome: Three-dimensional echocardiography provides additional information in describing jet location," *Journal of the American Society of Echocardiography*, vol. 34, no. 5, pp. 529–536, 2021.

[138] R. G. Ohye, C. A. Gomez, C. S. Goldberg, H. L. Graves, E. J. Devaney, and E. L. Bove, "Repair of the tricuspid valve in hypoplastic left heart syndrome," *Cardiology in the Young*, vol. 16, no. S3, pp. 21–26, 2006.

[139] R. G. Ohye, C. A. Gomez, C. S. Goldberg, H. L. Graves, E. J. Devaney, and E. L. Bove, "Tricuspid valve repair in hypoplastic left heart syndrome," *The Journal of Thoracic and Cardiovascular Surgery*, vol. 127, no. 2, pp. 465–472, 2004.

[140] H. R. Bellsham-Revell, S. M. Tibby, A. J. Bell, T. Witter, J. Simpson, P. Beerbaum, D. Anderson, C. B. Austin, G. F. Greil, and R. Razavi, "Serial magnetic resonance imaging in hypoplastic left heart syndrome gives valuable insight into ventricular and vascular adaptation," *Journal of the American College of Cardiology*, vol. 61, no. 5, pp. 561–570, 2013.

[141] D. Forsha, L. Li, N. Joseph, S. Kutty, and M. K. Friedberg, "Association of left ventricular size with regional right ventricular mechanics in hypoplastic left heart syndrome," *International Journal of Cardiology*, vol. 298, pp. 66–71, 2020.

[142] K. Laohachai, D. Winlaw, G. Sholler, S. Veerappan, A. Cole, and J. Ayer, "The degree of left ventricular hypoplasia is associated with tricuspid regurgitation severity in infants with hypoplastic left heart syndrome," *Pediatric Cardiology*, vol. 40, pp. 1035–1040, 2019.

[143] V. Muthurangu, A. M. Taylor, S. R. Hegde, R. Johnson, R. Tulloh, J. M. Simpson, S. Qureshi, E. Rosenthal, E. Baker, D. Anderson, *et al.*, "Cardiac magnetic resonance imaging after stage I Norwood operation for hypoplastic left heart syndrome," *Circulation*, vol. 112, pp. 3256–3263, 2005.

[144] T. Tongsong, R. Sittiwangkul, S. Khunamornpong, and C. Wanapirak, "Prenatal sonographic features of isolated hypoplastic left heart syndrome," *Journal of Clinical Ultrasound*, vol. 33, no. 7, pp. 367–371, 2005.

[145] C. R. Mart, A. W. Eckhauser, M. Murri, and J. T. Su, "A systematic method for using 3D echocardiography to evaluate tricuspid valve insufficiency in hypoplastic left heart syndrome," *Annals of Pediatric Cardiology*, vol. 7, no. 3, pp. 193–200, 2014.

[146] W. Tworetzky, D. B. McElhinney, V. M. Reddy, M. M. Brook, F. L. Hanley, and N. H. Silverman, "Improved surgical outcome after fetal diagnosis of hypoplastic left heart syndrome," *Circulation*, vol. 103, no. 9, pp. 1269–1273, 2001.

[147] A. K. Kipps, C. Feuille, A. Azakie, J. I. Hoffman, S. Tabbutt, M. M. Brook, and A. J. Moon-Grady, "Prenatal diagnosis of hypoplastic left heart syndrome in current era," *The American Journal of Cardiology*, vol. 108, no. 3, pp. 421–427, 2011.

[148] S. C. Stoica, A. B. Philips, M. Egan, R. Rodeman, J. Chisolm, S. Hill, J. P. Cheatham, and M. E. Galantowicz, "The retrograde aortic arch in the hybrid approach to hypoplastic left heart syndrome," *The Annals of Thoracic Surgery*, vol. 88, no. 6, pp. 1939–1947, 2009.

[149] W. Tworetzky, L. Wilkins-Haug, R. W. Jennings, M. E. van der Velde, A. C. Marshall, G. R. Marx, S. D. Colan, C. B. Benson, J. E. Lock, and S. B. Perry, "Balloon dilation of severe aortic stenosis in the fetu: Potential for prevention of hypoplastic left heart syndrome: Candidate selection, technique, and results of successful intervention," *Circulation*, vol. 110, pp. 2125–2131, 2004.

[150] A. Szwast, Z. Tian, M. McCann, D. Donaghue, and J. Rychik, "Vasoreactive response to maternal hyperoxygenation in the fetus with hypoplastic left heart syndrome," *Circulation: Cardiovascular Imaging*, vol. 3, no. 2, pp. 172–178, 2010.

[151] L. R. Freud, D. B. McElhinney, A. C. Marshall, G. R. Marx, K. G. Friedman, P. J. del Nido, S. M. Emani, T. Lafranchi, V. Silva, L. E. Wilkins-Haug, *et al.*, "Fetal aortic valvuloplasty for evolving hypoplastic left heart syndrome: Postnatal outcomes of the first 100 patients," *Circulation*, vol. 130, pp. 638–645, 2014.

[152] S. Sano, K. Ishino, H. Kado, Y. Shiokawa, K. Sakamoto, M. Yokota, and M. Kawada, "Outcome of right ventricle–to–pulmonary artery shunt in first-stage palliation of hypoplastic left heart syndrome: A multi-institutional study," *The Annals of Thoracic Surgery*, vol. 78, no. 6, pp. 1951–1958, 2004.

[153] H. Asakai, J. C. Galati, S. Weskamp, B. Jones, J. Millar, I. E. Konstantinov, Y. d'Udekem, C. P. Brizard, and M. M. Cheung, "Impact of Blalock-Taussig shunt size on tricuspid regurgitation in hypoplastic left heart syndrome," *The Annals of Thoracic Surgery*, vol. 97, no. 6, pp. 2123–2128, 2014.

[154] C. Pizarro, T. Mroczek, E. Malec, and W. I. Norwood, "Right ventricle to pulmonary artery conduit reduces interim mortality after stage 1 Norwood for hypoplastic left heart syndrome," *The Annals of Thoracic Surgery*, vol. 78, no. 6, pp. 1959–1964, 2004.

[155] C. L. Cua, R. R. Thiagarajan, K. Gauvreau, L. Lai, J. M. Costello, D. L. Wessel, J Pedro, J. E. Mayer Jr, J. W. Newburger, and P. C. Laussen, "Early postoperative outcomes in a series of infants with hypoplastic left heart syndrome undergoing stage I palliation operation with either modified Blalock-Taussig shunt or right ven-

tricle to pulmonary artery conduit," *Pediatric Critical Care Medicine*, vol. 7, no. 3, pp. 238–244, 2006.

[156] J. Y. Cao, K. Phan, J. Ayer, D. S. Celermajer, and D. S. Winlaw, "Long term survival of hypoplastic left heart syndrome infants: Meta-analysis comparing outcomes from the modified Blalock–Taussig shunt and the right ventricle to pulmonary artery shunt," *International Journal of Cardiology*, vol. 254, pp. 107–116, 2018.

[157] V. Bautista-Hernandez, M. Scheurer, R. Thiagarajan, J. Salvin, F. A. Pigula, S. Emani, F. Fynn-Thompson, H. Loyola, J. Schiff, P. J. del Nido, *et al.*, "Right ventricle and tricuspid valve function at midterm after the fontan operation for hypoplastic left heart syndrome: Impact of shunt type," *Pediatric Cardiology*, vol. 32, pp. 160–166, 2011.

[158] M. Galantowicz and J. P. Cheatham, "Lessons learned from the development of a new hybrid strategy for the management of hypoplastic left heart syndrome," *Pediatric Cardiology*, vol. 26, pp. 190–199, 2005.

[159] D. Lim, B. Peeler, G. Matherne, I. Kron, and H. Gutgesell, "Risk-stratified approach to hybrid transcatheter–surgical palliation of hypoplastic left heart syndrome," *Pediatric cardiology*, vol. 27, pp. 91–95, 2006.

[160] J. Philip, K. Reyes, M. Ebraheem, D. Gupta, J. C. Fudge, and M. S. Bleiweis, "Hybrid procedure with pulsatile ventricular assist device for hypoplastic left heart syndrome awaiting transplantation," *The Journal of Thoracic and Cardiovascular Surgery*, vol. 158, no. 2, e59–e61, 2019.

[161] D. Chetan, Y. Kotani, F. Jacques, J. A. Poynter, L. N. Benson, K.-J. Lee, R. R. Chaturvedi, M. K. Friedberg, G. S. Van Arsdell, C. A. Caldarone, *et al.*, "Surgical palliation strategy does not affect interstage ventricular dysfunction or atrioventricular valve regurgitation in children with hypoplastic left heart syndrome and variants," *Circulation*, vol. 128, no. 11_suppl_1, S205–S212, 2013.

[162] H. B. Grotenhuis, B. Ruijsink, D. Chetan, A. Dragulescu, M. K. Friedberg, Y. Kotani, C. A. Caldarone, O. Honjo, and L. L. Mertens, "Impact of Norwood versus hybrid palliation on cardiac size and function in hypoplastic left heart syndrome," *Heart*, vol. 102, pp. 966–974, 2016.

[163] C. D. Fraser Jr and R. B. Mee, "Modified Norwood procedure for hypoplastic left heart syndrome," *The Annals of Thoracic Surgery*, vol. 60, no. 3, S546–S549, 1995.

[164] D. A. Ashburn, B. W. McCrindle, C. I. Tchervenkov, M. L. Jacobs, G. K. Lofland, E. L. Bove, T. L. Spray, W. G. Williams, E. H. Blackstone, and C. H. S. Society, "Outcomes after the Norwood operation in neonates with critical aortic stenosis or aortic valve atresia," *The Journal of Thoracic and Cardiovascular Surgery*, vol. 125, no. 5, pp. 1070–1082, 2003.

[165] J. Kasnar-Samprec, A. Kühn, J. Hörer, M. Vogt, J. Cleuziou, R. Lange, and C. Schreiber, "Unloading of right ventricle by bidirectional superior cavopulmonary anastomosis in hypoplastic left heart syndrome patients promotes remodeling of systemic right ventricle but does not improve tricuspid regurgitation," *The Journal of Thoracic and Cardiovascular Surgery*, vol. 144, no. 5, pp. 1102–1109, 2012.

[166] J. H. Hansen, A. Uebing, A. K. Furck, J. Scheewe, O. Jung, G. Fischer, and H.-H. Kramer, "Risk factors for adverse outcome after superior cavopulmonary anastomosis for hypoplastic left heart syndrome," *European Journal of Cardio-Thoracic Surgery*, vol. 40, no. 1, e43–e49, 2011.

[167] I. Salik, B. Mehta, and S. Ambati, "Bidirectional Glenn procedure or Hemi-Fontan," *StatPearls [Internet]*, 2020, URL = https://pubmed.ncbi.nlm.nih.gov/33085446/.

[168] W. I. Douglas, C. S. Goldberg, R. S. Mosca, I. H. Law, and E. L. Bove, "Hemi-Fontan procedure for hypoplastic left heart syndrome: Outcome and suitability for Fontan," *The Annals of Thoracic Surgery*, vol. 68, no. 4, pp. 1361–1367, 1999.

[169] J. B. Edelson, C. Ravishankar, H. Griffis, X. Zhang, J. Faerber, M. M. Gardner, M. Y. Naim, C. E. Macsio, A. C. Glatz, and D. J. Goldberg, "A comparison of bidirectional Glenn vs. Hemi-Fontan procedure: An analysis of the single ventricle reconstruction trial public use dataset," *Pediatric Cardiology*, vol. 41, pp. 1166–1172, 2020.

[170] S. Ugaki, N. S. Khoo, D. B. Ross, I. M. Rebeyka, and I. Adatia, "Tricuspid valve repair improves early right ventricular and tricuspid valve remodeling in patients with hypoplastic left heart syndrome," *The Journal of Thoracic and Cardiovascular Surgery*, vol. 145, no. 2, pp. 446–450, 2013.

[171] E. L. Bove, R. G. Ohye, E. J. Devaney, and J. Hirsch, "Tricuspid valve repair for hypoplastic left heart syndrome and the failing right ventricle," in *Seminars in Thoracic and Cardiovascular Surgery: Pediatric Cardiac Surgery Annual*, Elsevier, vol. 10, 2007, pp. 101–104.

[172] O. Honjo, C. R. Atlin, L. Mertens, O. O. Al-Radi, A. N. Redington, C. A. Caldarone, and G. S. Van Arsdell, "Atrioventricular valve repair in patients with functional single-ventricle physiology: Impact of ventricular and valve function and morphology on survival and reintervention," *The Journal of Thoracic and Cardiovascular Surgery*, vol. 142, no. 2, pp. 326–335, 2011.

[173] A. Anssari-Benam, D. Bader, and H. Screen, "A combined experimental and modelling approach to aortic valve viscoelasticity in tensile deformation," *Journal of Materials Science: Materials in Medicine*, vol. 22, pp. 253–262, 2011.

[174] Y. Zou and Y. Zhang, "The orthotropic viscoelastic behavior of aortic elastin," *Biomechanics and Modeling in Mechanobiology*, vol. 10, pp. 613–625, 2011.

[175] J. Stella, J. Liao, and M. Sacks, "Time-dependent biaxial mechanical behavior of the aortic heart valve leaflet," *Journal of Biomechanics*, vol. 40, no. 14, pp. 3169–3177, 2007.

[176] C. Lee, R. Midura, V. Hascall, and I. Vesely, "The effect of elastin damage on the mechanics of the aortic valve," *Journal of Biomechanics*, vol. 34, no. 2, pp. 203–210, 2001.

[177] T. Doehring, A. Freed, E. Carew, and I. Vesely, "Fractional order viscoelasticity of the aortic valve cusp: An alternative to quasilinear viscoelasticity," *Journal of Biomechanical Engineering*, vol. 127, no. 4, pp. 700–708, 2005.

[178] C. M. Pierlot, A. D. Moeller, J. M. Lee, and S. M. Wells, "Biaxial creep resistance and structural remodeling of the aortic and mitral valves in pregnancy," *Annals of Biomedical Engineering*, vol. 43, pp. 1772–1785, 2015.

[179] E. L. Bove, F. Migliavacca, M. R. de Leval, R. Balossino, G. Pennati, T. R. Lloyd, S. Khambadkone, T.-Y. Hsia, and G. Dubini, "Use of mathematic modeling to compare and predict hemodynamic effects of the modified Blalock–Taussig and right ventricle–pulmonary artery shunts for hypoplastic left heart syndrome," *The Journal of Thoracic and Cardiovascular Surgery*, vol. 136, no. 2, 312–320.e2, 2008.

[180] R. Simón-Allué, A. Cordero, and E. Peña, "Unraveling the effect of boundary conditions and strain monitoring on estimation of the constitutive parameters of elastic membranes by biaxial tests," *Mechanics Research Communications*, vol. 57, pp. 82–89, 2014.

[181] A. Avanzini and D. Battini, "Integrated experimental and numerical comparison of different approaches for planar biaxial testing of a hyperelastic material," *Advances in Materials Science and Engineering*, vol. 2016, 2016.

[182] Y. C. Fung, "Biorheology of soft tissues," *Biorheology*, vol. 10, no. 2, pp. 139–155, 1973.

[183] G. F. Caetano, M. Fronza, M. N. Leite, A. Gomes, and M. A. C. Frade, "Comparison of collagen content in skin wounds evaluated by biochemical assay and by computer-aided histomorphometric analysis," *Pharmaceutical Biology*, vol. 54, no. 11, pp. 2555–2559, 2016.

[184] W. Zhang, S. Ayoub, J. Liao, and M. S. Sacks, "A meso-scale layer-specific structural constitutive model of the mitral heart valve leaflets," *Acta Biomaterialia*, vol. 32, pp. 238–255, 2016.

[185] S. H. Alavi, V. Ruiz, T. Krasieva, E. L. Botvinick, and A. Kheradvar, "Characterizing the collagen fiber orientation in pericardial leaflets under mechanical loading conditions," *Annals of Biomedical Engineering*, vol. 41, pp. 547–561, 2013.

[186] G. A. Holzapfel, *Nonlinear Solid Mechanics. A Continuum Approach for Engineering*. Chichester: John Wiley & Sons, 2000.

[187] J. N. Reddy, *An Introduction to Continuum Mechanics*. Cambridge University Press, 2013.

[188] K. May-Newman and F. C. Yin, "Biaxial mechanical behavior of excised porcine mitral valve leaflets," *American Journal of Physiology: Heart and Circulatory Physiology*, vol. 269, no. 4, H1319–H1327, 1995.

[189] S. M. Wells, C. M. Pierlot, and A. D. Moeller, "Physiological remodeling of the mitral valve during pregnancy," *American Journal of Physiology: Heart and Circulatory Physiology*, vol. 303, no. 7, H878–H892, 2012.

[190] D. O. Craiem, F. J. Rojo, J. M. Atienza, G. V. Guinea, and R. L. Armentano, "Fractional calculus applied to model arterial viscoelasticity," *Latin American Applied Research*, vol. 38, no. 2, pp. 141–145, 2008.

[191] R. Storn and K. Price, "Differential evolution – a simple and efficient heuristic for global optimization over continuous spaces," *Journal of Global Optimization*, vol. 11, pp. 341–359, 1997.

[192] C.-H. Lee, C. A. Carruthers, S. Ayoub, R. C. Gorman, J. H. G. III, and M. S. Sacks, "Quantification and simulation of layer-specific mitral valve interstitial cells deformation under physiological loading," *Journal of Theoretical Biology*, vol. 373, pp. 26–39, 2015.

[193] M.-J.Chow, J. Mondonedo, V. Johnson, and Y. Zhang, "Progressive structural and biomechanical changes in elastin degraded aorta," *Biomechanics and Modeling in Mechanobiology*, vol. 12, pp. 361–372, 2013.

[194] K. S. Kunzelman and R. P. Cochran, "Stress/strain characteristics of porcine mitral valve tissue: Parallel versus perpendicular collagen orientation," *Journal of Cardiac Surgery*, vol. 7, no. 1, pp. 71–78, 1992.

[195] A. Balguid, M. P. Rubbens, A. Mol, R. A. Bank, A. J. J. C. Bogers, J. P. van Kats, B. A. J. M. de Mol, F. P. T. Baaijens, and C. V. C. Bouten, "The role of collagen cross-links in biomechanical behavior of human aortic heart valve leaflets—relevance for tissue engineering," *Tissue Engineering*, vol. 13, no. 7, pp. 1501–1511, 2007.

[196] K. Gelse, E Pöschl, and T Aigner, "Collagens–structure, function, and biosynthesis," *Advanced Drug Delivery Reviews*, vol. 55, no. 12, pp. 1531–1546, 2003.

[197] L. Debelle and A. J. Alix, "The structures of elastins and their function," *Biochimie*, vol. 81, no. 10, pp. 981–994, 1999.

[198] G. A. Holzapfel, "Determination of material models for arterial walls from uniaxial extension tests and histological structure," *Journal of Theoretical Biology*, vol. 238, pp. 290–302, 2006.

[199] T. Gasser, R. Ogden, and G. Holzapfel, "Hyperelastic modelling of arterial layers with distributed collagen fibre orientations," *Journal of the Royal Society Interface*, vol. 3, no. 6, pp. 15–35, 2006.

[200] B. Wang, Y. Hua, B. Brazile, B. Yang, and I. Sigal, "Collagen fiber interweaving is central to sclera stiffness," *Acta Biomaterialia*, vol. 113, pp. 429–437, 2020.

[201] A. Henney, J. Parker, and M. Davies, "Collagen biosynthesis in normal and abnormal human heart valves," *Cardiovascular Research*, vol. 16, no. 11, pp. 624–630, 1982.

[202] V. Gupta, J. E. Barzilla, J. S. Mendez, E. H. Stephens, E. L. Lee, C. D. Collard, R. Laucirica, P. H. Weigel, and K. J. Grande-Allen, "Abundance and location of proteoglycans and hyaluronan within normal and myxomatous mitral valves," *Cardiovascular Pathology*, vol. 18, no. 4, pp. 191–197, 2009.

[203] K. Barbour and H.-S. Huang, "Strain effects on collagen proteolysis in heart valve tissues," *Mechanics of Time-Dependent Materials*, vol. 24, pp. 85–100, 2020.

[204] E. Stephens, T. Nguyen, A. Itoh, B. N. N.B. Ingels Jr., D. Miller, and K. Grande-Allen, "The effects of mitral regurgitation alone are sufficient for leaflet remodeling," *Circulation*, vol. 118, S243–S249, 2008.

[205] E. M. Joyce, J. Liao, F. J. Schoen, J. E. Mayer, and M. S. Sacks, "Functional collagen fiber architecture of the pulmonary heart valve cusp," *The Annals of Thoracic Surgery*, vol. 87, no. 4, pp. 1240–1249, 2009.

[206] M. J. Scott and I. Vesely, "Morphology of porcine aortic valve cusp elastin," *The Journal of Heart Valve Disease*, vol. 5, no. 5, pp. 464–471, 1996.

[207] S. V. Jett, L. T. Hudson, R. Baumwart, B. N. Bohnstedt, A. Mir, H. M. Burkhart, G. A. Holzapfel, Y. Wu, and C.-H. Lee, "Integration of polarized spatial frequency domain imaging (pSFDI) with a biaxial mechanical testing system for quantification of load-dependent collagen architecture in soft collagenous tissues," *Acta Biomaterialia*, vol. 102, pp. 149–168, 2020.

[208] S. Garg, P. Singh, A. Sharma, and G. Gupta, "A gross comparative anatomical study of hearts in human cadavers and pigs," *International Journal of Medical and Dental Sciences*, vol. 2, no. 2, pp. 170–176, 2013.

[209] X. Wang, M. Ali, and C. Lacerda, "A three-dimensional collagen-elastin scaffold for heart valve tissue engineering," *Bioengineering*, vol. 5, no. 3, p. 69, 2018.

[210] F. Neto, L. Marques, and V. Aiello, "Myxomatous degeneration of the mitral valve," *Autopsy Case Reports*, vol. 8, no. 4, e2018058, 2018.

[211] M. S. Sacks, D. B. Smith, and E. D. Hiester, "A small angle light scattering device for planar connective tissue microstructural analysis," *Annals of Biomedical Engineering*, vol. 25, pp. 678–689, 1997.

[212] M. S. Sacks, D. B. Smith, and E. D. Hiester, "The aortic valve microstructure: Effects of transvalvular pressure," *Journal of Biomedical Materials Research*, vol. 41, no. 1, pp. 131–141, 1998.

[213] T. J. R. Hughes, *The Finite Element Method: Linear Static and Dynamic Finite Element Analysis*. Courier Corporation, 1987.

[214] T. Belytschko, Y. Y. Lu, and L. Gu, "Element-free Galerkin methods," *International Journal for Numerical Methods in Engineering*, vol. 37, no. 2, pp. 229–256, 1994.

[215] C. J. Ross, B. T. Mullins, C. E. Hillshafer, A. Mir, H. M. Burkhart, and C.-H. Lee, "Evaluation of affine fiber kinematics in porcine tricuspid valve leaflets using polarized spatial frequency domain imaging and planar biaxial," *Journal of Biomechanics*, vol. 123, p. 110 475, 2021.

[216] W. Krasny, C. Morin, H. Magoariec, and S. Avril, "A comprehensive study of layer-specific morphological changes in the microstructure of carotid arteries under uniaxial load," *Acta Biomaterialia*, vol. 57, pp. 342–351, 2017.

[217] S. P. Lake, M. F. Hadi, V. K. Lai, and V. H. Barocas, "Mechanics of a fiber network within a non-fibrillar matrix: Model and comparison with collagen-agarose co-gels," *Annals of Biomedical Engineering*, vol. 40, pp. 2111–2121, 2012.

[218] T. Liu, T. J. Hall, P. E. Barbone, and A. A. Oberai, "Inferring spatial variations of microstructural properties from macroscopic mechanical response," *Biomechanics and Modeling in Mechanobiology*, vol. 16, pp. 479–496, 2017.

[219] P. L. Chandran and V. H. Barocas, "Affine versus non-affine fibril kinematics in collagen networks: Theoretical studies of network behavior," *Journal of Biomechanical Engineering*, vol. 128, no. 2, pp. 259–270, 2006.

[220] C. J. Ross, M.-C. Hsu, R. Baumwart, A. Mir, H. M. Burkhart, G. A. Holzapfel, and C.-H. Lee, "Quantification of load-dependent changes in the collagen fiber architecture for the strut chordae tendineae-leaflet insertion of porcine atrioventricular heart valves," *Biomechanics and Modeling in Mechanobiology*, vol. 20, pp. 223–241, 2020.

[221] A. Anssari-Benam, H. Gupta, and H. Screen, "Strain transfer through the aortic valve," *Journal of Biomechanical Engineering*, vol. 134, no. 6, 2012.

[222] A. Anssari-Benam, H. Screen, and A. Bucchi, "Insights into the micromechanics of stress-relaxation and creep behaviours in the aortic valve," *Journal of the Mechanical Behavior of Biomedical Materials*, vol. 93, pp. 230–245, 2019.

[223] A. B. Scanlan, A. V. Nguyen, A. Ilina, A. Lasso, L. Cripe, A. Jegatheeswaran, E. Silvestro, F. X. McGowan, C. E. Mascio, and S. Fuller, "Comparison of 3D echocardiogram-derived 3D printed valve models to molded models for simulated repair of pediatric atrioventricular valves," *Pediatric Cardiology*, vol. 39, pp. 538–547, 2018.

[224] A. Fedorov, R. Beichel, J. Kalpathy-Cramer, J. Finet, J.-C. Fillion-Robin, S. Pujol, C. Bauer, D. Jennings, F. Fennessy, M. Sonka, *et al.*, "3D Slicer as an image computing platform for the Quantitative Imaging Network," *Magnetic Resonance Imaging*, vol. 30, no. 9, pp. 1323–1341, 2012.

[225] M. K. Rausch, W. Bothe, J.-P. E. Kvitting, S. Göktepe, D. C. Miller, and E. Kuhl, "*In vivo* dynamic strains of the ovine anterior mitral valve leaflet," *Journal of Biomechanics*, vol. 44, no. 6, pp. 1149–1157, 2011.

[226] T. Belytschko, Y. Krongauz, D. Organ, M. Fleming, and P. Krysl, "Meshless methods: An overview and recent developments," *Computer Methods in Applied Mechanics and Engineering*, vol. 139, no. 1-4, pp. 3–47, 1996.

[227] J.-S. Chen, C. Pan, C.-T. Wu, and W. K. Liu, "Reproducing kernel particle methods for large deformation analysis of non-linear structures," *Computer Methods in Applied Mechanics and Engineering*, vol. 139, no. 1-4, pp. 195–227, 1996.

[228] A. M. Pouch, A. H. Aly, A. Lasso, A. V. Nguyen, A. B. Scanlan, F. X. McGowan, G. Fichtinger, R. C. Gorman, J. H. Gorman III, P. A. Yushkevich, *et al.*, "Image segmentation and modeling of the pediatric tricuspid valve in hypoplastic left heart syndrome," in *Functional Imaging and Modelling of the Heart: 9th International Conference, FIMH 2017, Toronto, ON, Canada, June 11-13, 2017, Proceedings 9*, Springer, 2017, pp. 95–105.

[229] M. K. Rausch, M. Malinowski, P. Wilton, A. Khaghani, and T. A. Timek, "Engineering analysis of tricuspid annular dynamics in the beating ovine heart," *Annals of Biomedical Engineering*, vol. 46, pp. 443–451, 2018.

[230] G. B. Haycock, G. J. Schwartz, and D. H. Wisotsky, "Geometric method for measuring body surface area: A height-weight formula validated in infants, children, and adults," *The Journal of Pediatrics*, vol. 93, no. 1, pp. 62–66, 1978.

[231] C. J. Ross, E. J. Trimble, E. L. Johnson, R. Baumwart, M. A. Jolley, A. Mir, H. M. Burkhart, and C.-H. Lee, "A pilot investigation of the tricuspid valve annulus in newborns with hypoplastic left heart syndrome," *JTCVS Open*, vol. 10, pp. 324–339, 2022.

[232] C. Petko, A. Uebing, A. Furck, C. Rickers, J. Scheewe, and H.-H. Kramer, "Changes of right ventricular function and longitudinal deformation in children with hypoplastic left heart syndrome before and after the Norwood operation," *Journal of the American Society of Echocardiography*, vol. 24, no. 11, pp. 1226–1232, 2011.

[233] E. Pettersen, T. Helle-Valle, T. Edvardsen, H. Lindberg, H.-J. Smith, B. Smevik, O. A. Smiseth, and K. Andersen, "Contraction pattern of the systemic right ventricle: Shift from longitudinal to circumferential shortening and absent global ventricular torsion," *Journal of the American College of Cardiology*, vol. 49, no. 25, pp. 2450–2456, 2007.

[234] M. Malinowski, T. Jazwiec, M. Goehler, N. Quay, J. Bush, S. Jovinge, M. K. Rausch, and T. A. Timek, "Sonomicrometry-derived 3-dimensional geometry of the human tricuspid annulus," *The Journal of Thoracic and Cardiovascular Surgery*, vol. 157, no. 4, 1452–1461.e1, 2018.

[235] M. Malinowski, H. Schubert, J. Wodarek, H. Ferguson, L. Eberhart, D. Langholz, T. Jazwiec, M. K. Rausch, and T. A. Timek, "Tricuspid annular geometry and strain after suture annuloplasty in acute ovine right heart failure," *The Annals of Thoracic Surgery*, vol. 106, no. 6, pp. 1804–1811, 2018.

[236] A. M. Pouch, C. Xu, P. A. Yushkevich, A. S. Jassar, M. Vergnat, J. H. Gorman III, R. C. Gorman, C. M. Sehgal, and B. M. Jackson, "Semi-automated mitral valve morphometry and computational stress analysis using 3D ultrasound," *Journal of Biomechanics*, vol. 45, no. 5, pp. 903–907, 2012.

[237] C. Herz, D. F. Pace, H. H. Nam, A. Lasso, P. Dinh, M. Flynn, A. Cianciulli, P. Golland, and M. A. Jolley, "Segmentation of tricuspid valve leaflets from transthoracic 3D echocardiograms of children with hypoplastic left heart syndrome using deep learning," *Frontiers in Cardiovascular Medicine*, vol. 8, p. 1839, 2021.

[238] A. M. Pouch, H. Wang, M. Takabe, B. M. Jackson, C. M. Sehgal, J. H. Gorman III, R. C. Gorman, and P. A. Yushkevich, "Automated segmentation and geometrical modeling of the tricuspid aortic valve in 3D echocardiographic images," in *Medical Image Computing and Computer-Assisted Intervention–MICCAI 2013: 16th Inter-*

*national Conference, Nagoya, Japan, September 22-26, 2013, Proceedings, Part I 16*, Springer, 2013, pp. 485–492.

[239] H. S. Kim, S. B. Park, S. S. Lo, J. I. Monroe, and J. W. Sohn, "Bidirectional local distance measure for comparing segmentations," *Medical Physics*, vol. 39, no. 11, pp. 6779–6790, 2012.

[240] P. I. Frazier, "A tutorial on Bayesian optimization," *arXiv preprint arXiv:1807.02811*, 2018.

[241] J. A. Weis, M. I. Miga, F. Granero-Moltó, and A. Spagnoli, "A finite element inverse analysis to assess functional improvement during the fracture healing process," *Journal of Biomechanics*, vol. 43, no. 3, pp. 557–562, 2010.

[242] T. Mansi, I. Voigt, B. Georgescu, X. Zheng, E. A. Mengue, M. Hackl, R. I. Ionasec, T. Noack, J. Seeburger, and D. Comaniciu, "An integrated framework for finite-element modeling of mitral valve biomechanics from medical images: Application to MitralClip intervention planning," *Medical Image Analysis*, vol. 16, no. 7, pp. 1330–1346, 2012.

[243] W. Sun, C. Martin, and T. Pham, "Computational modeling of cardiac valve function and intervention," *Annual Review of Biomedical Engineering*, vol. 16, pp. 53–76, 2014.

[244] V. Prot, B. Skallerud, and G. Holzapfel, "Transversely isotropic membrane shells with application to mitral valve mechanics. constitutive modelling and finite element implementation," *International Journal for Numerical Methods in Engineering*, vol. 71, no. 8, pp. 987–1008, 2007.

[245] T. E. David, C. M. David, and C. Manlhiot, "Tricuspid annulus diameter does not predict the development of tricuspid regurgitation after mitral valve repair for mitral regurgitation due to degenerative diseases," *The Journal of Thoracic and Cardiovascular Surgery*, vol. 155, no. 6, pp. 2429–2436, 2018.

[246] Z. Dai, B. K. H. Low, and P. Jaillet, "Federated Bayesian optimization via Thompson sampling," in *Advances in Neural Information Processing Systems 33 (NeurIPS 2020)*, 2020.

[247] M. Balandat, B. Karrer, D. Jiang, S. Daulton, B. Letham, A. G. Wilson, and E. Bakshy, "BoTorch: A framework for efficient Monte-Carlo Bayesian optimization," in *Advances in Neural Information Processing Systems 33 (NeurIPS 2020)*, 2020.

[248] N. Stander and K. Craig, "On the robustness of a simple domain reduction scheme for simulation-based optimization," *Engineering Computations*, vol. 19, no. 4, pp. 431–450, 2002.

[249] A. H. Khalighi, B. V. Rego, A. Drach, R. C. Gorman, J. H. Gorman III, and M. S. Sacks, "Development of a functionally equivalent model of the mitral valve chordae tendineae through topology optimization," *Annals of Biomedical Engineering*, vol. 47, pp. 60–74, 2019.

[250] D. P. Howsmon, B. V. Rego, E. Castillero, S. Ayoub, A. H. Khalighi, R. C. Gorman, J. H. Gorman III, G. Ferrari, and M. S. Sacks, "Mitral valve leaflet response to ischaemic mitral regurgitation: From gene expression to tissue remodelling," *Journal of the Royal Society Interface*, vol. 17, no. 166, 2020.

[251] A. Lee and D. M. Elliott, "Freezing does not alter multiscale tendon mechanics and damage mechanisms in tension," *Annals of the New York Academy of Sciences*, vol. 1409, no. 1, pp. 85–94, 2017.

[252] D. W. Laurence, C. J. Ross, M.-C. Hsu, A. Mir, H. M. Burkhart, G. A. Holzapfel, and C.-H. Lee, "Benchtop characterization of the tricuspid valve leaflet pre-strains," *Acta Biomaterialia*, vol. 152, pp. 321–334, 2022.

[253] S. A. Maas, A. Erdemir, J. P. Halloran, and J. A. Weiss, "A general framework for application of prestrain to computational models of biological materials," *Journal of the Mechanical Behavior of Biomedical Materials*, vol. 61, pp. 499–510, 2016.

[254] J. Vicory, C. Herz, D. Allemang, H. H. Nam, A. Cianciulli, C. Vigil, Y. Han, A. Lasso, M. A. Jolley, and B. Paniagua, "Statistical shape analysis of the tricuspid valve in hypoplastic left heart syndrome," in *International Workshop on Statistical Atlases and Computational Models of the Heart*, Springer, 2021, pp. 132–140.

[255] J. Chen, H. Li, G. He, F. Yao, L. Lai, J. Yao, and L. Xie, "Automatic 3D mitral valve leaflet segmentation and validation of quantitative measurement," *Biomedical Signal Processing and Control*, vol. 79, no. 2, p. 104 166, 2023.

[256] A. Kusiak, C. A. Caldarone, M. D. Kelleher, F. S. Lamb, T. J. Persoon, and A. Burns, "Hypoplastic left heart syndrome: Knowledge discovery with a data mining approach," *Computers in Biology and Medicine*, vol. 36, no. 1, pp. 21–40, 2006.

[257] E. L. Johnson, D. W. Laurence, F. Xu, C. E. Crisp, A. Mir, H. M. Burkhart, C.-H. Lee, and M.-C. Hsu, "Parameterization, geometric modeling, and isogeometric analysis of tricuspid valves," *Computer Methods in Applied Mechanics and Engineering*, vol. 384, p. 113 960, 2021.

[258] V. Fonti and E. Belitser, "Feature selection using LASSO," *VU Amsterdam research paper in business analytics*, vol. 30, pp. 1–25, 2017.

[259] A. K. Waljee, P. D. Higgins, and A. G. Singal, "A primer on predictive models," *Clinical and Translational Gastroenterology*, vol. 5, no. 1, e44, 2014.

[260] D. Bates, M. Mächler, B. Bolker, and S. Walker, "Fitting linear mixed-effects models using *lme4*," *arXiv*, 2014.

[261] J. J. Faraway, *Extending the Linear Model with R: Generalized Linear, Mixed Effects and Nonparametric Regression Models*. Chapman and Hall/CRC, 2016.

[262] J. P. Vande Geest, D. H. Wang, S. R. Wisniewski, M. S. Makaroun, and D. A. Vorp, "Towards a noninvasive method for determination of patient-specific wall strength distribution in abdominal aortic aneurysms," *Annals of Biomedical Engineering*, vol. 34, pp. 1098–1106, 2006.